

Simulation and Analysis of Electrochemical Systems

A DISSERTATION PRESENTED
BY
MICHAEL STEVEN EMANUEL
TO
THE SCHOOL OF ENGINEERING AND APPLIED SCIENCES

IN PARTIAL FULFILLMENT OF THE REQUIREMENTS
FOR THE DEGREE OF
DOCTOR OF PHILOSOPHY
IN THE SUBJECT OF
APPLIED MATHEMATICS

HARVARD UNIVERSITY
CAMBRIDGE, MASSACHUSETTS
APRIL 2025

©2025 – MICHAEL STEVEN EMANUEL
ALL RIGHTS RESERVED.

Simulation and Analysis of Electrochemical Systems

ABSTRACT

Porous electrodes are essential components in redox flow batteries, a promising technology for long duration, grid-scale energy storage, which will be a vital part of the clean energy transition. Carbon capture and storage (CCS) can mitigate and eventually reverse global warming. In this thesis I present four works, in which a porous electrode and a CCS system are each subject to one simulation and one analysis. First, I show a 3D digital twin for porous electrodes that uses direct numerical solution of the governing Navier-Stokes and Nernst-Plank equations for incompressible flow and electrochemical mass transport with Butler-Volmer reaction kinetics. Our performant, open source code handles systems approaching a billion cells at $1.25 \mu\text{m}$ resolution on a single workstation, and will scale well on modern scientific supercomputers. This work also includes a novel reformulation of the steady state concentration problem, and introduces a figure of merit, the mass-transport limiting utilization of an electrode U_{mt} . Second, I simulate the steady state concentrations in an electrochemical acid-base generator that was experimentally characterized by my collaborators and is suitable for CCS. Third, I solve for the equilibrium concentrations in another experimental CCS system, in which aqueous quinones capture CO_2 via both pH-swing and nucleophilicity swing mechanisms. Finally, I perform an elaborate nonlinear iterative calibration to measure the state of charge of an operating porous electrode given experimental image intensity and electrochemical data obtained by fluorescence microscopy.

Contents

TITLE PAGE

COPYRIGHT

ABSTRACT iii

TABLE OF CONTENTS vi

LIST OF FIGURES viii

LIST OF TABLES ix

LIST OF ALGORITHMS x

DEDICATION xi

ACKNOWLEDGMENTS xii

FOREWORD 1

INTRODUCTION 8

1 DIGITAL TWIN FOR POROUS ELECTRODES IN REDOX FLOW BATTERIES 17

1.1 Abstract	18
1.2 Introduction	18
1.3 Theoretical Background	25
1.4 Computational Methods	51
1.5 Results and Discussion - Fluid Flow	75
1.6 Results and Discussion - Chemical Reaction	88
1.7 Conclusions	95
1.8 Code Availability Statement	98

2 SIMULATING AN ACID-BASE GENERATOR 99

2.1 Abstract	100
2.2 Background	100

2.3	Carbon Capture Methods	102
2.4	Acid-Base Generator Design	104
2.5	Experimental Measurement of Crossover in the Acid-Base Generator	107
2.6	Crossover Analysis in the Acid-Base Generator	110
2.7	Numerical Simulation of the Acid-Base Generator	113
2.8	Conclusions	122
2.9	Data and Code Availability Statement	124
3	THERMODYNAMICS OF QUINONE-MEDIATED CARBON CAPTURE	125
3.1	Abstract	126
3.2	Introduction	126
3.3	Thermodynamic Overview	128
3.4	Impact of Capture Mechanisms on System Performance	136
3.5	Numerical Methods for Determining Equilibrium Concentrations	138
3.6	Conclusions	148
3.7	Data and Code Availability Statement	149
4	QUANTITATIVE STATE OF CHARGE MAPPING BY FLUORESCENCE MICROSCOPY IN POROUS ELECTRODES	151
4.1	Abstract	152
4.2	Introduction	153
4.3	Working Principles and Experimental Setup of <i>Operando</i> QEFSM	158
4.4	Results and Discussion	166
4.5	Numerical Methods for Concentration Mapping	179
4.6	Conclusions	191
4.7	Data and Code Availability Statement	193
CONCLUSION		194
4.8	Scientific Conclusions	194
4.9	Comments on Scientific Computing	196
4.10	Future Research Directions	200
4.11	Parting Thoughts	206
AFTERWORD		208
APPENDIX A	SUPPLEMENTARY MATERIAL FOR CHAPTER I	216
APPENDIX B	SUPPLEMENTARY MATERIAL FOR CHAPTER 3	221
APPENDIX C	MUSICAL EPIGRAPHS	227

APPENDIX D YOUTHFUL EPIGRAPHS	229
STATEMENT ON THE USE OF ARTIFICIAL INTELLIGENCE	230
REFERENCES	231

List of Figures

1.1	A redox flow battery being charged	22
1.2	Negolyte redox pair	23
1.3	Overview of three reaction models	24
1.4	Boundary conditions for negolyte half cell simulation	26
1.5	Dependence of equilibrium SOC (s_{eq}) on applied reducing voltage (V_{ar})	39
1.6	Nondimensionalized reaction rate $\tilde{\mathbf{R}}$ and overpotential $\tilde{\eta}$ vs. the state of charge s	47
1.7	Embedded boundary approach in AMReX	52
1.8	Logpile lattice geometry	76
1.9	Streamlines of steady state flow on logpile geometry with 100 Pa pressure at inlet	77
1.10	Convergence of flow simulations	79
1.11	Convergence of flow simulations with mesh refinement	81
1.12	Reference flow simulation at $p = 100$ Pa on mid-plane $z = 80 \mu\text{m}$	84
1.13	Relative error of upsampled simulation vs. reference simulation	85
1.14	Flow simulations at pressures spanning five orders of magnitude	87
1.15	Simulated state of charge with $p = 100$ Pa and $V_{\text{ar}} = 0$ mV	89
1.16	Simulated reaction steady state using SBV model with $p = 10$ Pa and $V_{\text{ar}} = 0$ mV	90
1.17	Convergence of reaction simulations	92
1.18	SOC difference between BV and SBV models	93
1.19	Simulated potential ϕ_L in the BV model with $p = 10$ Pa and $V_{\text{ar}} = 0$ mV	95
2.1	Cell structure with technique comparison	105
2.2	Hydroxide and proton crossover test	109
2.3	Regression fit of hydroxide ion crossover data	113
2.4	Unfurling of serpentine flow field for 2D modeling	114
2.5	Schematic of acid-base generator simulation	115
2.6	Simulated acid-base generator	120
3.1	Equilibrium concentrations resulting from solving equilibrium equations (3.1–3.10)	132
3.2	Equilibrium concentrations with varying parameter values for $pK_{\text{a}2}$ and $p\text{CO}_2$	134
4.1	State of charge mapping by <i>operando</i> electrochemical fluorescence microscopy in a porous electrode	152
4.2	Microfluidic flow cell compatible with electrochemistry and confocal microscopy	158
4.3	Fluorescence properties of AQDS/H ₂ AQDS redox couple	162
4.4	Characteristic plots from multi-step chronoamperometry of AQDS at different concentrations flowing through a porous carbon electrode	167

4.5	Polarization curves from multi-step chronoamperometry	170
4.6	Local SOC deduced from fluorescence intensity maps	174
4.7	Operando concentration profiles	178
4.8	1:1 (AQDS:H ₂ AQDS) binding dimer model	181
4.9	Schematic depiction of different contributions to spatially averaged raw intensity I_{total}	184
4.10	Selection of valid pixels for SOC maps	185
4.11	Schematic of simple constant gradient assumption	190
4.12	Spatial mapping of the simplified model featuring a constant gradient	191
4.13	Learning loops to understand electrode processes and behavior	201
4.14	Signed distance to the nearest electrode surface in a 2D geometry	203
B.1	Increased capital and operating costs with higher area-specific resistance	222
B.2	<i>In-situ</i> pH change of the anolyte during hydroxide ion crossover test	224
B.3	Area normalized molarity of hydroxide ions in the anolyte over time during hydroxide crossover test	225
B.4	Area normalized molarity of protons in the catholyte over time during proton crossover test with various center flow rates	226

List of Tables

1.1	Flow convergence fit for three simulated geometries	80
1.2	Convergence of mesh refined simulations	82
1.3	Comparison of mesh refined simulations to reference	93
1.4	Comparison of alternative models to SBV	94
2.1	Predicted electrical summary statistics for acid-base generator	121
A.1	Symbols	216
A.2	SimulationParameters	220
B.1	Comparison between electrochemical acid-base generators	223
B.2	Experimental conditions used for hydroxide ion crossover tests	224
B.3	Linear fitting results for hydroxide ion crossover tests	225
B.4	Linear fitting results for proton crossover tests with various center flow rates	226

List of Algorithms

1.1	Flow Simulation	57
1.2	Butler-Volmer Fixed Point Iteration	62
1.3	Butler-Volmer Time Step	64
1.4	Butler-Volmer Simulation	65
1.5	Simplified Butler-Volmer Model	68
1.6	Nernst Model	70
1.7	SOC at Mass Transport Limit	72
1.8	Explicit Nernst Model	74
3.1	Objective Function for Equilibrium Concentrations	146

TO MY WIFE, CHRISTIE.



IN MY LIFE, I'VE LOVED YOU MORE.

Acknowledgments

Writing the acknowledgments to a dissertation at the age of forty eight is an emotional experience of intense personal reflection leading to profound feelings of gratitude. It amounts to a thorough inventory of my life and the people important to me when I'm likely past the half way point. I am willing to run the risk of appearing self absorbed to spill so much ink here—in living longer, I've accumulated a longer list of people to thank.

The last four years of my PhD have been funded by the U.S. Department of Energy through the Office of Basic Energy Sciences (DE-SC0020170). This is no rote incantation or bookkeeping requirement—I write with genuine gratitude to both the grant administrators in our federal government and my fellow taxpayers who have generously supported scientific research including my own.

My education began with the kind and dedicated preschool staff at Beth El Synagogue in New Rochelle, NY, the “Queen City of the Sound” in Westchester County, just north of New York City. I received an excellent primary and secondary education in the New Rochelle public schools that included programming for academically advanced students while maintaining strong connections among students with diverse backgrounds. It is only now, as a parent, that I can truly appreciate the quality and value of my early education, which maintained high standards without imposing ruinously high tuition and taxes on my parents and neighbors. My AP Physics teacher, Anthony Soldano, was a radioman in the Korean War who reminded us to “utilize the utilities” to solve whatever problem we faced. My AP U.S. History teacher Paula Porricelli passed on an enduring optimism and belief in the United States as a continuing effort to achieve a more perfect union notwithstanding the ways we have fallen short. My track coaches Joe Soprano and Bill Martin were both elite half milers in their day¹ and taught me the importance of hard work, how to suck it up, and the value of competition in achieving excellence—in short, what I call “building character.”

I enjoyed an embarrassing array of phenomenal professors during my Harvard undergraduate experience, receiving an A.B. in mathematics in 1999. I learned quantum mechanics from Michael Tinkham, and will never forget the joy of finally learning where electron orbitals came from, or his description of himself as a “low temperature man.” I learned graduate real analysis from Curt McMullen, and got to touch his Fields Medal in the math lounge in 1998. I took inorganic chemistry from Roy Gordon and decades later became his coauthor. I learned about chamber music from Robert Levin and paleontology from Stephen Jay Gould. Next to these famously accomplished scholars, I basked in the personal attention and warmth of younger professors in the math department.

¹Coach Sap ran the half mile in 1:50 on a cinder track wearing archaic leather spikes; Coach Martin had a 1:45 PR over 800m and qualified for the U.S. Olympic team in 1980 when Jimmy Carter boycotted the Moscow games.

Mike Nakamaye shared his love of Pelikan fountain pens with purple ink. Kamal Khuri-Makdisi taught me how to write a math proof, and was extremely gracious to write me a recommendation letter for graduate school decades later. I must not forgot the friends I made in the class of 1999. Not one, but three of my former classmates became professors and wrote me recommendation letters for a return to graduate school in 2018—Thomas Knox, Constantine Caramanis and Samuel Grushevsky. And my loyal friends Leonid Yuditsky and Oksana Cherniavsky are traveling from New York to Cambridge to attend my PhD defense.

My career in fixed income portfolio management was a middling success before I went to work at Convexity Capital Management, a firm founded by a senior team at the Harvard Management Company (HMC) from the days when the Harvard endowment was the envy of not just the Ivy League but the whole investment world. Jack Meyer, Dave Mittelman, and Maurice Samuels were all class acts who gave me the opportunity to excel, and always treated me more than fairly. Ed DeNoble was the best boss I ever had, and had an uncanny genius to navigate the global financial crisis. The seven fat years we had together saw me through seven lean years as a PhD student with three kids. I only wish Dave was still here—he loved science and astronomy, and would have gotten a kick from attending my defense.

I was again fortunate in my professors upon my return to graduate school in 2018. Pavlos Protopapas taught me about machine learning and astronomy, and welcomed me into his research group. Joe Blitzstein shared his uniquely insightful approach to statistics, and while I found his exams to be stressful, the preparation required to get fast enough to confidently finish on time really was an effective pedagogical technique. But the professor who changed my career trajectory was, unsurprisingly, my advisor Chris Rycroft.

When I joined the Data Science masters program, I was unsure of my next steps and thought they might involve the nascent AI boom. But as soon as I took AM 205² with Chris, I was hooked. Chris had rekindled my love of science and scientific computing, and I knew in my heart I was going to try for a PhD before my head caught up. Chris is an extraordinary teacher who delivers crisp, fast paced lectures and assigns challenging problems that push you to master key numerical techniques. But separately from his technical excellence, at a time when I felt like I didn’t fit in—I was twice the age of some of my classmates and lived off campus with my family—Chris made me feel welcome, and that I belonged. He was also willing to take a chance on what I have jokingly called a “superannuated graduate student” with an unconventional background. Chris has been everything I could have asked for in an advisor. He found an ideal scientific project for me simulating flow batteries. He also had a light touch and kept me on track without micromanaging me, and maintained a strong esprit de corps in the Rycroft group. I’ve learned so much from Chris about scientific computing, scientific research, and scientific writing.

My PhD took an unexpected turn when Chris left Harvard. I had a contentious negotiation with the Harvard administration in which I insisted on maintaining Chris as my advisor. As part of that arrangement, Mike Aziz stepped in to act as my co-advisor. This was not a pro-forma role signing study cards; Mike has provided valuable

²AM 205 is the flagship introduction to scientific computing in the Applied Math department.

and substantive academic guidance. Attending Aziz group meetings in person has been hugely beneficial to both my scientific development and avoiding a sense of social isolation, and directly led to two papers appearing as chapters in this thesis. I've learned a great deal from Mike, especially about how to do the job of a senior scientist supervising many graduate students and multidisciplinary research collaborations, and how to secure grant funding for research. I also acknowledge and thank Boris Kozinsky for his service on my PhD committee.

To the many members of the Rycroft group, the Aziz group, and the BES Porous Electrodes collaboration team: I could not have asked for a better group of scientific collaborators. You have enriched my PhD studies immeasurably through your inspiring research projects—on which I was occasionally fortunate enough to collaborate, your penetrating questions, your perceptive feedback, and your friendship. I particularly wish to recognize: Simone Dussi, Yue Sun, Shmuel Rubinstein, Thomas Cochard, Anton Graf, Kiana Amini, Jennifer Lewis, Dylan Barber, Sofía Edgar, Dawei Xi, Thomas George, Eric Fell and Jordan Sosa.

Finally, I thank my family for their unwavering love and support. My parents—Marilyn and Steven—have always believed in me, and worked hard to give me every opportunity to succeed. They encouraged my scholarship and interest in science, and gave me the secure emotional foundation required to take chances. My four siblings—Meredith, Jeffrey, Samuel and Allison—remain close and have always been in my corner. My parents-in-law Betsy and Stan Gibson, and sisters-in-law Carolyn and Julia Gibson, all live close by. Stan and Betsy have treated me like the son they never had; and the Gibsons have provided child care help at pivotal moments. I am blessed with three children: Victor (10), Renée (7), and Ruth (4). They are the joy of my life and kept my spirits up through the toughest times of Covid isolation, segmentation faults caused by misplaced ampersands, and MLMG solvers that failed to converge.³ Victor and I are planning to outlast a rogue presidential administration with a 1461 day win streak on the NYT crossword; Renée is my photography / videography helper; and Ruth is my space heater who shares my taste for fancy clothes. Last and most of all, my wife Christie has been my rock and source of strength through all the ups and downs, the highs and lows. She married a prince of fixed income (well, maybe a count) and enthusiastically accepted a swap for a research assistant because she believed in me and the value of my scientific work. She is always ready to listen to a tale of a research problem overcome or a rant better shared at home. She has a great sense of humor, deep roots in the community, and is an excellent cook. After twelve years of marriage, she's still got it. There is no way I could have made it without her love and companionship. To all of you, thank you so much.

³Multi-Level, Multi-Grid solvers are used extensively in the redox flow battery simulation code in Chapter 1.

“Madamina, il catalogo è questo ...”

[My dear lady, this is the list ...]

Leporello, *Don Giovanni*, Act 1 - the Catalogue Aria

Allegro

Ma-da - mi - na! Il ca-ta - lo-go'è ques - to,

Wolfgang Amadeus Mozart, *Don Giovanni*, K. 527. Libretto by Lorenzo DaPonte.

Foreword

I have conducted an eclectic and multidisciplinary research program during my PhD studies. Rather than focusing on a particular mathematical problem or approach, I have instead been guided by substantive problems that I wanted to investigate in two areas relevant to addressing climate change: porous electrodes used in redox flow batteries (RFBs) and CO₂ capture systems. As a result of this emphasis on solving specific problems rather than on the mathematics used to arrive at the results, this thesis runs a gamut of numerical simulations and analysis. The unifying thread is the use of numerical methods to advance efforts to limit and eventually reverse global warming before catastrophic consequences for humankind. A second lodestone in my research has been the Nernst-Planck equation, which describes many phenomena relating on mass transport. Without further ado, I will now briefly outline the contents of the four chapters in my thesis.

Chapter 1 is my would-be *magnus opus*. This epic chapter recounts the tale of four years of work to simulate and understand porous electrodes as they operate in RFBs. It is a reprint of *Digital Twin for Porous Electrodes in Redox Flow Batteries*, a preprint on arXiv which will be submitted shortly to *Physics*

of Fluids [1]. My advisor Chris Rycroft and I performed the highest fidelity numerical simulation ever done of a porous electrode, directly solving the governing partial differential equations for both an incompressible fluid flow and an electrochemical reaction at steady state. This simulation was carried out in three dimensions at a resolution of $1.25 \mu\text{m}$ and a scale approaching a billion cells. We have developed a highly performant, scalable, and open source code that is compatible with the world's most advanced scientific supercomputing facilities. This is a project conceived for the era of exascale computing, when for the first time in history, it is both technically and economically feasible to perform scientific calculations at this scale.

Along the way, we have also developed a number of unexpected insights into the steady state concentration profiles by changing the way we think about the system. Instead of the usual question—how fast are species being transformed on the reactive surface?—we posed a dual problem—what is the overpotential on the reactive surface such that diffusive mass transport offsets electrochemical conversion at steady state? This one idea is surprisingly powerful both for simulating and understanding porous electrodes.

[Chapter 2](#) arose as a serendipitous collaboration when Dawei Xi commented in a group meeting that he was trying to do a numerical simulation for a system he had experimentally characterized, but that COMSOL “didn’t work.” This was music to my ears. After years of toil debugging obscure errors in a hand-rolled C++ code, I have grown increasingly agitated every time I read another numerical methods manuscript where the authors outsourced all the computation to COMSOL. As a practitioner of the old school, labor intensive approach, I smelled an opportunity and offered to jump in and model this system.

The governing equation for the acid-base generator turns out to be the same Nernst-Planck equation I solved via a custom C++ code in [Chapter 1](#). The boundary conditions are different this time: instead of an electrochemical reaction occurring on a solid-liquid boundary, there are constraints on the ionic fluxes admitted by cation exchange membranes (CEMs) on two faces. A second, crucial difference to the porous electrode is that the acid-base generator can be described well with a two dimensional idealization. If we imagine unfurling a serpentine flow channel in the electrode and make this the x -axis, there is only one additional spatial dimension that has interesting physics occurring, the transport of ions over a short distance between the two CEMs in an applied electric field. The third spatial dimension factors out of the model. This reducibility to two dimensions enabled me to simulate the system with a much simpler code that was written in Python using the numpy back end. The results of the simulations were intuitive and in good agreement with experimental findings. [Chapter 2](#) is excerpted and adapted from the publication *Electrochemical Acid-Base Generators for Decoupled Carbon Management* appearing in Energy & Environmental Science [2].

Whereas [Chapter 1](#) was my version of a Wagnerian epic, [Chapter 3](#) was a delightful romp in the light-hearted style of Rossini.⁴ I walked into a group meeting one day and Kiana Amini said she “had a problem and needed help.” Kiana and a whole slew of collaborators had done an extensive set of experiments to characterize two competing mechanisms by which CO₂ is captured in various solutions containing

⁴Richard Wagner took more twenty five years to complete *Der Ring des Nibelungen* [The Ring of the Nibelung] between 1848 and 1874 [3]. Gioachino Rossini, on the other hand, was famously quick, and completed one of his best known works, *La Cenerentola* [Cinderella], in just three weeks [4]!

redox-active organic materials in the anthraquinone family. These two mechanisms are called pH swing and nucleophilicity swing. The idea of the pH swing is simple: by making a solution basic, hydroxide ions react with dissolved CO₂ to form carbonate and bicarbonate, thereby pulling carbon dioxide into the solution.⁵ This gas can then later be released and stored. Whereas the pH swing mechanism can be implemented with many different approaches, the nucleophilicity swing mechanism is somewhat distinctive to the quinones being studied. When the quinone is electrochemically reduced to its hydroquinone form, an operation akin to charging the flow battery, the hydroquinone can form an adduct with CO₂. The CO₂ can be subsequently released when the hydroquinone is oxidized, i.e. when the flow battery is discharged.

Kiana's problem was that the whole paper hinged on a thermodynamic analysis of these competing reactions that wasn't working out. She had written down a set of nine equations in nine unknowns, and she was sure that there had to a unique solution for the equilibrium concentrations. But when she put these equations into a numerical optimizer, she was getting nonsensical results, which indeed were not even consistent between successive runs of her program. I recognized that this was a straightforward problem that could be solved by applying a few numerical techniques I've learned in my applied math coursework. Sure enough, I had a working prototype within two days. Chapter 3 is an adapted excerpt of the paper *In Situ Techniques for Aqueous Quinone-Mediated Electrochemical Carbon Capture and Release*, which appeared in Nature Chemical Engineering [6].

⁵Earth's oceans are mildly alkaline, and by this mechanism they hold a stupendous quantity of carbon dioxide [5].

The publication associated with the last chapter was actually submitted first. Chapter 4 is a minimally adapted reprint of *Quantitative Local State of Charge Mapping by Operando Electrochemical Fluorescence Microscopy in Porous Electrodes*, which appeared in Energy Advances [7]. This work is based on experiments that were done on the multidisciplinary porous electrodes project before I joined the team. The goal of this work was to measure the state of charge in an operating porous electrode using fluorescence microscopy. The key idea is to use a difference in the optical behavior between the oxidized and reduced species in a redox couple to measure their concentrations. The experiment used a redox active molecule called anthraquinone disulfonic acid (AQDS)⁶. AQDS has the useful property that when a solution is exposed to violet-blue laser light at 405 nm, the reduced species H₂AQDS has a fluorescence emission profile that is distinctly different from the spectrum of the oxidized species AQDS; in particular, H₂AQDS has a broad emission peak between 500 and 525 nm that is absent in AQDS. This difference in fluorescence properties generates a strong optical signal that differentiates the two species.

My collaborators had obtained a number of good quality experimental images. But when they attempted to calculate the state of charge from their image data, the results were confounded by three problems. First, the commercial electrode is a tangle of fibers that cast shadows in the image. Second, the relationship between state of charge and brightness is distinctly nonlinear because AQDS and H₂AQDS combine to form a dimer that is much dimmer than H₂AQDS. A third challenge was that the images were not quite perfectly aligned, and small position shifts often corresponded to large shifts in brightness

⁶In particular, the 2,7 isomer of AQDS was used: 2,7-anthraquinone disulfonate.

because of the shadows. The net result of these problems was a manuscript languishing unpublished because the key figures had severe artifacts that distorted the results and looked obviously wrong.

I volunteered to calculate the state of charge from this data using an indirect approach that has more of a flavor of statistical estimation than of the direct linear calibration methods typically used in this context. I began by recognizing that image alignment is a well studied problem, and applied a mature image processing library to align all 29 images. I next formulated an idealized model of the observed image intensity. This model had two parts, light production and optical properties. The light production model posits that each of the three interacting chemical species (AQDS, H₂AQDS, and dimer) has a distinct emissions spectrum and contributes light to the signal that is linear in its concentration. There is also a constant term for light emitted by the supporting electrolyte. The optical model is the simplest nontrivial idea one can imagine: the brightness of each pixel is the product of two terms, the light production at that location multiplied by an optical factor at that location.

Using electrochemical utilization data, we had good estimates for the mean concentration of each species in each image. A single linear regression in turn yielded accurate estimates of the four brightness coefficients, which correspond to AQDS, H₂AQDS, dimer, and the electrolyte. Likewise, we had an image taken from a sample that had a high and uniform concentration of H₂AQDS, from which we obtained initial estimates of the brightness factors. Starting from these initial values, I iteratively improved the estimates at each step until the process converged. The resulting images were a major improvement from the raw intensities, and allowed us to generate publication quality figures.

I have reached the end of this litany of scientific “conquests.” Like Leporello, I now invite you

Osservate, leggete con me.

Observe, read along with me.

Together, let us observe our data, discuss the results, and draw our conclusions...

“Nothing is too wonderful to be true, if it be consistent with the laws of nature; and in such things as these, experiment is the best test of such consistency.”

Michael Faraday [21]



Ludwig van Beethoven, Ninth Symphony in D minor, op. 125. Fourth movement.

Introduction

Here I present four scientific works relating to electrochemical systems. Two kinds of systems—porous electrodes in redox flow batteries and carbon capture systems—were each the subject of one simulation and one analysis. Before I place my work in the context of the larger scientific literature, I will briefly state why these are important problems worthy of attention and research. Simply put, climate change is an impending catastrophe for human well being [8]. Global warming is accelerating [9, 10] even as the governments of some of the largest emitting nations are backsliding on previous commitments [11] to reduce greenhouse gas emissions. If the current adult inhabitants of planet Earth continue business as usual, we are on track to bequeath our grandchildren a bespoiled world that will be hostile to human life in many areas that are today heavily inhabited by the end of this century [12, 13].

If we are to avoid this fate, there is an urgent need for a clean energy transition, away from polluting fossil fuels to clean sources that don't emit climate warming gases like CO₂ [14]. This will necessitate huge investments in clean, renewable energy sources such as photovoltaic cells (solar power) and wind turbines. These two leading renewable energy sources are also intermittent—unlike dispatchable power

sources such as natural gas turbines, electric system operators cannot control when the wind blows and the sun shines through cloud cover. The rapidly rising fraction of intermittent sources in electric grids thus necessitates tremendous investments in long duration energy storage systems starting from a very small base [15, 16]. Redox flow batteries are a promising technology for grid scale energy storage, in part because they have the unusual property that their power can be effectively decoupled from their energy storage capacity [17, 18]. Meanwhile, even if significant progress is made on reducing emissions, Earth is already on track for a substantial warming [12]. While reducing the combustion of fossil fuels should be the immediate policy response of responsible governments to global warming, carbon capture and storage (CCS) may nevertheless play an important secondary role in limiting emissions [19]. Furthermore, CCS may also be a key technology for future generations to rectify the harms of currently ongoing planetary warming [20].

I will now review the scientific literature to put each of my works in its larger context. I present a multiphysics model of a porous electrode in [Chapter 1](#). The standard against which newer models of this kind are still judged is the venerable Newman theory, dating back to the 1960s. Newman's approach uses volume averaging over regions that are large enough to idealize the electrode as a homogeneous, isotropic medium with a uniform porosity [22, 23]. This method has been highly successful in many cases where its assumptions are justified, and has continued as a foundational theory for extensions such as descriptions of phase-separating materials [24]. But the Newman model is completely unable to explain experimentally observed phenomena such as inhomogeneities at length scales orders of magnitude larger than

a typical pore size [25], motivating the development of richer models with the capacity to replicate this behavior.

Pore Network Models (PNMs) were developed in the 1980s and treat the electrode as a collection of spherical pores connected by a network of cylinders via hydraulic flow [26–28]. PNMs can be evaluated using the OpenPNM software package [29], and their validity has been experimentally assessed with favorable results on some commercial carbon electrodes [30]. More recently, PNMs have been used as the fitness function for an electrode design optimization [31]. Despite these promising results, PNMs raise some concerns. Most prominent among these is the critique that the geometric description of the electrode fails to account for the intersection of pores and cylinders, and thus does not reproduce the total volume of the electrode accurately.

The lattice Boltzmann method (LBM) is another technique that approximates the governing equations for the sake of computational speed. LBM uses the abstraction that the continuous velocity distribution of the particles of each species is simplified to a discrete distribution at every node on a mesh. LBM has been used with good results in a wide range of numerical applications. A representative sample includes: simulating commercially available carbon electrodes using geometry obtained from X-ray computed tomography in good agreement with experimental characterizations [32]; modeling transport phenomena in fuel cells [33]; optimizing the design of carbon felt electrodes [34]; and simulating fluid-structure interactions [35]. While these results demonstrate that LBM is a promising approach, there remains a concern that a continuous PDE has been replaced by a highly quantized discretization on length

scales that are comparable to pore sizes, rather than the much smaller fractions of a pore where we could have high confidence the results were converging to reality.

The question of whether either a PNM or LBM accurately yields a solution near that of the true governing equations remains open, with an answer depending on the particular electrode geometry and flow rate being considered. This is a question in mathematical physics that can be definitively answered with a high fidelity digital twin of the kind I present in [Chapter 1](#). A closely related and messier question—one that requires both simulations and experiments—is whether the Navier-Stokes, Nernst-Planck, and Poisson equations are together sufficient to describe what is happening in a wet electrochemical cell containing many other secondary phenomena outside the scope of this description. Just because a simplified model like PNM or LBM claims a degree of consistency with experimental results that captured a few scalars on a handful of electrodes, it does not necessarily follow that this class of model is generally reliable at predicting the entire steady state concentration profile on electrodes of arbitrary design. I will readily acknowledge that PNM and LBM appear to produce good results for electrodes that are qualitatively similar to commercial electrodes, with bundles of fibers and possibly tunable parameters including porosity, fiber sizes and pore size distributions. But there remain entire vistas of design ideas for porous electrodes that are more heavily engineered [36] and may not be described nearly as well by the simplified models. This observation motivates approaches based on the direct numerical solutions of the governing PDEs.

A popular approach to modeling porous electrodes in recent literature is to use the COMSOL Multi-

physics package [37] to solve the Nernst-Planck equation, typically using some form of volume averaging in 2D at length scales well above pore sizes. The use of a commercial modeling back end avoids time consuming software development and provides ready access to other COMSOL features such as optimization engines, but incurs expensive software licenses and depends on opaque, unmodifiable source code [24]. Some recent work using COMSOL to model porous electrodes includes: optimizing the design of the cathode of a vanadium flow battery consisting of three planar layers with varying fiber sizes and porosity [38]; performing a topology optimization on 3D flow fields for RFBs [39]; and computationally designing porous electrodes with spatially varying porosity [40].

In contrast to PNMs and LBMs, which make compromises on the governing equations, and COMSOL approaches, which accept volume averages above pore scale and closed source software, Chris and I have developed a constructive, direct numerical simulation of the Nernst-Planck equation using only open source C++ code. We achieved spatial resolutions substantially smaller than pore scales. This modeling framework was first introduced by Dussi and Rycroft in two dimensions [41]. Our model was used to simulate a microfluidic flow battery system described by Barber et al. [36] and achieved good qualitative agreement with experimental images. These two works—the earlier 2D model in 2022 [41] and the current 3D digital twin [1]—are the only works we find in the literature that perform a direct numerical solution of the governing equations in three dimensions on a length scale well below pore sizes.

I offer a numerical simulation of an acid-base generator in [Chapter 2](#). A literature search on this topic found only three directly relevant papers, beginning with my own manuscript, before branching

out into some tangentially related works. Van Wyscic et al. simulated an aqueous redox flow battery including water dissociation using bipolar membranes [42]. They numerically solved the Nernst-Planck and Poisson equations in the BPM in an approach thematically similar to my work in this chapter. Their work was done in COMSOL, whereas mine was coded by hand after an earlier attempt using COMSOL failed. Liu et al. performed a numerical model of direct air capture systems including an empirical simulation of CO₂ using mass transfer coefficients [43]. After these two papers, topics run further afield, e.g. an analysis of transient effects in a photoelectrochemical water splitting cell [44].

A more comprehensive picture of the relevant context for my work can be obtained by searching the larger literature on carbon capture, and then searching within these articles for mentions of any simulations that were done. A thorough review of the relevant references in our published acid-base generator manuscript [2] shows that only a small number of them included any numerical simulations at all. Four works included simulations loosely comparable to mine, all done in COMSOL. Xu et al. reported a direct air capture system using an electrocatalytic pH swing mechanism and included a 1D COMSOL model of surface concentrations of three species (I₂, I⁻ and I₃⁻) and the simulation of an electric double layer [45]. Digdaya et al. characterized an electrochemical system for capturing CO₂ from seawater and provided a 1D COMSOL model of electrodialysis within a bipolar membrane [46]. Zhu et al. demonstrated an electrochemical carbon capture system using water splitting in a solid-electrolyte reactor and included a 2D COMSOL model to establish upper limits on DAC as a function of catalyst thickness and porosity [47]. The nearest comparison to my work was an acid-base generator for carbon capture in seawater us-

ing a bicarbonate buffer demonstrated by Schiffer et al. [48]. They modeled the system in COMSOL using Butler-Volmer reaction kinetics; they were forced to simulate current densities 5,000 times smaller than their experiments to avoid convergence problems. None of these simulation works was as involved as, or as integral to the larger publications, as the full simulation of the Nernst-Planck equation I coded by hand for the entire acid-base generator being studied after we were unable to simulate it in COMSOL. Concluding this review of the two simulations in my thesis, both are unusual because they are direct solutions of the Nernst-Planck equation at a small, sub-pore scale that did not use COMSOL, and provided rich simulated concentration profiles of working electrochemical systems.

I present a thermodynamic analysis of a carbon-capture system including two separate capture mechanisms in Chapter 3. Mores et al. present a model that was used to determine optimal operating conditions for CO₂ capture from flue gas using a monoethanolamine aqueous solution [49]. Stolaroff summarizes the use of metal carbonate solutions for carbon capture using the pH swing cycle [50]. Monazam et al. developed a phenomenological kinetic model of CO₂ adsorption on mesoporous silica, using a Weibull distribution and nucleation growth theory [51]. Oreggioni et al. published a full equilibrium solver for pressure swing adsorption cycles, solving a system of PDEs in time and one spatial dimension (height in a column) that arise from a linear driving force mass transfer model [52].

As was the case for my supporting work on acid-base generator, a more representative picture of relevant work in the field may be obtained by scrutinizing the references of the published work for comparable numerical contributions to my own. A review of the relevant references from the published paper

[2] reveals only a few works with similar thermodynamic calculations. The nearest precedent is a calculation of equilibrium concentrations for a pH swing in the absence of a nucleophilicity swing [53]. This is essentially a much simpler special case of the problem I solved. The main chemical equilibria are the protonations of carbonate and bicarbonate. The result is a set of simple analytical equations for all the concentrations as a function of total alkalinity. A thermodynamic lower bound on the energy required for another electrochemical pH swing included some similar calculations [54]. A zero dimensional model of flow batteries containing a mixture of two redox active molecules calculated the equilibrium potential and current in an explicit method using the Nernst and Butler-Volmer equations [55]. All three of these works included straightforward, direct calculations which employed no notable numerical methods, and indeed numerical methods were not discussed in any of them.

My work in [Chapter 4](#) can be placed in the broader context of state of charge mapping in porous electrodes. Literature searches for SOC measurement and mapping in porous electrodes reveal a diverse range of approaches to this problem. Nanda et al. use Raman spectroscopy to map SOC in a lithium ion battery at micron scale resolutions [56]. They used a simple ratio of band peak intensities to obtain a qualitative indication of SOC. Feng et al. also used an optical approach for SOC mapping called oblique incident reflection difference, in which a sample is exposed to elliptically polarized monochromatic light, and the changes in both s- and p-polarized reflection coefficients are measured. A single analytical equation was used to calculate the change in ion intercalation from the measured emission coefficients and exposure angles. Chueh et al. mapped the state of charge in a lithium iron phosphate battery using X-

ray microscopy to achieve a 40 nm resolution [57], using a simple linear mapping from photon energy to SOC that merited minimal discussion. The nearest precedent to this work was the SOC mapping of an operando porous electrode using fluorescence microscopy done by Wong et al. [25]. This work used a simple linear mapping between two calibration images at 0% and 100% SOC as explained briefly in note S6 of the SI. In summary, none of the analytical techniques for calculating state of charge from experimental data in any of these prior works had a comparable complexity to the elaborate nonlinear calibration required in my work.

We can now identify a few themes from my work in its broader scholarly milieu. I have presented two simulations of working electrochemical systems that were done at the highest level of fidelity present anywhere in the relevant literature for each problem. In each case, I introduced new ideas that were required to get a solution after standard techniques proved inadequate. A clear pattern in the simulation literature shows increasing numbers of numerical analysts using COMSOL for their work, raising significant concerns in my opinion about expensive and opaque source code that cannot be freely replicated by all scientists. The two analyses I offered were both original solutions to tricky problems that were well beyond the scope of the analysis typically required in the relevant literature. Indeed, in three of the four chapters of this thesis, I made a late entry as a collaborator to solve a problem that had confounded the original research team. I have greatly enjoyed my role as “numerical analyst of last resort” on multiple author teams. As a mathematician, it is “a consummation devoutly to be wished” to perform the decisive calculation that pushes a work over the threshold from an unfinished manuscript to a published article.

„Eine neue wissenschaftliche Wahrheit siegt nicht dadurch, daß ihre Gegner überzeugt werden und sich ihnen der Sinn der Sache erschließt, sondern dadurch, daß sich ihre Gegner allmählich abwenden und sterben, und eine neue Generation aufwächst, die mit ihr vertraut ist.“

[A new scientific truth does not triumph by convincing its opponents and making them see the light, but rather because its opponents eventually die and a new generation grows up that is familiar with it.]

Max Planck, *Scientific Autobiography* [58]



Richard Wagner, *Götterdämmerung* [Twilight of the Gods], WWV 86D. Siegfried's funeral march.

1

Digital Twin for Porous Electrodes in Redox Flow Batteries

This chapter is adapted from M. S. Emanuel and C. H. Rycroft, *Digital Twin for Porous Electrodes in Redox Flow Batteries*, a preprint to be submitted to Physics of Fluids (2025) ([arXiv:2502.08034](https://arxiv.org/abs/2502.08034)) [1].

I.I ABSTRACT

Porous electrodes are a vital component of redox flow batteries, fuel cells and electrolyzers. We present a 3D digital twin for a porous electrode by direct numerical solution of the governing Navier-Stokes and Nernst-Planck equations for incompressible flow and electrochemical mass transport with Butler-Volmer reaction kinetics. We demonstrate our method by simulating a laboratory sized system at a sub-fiber scale of $1.25 \mu\text{m}$ using a single workstation. We establish convergence and the consistency of mesh refined lattices, and review an experimental validation of our model. We show the efficacy of two novel techniques to speed convergence to steady state, iterative upsampling and model refinement. We prove that the state of charge (s) at steady state can be formulated as the solution to a single PDE in s with a Dirichlet boundary condition, and introduce a novel figure of merit U_{mt} , the utilization of an electrode geometry at the mass transport limit, both of which can be rapidly simulated with explicit methods from a given fluid velocity field. All of our code is highly performant, parallelizable, open source C++ that is published with this work and compatible with the largest modern scientific supercomputers available today.

I.2 INTRODUCTION

Anthropogenic climate change poses a generational challenge to human well-being and prosperity [8]. The clean energy transition will require vast amounts of renewable energy from intermittent sources such as solar and wind, which will in turn drive demand for long duration energy storage [15, 16]. Redox flow batteries (RFBs) are a promising energy storage technology with the unusual feature that their storage

capacity can be scaled independently of their power, making them ideally suited to long duration grid scale energy storage applications [17, 18].

Porous electrodes are a vital component of flow battery systems and strongly influence mass transfer, charge transfer, ohmic resistance and hydraulic resistance [59]. They are porous media that admit hydraulic flow and also provide the active surface for electrochemical reactions. This dual role creates an inherent design tension between greater porosity to reduce hydraulic resistance and greater surface area to improve mass and charge transfer.

The oldest approach to model porous electrodes dating to Newman et al. in the 1960s is to use volume averaging over sufficiently large regions of the electrode to treat it as homogeneous and isotropic [22, 23]. This approach has been highly successful and is still leading to new refinements, e.g. Smith and Bazant's extension of Newman's porous electrode theory to phase-separating materials [24].

A popular approach to modeling porous electrodes in recent literature is to use the COMSOL Multiphysics package [37] to solve the Nernst-Planck equation, typically using some form of volume averaging above pore scales, and often in 2D. This has the advantages of avoiding time consuming effort in software development and ready access to other COMSOL features such as optimization engines, against the disadvantages of costly software licenses and opaque, unmodifiable source code for the underlying model [24]. Lee et al. used COMSOL to simulate the cathode of a vanadium flow battery consisting of a "sandwich" of three planar layers with varying fiber sizes and porosity and optimize its design [38], while Lin et al. performed topology optimization on 3D flow fields for RFBs [39] and Beck et al. computationally

designed porous electrodes with spatially varying porosity [40].

Pore Network Models (PNMs) have also been used to simulate and optimize porous electrodes. As suggested by their name, PNMs treat the electrode as a collection of spherical pores (“throats”) connected by a network of cylindrical “pipes” via hydraulic flow in a modeling approach dating back to the 1980s [26–28]. Gostick et al. introduced the OpenPNM package [29] to solve PNMs. Later van der Heijden et al. experimentally assessed their validity with two commercial carbon electrodes [30], and went on to use PNMs as the fitness function for an optimization using a genetic algorithm [31].

The lattice Boltzmann method (LBM) is a second technique that approximates the governing equations for the sake of computational speed. The key idea in LBM is to describe the motion of each species in a fluid using discrete particle density distribution functions. Zhang et al. used LBM to simulate the electrochemical behavior of three commercially available carbon electrodes, using a geometry obtained from X-ray computed tomography and LBM equations from Dawson et al. to obtain good agreement with experimental characterization of the electrodes [32, 60].

In contrast to PNMs and LBMs, which make compromises on the governing equations, and COM-SOL approaches, which accept volume averages above pore scale and closed source software, we present here a constructive, direct numerical simulation of the Nernst-Planck equation using only open source C++ code which is published along with this work. The spatial resolution of $1.25 \mu\text{m}$ is substantially below the pore scale, and is in fact a fraction of a typical fiber diameter in carbon electrodes, e.g. $8 \mu\text{m}$ for SGL39AA [38], hence we refer to this as a *fiber-scale* simulation. We employ the framework introduced

by Dussi and Rycroft [41], stepping up from two to three dimensions and making some technical adjustments that were necessary. We also introduce several new ideas, including reformulating the governing PDE to have a Dirichlet boundary condition, which collectively make it feasible to calculate a converged steady state. This model was used to simulate a microfluidic flow battery system described by Barber et al. [36] and achieved good qualitative agreement with experimental images, faithfully reproducing convective tails and large scale concentration gradients.

A redox flow battery includes two half cells separated by an ion exchange membrane. Each half cell includes an electrolyte tank, a porous electrode, and a current collector. Electrolyte is pumped through the two electrodes and undergoes a reaction with electrons moving between the current collectors while charge is balanced by an offsetting ionic current through the membrane. A voltage source is applied during charging, and a load can be powered during discharge.

This work presents simulation results and modeling approaches that are broadly applicable to porous electrodes in RFBs. Notwithstanding this general approach, the simulation was designed with a particular model system in mind, a quinone based negolyte that is being reduced (charged) as shown in Figure 1.1. This system was chosen because our collaborators fabricated and experimentally characterized it [36]. The active surface for the reaction is a 3D printed electrode with precisely engineered features matching a design geometry of cylindrical conducting surfaces and a relatively low specific area compared to commercial electrodes. The counterelectrode is a commercial carbon paper with much larger surface area that is assumed to be faster due to its larger area. The posolyte is a V^{+4} / V^{+5} redox pair with $E^\circ = +1.00$ V.

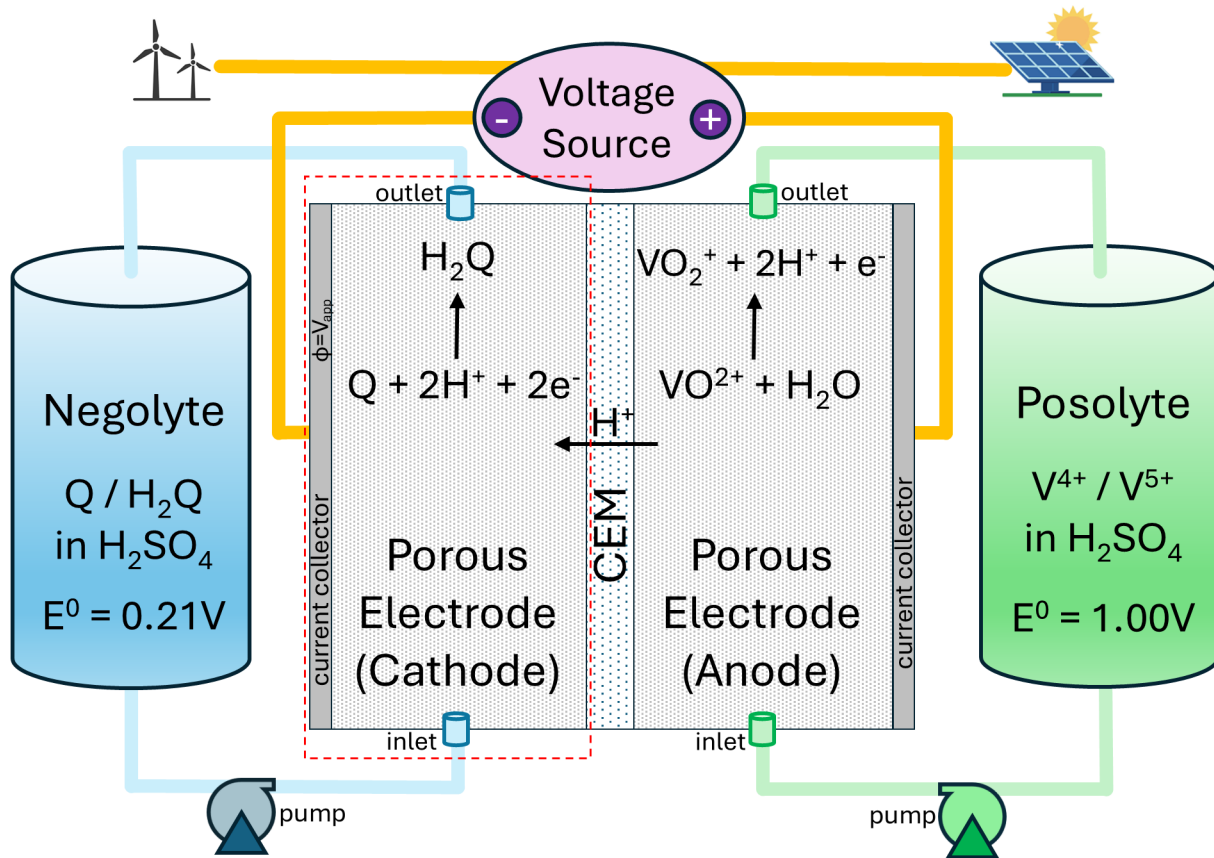


Figure 1.1: A redox flow battery being charged. A quinone Q is reduced to a hydroquinone H_2Q in the cathode by an applied reducing voltage. V^{4+} is oxidized to V^{5+} in the anode. Protons flow across a cation exchange membrane (CEM) to balance charge. Only the negolyte electrode (in red dashed rectangle) is simulated.

The quinone negolyte consists of a dilute 20 mM solution of anthraquinone-2,7-disulfonate (AQDS) in a supporting electrolyte of 1M sulfuric acid and $E^\circ = +0.21\text{ V}$ [61]. One molecule of AQDS is reduced to one molecule of H_2AQDS in a proton coupled electron transfer where two electrons are transferred (Figure 1.2). Both species have a -2 charge in solution.

All of the simulations presented in this work pertain to this model system. These are half cell simulations for just the AQDS side of the system rather than full cell simulations. The simulated applied

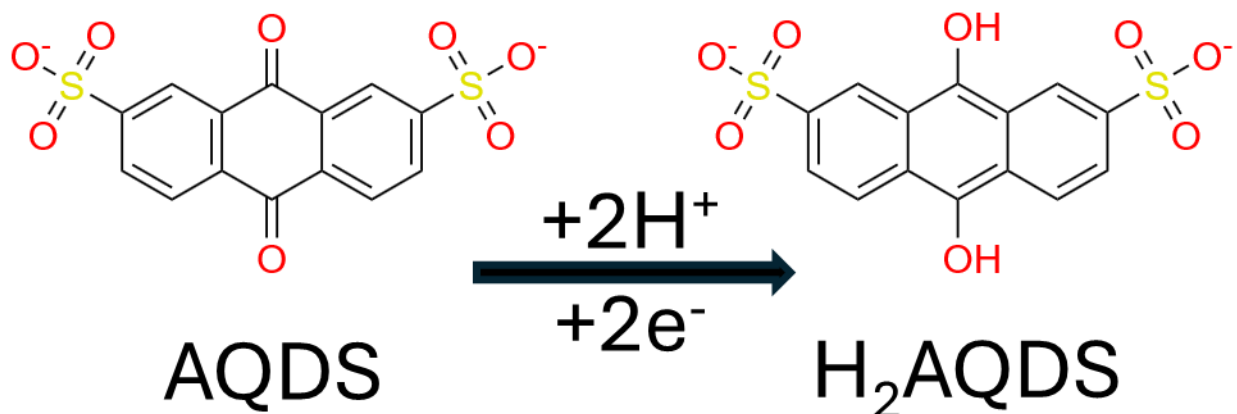


Figure 1.2: Negolyte redox pair. The oxidized species, the anthraquinone AQDS, is reduced to its hydroquinone H₂AQDS with the addition of two protons and two electrons. Both species have a -2 charge in solution, and $E^\circ = 0.21 \text{ V}$ [61].

electric potential is the potential difference between the electrode and the electrolyte at the membrane, i.e. $\phi_S - \phi_M$. This voltage difference is *not* the same as the full cell potential, and omits effects including the standard potential of the counterelectrode and ohmic losses through the membrane. The voltage difference between the electrode and electrolyte can be measured experimentally using a reference electrode that is placed in the spent electrolyte as it exits the electrode.¹ We emphasize here that to obtain a steady state simulation of a full cell, two half cell simulations at the same current can be combined along with a simple model for ohmic losses through the membrane. This procedure is significantly simpler and computationally cheaper than a coupled full cell simulation that would need to resolve transient effects on both half cells and either resolve the electric field through the membrane or solve for the current balancing

¹This requires that the ionic current density profiles across the membrane be matched. Spatially homogeneous current density is sufficient for this, but a real cell might have higher current density near the inlet than near the exit.

applied potential on the two half cells at every time step.

We develop three models for the electrochemical reaction in a half cell with varying levels of fidelity and speed (Figure 1.3). The Butler-Volmer (BV) model is the most faithful and computationally expensive.

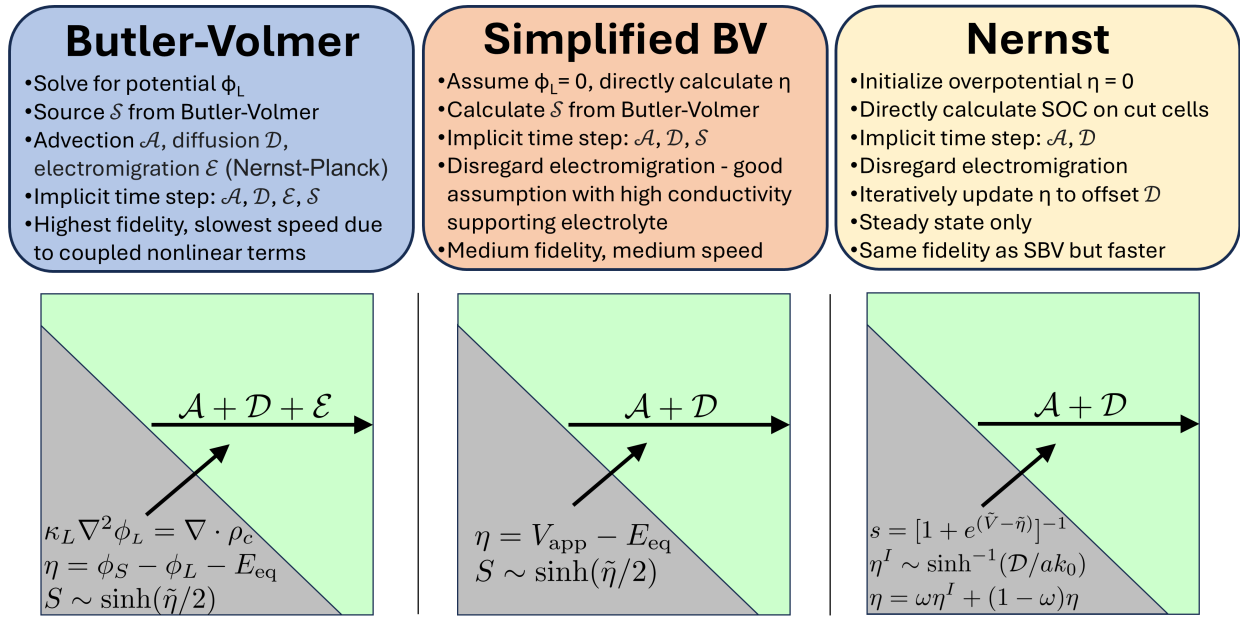


Figure 1.3: Overview of three reaction models. The Butler-Volmer model solves the Nernst-Planck equation including advection, diffusion and electromigration. It has the highest fidelity and slowest speed. The simplified Butler-Volmer model disregards electromigration to gain significant speed with a small compromise in accuracy. The Nernst model makes the same assumption, but only solves for steady state. Gray regions represent solids (electrode) and green regions represent liquids (electrolyte). See 1.3 for definitions of all algebraic symbols used.

It solves the Nernst-Planck equation including advection, diffusion and electromigration. The chemical source term is obtained using Butler-Volmer reaction kinetics. The simplified Butler-Volmer (SBV) model makes the simplifying assumption that the potential in the electrolyte ϕ_L is uniformly zero, and therefore drops the electromigration term. This approximation is good in the presence of a strong sup-

porting electrolyte such as 1M sulfuric acid, where the high conductivity leads to small potential differences in the electrolyte; and its validity is verified numerically for the specific systems we simulated here. The SBV model is significantly faster than the BV model because it eliminates coupled nonlinear terms arising from electromigration and solving a Poisson equation for ϕ_L . Finally, the Nernst model makes the same physical assumption as the BV model, but directly calculates the steady state. This is done by iteratively updating estimates of the activation overpotential and state of charge on the reactive surface until mass balance between diffusion and the reaction is achieved.

One goal of this work is to introduce a numerical solution to the Nernst-Planck equation of sufficient fidelity that it is accepted as a digital twin of the true solution to the PDE. This would allow it to be used to validate other models that trade fidelity for greater speed, including PNMs, LBMs, and PDE solutions at lower spatial resolution. A second goal is to build useful intuition for designers of porous electrodes and batteries by developing a theory to compute the mass transport utilization limit of a given velocity field.

I.3 THEORETICAL BACKGROUND

We model the behavior of a porous electrode at steady state by direct numerical simulation of the governing equations. While our simulation apparatus can resolve transient phenomena, we limit our investigation to the steady state because it is of predominant importance for applications of porous electrodes in areas including flow batteries, electrolyzers, and fuel cells. We treat this system as having two separable parts, an incompressible Newtonian fluid flow and a mass transport system including an elec-

trochemical source term with Butler-Volmer reaction kinetics. We first solve for the incompressible fluid flow at a steady state, making the assumption that the chemical reactions do not affect the fluid rheology or the flow. Once the fluid velocity field \mathbf{u} is obtained, we simulate the mass transport phenomena of advection, diffusion, electromigration, and electrochemical reaction on the electrode surface. In this section, we state the governing equations and outline the mathematical theory used to solve them, beginning with the incompressible fluid flow. We close by introducing various approximations that simplify the computation without sacrificing the essential accuracy in the results.

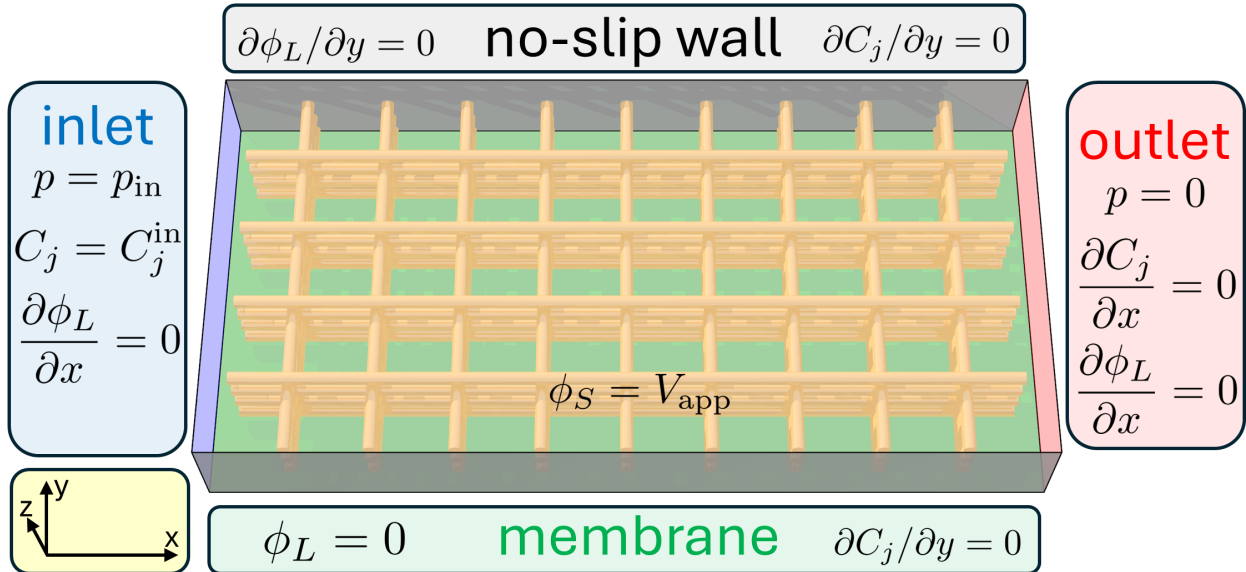


Figure 1.4: Boundary conditions for negolyte half cell simulation. Electrolyte at pressure p_{in} and known concentration enters the **inlet** ($x = 0$) and flows along the x -axis, exiting through the **outlet** at zero pressure. The **membrane** ($z = 0$) is a no-slip wall with fixed potential $\phi_L = 0$ and the electrode surface is held at a reducing potential $\phi_S = V_{\text{app}}$. The top, front and back faces are all no slip walls with zero concentration gradient and zero electric field normal to the wall.

Figure 1.4 shows the boundary conditions for the simulation. The domain Ω is a rectangular channel,

though more complex geometries can be accommodated using embedded boundaries. Flow moves along the x -axis, and at the inlet ($x = 0$) there is an applied pressure p_{in} , known concentrations C_j^{in} for each species, and zero electric field component E_x normal to the wall. The outlet conditions are zero pressure and no electric field or concentration gradient along x . The top, left and right walls (in gray) have a no-slip condition with zero fluid velocity and no concentration gradient or electric field normal to the wall. The bottom wall corresponds to the membrane, and has the same no-slip conditions as the top, except it has a fixed potential $\phi_L = 0$ rather than zero electric field E_y . The surface of the electrodes is held at a fixed potential ϕ_S , with a lower potential $\phi_S < \phi_L$ required to drive a reduction reaction.

1.3.1 INCOMPRESSIBLE FLUID FLOW

We begin with the Navier-Stokes equation for an incompressible Newtonian fluid with constant density ρ , a standard result [62, Eq. 7.1.6],

$$\rho \left(\frac{\partial \mathbf{u}}{\partial t} + (\mathbf{u} \cdot \nabla) \mathbf{u} \right) = -\nabla p + \mu \nabla^2 \mathbf{u}, \quad (1.1)$$

where \mathbf{u} is the fluid velocity, p is the pressure, and μ is the dynamic viscosity (in $\text{Pa} \cdot \text{s} = \text{kg} \cdot \text{m}^{-1} \cdot \text{s}^{-1}$).

We also have the incompressibility condition [62, Eq. 5.1.5],

$$\nabla \cdot \mathbf{u} = 0. \quad (1.2)$$

The incompressible flow problem of Eqs. (1.1–1.2) is solved using the Chorin projection method [63] as detailed in 1.4.1.

The Reynolds number Re is the dimensionless ratio $\text{Re} = \rho LV/\mu$, where L is the characteristic length scale and V is the characteristic speed. For this problem, we propose that $L = L_z$ is the height of the channel (the smallest dimension) [64] and $V = q$ is the volumetric flux (superficial velocity) as discussed below in Eq. (1.5). A classical result of fluid dynamics [62, Eq. 7.4.3] states that in the limiting case of a small Reynolds number $\text{Re} \ll 1$, the steady state fluid flow simplifies from Eq. (1.1) to Stokes's approximation,

$$\nabla p = \mu \nabla^2 \mathbf{u}. \quad (1.3)$$

We refer to flows in this regime as Stokes flows, and note the physical intuition that in a Stokes flow, an applied pressure gradient is dissipated by viscous forces, while momentum transport is negligible. One immediate consequence of Eq. (1.3) is that the steady state fluid velocity is linear in the applied pressure. This enables us to approximate a whole series of flows in the Stokes regime by running a single simulation at one applied pressure and then scaling the results for varying pressures.

The presence of gravitational forces is a complication that can be avoided by incompressible flow theory. The dynamic pressure \mathcal{P} is defined by

$$\nabla \mathcal{P} = \nabla p - \rho g, \quad (1.4)$$

where g is the gravitational field. As discussed by Deen [65, §6-3], it is often advantageous to treat incompressible flow problems in the presence of gravity in terms of the dynamic pressure \mathcal{P} . For the case of a steady state flow of an incompressible fluid with fixed solid boundaries as we have here, the solution of

a problem in terms of the true pressure p including gravitational body forces will match the solution in terms of the dynamic pressure. In the remainder of this work, we will only consider the dynamic pressure and disregard gravitational body forces. We will denote the dynamic pressure by p moving forward for notational ease. There is no risk of confusion of pressure gradients between applied pumping pressure and gravity, because we always have the applied pressure and flow in the x direction.

Darcy's law describes the flow of fluid through a porous medium [66] and can be written

$$q = -\left(\frac{\kappa}{\mu}\right)\nabla p, \quad (1.5)$$

where q is the volumetric flux in $\text{m} \cdot \text{s}^{-1}$ (sometimes called the superficial velocity), and κ is the permeability of the porous medium in m^2 . Darcy's law can be derived directly from the Navier-Stokes equations by volume averaging Stokes flow through a porous medium [67, 68]. Even though the porous electrodes considered here are far from being homogeneous porous media, we can nevertheless empirically describe the flow through a porous electrode using Darcy's law. Let Q denote the volumetric flow rate in $\text{m}^3 \cdot \text{s}^{-1}$, A the cross sectional area of the inlet (yz plane) in m^2 , and $\Delta p = p_{\text{in}} - p_{\text{out}}$ the pressure drop. Volumetric flux is flow per unit area, so $Q = Aq$, and the mean pressure gradient is $\nabla p = \Delta p/L$. This gives us the integral form of Darcy's law for a homogeneous permeable medium,

$$Q = \left(\frac{\kappa A}{\mu L}\right)\Delta p. \quad (1.6)$$

We can define the hydraulic resistance R_H so it appears in the denominator on the right hand side of

Eq. (1.6), giving us

$$R_H = \frac{\mu L}{\kappa A} = \frac{\Delta p}{Q}. \quad (1.7)$$

As long as a fluid flow is in the Stokes regime, the hydraulic resistance will be approximately constant. R_H will increase as the flow becomes turbulent, a result seen in 1.5.5.

I.3.2 THE NERNST EQUATION AND BUTLER-VOLMER REACTION KINETICS

In this section we review the Butler-Volmer theory of reaction kinetics. Consider a reversible proton-coupled redox reaction between two electroactive species, denoted O and R for the oxidized and reduced species respectively, which exchange n_e electrons and n_p protons in the reaction,



The equilibrium potential E_{eq} for this reaction is given by the Nernst Equation [41, Eq. 8] or [69, Eq. 3.7.11],

$$E_{eq} = E^\circ + \frac{RT}{n_e F} \log\left(\frac{C_O (C_{H^+})^{n_p}}{C_R}\right), \quad (1.9)$$

where E° is the voltage under standard conditions, R is the ideal gas constant, T is the temperature, and \log denotes the natural logarithm. The activation overpotential, denoted η_{act} with units of volts, is the difference between the interfacial voltage across the electrode $\phi_s - \phi_L$ and its equilibrium value E_{eq} , and is given by

$$\eta_{act} = \phi_s - \phi_L - E_{eq}. \quad (1.10)$$

Denote by C_T the total concentration of electroactive species, $C_T = C_O + C_R$. We will show in 1.3.4 that under the conditions in the model AQDS system, C_T is mathematically conserved. We will further demonstrate that even in systems where C_T is not exactly conserved, it is very close to being a spatially uniform constant in practice. We can therefore think of C_T as simplifying to a constant c_0 for practical purposes, and in the results presented here $c_0 = 20 \text{ mol} \cdot \text{m}^{-3}$. (Note that $1 \text{ mol} \cdot \text{m}^{-3}$ corresponds to a one millimolar (mM) concentration.) Define the local state of charge (SOC) s by

$$s = \frac{C_R}{C_O + C_R} = \frac{C_R}{C_T} \approx \frac{C_R}{c_0}. \quad (1.11)$$

The state of charge is a dimensionless parameter that ranges between 0 and 1, which correspond respectively to completely discharged and completely charged internal states for a battery. While SOC is often treated as a single scalar to describe an entire battery system, here it is a scalar field defined throughout the electrolyte, i.e. over the same region as ϕ_L . An immediate consequence of Eq. (1.11) is that we can make the substitutions

$$C_R = s C_T \approx s c_0, \quad C_O = (1 - s) C_T \approx (1 - s) c_0. \quad (1.12)$$

The Butler-Volmer theory predicts the current density j (in $\text{A} \cdot \text{m}^{-2}$) of an electrochemical reaction at the surface of an electrode. Following Bard and Faulkner [69, §3.4], define the exchange current density j_0 ($\text{A} \cdot \text{m}^{-2}$) as

$$j_0 = n_e F a k_0 C_O^{(1-\alpha)} C_R^\alpha, \quad (1.13)$$

where F is Faraday's constant, k_0 is the rate constant in $\text{m} \cdot \text{s}^{-1}$ and α is a dimensionless charge transfer

coefficient. The specific area a is the ratio of surface area to volume, $a = A/V$ integrated over a test region. a has units of m^{-1} and scales as one over the fiber diameter in real world electrodes, e.g. carbon cloth, paper or felt.

Define the thermal voltage $V_T = RT/F$, which is approximately 25.7 mV at standard conditions.

The Butler-Volmer equation [69, Eq. 3.4.11] states that the current density j is given by

$$j = j_0 [e^{-\alpha n_e \eta_{\text{act}}/V_T} - e^{(1-\alpha)n_e \eta_{\text{act}}/V_T}]. \quad (1.14)$$

Let S be the chemical source term, the rate at which the entire reaction in Eq. (1.8) moves forward in units of $\text{mol} \cdot \text{m}^{-3} \cdot \text{s}^{-1}$, and let n_k denote the signed stoichiometric number of species k . For the example reaction shown, $n_R = 1$ and $n_O = -1$, since the reaction produces one molecule of R and consumes one molecule of O. The source term S_k for species k is the change in concentration over time for that species, and therefore $S_k = n_k S$.

We can relate the description of the reaction rate in terms of current in Eq. (1.14) to the source term S by conservation of charge in a test region. If A is the area of the electrode surface and V is the liquid volume, then the current Aj must match the rate of consumption of electrons $n_e F V S$. Setting these two equal and solving for S we find $S = (A/n_e F V)j = (a/n_e F)j$. Substituting for the Butler-Volmer equation Eq. (1.14), the terms $n_e F$ cancel and we recover [41, Eq. (6)], obtaining

$$S = a k_0 C_O^{(1-\alpha)} C_R^\alpha [e^{-\alpha n_e \eta_{\text{act}}/V_T} - e^{(1-\alpha)n_e \eta_{\text{act}}/V_T}]. \quad (1.15)$$

The Butler-Volmer equation appears in a number of variations, some of which introduce a mass trans-

fer coefficient k_m linking the bulk and surface concentrations [70–73]. In this work, we do *not* use these surface / bulk formulations of the Butler-Volmer equation because we are explicitly modeling the concentration in cells on a sub-fiber scale. The role of the mass transfer coefficient is therefore supplanted by a direct simulation of mass transfer due to diffusion and advection near the reactive surface. Eqs. (1.13) and (1.14) follow what Dickinson and Wain call the electroanalytical formulation of the Butler-Volmer equation [70].

We make the common assumption that the charge transfer coefficient $\alpha = 1/2$ [41]. This allows us to simplify Eq. (1.15) with the relation $\sinh(x) = (e^x - e^{-x})/2$. Define the dimensionless reducing overpotential $\tilde{\eta}$ by

$$\boxed{\tilde{\eta} = -\frac{n_e \eta_{act}}{V_T}.} \quad (1.16)$$

Note that the sign of $\tilde{\eta}$ is reversed from the definition of the overpotential η_{act} ; $\tilde{\eta}$ is a nondimensionalized overpotential in the reducing direction, where a lower value of η_{act} drives the reducing reaction forward at a faster rate. This definition of $\tilde{\eta}$ is motivated by the model system, in which AQDS that starts at state of charge near zero is reduced. In an electrode that is being charged for energy storage applications, a positive value of $\tilde{\eta}$ would be selected with the goal of achieving a state of charge s near one for the solution at the outlet. The intuition is that $\tilde{\eta}$ is a control variable—the operator selects a reducing potential to apply to the flowing electrolyte—and the result is the state of charge at the outlet. A higher reducing voltage leads to a higher SOC at the outlet. Substitute for the two concentrations in Eq. (1.15) using Eq. (1.12) and

for the overpotential terms using Eq. (1.16) and we obtain

$$S = 2a k_0 C_T \sqrt{s(1-s)} \sinh(\tilde{\eta}/2). \quad (1.17)$$

We now rewrite the Nernst equation (1.9) in terms of the state of charge s and separate the small effect of changes in the proton concentration C_{H^+} from its initial value $C_{\text{H}^+}^{(0)}$. Define the adjusted standard potential $E^{\circ'}$ by [41]

$$E^{\circ'} = E^{\circ} + \frac{n_p R T}{n_e F} \log(C_{\text{H}^+}^{(0)}). \quad (1.18)$$

Substituting for C_R and C_O in terms of the state of charge with Eq. (1.12), and shifting the reference from E° to $E^{\circ'}$, we obtain

$$E_{\text{eq}} = \underbrace{E^{\circ'}}_{\text{Standard}} - \underbrace{\left(\frac{V_T}{n_e} \right) \log \left(\frac{s}{1-s} \right)}_{\text{SOC dependence}} + \underbrace{\left(\frac{n_p V_T}{n_e} \right) \log \left(1 + \frac{C_{\text{H}^+} - C_{\text{H}^+}^{(0)}}{C_{\text{H}^+}^{(0)}} \right)}_{\text{pH Dependence}}. \quad (1.19)$$

The leading terms are the adjusted standard potential $E^{\circ'}$ and the dependence on the state of charge. The last term reflects the change in proton concentration (pH) from its starting values. For a strong supporting electrolyte as is typically the case in practice, this last term is dominated by the state of charge dependence. In the model system, $C_{\text{H}^+}^{(0)}$ is larger than c_0 by a factor of 50, and numerical simulations show only very small relative changes in C_{H^+} as the simulation runs, i.e. $|C_{\text{H}^+} - C_{\text{H}^+}^{(0)}| \ll C_{\text{H}^+}^{(0)}$. In the ensuing discussion, we will disregard the pH dependence and rely on the simplified Nernst equation for

this system,

$$E_{\text{eq}} \approx E^{\circ'} - \left(\frac{V_T}{n_e} \right) \log \left(\frac{s}{1-s} \right). \quad (1.20)$$

1.3.3 ELECTROCHEMICAL REACTION WITH VARIABLE POTENTIAL IN ELECTROLYTE - “BUTLER-VOLMER MODEL”

The Nernst-Planck equation describes mass transport phenomena due to advection, diffusion, and electromigration,

$$\boxed{\frac{\partial C_j}{\partial t} = -\underbrace{\mathbf{u} \cdot \nabla C_j}_{\text{Advection}} + \underbrace{D_j \nabla^2 C_j}_{\text{Diffusion}} + \underbrace{\frac{z_j D_j F}{RT} \nabla \cdot (C_j \nabla \phi_L)}_{\text{Electromigration}} + \underbrace{S_j}_{\text{Source}}, \quad (1.21)}$$

where C_j is the concentration of species j in $\text{mol} \cdot \text{m}^{-3}$, D_j is the diffusivity of species j in $\text{m}^2 \cdot \text{s}^{-1}$, z_j is the dimensionless charge number as an integer, ϕ_L is the electric potential in the liquid electrolyte in volts, and S_j is the chemical source term, also in $\text{mol} \cdot \text{m}^{-3} \cdot \text{s}^{-1}$ [74, Eq. 11.30]. The form of the equation shown in Eq. (1.21) can be derived from the more common form with fluxes, e.g. [69, Eq. 4.1.10], by noting that $\partial C_j / \partial t = -\nabla \cdot \mathbf{N}_j$, where \mathbf{N}_j is the flux of species j in $\text{mol} \cdot \text{m}^{-2} \cdot \text{s}^{-1}$. The boundary conditions at the inlet include known concentrations for all the species.

We obtain the potential in the electrolyte ϕ_L by solving a Poisson equation for ϕ_L with a suitable adjustment for a solution where electroneutrality holds, [41, Eq. 9],

$$\boxed{\kappa_L \nabla^2 \phi_L = S_\phi - F \sum_k z_k D_k \nabla^2 C_k, \quad (1.22)}$$

where $S_\phi = n_e F S$ is the source term for electrons generated in the reaction. Eq. (1.22) is analogous to

Gauss's law in electrostatics $\nabla \cdot E = \rho_c/(\epsilon_0\epsilon_r)$ where $E = -\nabla\phi_L$ is the electric field; ρ_c is the charge density; ϵ_0 is the permittivity of a vacuum; and ϵ_r is the relative permittivity. The ionic conductivity of the electrolyte κ_L can be obtained as the sum of the conductivities of each charged species in the electrolyte,

$$\kappa_L = \frac{F^2}{RT} \sum_k z_k^2 D_k C_k. \quad (1.23)$$

This is a standard result [41, Eq. (10)], and can be derived by substituting for mobility u_i in Newman and Balsara's discussion [74, Eq. 11.7] with the formula $u_i = D_i/RT$ [74, Eq. 11.41]. In the model system, we explicitly simulate the concentration of three species, AQDS, H₂AQDS, and H⁺. The fourth species in the simulation is HSO₄⁻, which is treated implicitly by imposing an electroneutrality condition,

$$\sum_j z_j C_j = 0. \quad (1.24)$$

We are making a modeling approximation by ignoring the second dissociation of HSO₄⁻ into SO₄²⁻ and H⁺, but in principle the approach here could be extended to include one more species explicitly. The topics of electroneutrality and electric fields in dilute solutions are discussed extensively by Newman and Balsara [74, §11], and this treatment is consistent. For the common case where a flow battery is operated with a supporting electrolyte, κ_L will be dominated by the supporting electrolyte and can be treated as a constant κ_0 with minimal error.

The potential at the membrane is also a boundary condition, and in this work it is set to zero, i.e. $\phi_L = 0$ on the bottom wall where $z = 0$ [41]. The governing equations are invariant to a constant offset to the potential, so the only assumption made here is that the membrane potential is uniform. We

further assume a high electrical conductivity in the electrode, and set the potential ϕ_s to a constant that is specified as one of the operating conditions in the simulation. We define the applied reducing potential V_{ar} so that a higher value of V_{ar} drives a higher state of charge at equilibrium, and a setting of $V_{ar} = 0$ corresponds to a state of charge of 1/2 for a solution in contact with an electrode at this potential and a liquid electrolyte at zero potential. These choices lead to the definition

$$\boxed{\phi_s = E^{\circ'} - V_{ar}.} \quad (1.25)$$

At the walls other than the membrane, the boundary condition on ϕ_L is $\nabla\phi_L \cdot \hat{n} = 0$ where \hat{n} is a normal vector pointing outward through the exterior wall. This is justified because there cannot be any net charge flux moving through the walls other than the membrane.

We can verify that this definition of V_{ar} has the desired properties by solving for the equilibrium state of charge s_{eq} in Eq. (1.20) when E_{eq} is set to ϕ_s , in which case we obtain $(E^{\circ'} - V_{ar}) - \phi_L = E^{\circ'} - \frac{V_T}{n_e} \log \left(\frac{s_{eq}}{1-s_{eq}} \right)$. The adjusted standard potential $E^{\circ'}$ cancels out, leaving

$$V_{ar} + \phi_L = \frac{V_T}{n_e} \log \left(\frac{s_{eq}}{1-s_{eq}} \right). \quad (1.26)$$

Define the dimensionless applied reducing voltage \tilde{V}_{ar} and the dimensionless potential in the electrolyte $\tilde{\phi}_L$ by

$$\tilde{V}_{ar} = \frac{n_e V_{ar}}{V_T}, \quad \tilde{\phi}_L = -\frac{n_e \phi_L}{V_T}. \quad (1.27)$$

The negative sign on $\tilde{\phi}_L$ is introduced for consistency with \tilde{V}_{ar} . A lower value of ϕ_L boundary cells corre-

sponds to greater losses due to charge transport in the electrolyte. A more conductive electrolyte (larger κ_0) will minimize this loss term. The sigmoid function $\sigma(x) = 1/(1 + e^{-x})$ used in machine learning is the inverse of the logit function, $\text{logit}(x) = \log(x/(1 - x))$. A straightforward simplification shows that the equilibrium state of charge in contact with the electrodes is given by

$$s_{\text{eq}} = \sigma(\tilde{V}_{\text{ar}} - \tilde{\phi}_L) = (1 + e^{-n_e(V_{\text{ar}} + \phi_L)/V_T})^{-1}. \quad (1.28)$$

In physical terms, this definition of V_{ar} implies that when $V_{\text{ar}} = 0$ and $\phi_L = 0$, the state of charge for an electrolyte solution in equilibrium with an electrode is 1/2, and the equilibrium state of charge s_{eq} increases monotonically with V_{ar} according to Eq. (1.28) as shown in Figure 1.5.

We can extend this idea to see the dependence of the nondimensionalized reducing overpotential $\tilde{\eta}$ on the nondimensionalized applied reducing potential \tilde{V}_{ar} . Start with Eq. (1.10) and substitute for ϕ_s using Eq. (1.25) and for E_{eq} with Eq. (1.20). After cancelling out $E^{\circ'}$ we find $\eta_{\text{act}} = \frac{V_T}{n_e} \log\left(\frac{s}{1-s}\right) - V_{\text{ar}} - \phi_L$. Now nondimensionalize η , V_{ar} and ϕ_L by multiplying the whole equation by $-n_e/V_T$, substitute for η_{act} with Eq. (1.16) and finally substitute for V_{ar} and ϕ_L with Eq. (1.27) to obtain

$$\tilde{\eta} = \tilde{V}_{\text{ar}} - \tilde{\phi}_L - \log\left(\frac{s}{1-s}\right).$$

(1.29)

This expression for $\tilde{\eta}$ immediately shows the separate contributions from the applied reducing voltage \tilde{V}_{ar} , the electric potential $\tilde{\phi}_L$ in the electrolyte touching the electrode surface, and the local state of charge

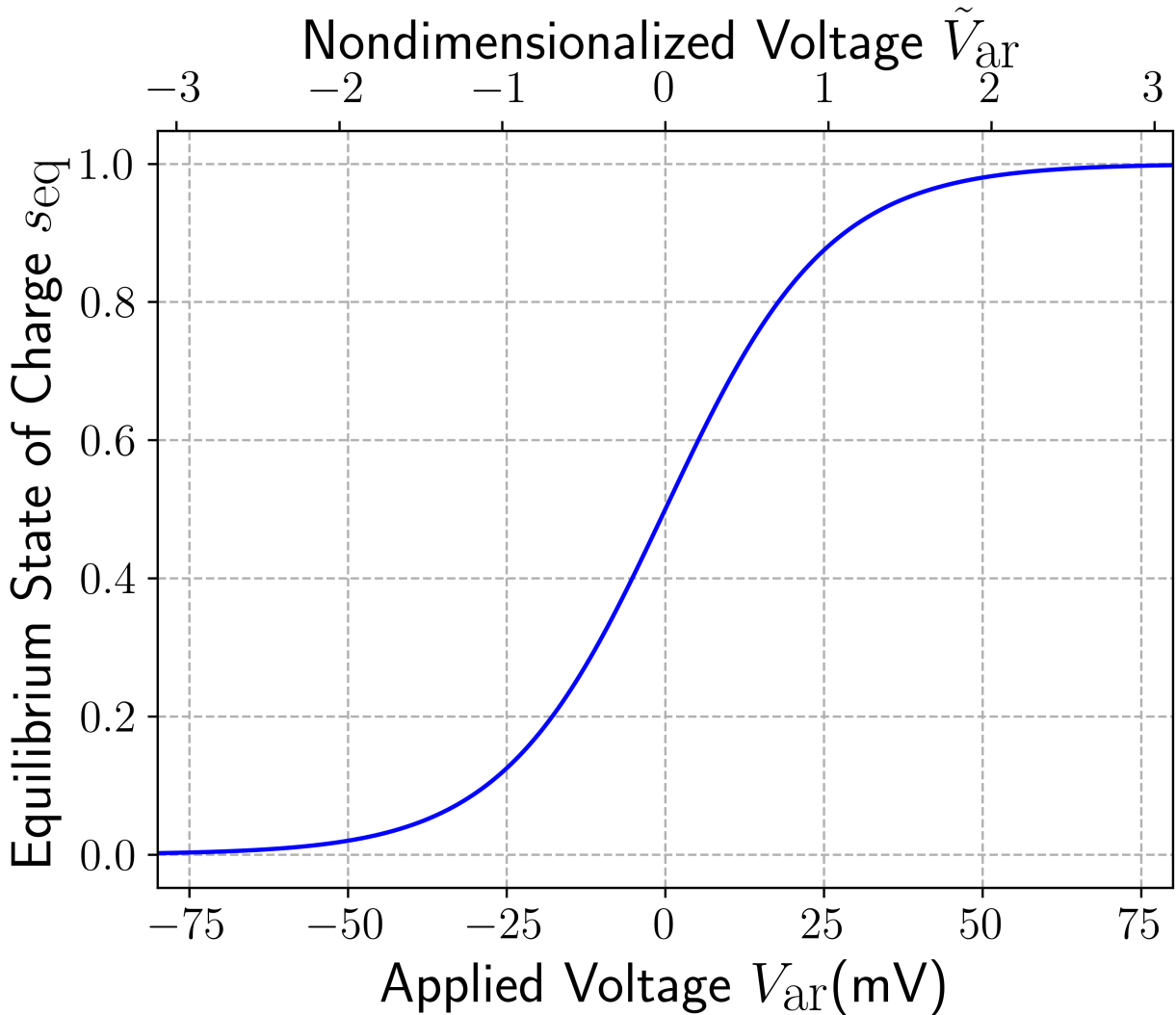


Figure 1.5: Dependence of equilibrium SOC (s_{eq}) on applied reducing voltage (V_{ar}). Calculated from Eq. (1.28) with $\phi_L = 0$. s_{eq} has a sigmoid shape like $\sigma(x)$ and is monotonically increasing in V_{ar} . The applied reducing voltage, both with units (V_{ar}) and nondimensionalized (\tilde{V}_{ar}), is defined in Eq. (1.27), and includes the number of transferred electrons $n_e = 2$ in the numerator.

s. When there is a strong supporting electrolyte, κ_L will be large and the electric potential in the liquid ϕ_L will be small and dominated by \tilde{V}_{ar} . The dependence on s is a form of mass transport overpotential. As s

becomes higher on the reactive surface, a greater reducing voltage is necessary to overcome the unfavorable concentration ratio $s/(1 - s)$ in the Nernst equation. This effect can become quite important at high states of charge; to achieve $s = 0.99$ for example, the Nernst term leads to 59 mV of mass transport overpotential. Eq. (1.28) for the equilibrium state of charge s_{eq} is immediately seen to be consistent with setting the overpotential to zero in Eq. (1.29).

The Butler-Volmer model in this work jointly solves the Nernst-Planck equation (1.21) and the Poisson equation for potential (1.22) with implicit time steps. The chemical source term in Eq. (1.21) is evaluated using Butler-Volmer kinetics with Eq. (1.17), and the overpotential $\tilde{\eta}$ is calculated from Eq. (1.29). To obtain the steady state of a known fluid flow with a specified applied potential V_{ar} , we run time steps until convergence criteria are met for small changes in both the state of charge and potential. The Butler-Volmer model uses adaptive time stepping because it has a nonlinear source term that can vary significantly as the simulation evolves. For that reason, we introduce a dimensionless measure of the relative change over a time step. Let τ denote the nominal time for fluid to flow through the electrode; $\tau = V/Q$ where V is the volume of the electrode in m^3 and Q is the volumetric flow rate in $\text{m}^3 \cdot \text{s}^{-1}$. The convergence criteria for the Butler-Volmer model are

$$\begin{aligned} (\tau/\Delta t) \|s^{(n+1)} - s^{(n)}\| &< \varepsilon_s \\ (\tau/\Delta t) \|\phi_L^{(n+1)} - \phi_L^{(n)}\| &< \varepsilon_\phi \|\phi_L^{(n)}\|. \end{aligned} \tag{1.30}$$

The norm used to calculate the size of the change for convergence criteria is the root mean square, i.e. $\|x\| = \|x\|_2 / \sqrt{N}$.

An additional convergence criterion may be introduced to ensure that electrochemical conversion and mass transport between the inlet and outlet are in balance. Denote the flow of electrons carried by electroactive species at the inlet and outlet by

$$\mathcal{F}_{\text{in}} = n_e c_0 \sum_{\text{inlet}} A_i u_i s_i, \quad \mathcal{F}_{\text{out}} = n_e c_0 \sum_{\text{outlet}} A_i u_i s_i, \quad (1.31)$$

where A_i is cross sectional area in the inlet or outlet plane of cell i (h^2 for each cell), u_i is the x component of the flow velocity, and s_i is the state of charge of cell i . \mathcal{F}_{in} and \mathcal{F}_{out} are current-like quantities with units of A. The net current flow

$$\mathcal{F}_{\text{net}} = \mathcal{F}_{\text{out}} - \mathcal{F}_{\text{in}} \quad (1.32)$$

is therefore the number of moles of electrons that are being added to the electrolyte per second. At steady state, \mathcal{F}_{net} must be equal to the total current generated electrochemically on the electrode surface,

$$I_{\text{tot}} = n_e F \sum_{\text{elec}} V_i S_i. \quad (1.33)$$

A tolerance ε_I is set on the maximum relative difference between these currents which must be equal at steady state,

$$|I_{\text{tot}} - \mathcal{F}_{\text{net}}| < \varepsilon_I I_{\text{tot}}. \quad (1.34)$$

The comparison of the total current and the flow of charge through the electrode motivates the definition of an important figure of merit. Define the utilization U as the ratio of the current at steady state I_{tot} to the maximum current that would be possible if the electrolyte at the outlet were completely reduced

[75], i.e.

$$U = \frac{I_{\text{tot}}}{n_e c_0 F Q (1 - s_{\text{in}})} = \frac{\sum_{\text{outlet}} A_i u_i s_i}{(1 - s_{\text{in}}) \sum_{\text{outlet}} A_i u_i}. \quad (1.35)$$

The second expression for U is shown as ratio of two sums over cells comprising the outlet in a discretized geometry. It cancels $n_e F c_0$ and uses the fact that the volumetric flow rate Q is the sum of the flows out of each cell at the outlet, i.e. $Q = \sum_{\text{out}} A_i u_i$.

1.3.4 ELECTROCHEMICAL REACTION WITH UNIFORM POTENTIAL IN ELECTROLYTE - “SIMPLIFIED BUTLER-VOLMER MODEL”

The Butler-Volmer model (1.3.3) provides a rich description of an operating porous electrode, but it requires solving coupled mass transport and charge transport equations, making it computationally demanding. A number of simplifications can be made to this model without sacrificing its essential accuracy. The biggest simplification is to disregard the electromigration term in the Nernst-Planck equation (1.21) to obtain

$$\frac{\partial C_j}{\partial t} = -\mathbf{u} \cdot \nabla C_j + D_j \nabla^2 C_j + S_j, \quad (1.36)$$

thereby sidestepping the entire charge problem. This turns out to be an excellent approximation in the model system because the supporting electrolyte is highly effective at moving charge to neutralize any standing electric field. This fact does not come as a surprise, since that is precisely the engineering function served by the supporting electrolyte. The nondimensionalized reducing overpotential $\tilde{\eta}$ is obtained

from Eq. (1.29) by ignoring $\tilde{\phi}_L$, which is implicitly set to zero in this model, yielding

$$\boxed{\tilde{\eta} = \tilde{V}_{\text{ar}} - \log \left(\frac{s}{1-s} \right).} \quad (1.37)$$

The source term S does not change and is still given by Eq. (1.17).

We now demonstrate that under relatively mild assumptions that are true in the model system, this system can be further simplified to a mass transport problem in only the state of charge s . Suppose that the diffusion coefficients D_O and D_R for the oxidized and reduced species are identical, and denote their common value by D . This assumption holds for the model system, where the experimental values for AQDS and H₂AQDS both match to the one significant figure available with $D = 4 \cdot 10^{-10} \text{ m}^2 \cdot \text{s}^{-1}$, and is close to holding for most redox pairs, which typically have two species of similar size and shape. With this one assumption, the total concentration of redox active species C_T will remain a uniform constant. Since Eq. (1.36) is linear, we can sum the diffusion and advection terms for the oxidized and reduced species to get corresponding terms for C_T . The source term for C_T is zero, because the reduction reaction converts O to R without changing the total concentration C_T ; this assumption would break down if we were modeling degradation side reactions. The resulting transport equation for C_T is thus

$$\frac{\partial C_T}{\partial t} = -\mathbf{u} \cdot \nabla C_T + D \nabla^2 C_T. \quad (1.38)$$

The fluid at the inlet is uniformly mixed with $C_T = c_0$, a known constant set at 20 mM in these simulations. Evaluating Eq. (1.38) when $C_T(x) = c_0$ is spatially uniform, we find $\frac{\partial C_T}{\partial t} = 0$ at $t = 0$, and

C_T does not change over time. In fact, the diffusion term in Eq. (1.38) also shows that any initial imbalance would even out over time as diffusion moved material from regions of high concentration to lower concentration. The advection term also tends to make C_T spatially uniform as the uniformly mixed inlet propagates through the channel. This argument can thus be extended to explain why C_T is a uniform constant and justifies the further simplification $C_T \approx c_0$ in the simplified Butler-Volmer model.

Since C_T is a constant, we can take the transport equation for the reduced species, divide it by C_T , and obtain the Nernst-Planck transport equation for the state of charge,

$$\boxed{\frac{\partial s}{\partial t} = -\mathbf{u} \cdot \nabla s + D \nabla^2 s + 2ak_0 \sqrt{s(1-s)} \sinh(\tilde{\eta}/2).} \quad (1.39)$$

The source term for SOC on the right hand side is found by taking the source term S in Eq. (1.17) and dividing by C_T . An immediate consequence of Eq. (1.39) is that for the dilute theory developed here where chemical activities are assumed to match concentrations, not only is the total concentration c_0 of redox species invariant, it does not have any effect on the state of charge distribution or utilization of an electrode at steady state. c_0 is simply a scalar that factors out of the PDE to be solved for the state of charge at steady state. The richer Butler-Volmer model will show a slight scaling up in ϕ_L as c_0 increases. The convergence criteria for steady state are the same as those given in Eq. (1.30) and Eq. (1.34), except the potential ϕ_L and its change are no longer applicable.

The right hand side of Eq. (1.39) includes a source term for the state of charge with units of s^{-1} . Denote this by $\tilde{S} = S/C_T$. We can completely nondimensionalize the reaction rate by factoring out the specific

area a and the rate constant k_0 to obtain

$$\tilde{R} = \frac{S}{ak_0C_T} = 2\sqrt{s(1-s)} \sinh(\tilde{\eta}/2). \quad (1.40)$$

We can simplify Eq. (1.40) to eliminate $\tilde{\eta}$ and express the reaction rate \tilde{R} using only the state of charge s and the applied reducing voltage \tilde{V}_{ar} . Substitute for $\tilde{\eta}$ using Eq. (1.37) and a straightforward simplification shows that

$$\tilde{R} = \exp(\tilde{V}_{\text{ar}}/2) - \left\{ 2 \cosh(\tilde{V}_{\text{ar}}/2) \right\} s. \quad (1.41)$$

We can verify that Eq. (1.41) is consistent with the equilibrium state of charge calculation in Eq. (1.28) by solving $\tilde{S}(s_{\text{eq}}) = 0$.

We can generalize Eq. (1.41) to the case where the charge transfer coefficient α is not necessarily one half. The source term in Eq. (1.17) generalizes to

$$S = ak_0C_T s^\alpha (1-s)^{(1-\alpha)} \left\{ e^{\alpha\tilde{\eta}} - e^{(\alpha-1)\tilde{\eta}} \right\} \quad (1.42)$$

and the reaction rate in Eq. (1.41) generalizes to

$$\tilde{R} = e^{\alpha\tilde{V}_{\text{ar}}} \left\{ 1 - \left(1 + e^{-\tilde{V}_{\text{ar}}} \right) s \right\}. \quad (1.43)$$

We can verify the consistency of Eq. (1.43) with the special case $\alpha = 1/2$ to recover Eq. (1.41). We can also see on inspection that $\tilde{R} = 0$ when $s = \sigma(V_{\text{ar}}) = s_{\text{eq}}$. Equation (1.43) is a striking result. It states that for any charge transfer coefficient α , the reaction rate is an affine function of the state of charge,

with a maximum source term $S(0) = ak_0e^{\alpha\tilde{V}_{ar}}$. The reaction rate \tilde{R} decreases linearly in s with slope $e^{\alpha\tilde{V}_{ar}} + e^{(1-\alpha)\tilde{V}_{ar}}$. This matches the physical intuition that a higher local state of charge leads to a lower reaction rate, with a high enough SOC leading to a negative sign. While this is a direct consequence of a simple calculation on the Butler-Volmer rate law, it provides a different perspective on the relationship between the rate and the local state of charge that abstracts away a complex nonlinear dependence on the activation overpotential $\tilde{\eta}$. To our knowledge this is a novel result relating local reaction rates to local state of charge that will apply whenever a battery system follows dilute solution thermodynamics and Butler-Volmer rate kinetics and is operated at a controlled voltage.

1.3.5 REACTION STEADY STATE FROM NERNST EQUILIBRIUM BOUNDARY CONDITION - “NERNST MODEL”

In this section we introduce a second model to obtain the steady state of the simplified Butler Volmer model shown in 1.3.4 with less computational work. The obvious way to use the PDE Eq. (1.39) to find the steady state is to time step the system until steady state is achieved. This can require many time steps, and the presence of a nonlinear source term implies that the time steps may be significantly shorter than the CFL criterion alone would imply. To motivate this model, consider the limiting case where the kinetic rate k_0 became infinitely fast. In this limit, the state of charge on the electrode surface would equal its equilibrium value s_{eq} implied by Eq. (1.28), since any departure would lead to an infinitely fast source term to neutralize it. In the fast kinetic limit, the Nernst-Planck equation for the state of charge at steady state therefore simplifies to advection and diffusion terms on the interior with a Dirichlet boundary

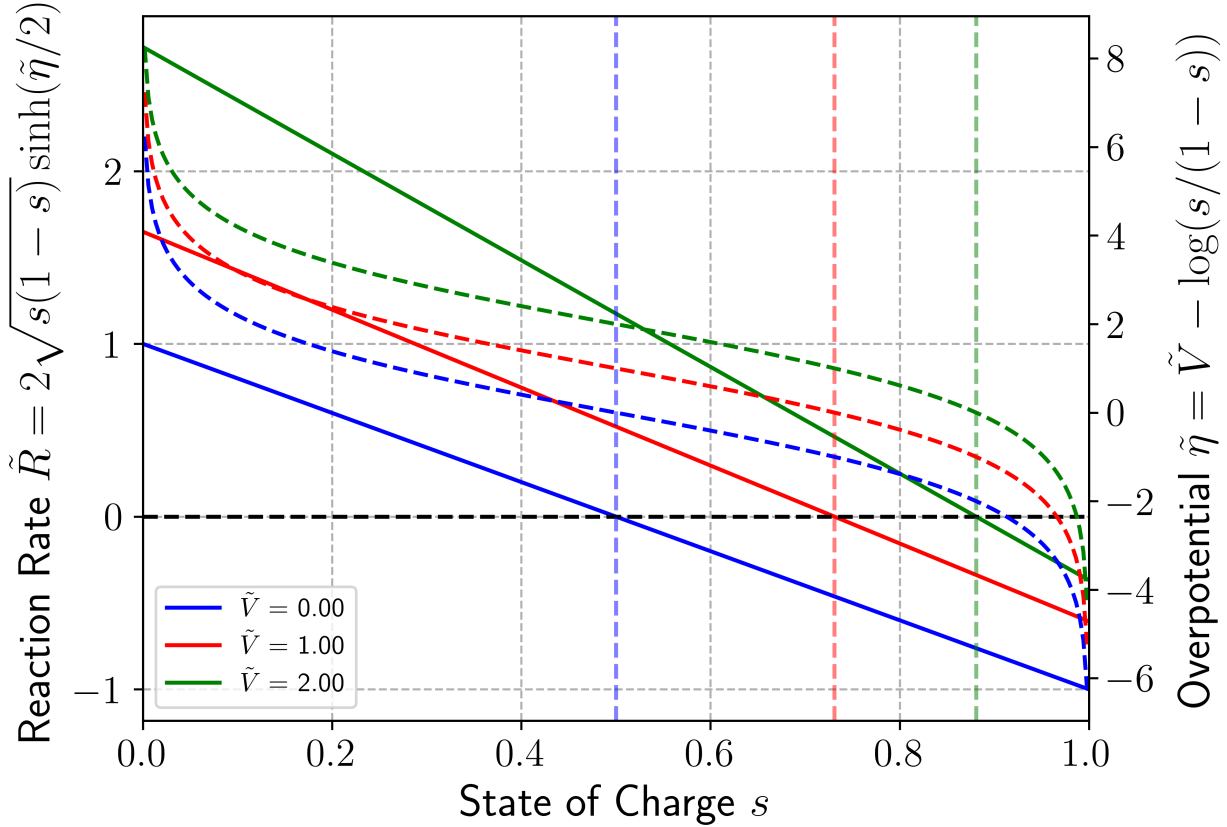


Figure 1.6: Nondimensionalized reaction rate \tilde{R} and overpotential $\tilde{\eta}$ vs. the state of charge s . The reaction rate (solid lines) is an affine function of s . The overpotential (dashed lines) has a sigmoid shape. The horizontal line at $\tilde{R} = 0$ corresponds to the equilibrium condition. The vertical lines indicate the equilibrium SOC at each applied voltage. Increasing voltage drives faster rates and higher equilibrium SOC.

condition on the electrode surface:

$$\begin{cases} \mathbf{u} \cdot \nabla s = D \nabla^2 s & \text{(electrolyte interior)} \\ s = \sigma(\tilde{V}_{\text{ar}}) & \text{(electrode surface).} \end{cases} \quad (1.44)$$

Eq. (1.44) on the interior is obtained from Eq. (1.39) by omitting the reaction term, which is zero away from the electrode surface, and using the fact that $\partial s / \partial t = 0$ at steady state. This system can be solved

more straightforwardly than the original Nernst-Planck equation for the state of charge Eq. (1.39) because there is no longer a nonlinear source term. It is a linear PDE and it can be solved efficiently by either explicit time stepping or with a direct linear solver. A further simplification is that all of the boundary cells are controlled by the Dirichlet boundary condition in Eq. (1.45), so the PDE to be solved in Eq. (1.44) is confined to regular cubic cells, allowing faster and simpler explicit methods to be used.

With this idea in mind, consider the same PDE in Eq. (1.39), but this time at steady state with a finite rate constant k_0 . The SOC at steady state s is an unknown scalar field, and there is an overpotential $\tilde{\eta}$ associated with it. At this steady state, the three terms on the right hand side of Eq. (1.39) must sum to zero on the boundary cells. The advection term vanishes because of the no-slip condition. The diffusion and source terms must cancel, with the chemical source producing reduced species that is transported away from the electrode surface by diffusion, so

$$2ak_0\sqrt{s(1-s)} \sinh(\tilde{\eta}/2) = -D\nabla^2 s. \quad (1.46)$$

Observe that because Eq. (1.46) includes the specific area a , it is implicitly defined only for a small test region, e.g. one cell in a finite volume method. We can also write a local version of Eq. (1.46) that applies on the boundary itself without any averaging over cells, by setting the source flux equal to the diffusive flux,

$$2k_0\sqrt{s(1-s)} \sinh(\tilde{\eta}/2) = -D\nabla s \cdot \hat{n}, \quad (1.47)$$

where \hat{n} is a normal pointing out of the surface of the electrode. In Eq. (1.47), the specific area term is

dropped from Eq. (1.46) because this is an equality of fluxes, and the diffusive flux on the right hand side is now given by Fick's first law, $J = -D\nabla s$.

We can invert Eq. (1.46) to solve for $\tilde{\eta}$ in terms of $\nabla^2 s$. This amounts to an instantaneous estimate of $\tilde{\eta}$ that is consistent with the current rate of mass transport away from the reactive surface. Denote this new estimate $\tilde{\eta}_I$, with

$$\tilde{\eta}_I = 2 \sinh^{-1} \left(\frac{-D\nabla^2 s}{2ak_0\sqrt{s(1-s)}} \right). \quad (1.48)$$

On the other hand, $\tilde{\eta}$ can be mapped monotonically to s by inverting Eq. (1.37):

$$s(\tilde{\eta}) = \sigma(\tilde{V}_{\text{ar}} - \tilde{\eta}). \quad (1.49)$$

Putting all of these ideas together, the following coupled PDE reformulates the steady state problem as a Dirichlet boundary condition with an auxiliary variable for the overpotential,

$$\mathbf{u} \cdot \nabla s = D\nabla^2 s \quad (\text{interior}) \quad (1.50)$$

$$s = \sigma(\tilde{V}_{\text{ar}} - \tilde{\eta}) \quad (\text{electrode}) \quad (1.51)$$

$$\sinh(\tilde{\eta}/2) = - \left(\frac{D/2ak_0}{\sqrt{s(1-s)}} \right) \nabla^2 s \quad (\text{electrode}). \quad (1.52)$$

This problem formulation leads to the Nernst model, which jointly builds consistent estimates of s and $\tilde{\eta}$ by updating an iterative estimate of the overpotential $\tilde{\eta}$ as a moving average of $\tilde{\eta}_I$. This is done by replacing $\tilde{\eta}$ with a convex combination of its previous value and the new estimate $\tilde{\eta}_I$, with the weighting of the moving average controlled by a relaxation parameter ω via Eq. (1.53). The value of s on the electrode

surface is a Dirichlet boundary condition from Eq. (1.49) evaluated with the overpotential estimate $\tilde{\eta}$ as in Eq. (1.54). The entire update for the Nernst model is therefore given by

$$\tilde{\eta}^{(n+1)} = (1 - \omega)\tilde{\eta}^{(n)} + \omega\tilde{\eta}_I(s^{(n)}), \quad (1.53)$$

$$s^{(n+1)} = \sigma \left(\tilde{V}_{\text{ar}} - \tilde{\eta}^{(n+1)} \right). \quad (1.54)$$

The Nernst model can be initialized with $s^{(0)}$ matching the value at the inlet and $\tilde{\eta}^{(0)} = 0$.

We can combine the ideas of the fast kinetic limit and the utilization Eq. (1.35) to define a figure of merit for an electrode's flow velocity field: the utilization in the mass transport limit U_{mt} . Let s_{mt} denote the state of charge field that solves the Nernst-Planck equation in the fast kinetic limit (Eqs. 1.44-1.45) where the boundary conditions are $s_{\text{mt}} = 0$ at the inlet and $s_{\text{mt}} = 1$ on the electrode surface. Then we define the mass transport utilization by substituting s_{mt} into Eq. (1.35) to obtain

$$U_{\text{mt}} = \left(\sum_{\text{outlet}} A_i u_i [s_{\text{mt}}]_i \right) \Bigg/ \left(\sum_{\text{outlet}} A_i u_i \right). \quad (1.55)$$

U_{mt} abstracts out any dependence on the reaction kinetics or the applied voltage. It establishes an upper bound on the utilization that could be achieved in an operating electrode run at a high reducing potential and measures how effectively an electrode geometry and its velocity field accomplish mass transport. Algorithm 1.7 shows how to efficiently compute U_{mt} .

I.4 COMPUTATIONAL METHODS

This work is built using the rincflo code of Dussi and Rycroft [41] and extends from two dimensions to three. Rincflo, in turn, employed the incflo code developed by Sverdrup et al. [76] for incompressible flow problems. Both of these codes are built using the AMReX framework of Zhang et al. [77]. AMReX uses a finite volume approach for solving PDEs and includes facilities for constructing problem geometries using an embedded boundary (EB) description of solid / liquid boundaries. AMReX refers to a cell containing both solid and liquid as a *cut cell*. AMReX can do adaptive mesh refinement, allowing a geometric discretization to focus computing resources on the areas of greatest importance. We use a static refined mesh, refining cells that are within one cell of a cut cell.

The top (coarsest) level of the mesh contains the whole domain with no refinement and is indexed by 0. Cells are always cubes, with aspect ratios equal to one. At the top level, denote by h the cell size and the number of cells along each axis by (N_x, N_y, N_z) , so the dimensions of the box containing the problem domain are $(L_x, L_y, L_z) = (N_x h, N_y h, N_z h)$. Each level of refinement models a subset of the previous level, with twice the resolution, so the cell size on level k is $h_k = h/2^k$.

Figure 1.7 illustrates the AMReX approach to describing embedded boundaries with cut cells. The key abstraction is to treat each cut cell as having a plane that separates it into solid and liquid phases. This plane is built by calculating the normal vector from a real valued implicit function which follows the convention that positive values represent points outside the solid, negative values are inside the solid, and zero values represent the surface. The implicit function must be differentiable on the boundary so a

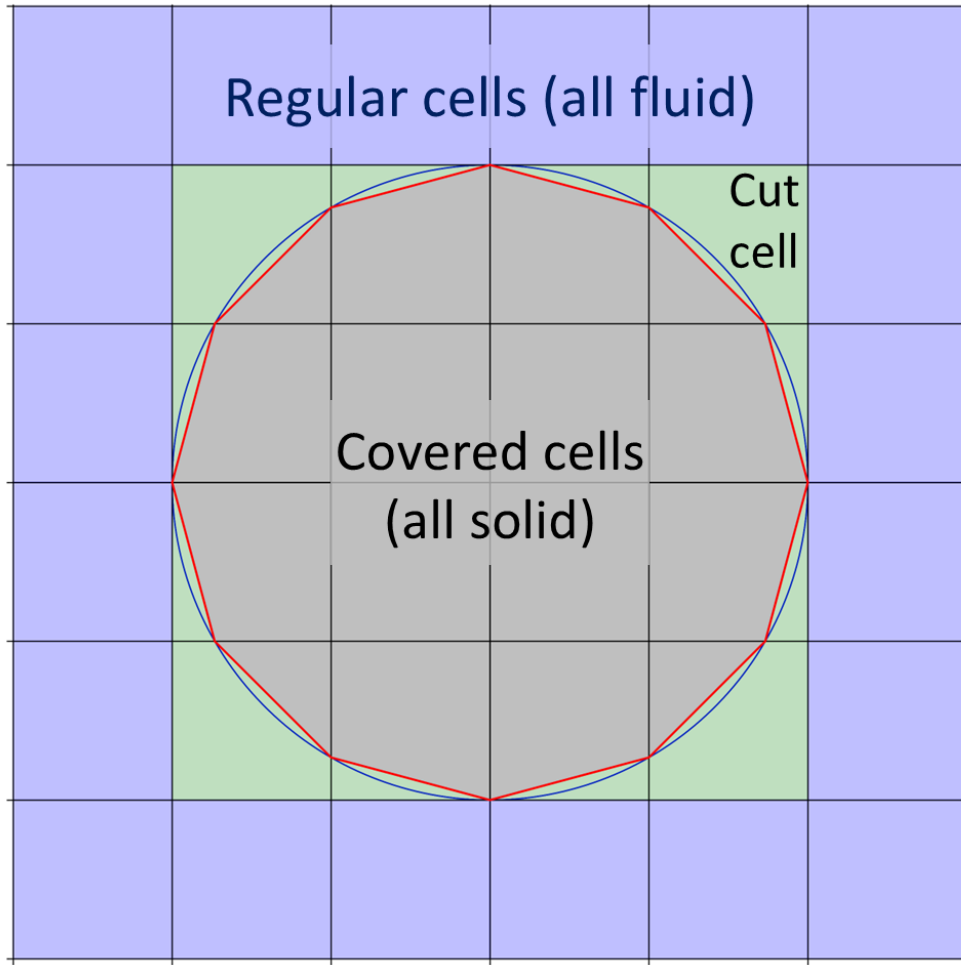


Figure 1.7: Embedded boundary approach in AMReX. The domain is split into a grid of cubic cells, shown in black lines. Regular cells contain only fluid and covered cells (all solid) are disregarded. The electrode surface is composed of cut cells, which are modeled using an implicit function and its normal vector. The exact solid/fluid boundary is shown as a blue circle, while its approximation from normal vectors is shown as set of red chords.

normal vector can be constructed. The canonical choice for the implicit function is a signed distance, e.g.

$f(\mathbf{p}) = \|\mathbf{p} - \mathbf{c}_0\|_2 - R$ for a sphere with center \mathbf{c}_0 and radius R . The implicit function for cylinders, the only primitive shape used in this work, follows a similar idea and is the distance from an arbitrary point

to the nearest point on the cylinder's symmetry axis. Figure 1.7 depicts the embedded boundaries in red as matching up on cell faces. In general, this will *not* be exactly true when the implicit function is approximated to first order about the cell center. However, when the grid resolution is adequate, the boundaries will be close, and in any case the discretized linear operators do not assume overlapping boundaries. Depending on the signs of the implicit function at the corners of a cell, it is not always possible to cleanly cut the cell with a single plane. AMReX calls such cells *multiply cut*, and because they are inconsistent with the conceptual geometry model, they pose significant challenges.

AMReX provides facilities for constructing linear operators and for solving linear equations of the general form $(\alpha A - \beta \nabla \cdot B \nabla) \psi = f$, where α and β are known scalar constants, A and B are known scalar fields, ψ is the unknown scalar field to be solved for, and f is a known scalar field on the right hand side. AMReX includes built in solvers for equations of this type as well as an interface to delegate their solution to the hypre library [78]. Following Dussi and Rycroft, we use the built-in geometric multigrid solver for diagonally dominated linear systems where $\alpha \neq 0$. We solve equations where $\alpha = 0$ using the generalized minimal residual method (GMRES) [79, 80] and an algebraic multigrid preconditioner from the hypre library called BoomerAMG. AMReX is built on an MPI back end and can be used with modern supercomputing facilities for massively parallel processing.

I.4.1 INCOMPRESSIBLE FLUID FLOW

Fluid flows along the x -axis as shown in Figure 1.4 with an applied pressure drop from the inlet to the outlet, and no-slip conditions on the exterior walls and on cut cells comprising the electrode surface. Ex-

perience modeling diverse geometries suggests that a simulation is more likely to run successfully when the constituent simple shapes do not intersect on more than a tangent line of contact. Complex geometries with three dimensional overlapping volumes between primitive shapes can be processed by AMReX, but they lead to large numbers of multiply cut cells and often resulted in convergence problems in the multi-level multi-grid linear solver. We calculate the steady state fluid flow by taking time steps until a convergence criterion is met,

$$\|\mathbf{u}^{(n+1)} - \mathbf{u}^{(n)}\| < \varepsilon_{\text{flow}} \|\mathbf{u}^{(n)}\|, \quad (1.56)$$

where $\|\mathbf{u}\|$ is the ℓ_2 norm and $\varepsilon_{\text{flow}}$ is a dimensionless tolerance for the flow to converge that was set to 10^{-9} in the flow simulations presented in this work.

Eqs. (1.1) and (1.2) are jointly solved using the Chorin projection method [63]. The key idea is to advance the discretized velocity $\mathbf{u}^{(n)}$ one time step Δt to $\mathbf{u}^{(n+1)}$ by an application of the incompressibility condition to construct a Poisson equation for the new discretized pressure $p^{(n+1)}$. First compute an intermediate velocity \mathbf{u}^* that accounts for the momentum advection and viscosity terms,

$$\frac{\mathbf{u}^* - \mathbf{u}^{(n)}}{\Delta t} = -(\mathbf{u}^{(n)} \cdot \nabla) \mathbf{u}^{(n)} + \left(\frac{\mu}{\rho}\right) \nabla^2 \mathbf{u}^{(n)}. \quad (1.57)$$

\mathbf{u}^* can be obtained either explicitly or implicitly using the discretized gradient and Laplacian operators for the problem geometry. To obtain the velocity $\mathbf{u}^{(n+1)}$ at the next time step, we solve

$$\frac{\mathbf{u}^{(n+1)} - \mathbf{u}^*}{\Delta t} = -\frac{\nabla p^{(n+1)}}{\rho} \quad (1.58)$$

for the new pressure $p^{(n+1)}$, which is not yet known. Observe that if we add Eqs. (1.57) and (1.58), the terms with \mathbf{u}^* cancel and we recover the discretized analog of Eq. (1.1) once it is rearranged so the term $\frac{\partial \mathbf{u}}{\partial t}$ is isolated on the left hand side. Next take the divergence of both sides of Eq. (1.58) to obtain

$$\nabla \cdot \mathbf{u}^{(n+1)} - \nabla \cdot \mathbf{u}^* = - \left(\frac{\Delta t}{\rho} \right) \nabla^2 p^{(n+1)}. \quad (1.59)$$

The velocity field at the end of the time step $\mathbf{u}^{(n+1)}$ is known to be divergence free by the incompressibility condition Eq. (1.2), leaving us to solve Poisson's equation for the new pressure,

$$\nabla^2 p^{(n+1)} = \left(\frac{\rho}{\Delta t} \right) \nabla \cdot \mathbf{u}^*. \quad (1.60)$$

Once $p^{(n+1)}$ is known, Eq. (1.58) can be easily inverted to directly solve for $\mathbf{u}^{(n+1)}$. The time step Δt is derived from the Courant-Friedrichs-Lowy (CFL) condition [81] and is updated each flow step. A dimensionless constant C_{CFL} is selected as one of the tuned simulation parameters, typically $C_{\text{CFL}} = 1/2$. The time step Δt is then computed following the approach of Sverdrup et al. [76, Eqs. 7-9]. Δt includes terms for advection C_A , viscous forces C_V and external forces C_F ,

$$\Delta t = \frac{1}{2} C_{\text{CFL}} \left(C_A + C_V + \sqrt{(C_A + C_V)^2 + 4C_F^2} \right)^{-1}. \quad (1.61)$$

The dimensions of C_A , C_F and C_V are all in s^{-1} . The advective term is

$$C_A = \max_{\Omega} \left(\frac{|u|}{\Delta x} + \frac{|v|}{\Delta y} + \frac{|w|}{\Delta z} \right), \quad (1.62)$$

where u_x , u_y and u_z are the three spatial components of the flow velocity \mathbf{u} and Δx , Δy and Δz are the

grid spacing of each cell, and \max_{Ω} is a maximum over all the cells in the geometry. The viscous term for Newtonian flows is given by

$$C_V = \left(\frac{2\mu}{\rho} \right) \max_{\Omega} \left(\frac{1}{\Delta x^2} + \frac{1}{\Delta y^2} + \frac{1}{\Delta z^2} \right) \quad (1.63)$$

and the forcing term is

$$C_F = \max_{\Omega} \left(\sqrt{\frac{|f_x|}{\Delta x} + \frac{|f_y|}{\Delta y} + \frac{|f_z|}{\Delta z}} \right), \quad (1.64)$$

where $\mathbf{f} = (f_x, f_y, f_z)$ is the acceleration due to external forces acting on each cell, which in this work is limited to the pressure gradient term, $\mathbf{f} = -\nabla p/\rho$.

Algorithm 1.1 summarizes how a flow simulation is run to steady state.

Algorithm 1.1 Flow Simulation

```
1: function CALCFLOWTIMESTEP( $\mathbf{u}^{(n)}$ ,  $p^{(n)}$ ,  $C_{CFL}$ )
2:   Calculate  $C_C$ ,  $C_V$ ,  $C_F$  from Eqs. (1.62), (1.63), and (1.64).
3:   return  $\frac{1}{2}C_{CFL} \left( C_A + C_V + \sqrt{(C_A + C_V)^2 + 4C_F^2} \right)^{-1}$ 
4: procedure FLOWSTEP( $\mathbf{u}^{(n)}$ ,  $p^{(n)}$ , ExplicitDiffusion)
5:   ApplyBoundaryCondition( $\partial\Omega$ )
6:    $\Delta t := \text{CalcTimeStep}(\mathbf{u}^{(n)}, p^{(n)}, C_{CFL})$ 
7:   if ExplicitDiffusion then
8:      $\mathbf{u}^* := \mathbf{u}^n - \Delta t (\mathbf{u}^{(n)} \cdot \nabla \mathbf{u}^{(n)} + (\mu/\rho) \nabla^2 \mathbf{u}^{(n)})$ 
9:   else
10:    Solve  $(1 - (\mu \Delta t / \rho) \nabla^2) \mathbf{u}^* =$ 
11:     $\mathbf{u}^n - \Delta t (\mathbf{u}^{(n)} \cdot \nabla \mathbf{u}^{(n)} + \rho^{-1} \nabla p^{(n)})$ 
12:     $\mathbf{u}^* := \mathbf{u}^* + (\Delta t / \rho) \nabla p^{(n)}$ 
13:    Solve  $\nabla^2 p^{(n+1)} = (\rho / \Delta t) \nabla \cdot \mathbf{u}^*$ 
14:     $\mathbf{u}^{(n+1)} := \mathbf{u}^* - (\rho^{-1} \Delta t) \nabla p^{(n+1)}$ 
15:    $n := 0$ 
16:   repeat
17:     FlowStep( $\mathbf{u}^{(n)}$ ,  $p^{(n)}$ , ExplicitDiffusion)
18:      $\Delta \mathbf{u} := \mathbf{u}^{(n+1)} - \mathbf{u}^{(n)}$ 
19:      $n := n + 1$ 
20:   until  $\|\Delta \mathbf{u}\| < \varepsilon_{\text{flow}} \|\mathbf{u}^{(n)}\|$ 
```

The expression for the time step in line (3) comes from Eq. (1.61). The explicit calculation of \mathbf{u}^* in line (8) matches Eq. (1.57) after it is rearranged so \mathbf{u}^* appears on the right. The implicit calculation of \mathbf{u}^* in line (11) is obtained by similar reasoning, except the viscous term is treated implicitly. This corresponds to replacing the momentum diffusion term $\nabla^2 \mathbf{u}^{(n)}$ with $\nabla^2 \mathbf{u}^*$ and then solving the resulting linear equation. The linear system in line (10) is solved using the built-in multigrid solver. The lagged pressure $p^{(n)}$ is used in this step and then added back; since $p^{(n)}$ solves the Laplace equation on the previous time, its gradient is also divergence free and line (11) retains the incompressibility condition on \mathbf{u}^* . The linear system for the new pressure in line (12) matches Eq. (1.60) and is solved using hypre. The unknown in these linear systems is shown in blue typeface. The density ρ and the viscosity μ are treated as constant scalars in this work. Note that this algorithm is modeling advection explicitly and solving for the viscous term (momentum diffusion) either explicitly or implicitly as a parameter. Sverdrup et al. advise against using explicit momentum diffusion with cut cells in incflo [76]. The elliptic equation for the pressure must always be solved implicitly with this approach.

The electrode is modeled as a solid occupying the union of a collection of simple convex shapes such as cylinders and spheres. Multiply cut cells pose a significant problem for Algorithm 1.1. The default AMReX geometric multigrid solver relies on building coarse grids by coarsening, and that procedure breaks down when the geometry contains multiply cut cells. The simulations presented by Dussi and Rycroft [41] were done in two dimensions with well separated circular electrode fibers. Those geometries did not produce multiply cut cells because a circle is a convex shape and the separation between circles

was large enough that two of them never occupied the same grid cell.

When running a simulation in three dimensions, there are many more configurations of the sign pattern for the eight corners of a cube leading to a multiply cut cell than in two dimensions, where only 2 of 16 patterns fail. Most plausible three dimensional electrode geometries contain contact points between convex primitive shapes, such as stacked cylinders in the “logpile” geometry simulated here. The complex geometries simulated with Barber et al. [36] contained three dimensional overlapping regions between pairs of filaments whose center lines were less than a diameter apart. This led to large numbers of multiply cut cells and posed substantial convergence challenges. One of the significant changes from Dussi and Rycroft’s original incflo code is a revised treatment of the parameters related to the handling of these multiply cut cells. In particular, we switched the mode used by AMReX to build the coarse levels in its geometric multigrid solver, changing from the default mode that builds a coarse level by geometrically coarsening a finer level.

We introduce a novel technique in this work to obtain the steady state flow for a refined mesh which we term *iterative upsampling*. The idea behind iterative upsampling is to first solve the entire system to steady state without any mesh refinement, i.e. using an unrefined domain with side length h . The next step is to solve the problem with one level of mesh refinement. Every cell that is either cut, or within one cell of a cut cell (by Manhattan distance) will be refined. This simulation is initialized with the converged steady state velocity $\mathbf{u}^{(0)}$ from the previous step. It is simple to do the initialization using the built-in facilities in AMReX for interpolating from coarse to fine levels. This one idea can dramatically speed up

convergence to steady state when using even a single level of mesh refinement. A second advantage is that refined geometries initialized with a warm start in this way are less likely to have convergence failures on the first time step than problems initialized with a cold start.

Iterative upsampling can be seen as an extension of the multigrid method. The multigrid method is more commonly used to solve a single time step in a PDE. In this case, when we solve the entire incompressible flow problem to its converged steady state at a coarse resolution, it is analogous to the smoothing step in the traditional multigrid method. The upsampling of the coarse solution to the refined grid is likewise analogous to interpolation in multigrid. Heath gives a brief introduction of multigrid methods for linear systems [82, §11.5.7] while classic extended treatments are given by Hackbusch [83] and Wesseling [84], the latter being freely available. Previous development of cascadic multigrid methods by Borne-mann and Deuflhard [85] and Pan et al. [86] take a one-shot approach from coarse to fine. Chow and Tsitliklis applied one-way multigrid methods to stochastic control problems [87], proceeding “one way” from coarse to fine grids.

I.4.2 DIRECT REACTION MODELS (BUTLER-VOLMER AND SIMPLIFIED BUTLER-VOLMER)

The main idea of the Butler-Volmer reaction model is to use a fixed point iteration to find a jointly consistent potential ϕ_L and concentration C at the end of the time step. The concentration is initialized from the previous step with explicit advection. On each step in the fixed point iteration, the latest estimates for the concentration and potential are used as inputs for all the terms in the Nernst-Planck equation (1.21). Diffusion is treated implicitly, and the concentration is updated by putting the electromigration

and chemical source terms on the right hand side. The potential is then updated implicitly by solving the Poisson equation (1.22) where the right hand side uses the latest estimates of the ionic flux and electron source terms. The fixed point iteration can optionally use a relaxation parameter ω to control the rate that updates are applied. The simulations shown here all use $\omega = 0$, i.e. no relaxation.

The specific area a of a cut cell is the ratio of surface area to volume, $a = A/V$, where A denotes the surface area of the embedded boundary (i.e. the plane that cuts the cell between the solid and liquid regions) and V is the volume of the liquid part of the cell. a has units of m^{-1} and scales as one over the fiber diameter in physical electrodes, and as $1/h$ multiplied by a dimensionless parameter of order 1 describing the local geometry in a single cut cell of side length h .

A small change from [41] is clipping the range of s and $\tilde{\eta}$ into admissible limits during time steps. The equilibrium state of charge s_{eq} defined in Eq. (1.28) is the maximum value that would be possible at steady state for a charging flow battery where the inlet concentration s_{in} is smaller than s_{eq} . The overpotential is also clipped to a range controlled by the parameter $\tilde{\eta}_{\text{max}}$. The maximum overpotential was typically set at 100-200 mV, corresponding to $\tilde{\eta}_{\text{max}}$ ranging between 3.9 and 7.8. When $\tilde{\eta}_{\text{max}}$ is set properly, it will not be a binding constraint at steady state, but limiting the overpotential makes the early time steps better behaved. These constraints are imposed at each step to mitigate problems arising from highly nonlinear behavior in the source term when s is near 0 or 1. Algorithm 1.2 summarizes the calculation of the source term and one step of the fixed point iteration.

Algorithm 1.2 Butler-Volmer Fixed Point Iteration

```

1: procedure CALC SOURCE( $C, \phi_L$ )
2:    $s := \text{Clip}(C_{\text{R}}/(C_{\text{O}} + C_{\text{R}}), s_{\min}, s_{\max})$ 
3:    $\tilde{\eta} := \tilde{V}_{\text{ar}} + (n_{\text{e}}\phi_L/V_T) - \log(s/(1-s))$ 
4:    $\tilde{\eta} := \text{Clip}(\tilde{\eta}, -\tilde{\eta}_{\max}, \tilde{\eta}_{\max})$ 
5:    $S := 2aC_{\text{T}}k_0\sqrt{s(1-s)} \sinh(\tilde{\eta}/2)$ 
6:    $\tilde{S} := S/C_{\text{T}}$ 

7: procedure FIXEDPOINTSTEPBV( $C^*, C^{(k)}, \phi_L^{(k)}, \Delta t$ )
8:   CalcSource( $C^{(k)}, \phi_L^{(k)}$ )
9:    $\varepsilon_j := (z_j D_j F / RT) \nabla \cdot (C_j^{(k)} \nabla \phi_L^{(k)})$ 
10:   $\kappa_L := (F^2 / RT) \sum_j z_j^2 D_j C_j^{(k)}$ 
11:   $F_I := F \sum_j Z_j D_j \nabla^2 C_j^{(k)}$ 
12:   $S_\phi := n_{\text{e}} F S$ 
13:  Solve  $(1 - \Delta t D_j \nabla^2) C_j^{(k+1)} = C_j^* + \Delta t (\varepsilon_j + n_j S)$ 
14:  Solve  $(\nabla \cdot (\kappa_L \nabla)) \phi_L^{(k+1)} = S_\phi - F_I$ 
15:   $C_j^{(k+1)} := (1 - \omega) C_j^{(k+1)} + \omega C_j^{(k)}$ 
16:   $\phi_L^{(k+1)} := (1 - \omega) \phi_L^{(k+1)} + \omega \phi_L^{(k)}$ 

```

The dimensionless reducing overpotential $\tilde{\eta}$ on line (3) comes from Eq. (1.37). The source term on line (5) comes from Eq. (1.17). The more general form with a charge transfer coefficient $\alpha \neq 1/2$ is also

supported in the code; the symmetric version is shown here for clarity. S and $\tilde{\eta}$ need only be calculated on the cut cells. The electromigration term on line (9) comes from Eq. (1.21). The conductivity κ_L on line (10) is from Eq. (1.23). There is an option to treat κ_L as a constant during the fixed point iteration by calculating it from the calling routine. This can be done to save time and has minimal effect on the results. The ionic flux term F_I on line (11) comes from Eq. (1.22). The linear system in line (13) treats diffusion implicitly and electromigration and the chemical source term explicitly.

The Butler-Volmer model takes a single time step by repeating the fixed point iteration until convergence criteria for a small change in both the state of charge and potential are met. It is shown in Algorithm 1.3.

Algorithm 1.3 Butler-Volmer Time Step

```
1: procedure REACTIONSTEPBV( $C^{(n)}$ ,  $\phi_L^{(n)}$ ,  $\theta_{mrc}$ )
2:   ApplyBoundaryCondition( $\partial\Omega$ ,  $s_{in}$ )
3:   CalcSource( $C^{(n)}$ ,  $\phi_L^{(n)}$ )
4:    $\Delta t := \text{CalcReactionTimeStep}(\theta_{mrc})$ 
5:    $C^* := C^{(n)} - \Delta t (\mathbf{u} \cdot \nabla C)$ 
6:    $k := 0$ 
7:   repeat
8:     FixedPointStepBV( $C^*$ ,  $C^{(n,k)}$ ,  $\phi_L^{(n,k)}$ ,  $\Delta t$ )
9:      $\Delta s := s^{(k+1)} - s^{(k)}$ ,  $\Delta \phi := \phi^{(k+1)} - \phi^{(k)}$ 
10:     $k := k + 1$ 
11:   until  $\|\Delta s\| < \varepsilon_s$  and  $\|\Delta \phi\| < \varepsilon_\phi$ 
12:    $C^{(n+1)} = C^{(n,k)}$ ,  $\phi_L^{(n+1)} = \phi_L^{(n,k)}$ 
```

The Butler-Volmer model runs time steps until convergence criteria for small changes in the SOC and potential are met. It is shown in Algorithm 1.4. This time, the changes are over a full reaction step rather than in the fixed point iteration as in Algorithm 1.3. The introduction of adaptive time stepping is a small but important change from [41] that has allowed simulations to converge without prohibitively short fixed time steps. These were a problem especially at the early stages of a simulation initialized to a uniform and very low state of charge.

Algorithm 1.4 Butler-Volmer Simulation

```

1: function CALCREACTIONTimestep( $s, \tilde{S}, \theta_{\text{mrc}}, \Delta t_{\text{flow}}$ )
2:    $\Delta t_{\text{react}} := \theta_{\text{mrc}} \cdot \min_{\Omega} \{ \max \left( (1-s)/\tilde{S}, -s/\tilde{S} \right) \}$ 
3:   return  $\min(\Delta t_{\text{react}}, \Delta t_{\text{flow}})$ 
4: procedure REACTIONSIMBV( $C^{(0)}, \phi_L^{(0)}$ )
5:    $\Delta t_{\text{flow}} := \text{CalcFlowTimeStep}(\mathbf{u}, p)$ 
6:    $\theta_{\text{mrc}} := 1/256$ 
7:    $n := 0$ 
8:   repeat
9:     ReactionStepBV( $C^{(n)}, \phi_L^{(n)}$ )
10:    if Successful then
11:       $\theta_{\text{mrc}} := \text{Clip}(\theta_{\text{mrc}} \cdot 2^{1/1024}, \theta_{\text{min}}, \theta_{\text{max}})$ 
12:       $\Delta s := s^{(n+1)} - s^{(n)}, \Delta \phi := \phi_L^{(n+1)} - \phi_L^{(n)}$ 
13:    else
14:       $\theta_{\text{mrc}} := \text{Clip}(\theta_{\text{mrc}}/2, \theta_{\text{min}}, \theta_{\text{max}})$ 
15:      RollBackReactionStep()
16:    until  $(\tau/\Delta t) \|\Delta s\| < \varepsilon_s$  and  $(\tau/\Delta t) \Delta \phi < \varepsilon_{\phi} \|\phi_L\|$ 

```

The method used to compute Δt_{react} ensures that the reaction doesn't consume too large a fraction of either the oxidized or reduced species. \tilde{S} is the source term for the state of charge in s^{-1} , so

$(1 - s)/\tilde{S}$ is the amount of time it would take for the chemical reaction to fully deplete the oxidized species when S is positive in the absence of the diffusion term. Conversely, $-s/\tilde{S}$ is the amount of time it would take to deplete the reduced species if S is negative. The prefactor θ_{mrc} controls the largest fraction of either O and R that would be consumed by the reaction term in any one step. The suffix “mrc” stands for maximum reactant consumption. The reaction time step can never be longer than the flow time step because of the CFL condition, so this constraint is applied separately.

The parameter θ_{mrc} is initially set at a low, cautious value, e.g. $\theta_{\text{mrc}} = 1/256$. A failed time step may be due to the problem being too nonlinear over the selected Δt . After a successful time step, θ_{mrc} is slightly increased by a ratio slightly larger than one, $2^{1/1024}$. After a failed time step, θ_{mrc} is cut in half and the concentrations and potential are rolled back. Notwithstanding the above rules to tune θ_{mrc} , it is always kept in a band between θ_{min} and θ_{max} , which were set at 1/1024 and 1/16 respectively for the simulations run in this work. In practice, we often observed very short time steps at the beginning of the simulation, but as the reaction slows down due to a buildup of reduced species, the time steps become comparable to the flow time step.

The criteria for steady state convergence include a factor $(\tau/\Delta t)$, where τ is the mean time for fluid to traverse the electrode as in Eq. (1.30). This term makes the convergence criterion indifferent to the current time step. It can be interpreted as testing whether the rate of change in the state of charge per unit of time to flow across the channel is small. This is a more stringent criterion than testing the change over an individual time step, so suitable thresholds for ε_s and ε_ϕ are higher. Different simulations in this

work used settings in the range of 10^{-4} to 10^{-2} .

The simplified Butler-Volmer model is analogous to the full Butler-Volmer model, except it disregards the potential in the electrolyte ϕ_L . Mathematically, this is equivalent to setting $\phi_L = 0$. Algorithm 1.5 shows the fixed point iteration and a full time step in the simplified Butler-Volmer model. The full simulation to steady state is essentially identical to Algorithm 1.4 except for the omission of ϕ_L , and it is thus omitted here.

Algorithm 1.5 Simplified Butler-Volmer Model

```
1: procedure FIXEDPOINTSTEPSBV( $C^*$ ,  $C^{(k)}$ ,  $\Delta t$ )
2:   CalcSource( $C^{(k)}$ ,  $\phi_L = 0$ )
3:   Solve  $(1 - \Delta t D_j \nabla^2) C_j^{(k+1)} = C_j^* + \Delta t (n_j S)$ 
4:    $C_j^{(k+1)} := (1 - \omega) C_j^{(k+1)} + \omega C_j^{(k)}$ 
5: procedure REACTIONSTEPSBV( $C^{(n)}$ ,  $\theta_{mrc}$ )
6:   ApplyBoundaryCondition( $\partial\Omega$ ,  $s_{in}$ )
7:   CalcSource( $C^{(n)}$ ,  $\phi_L = 0$ )
8:    $\Delta t := \text{CalcReactionTimeStep}(\theta_{mrc})$ 
9:    $C^* := C^{(n)} - \Delta t (\mathbf{u} \cdot \nabla C)$ 
10:  repeat
11:    FixedPointStepSBV( $C^{(n,k)}$ )
12:     $\Delta s := s^{(k+1)} - s^{(k)}$ 
13:    until  $\|\Delta s\| < \varepsilon_s$ 
14:     $C^{(n+1)} = C^{(n,k)}$ 
```

1.4.3 STEADY STATE REACTION MODEL (NERNST)

Unlike the BV and SBV models shown in the previous section, the Nernst model does not take time steps per se. It instead takes iterative steps that move closer to steady state, though they are analogous to time steps and have a time-like parameter Δt . The assumptions underlying the Nernst model are identical

to those of the simplified Butler-Volmer model. They should both converge to the same steady state solution. A step in the Nernst model begins by imposing boundary conditions at both the inlet and on the electrode surface using the latest overpotential estimate from Eq. (1.54). Advection and diffusion are then calculated. The change in the state of charge on the electrode surface due to advection and diffusion is then used to calculate a new estimate of the instantaneous overpotential according to Eq. (1.48). The term $D\nabla^2 S$ is replaced by $-\Delta s_{\text{elec}}/\Delta t$ because this is the average rate that the SOC is decreasing on this time step due to mass transport. The overpotential η is calculated as a moving average of η_I according to Eq. (1.53). The Nernst model is summarized in Algorithm 1.6.

Algorithm 1.6 Nernst Model

```

1: procedure NERNSTSTEP( $s^{(n)}$ ,  $\tilde{\eta}^{(n)}$ ,  $\Delta t$ )
2:    $s_{\text{in}}^{(n)} = s_{\text{in}}$ 
3:    $s_{\text{elec}}^{(n)} = 1 / \left(1 + \exp(-\tilde{V}_{\text{ar}} + \tilde{\eta}^{(n)})\right)$ 
4:    $s^* = s^{(n)} - \Delta t(\mathbf{u} \cdot \nabla s^{(n)})$ 
5:   Solve( $1 - \Delta t D \nabla^2$ )  $s^{(n+1)} = s^*$ 
6:    $\Delta s_{\text{elec}} = s_{\text{elec}}^{(n+1)} - s_{\text{elec}}^{(n)}$ 
7:    $\tilde{\eta}_I = 2 \sinh^{-1} \left[ -\left( \frac{\Delta s_{\text{elec}}}{\Delta t} \right) \middle/ \left( 2 a k_0 \sqrt{s^{(n)}(1 - s^{(n)})} \right) \right]$ 
8:    $\tilde{\eta}^{(n+1)} = (1 - \omega)\tilde{\eta}^{(n)} + \omega\tilde{\eta}^{(n+1)}$ 

9: procedure NERNSTSIM( $s^{(0)} = s_{\text{in}}$ ,  $\tilde{\eta}^{(0)} = 0$ )
10:   $\Delta t := \text{CalcFlowTimeStep}(\mathbf{u}, p)$ 
11:   $n := 0$ 
12:  repeat
13:    NernstStep( $s^{(n)}, \tilde{\eta}^{(n)}$ )
14:     $\Delta s = s^{(n+1)} - s^{(n)}$ 
15:     $n := n + 1$ 
16:  until  $(\tau/\Delta t) \|\Delta s\| < \varepsilon_s$ 

```

Numerical experiments have verified that the Nernst model converges to consistent results with the simplified Butler-Volmer model and that faster convergence is indeed possible. The simplified models

can still be used to advantage even if the desired output is a full Butler-Volmer model at steady state. We introduce the technique of *model refinement*. The idea is simple but powerful: run a simpler but faster model to steady state and use the resulting state to initialize a richer but slower model. The comparison showing consistent results and faster convergence with both simpler models and model refinement is in [1.6.3](#).

To close this section, we note that it is possible to reformulate Algorithm [1.6](#) so that it uses only explicit calculations. We have done a proof of concept implementation in numpy which is sufficient to show that this technique works well. The first step is to construct explicit sparse matrix representations for the advection and diffusion operators. It is straightforward to define advection on interior cells; the only subtlety is to use upwinding. For cells on the boundary of the domain (either walls or the electrode surface) the no-slip condition implies that advection vanishes. The diffusion operator is equally simple on interior cells. For cells on one of the walls, we use a one-sided second order stencil $f''(x) \approx [2f(x) - 5f(x + h) + 4f(x + 2h) - f(x + 3h)]/h^2$.

The mass transport utilization U_{mt} defined in Eq. [\(1.55\)](#) can be calculated explicitly using advection and diffusion operators defined only on interior cells because the state of charge on the boundary cells is a Dirichlet boundary condition. Thus we have a simple and efficient method to compute U_{mt} explicitly in Algorithm [1.7](#).

Algorithm 1.7 SOC at Mass Transport Limit

```
1: procedure SocMT( $\mathbf{u}, \Omega$ )
2:    $\Delta t := \text{CalcFlowTimeStep}(\mathbf{u}, p = 0)$ 
3:    $\mathbf{A} := \text{MakeAdvectionOpInt}(\Omega, \Delta t)$ 
4:    $\mathbf{D} := \text{MakeDiffusionOpInt}(\Omega, D, \Delta t)$ 
5:    $\mathbf{F} := \mathbf{A} + \mathbf{D}$ 
6:    $\mathbf{s}_0 := 0, \mathbf{s}_0[\text{elec}] := 1$ 
7:    $n := 0$ 
8:   repeat
9:      $i := n \% 2, j := (n + 1) \% 2$ 
10:     $\mathbf{s}_j := \mathbf{F} \mathbf{s}_i$ 
11:     $\mathbf{s}_j[\text{elec}] := 1$ 
12:     $\Delta s := \mathbf{s}_j - \mathbf{s}_i$ 
13:     $n := n + 1$ 
14:   until  $(\tau / \Delta t) \|\Delta s\| < \varepsilon_s$ 
```

We can also formulate a variation of the Nernst model in Algorithm 1.6 using only explicit operations. A precise treatment of diffusion on the cut cells requires intricate computations as discussed by Sverdrup et al. [76, §III.B.1], but it is possible to quickly obtain a good approximation by imposing the requirement that the diffusion operator conserves mass when it operates on interior cells. Let i and j denote the indices

of two neighboring cells in the fluid and boundary, respectively, and A be a generic operator acting only on interior cells. Then A can be extended to have a mass-conserving action on boundary cells by the formulas $A_{ji} = -A_{ij} \cdot V_i / V_j$ and $A_{jj} = -\sum_{i \neq j} A_{ji}$. Defining advection and diffusion according to this recipe leads to conservative operators that disregard the interactions between neighboring cut cells but are otherwise correct.

The procedure described above constructs explicit sparse $N \times N$ matrices for advection (A) and diffusion (D). The flow operator matrix $F = A + D$ will have on the order of $7N$ entries; each interior cell will have a diagonal entry plus at most six entries for its neighbors. We can combine the ideas of Algorithms 1.6 and 1.7 into Algorithm 1.8 for the explicit Nernst model.

Algorithm 1.8 Explicit Nernst Model

```
1: procedure NERNSTEXPLICIT( $\mathbf{u}$ ,  $\Omega$ ,  $\tilde{V}_{\text{ar}}$ )
2:    $\Delta t := \text{CalcFlowTimeStep}(\mathbf{u}, p = 0)$ 
3:    $\mathbf{A} := \text{MakeAdvectionOpFull}(\Omega, \Delta t)$ 
4:    $\mathbf{D} := \text{MakeDiffusionOpFull}(\Omega, \mathbf{D}, \Delta t)$ 
5:    $\mathbf{F} := \mathbf{A} + \mathbf{D}$ 
6:    $\mathbf{s}_0 := 0, \mathbf{s}_0[\text{elec}] := 1$ 
7:    $\eta := 0, \eta_I := 0$ 
8:    $n := 0$ 
9:   repeat
10:     $i := n \% 2, j := (n + 1) \% 2$ 
11:     $\mathbf{s}_j := \mathbf{F} \mathbf{s}_i$ 
12:     $\Delta_{\text{elec}} := \mathbf{s}_j[\text{elec}] - \mathbf{s}_i[\text{elec}]$ 
13:     $\eta_I := 2 \sinh^{-1} [-(\Delta_{\text{elec}} / \Delta t) / (2 a k_0 \sqrt{\mathbf{s}_i(1 - \mathbf{s}_i)})]$ 
14:     $\mathbf{s}_j[\text{elec}] := 1$ 
15:     $\Delta := \mathbf{s}_j - \mathbf{s}_i$ 
16:     $n := n + 1$ 
17:   until  $(\tau / \Delta t) \|\Delta s\| < \varepsilon_s$ 
```

Numerical experiments have demonstrated that the explicit Nernst model produces consistent results

with the implicit Nernst model and runs significantly faster.

1.5 RESULTS AND DISCUSSION - FLUID FLOW

We begin with a benchmark simulation of a logpile geometry that is an idealization of a woven design. We then demonstrate convergence of the flow simulations without considering mesh refinement. Once convergence is established, we further demonstrate the consistency of flow simulations done with and without mesh refinement. We demonstrate the efficacy of iterative upsampling and show that it leads to consistent results with faster convergence. We close by examining the effect of varying the applied pressure over five orders of magnitude. We see a clear transition between a Stokes flow regime at lower pressures and the emergence of turbulence with a concomitant increase in both hydraulic resistance and advective mixing.

1.5.1 INCOMPRESSIBLE FLOW SIMULATION FOR A LOGPILE LATTICE

Our benchmark geometry is a logpile lattice of dimensions $1280 \mu\text{m} \times 640 \mu\text{m} \times 160 \mu\text{m}$ as shown in Figure 1.8. It contains 43 cylindrical rods representing the electrode in seven layers. The layers are $20 \mu\text{m}$ apart on the z -axis, at heights of $20, 40, \dots, 140 \mu\text{m}$. The odd layers are oriented along the x -axis and the even layers are oriented along the y -axis. The diameter of each rod is $20 \mu\text{m}$. The cylinders are $128 \mu\text{m}$ apart in each plane, leaving four cylinders in each x -oriented layer and nine cylinders in each y -oriented layer. We simulated this system with an applied pressure of 100 Pa at the inlet. Our reference simulation was done at a high resolution without any mesh refinement. We set a spatial resolution $h = 1.25 \mu\text{m}$, leading to a discretized geometry of $1024 \times 512 \times 128$ cells and a total of $N = 2^{26} \approx 6.71 \times 10^7$ grid

cells. We ran this simulation until it converged with $\varepsilon_{\text{flow}} = 10^{-9}$ as per Eq. (1.56). The simulation took

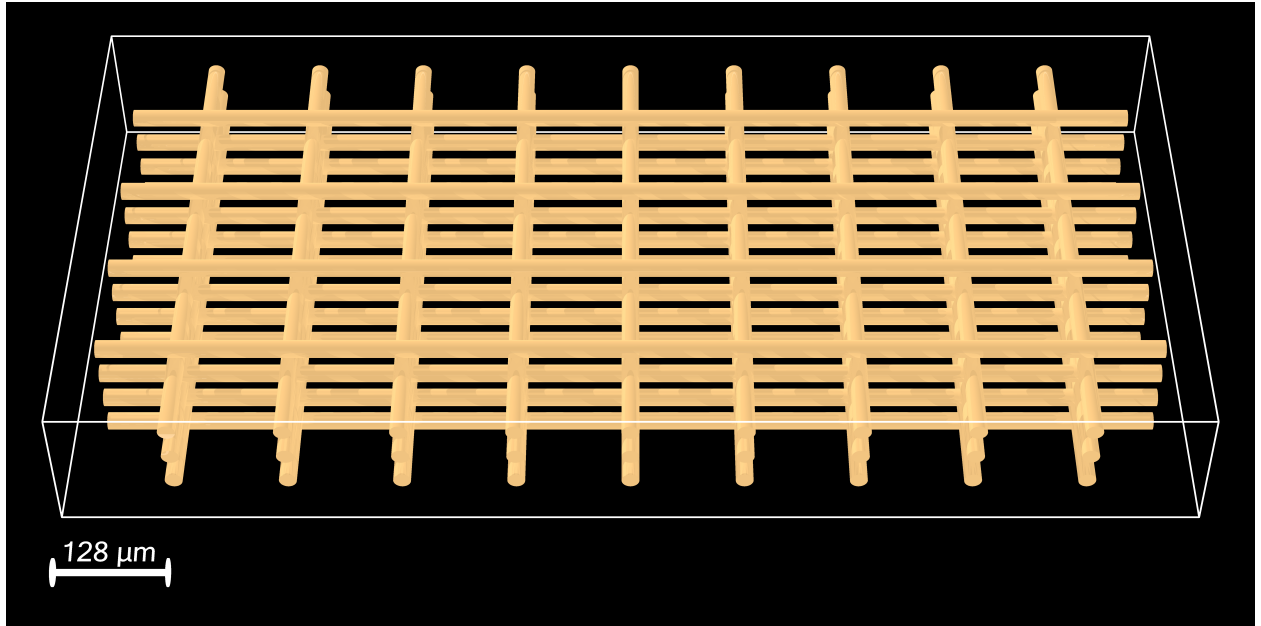


Figure 1.8: Logpile lattice geometry

2094 time steps to converge. The average time step took 170 seconds running on a single server with 192 CPU cores. The entire job took about 99h to complete. These steps evolved the system through 9.08 ms. The predicted volumetric flow rate was 3.45 mL / h.

Figure 1.9 presents a 3D rendering of the integrated streamlines on this flow. Streamlines were integrated using Ralston's method and evaluating the fluid velocity at an arbitrary point by linear interpolation against the values at the cell centers from the flow simulation. As fluid moves from left (inlet) to right (outlet), we can see the streamlines moving over or under transverse rods and hitting a higher speed as it does.

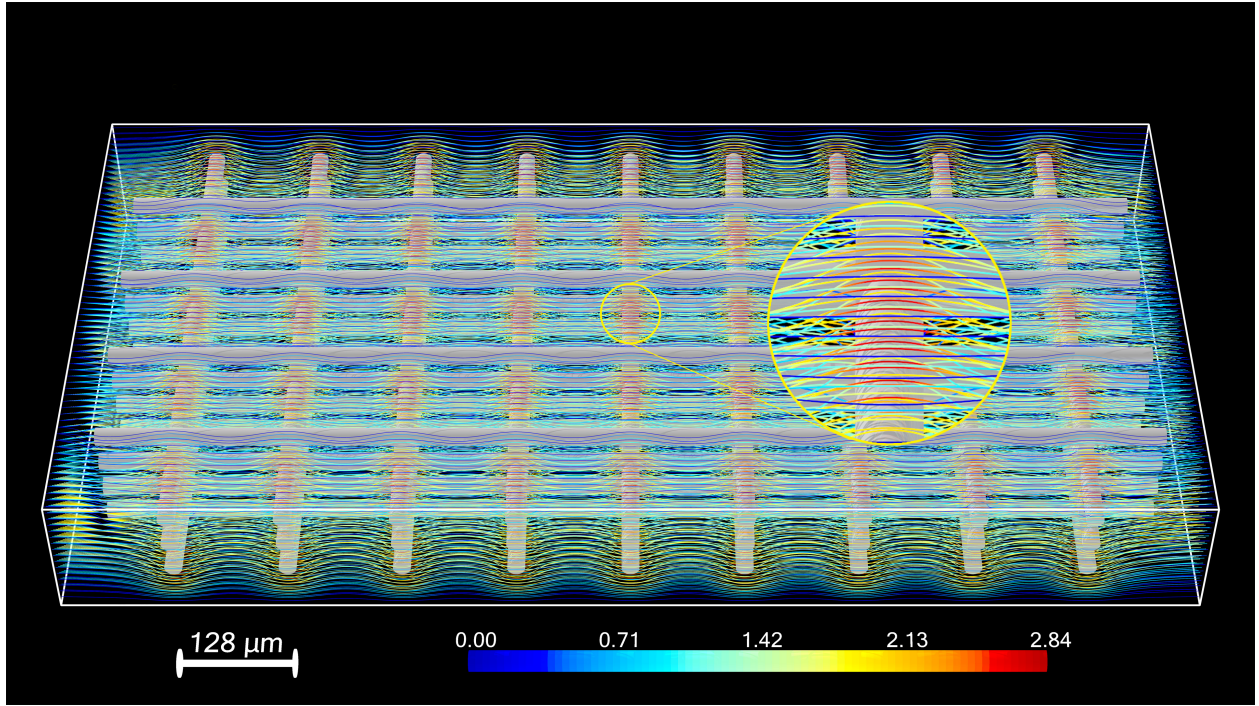


Figure 1.9: Streamlines of steady state flow on logpile geometry with 100 Pa pressure at inlet. Inset region is zoomed four times to demonstrate the finest resolution of $1.25 \mu\text{m}$. Scale bar indicates speed in $\text{cm} \cdot \text{s}^{-1}$.

1.5.2 CONVERGENCE OF FLOW SIMULATIONS

We demonstrate the convergence of our method by simulating three geometries at a series of different spatial resolutions. The three geometries are a single rod; two rods; and the logpile in Figure 1.8. For each of these geometries, we ran a reference simulation with $n_z = 120$ cells in the z -axis, i.e. spatial resolution of $h = (4/3) \mu\text{m}$ and a geometry with $960 \times 480 \times 120$ cells. When comparing the results of a coarse mesh against a fine mesh, the only way to avoid interpolation of some kind is for the spacing on the coarse mesh to be an integer multiple of the spacing on the fine mesh. With this in mind, we additionally attempted to simulate each geometry on a series of coarse meshes with n_z taking on all the proper divisors

of 120 between 5 and 60. In a handful of cases, these simulations either failed to converge or produced anomalous results due to an unlucky alignment of cut cells with an electrode filament. These outlier points were manually excluded from consideration.

For each geometry and coarse resolution with $n_z < 120$, we compute a relative error in the velocity field using the ℓ_2 norm by comparing the coarse resolution with the reference simulation done at $n_z = 120$. It is not immediately obvious how to compare two discretizations of a field on a coarse and a fine mesh. Let φ^c and φ^f denote a generic scalar field on a coarse and fine mesh, respectively, with refinement ratio $r = n_z^f/n_z^c$ between the meshes. We compute the difference by upsampling both fields to the fine resolution, i.e. $[\varphi^f - \varphi^c]_{i,j,k} = \varphi_{i,j,k}^f - \varphi_{i/r,j/r,k/r}^c$. A second subtlety in the convergence analysis is that in the absence of a known analytical solution, if we treat the reference numerical simulation as the exact solution, we may introduce a bias to the estimated convergence rate that is artificially flattering. This bias becomes larger as the coarse resolution gets closer to the reference resolution of $n_z = 120$. With this in mind, we estimate the convergence rate with the functional form

$$\varepsilon(h) = Ch^p(1 - \alpha r^p), \quad (1.65)$$

where $h = 1/n_z$ is the dimensionless step size in the test simulation; $r = h_f/h_c$ is the ratio of the fine step size to the coarse step size; and α is a tunable parameter that is inferred from the data to control the size of the discretization effect. This power law fit for estimating flow convergence follows the approach of Rycroft et al. in establishing convergence for the reference map technique for simulating solid / fluid

interactions of elastically deformable solids [88]. Figure 1.10 shows a plot of the convergence for all

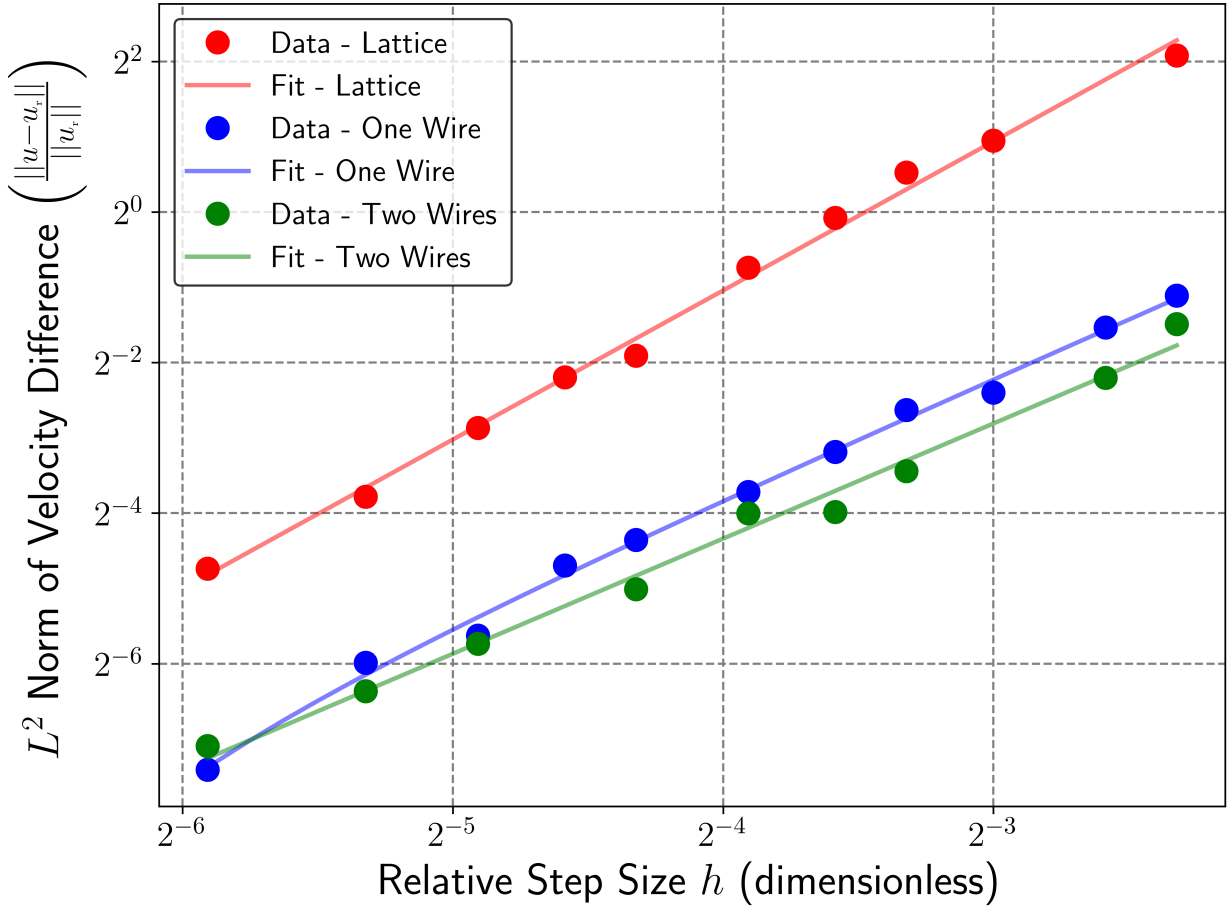


Figure 1.10: Convergence of flow simulations. Three geometries are simulated without mesh refinement (lattice, one filament, two filaments). The y -axis shows the ℓ_2 norm of the difference between each simulation and a reference simulation with $n_z = 120$. The x -axis is the relative step size $h = 1/n_z$. The fit is based on Eq. (1.65).

three geometries while Table 1.1 shows the fitted parameter values. The column RMSE has the root mean squared value of $\log(\varepsilon_j/f_j)$ where ε_j is the actual ℓ_2 error of the j -th point in the series, and f_j is the fitted value based on Eq. (1.65). The flow simulations for a logpile geometry are converging with a fitted power $p = 1.981$ that is very close to the theoretically expected value of 2 given that the Chorin

Geometry	C	p	α	RMSE
Lattice	117.9	1.981	0.000	0.0978
One Filament	5.7	1.575	1.000	0.0802
Two Filaments	3.4	1.530	0.000	0.1216

Table 1.1: Flow convergence fit for three simulated geometries.

projection method is accurate to second order. The other two geometries appear to be converging at somewhat slower rates, with $p \approx 1.55$. However, they are also more accurate than the dense geometries in terms of their relative errors to the reference simulation. These results are in line with those found by Rycroft et al. for geometries with solid / fluid interactions.[88]²

1.5.3 CONSISTENCY OF MESH REFINED FLOW SIMULATIONS

We evaluate the convergence of mesh refined geometries using a similar approach. This time, the reference simulation was carried out with $n_z = 128$ and $h = 1.25 \mu\text{m}$. Coarse geometries were also simulated with $n_z \in \{8, 16, 32, 64\}$. Each coarse geometry was refined successively until the finest resolution matched that of the reference simulation. The physical condition for each simulation was an applied pressure differential of 100 Pa across the channel. Errors were fit with the model

$$\varepsilon = \{C_c h_c^p + C_f h_f^p\} \{1 - \alpha(h_{\text{ref}}/h_c)^p\}, \quad (1.66)$$

where C_c and C_f are fitted coefficients for the error attributed to coarse and fine grained phenomena; p is the fitted power of convergence; α is a fitted discretization coefficient; h_{ref} is the grid spacing on the

²The boundary treatment in [88] was significantly different than the one here, limiting the applicability of a direct comparison in convergence rates.

reference mesh; and h_c and h_f are the grid spacings on the coarse and fine levels, respectively.

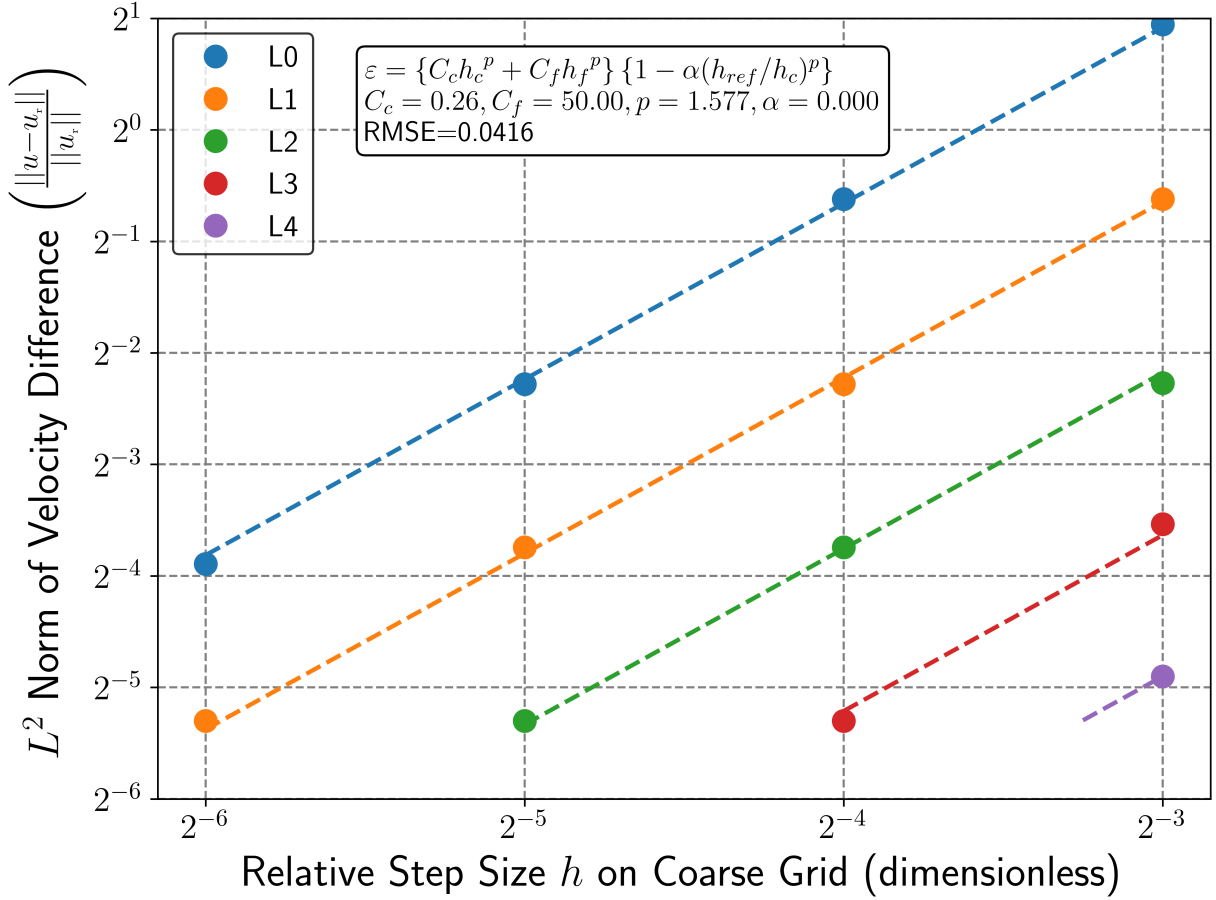


Figure 1.11: Convergence of flow simulations with mesh refinement. The y -axis shows the ℓ_2 norm of the difference between a mesh refined simulation and a reference simulation with $n_z = 128$ for the lattice geometry. The x -axis shows n_z at the coarse level of the mesh (L_0), with different colors for the level of mesh refinement. Errors are fit using Eq. (1.66).

Figure 1.11 shows the convergence of the lattice geometry. The fit captures the data almost perfectly with power of convergence of $p = 1.577$. The error is dominated by the term with $C_f h_f^p$, showing that successive mesh refinements are an effective way to reduce error on this geometry. The fitted power is

Geometry	C_c	C_f	p	α	RMSE
Lattice	0.26	50.00	1.577	0.000	0.0416
One Filament	0.00	1.00	1.228	0.507	0.1840
Two Filaments	0.00	3.85	1.410	0.542	0.4295

Table 1.2: Convergence of mesh refined simulations.

somewhat less than two, showing that there is some compromise to accuracy in refining only the mesh rather than the entire geometry. Table 1.2 shows the fitted results for all three geometries. The results are broadly in line with the trend seen in the lattice geometry, with high overall accuracy even on quite coarse simulations, but a slower rate of convergence. Taken together, these results support the conclusion that mesh refinement is an effective technique in simulating flows of this kind that will produce reliable results when the coarse and fine resolutions are sufficient to capture the relevant phenomena at large and small physical scales, respectively.

1.5.4 EFFICACY OF ITERATIVE UPSAMPLING FOR FLOW SIMULATIONS

We demonstrate the efficacy of the iterative upsampling technique by comparing the reference flow simulation from the previous section to an analogous mesh refined simulation. The reference simulation was run with a uniform grid and $n_z = 128$. The mesh refined simulation was run with $n_z = 64$ at the coarse level and 1 level of mesh refinement. The reference system required 2094 time steps and 99.3 h to achieve steady state. The upsampled simulation was first run to steady state without mesh refinement, requiring 1386 time steps and 4.6 h. This result was then used to initialized the mesh refined simulation, which required an additional 1575 time steps and 31.2 h to achieve steady state. The total run time for steady

state using upsampling was thus 35.8 h, and the reference simulation requires 2.77 times more run time on the same system.

The results are substantially similar. The root mean squared error between the two velocity fields is 3.10%. The errors are predominantly on unrefined cells that are far away from the reaction. When we consider only the mesh refined cells, which include the boundary cells and their neighbors, the root mean squared error drops more than a full order of magnitude to $1.5 \cdot 10^{-3}$. Figure 1.12(a) plots the speed of the reference flow simulation at the mid-plane ($z = 80 \mu\text{m}$). When this is plotted side by side with the results of the upsampled simulation, the results are almost indistinguishable visually. Figure 1.13 shows the relative error, defined as the norm of the velocity difference in a cell over the root mean square velocity. This plot shows that the differences are small through most of the plane with just a few regions where the flow pinches between the end of a rod and the outer boundary wall. Together with the previous section, these results support the conclusion that iterative upsampling is an effective technique to resolve a steady state flow field in significantly less computational work than would be required to simulated the same flow with a uniform mesh. Figure 1.12(b) shows the pressure of the reference simulation. The pressure is almost indistinguishable from a linear gradient. There are slight variations near the pinch points above and below the transverse filaments.

1.5.5 STOKES FLOW AND TURBULENT REGIMES AS PRESSURE VARIES

We simulated the incompressible flow at a broad range of pressures spanning five orders of magnitude to explore the Stokes flow regime as well as the onset of turbulent flow. Simulations were carried out on on

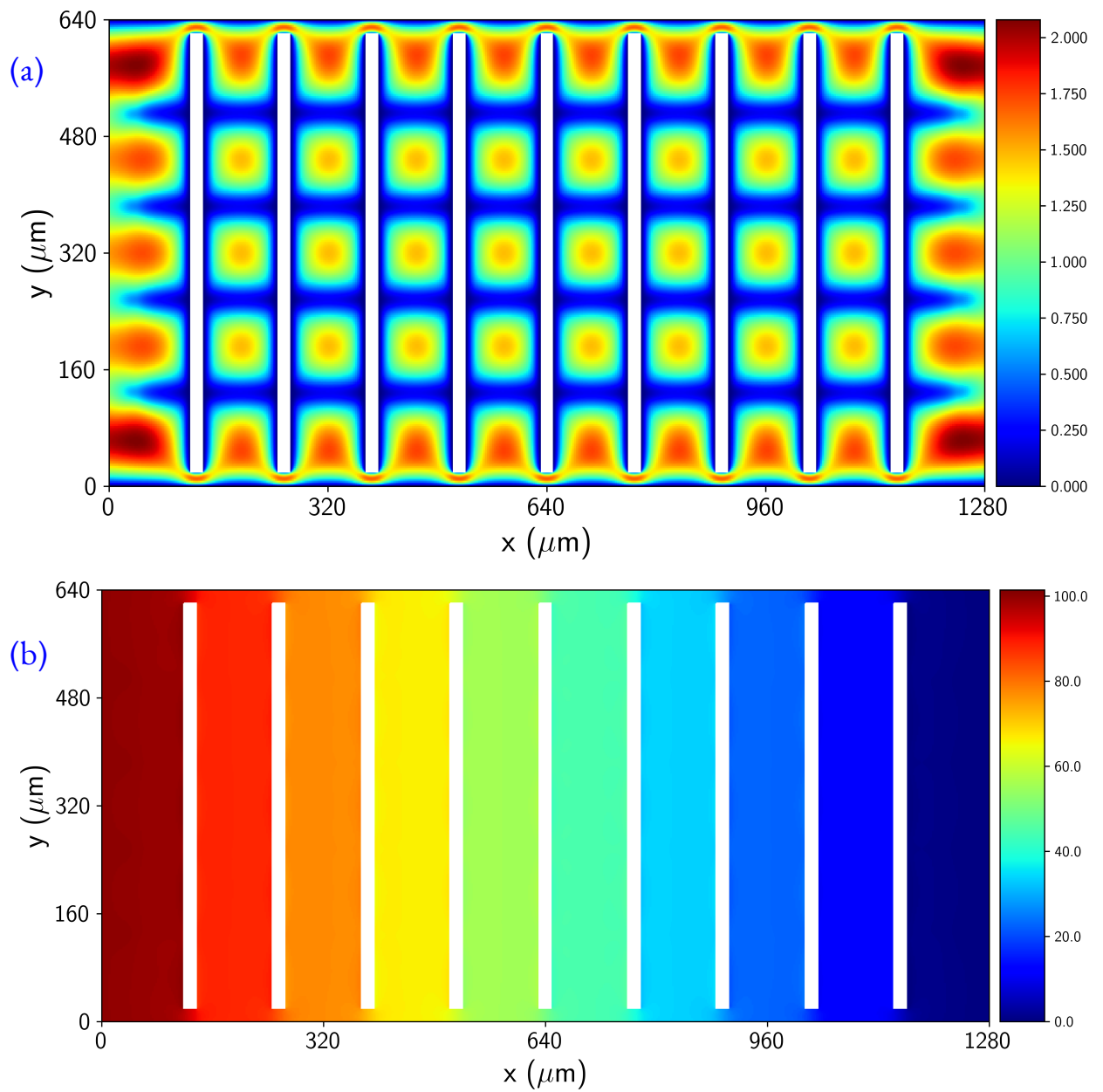


Figure 1.12: Reference flow simulation at $p = 100 \text{ Pa}$ on mid-plane $z = 80 \mu\text{m}$. Panel (a) is speed in $\text{cm} \cdot \text{s}^{-1}$ and (b) is pressure in Pa .

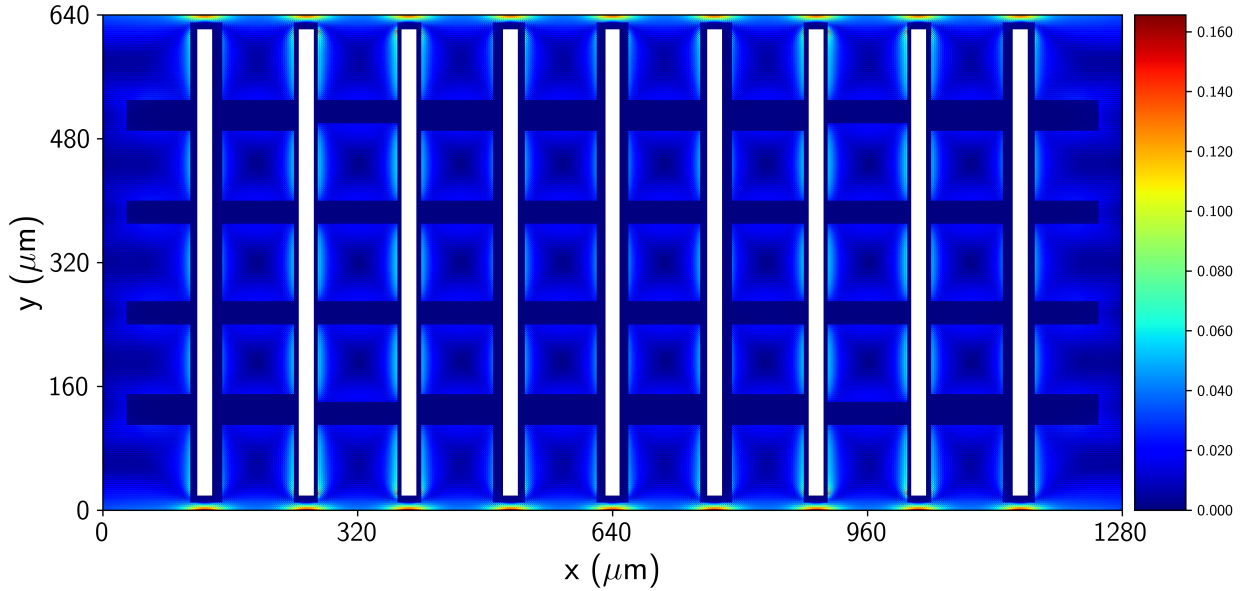


Figure 1.13: Relative error of upsampled simulation vs. reference simulation. The reference simulation has $n_z = 128$ and no meshing. The comparison simulation has $n_z = 64$ and one level of mesh refinement. The error is $\varepsilon_{ij} = (\|u'_{ijk} - u^r_{ijk}\| / \|u^r\|)$ where \mathbf{u} and \mathbf{u}' are the velocities on the reference and refined simulations, respectively.

the logpile geometry with 16 applied pressures of $1, 2, 5, 10, \dots 10^5$ Pa. All simulations were run with the same meshing as the upsampled simulation in the previous section, i.e. one level of mesh refinement and a fine resolution of $1.25 \mu\text{m}$. Simulations were run using the iterative upsampling technique. We calculated the Reynolds number of each flow as described in 1.3.1 using the superficial velocity and channel length.

Figure 1.14(a) shows the volumetric flow rate plotted against the applied pressure. A power law fit $Q \sim CP^r$ is overlaid along with dashed lines corresponding to the predicted onset of turbulence at $\text{Re} = 3000$ [64]. As predicted by theory, the flow vs. pressure relationship is very stable in the Stokes regime. Q then shows a slight bend lower as the flow starts to become turbulent. Figure 1.14(b) shows the

hydraulic resistance of each flow simulation calculated according to Eq. (1.7). The Stokes and turbulent regimes are plotted in different colors. We can see a rapid nonlinear increase in the hydraulic resistance as the flow exits the Stokes regime.

The entire velocity field is essentially linear in the applied pressure, not just the overall flow rate. A side by side plot of the flows at the lowest and highest pressure in the Stokes regime ($p = 1$ and 200 Pa) look almost identical. The root mean square relative difference between these flows after scaling for pressure is only 2.5%, a remarkably small amount given the factor of 200 spanning the pressures. Even after the flow starts to become turbulent, there is still a strong similarity to the Stokes flow. The RMS difference between the flows at 200 and 2000 Pa for instance is 0.164. This is close enough that the flows look qualitatively similar and generate similar streamlines.

We conclude from the above plots and calculations that these results are consistent with the prediction made by theory. Most practical applications of flow batteries are solidly in the Stokes regime because, aside from the problem of excessive pumping losses with increasing hydraulic resistance, turbulent flow speeds are far too fast for sufficient electrochemical utilization. We can therefore further conclude that a single numerical flow simulation done at a low Reynolds number broadly representative of battery operating conditions is sufficient to accurately characterize the whole regime of fluid flows relevant to flow battery operation. Flows at other pressures can be predicted by scaling them linearly to the one simulated pressure. If a more accurate flow is required, the scaled flow can be used as a starting point for a numerical simulation, dramatically speeding up the time to convergence.

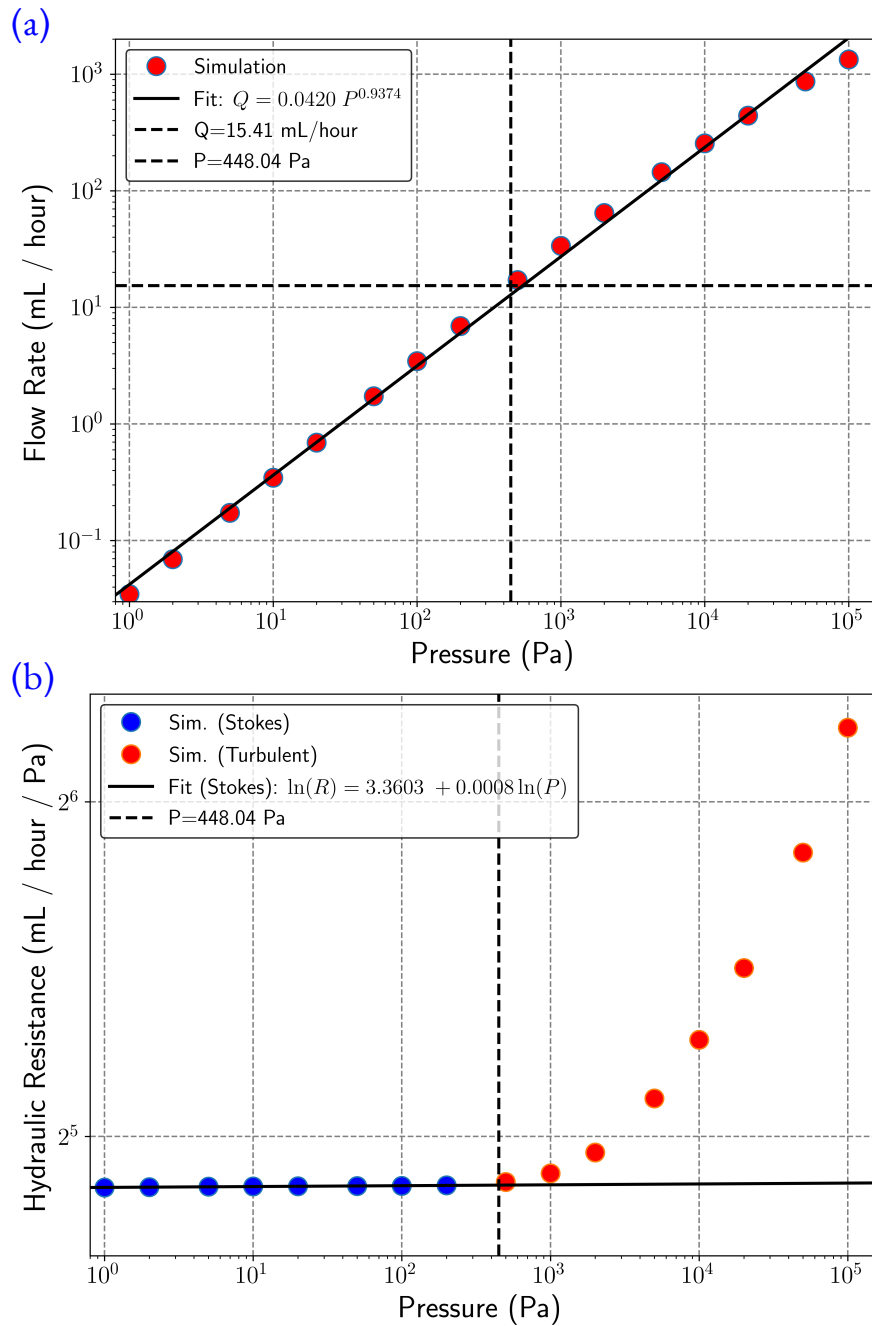


Figure 1.14: Flow simulations at pressures spanning five orders of magnitude. Panel (a) shows volumetric flow rate Q and (b) shows hydraulic resistance R_H . The x -axis is applied pressure in Pa.

1.6 RESULTS AND DISCUSSION - CHEMICAL REACTION

In this section we review the results of our electrochemical simulations on the logpile geometry. We begin by visualizing the results of a reference simulation of a single reaction condition in the simplified Butler-Volmer model. We then demonstrate spatial convergence and the consistence of mesh refined results using analogous techniques to those used for the flow simulations in 1.5. We further demonstrate that the results of various reaction models are all consistent with each other. We close this section by simulating the logpile electrode at a broad range of voltages and flow rates using the computationally efficient explicit Nernst model.

1.6.1 REFERENCE REACTION SIMULATION

Our reference reaction simulation is on the logpile geometry with an applied pressure of 10 Pa and an applied reducing voltage of 0 mV. This was run to convergence in the simplified Butler-Volmer model with a very tight tolerance of 10^{-6} on the RMS change in SOC per flow period. This simulation converged in about 125,000 time steps with 3.35 seconds of simulated reaction time. The predicted current was 0.09 mA, corresponding to a utilization of 0.243. The maximum state of charge for electrolyte in equilibrium with the electrode at this voltage is 0.50, so this utilization is a bit less than half of that upper bound, and this is a suitable test case for the simulation apparatus since it is balancing between advection, diffusion and reaction without any one dominating the others. Figure 1.15 shows a plane view of the state of charge in the center of the electrode. We can see characteristic tails of reduced species building

up along the x oriented fibers above and below this layer as seen experimentally by Barber et al. [36]. The vertically oriented filaments get better mass transport from advection and have a smaller buildup slowing down the reaction. The state of charge becomes more uniform as the flow moves to the right and diffusion increasingly mixes the reactants. Figure 1.16 shows a 3D rendering of key simulation outputs

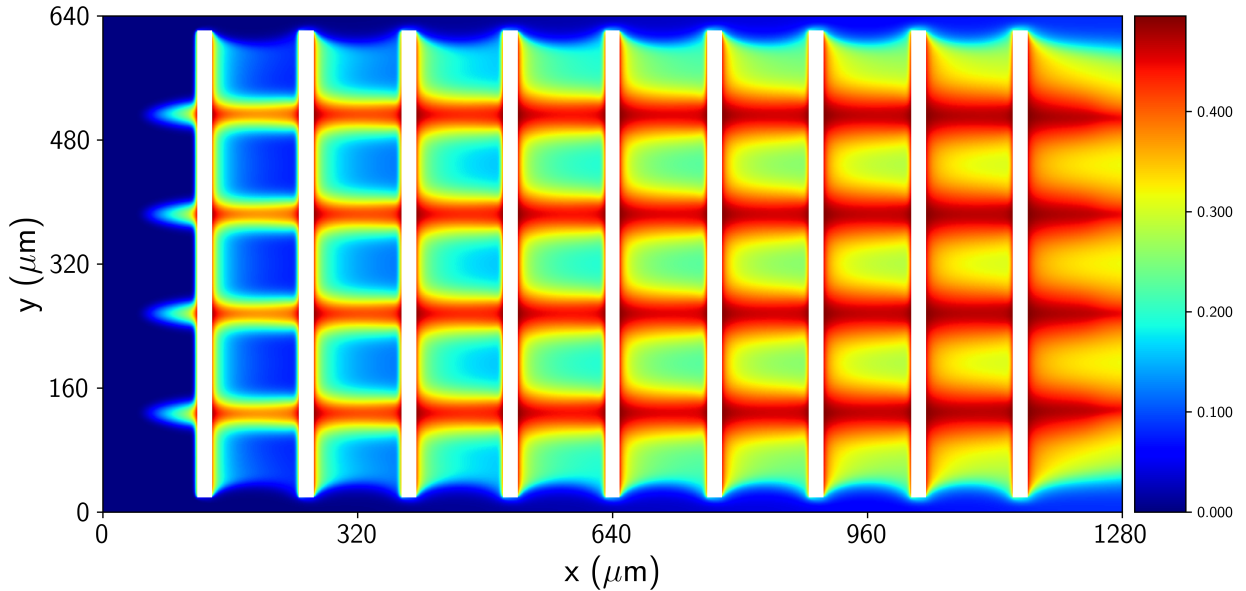


Figure 1.15: Simulated state of charge with $p = 100 \text{ Pa}$ and $V_{\text{ar}} = 0 \text{ mV}$. Plane view at mid-plane $z = 80 \mu\text{m}$.

plotted along streamlines. The three panels show the state of charge, overpotential and current density, respectively. We note that the current density on the transverse rods is much higher than on the axially aligned rods due to their superior mass transport. Advection moves material away from the reactive surface on the transverse rods, but along the reactive surface for the axial rods, limiting their reaction rate to diffusion transport.

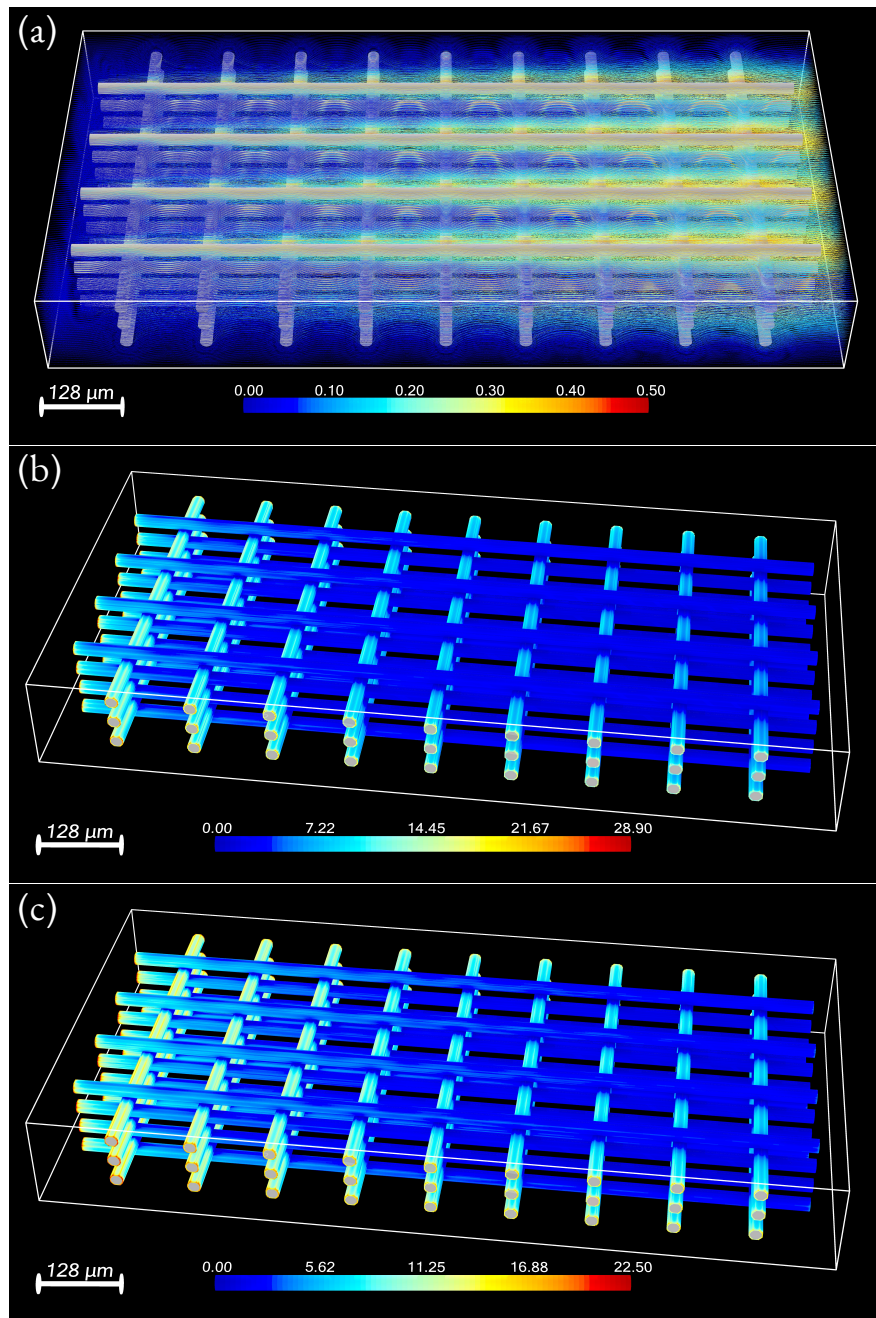


Figure 1.16: Simulated reaction steady state using SBV model with $p = 10 \text{ Pa}$ and $V_{\text{ar}} = 0 \text{ mV}$. (a) State of charge. (b) Overpotential (mV). (c) Current density ($\text{mA} \cdot \text{cm}^{-2}$).

I.6.2 CONVERGENCE AND MESH CONSISTENCY OF REACTION SIMULATIONS

We demonstrate convergence with the same approach used for the flow simulations. We simulated the same operating conditions for the reference reaction simulation ($p = 10$ Pa and $V_{\text{ar}} = 0$ mV) on a series coarse grids with $n_z \in \{5, 6, 8, 10, 12, 15, 20, 24, 60\}$. These were compared with a reference simulation with $n_z = 120$. The fluid flow for each of these simulations corresponds to the one used earlier in the flow convergence analysis. Errors were computed by averaging the predicted state of charge in the fine simulation down to match the coarse geometry and taking the root mean square of the difference in SOC. Figure 1.17 shows the convergence. We again fit the error using Eq. (1.65) and find $\varepsilon \sim Ch^p \cdot (1 - \alpha r^p)$ with $C = 0.408$, $p = 0.818$ and $\alpha = 0.498$. While $p = 0.818$ suggests sublinear empirical convergence, the leading coefficient is small and we can see that these results are in fact converging. The reaction simulations are expensive to run, and finding consistent termination criteria for the different simulations is a challenge that may confound the convergence analysis.

Because of these difficulties, we were unable to replicate the full mesh convergence study shown in Fig. 1.11. Instead, we compared the results of a reference reaction simulation with $n_z = 128$ to an upsampled meshed simulation with $n_z = 64$ and one level of mesh refinement in three reaction models. Table 1.3 shows the results. All three models showed excellent agreement between the upsampled and reference simulation, with errors in the range of $3.7 \cdot 10^{-3}$.

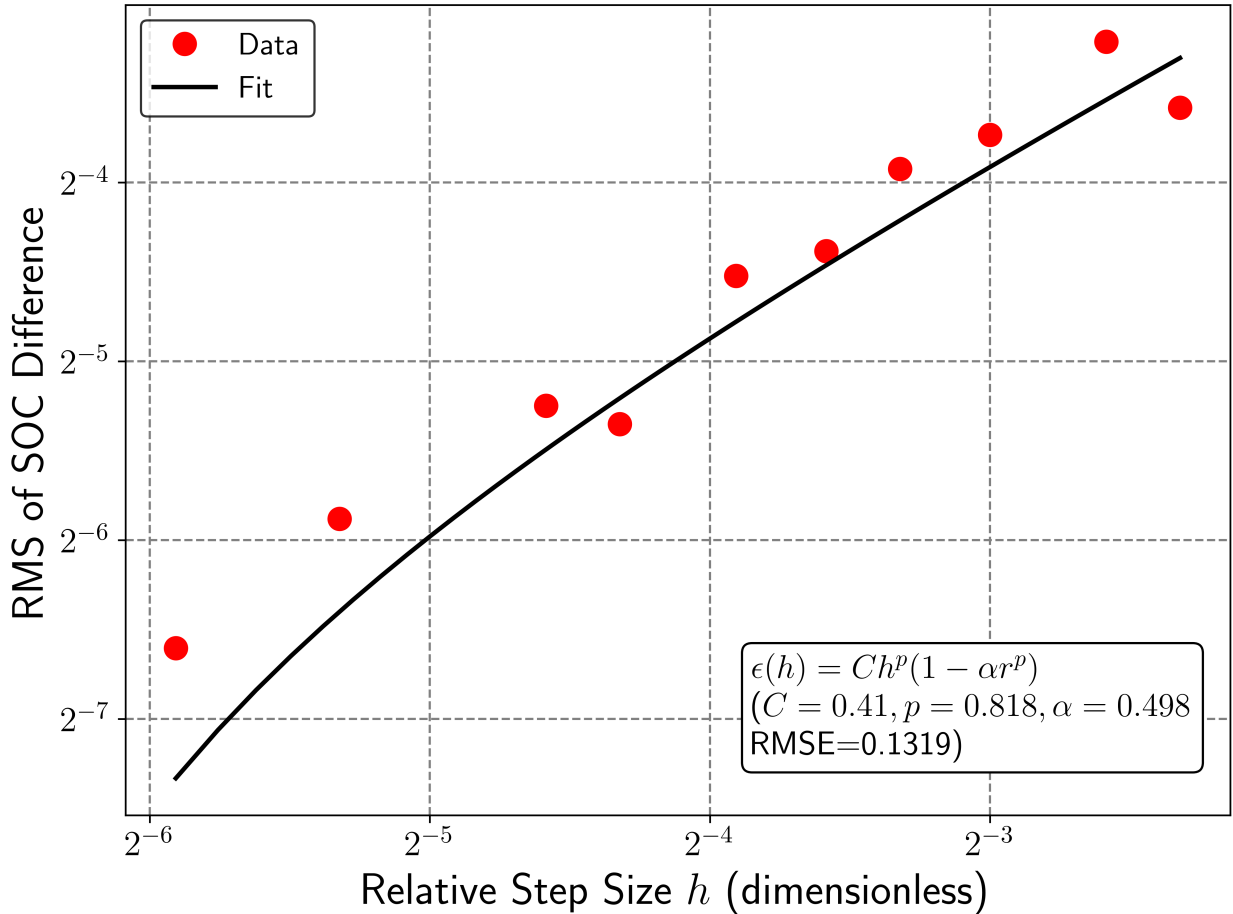


Figure 1.17: Convergence of reaction simulations. Simplified Butler-Volmer model, $p = 10$ Pa and $V_{\text{ar}} = 0$ mV on refined grid with $n_z \in \{5, 6, 8, 10, 12, 15, 20, 24, 40, 60\}$. y -axis shows root mean square difference in SOC vs. reference simulation with $n_z = 120$. x -axis shows relative step size $h = 1/n_z$.

I.6.3 CONSISTENCY OF VARIOUS MODELS FOR REACTION STEADY STATE

Figure 1.18 plots the difference in the state of charge between the Butler-Volmer and simplified BV models. The overall differences are small and concentrated on the y oriented filaments with good mass transport that appear early in the flow path. The reaction proceeds fastest in these areas, and they are unusual.

Model	RMSE
Simplified BV	$3.64 \cdot 10^{-3}$
Nernst	$3.50 \cdot 10^{-3}$
Butler-Volmer	$3.83 \cdot 10^{-3}$

Table 1.3: Comparison of mesh refined simulations to reference.

As reduced product builds up and diffusion smooths out the SOC field, the differences between the full and simplified models gets progressively smaller. This builds the intuition that in a larger electrode of practical interest, the differences between these models will be even smaller than what is shown here. Ta-

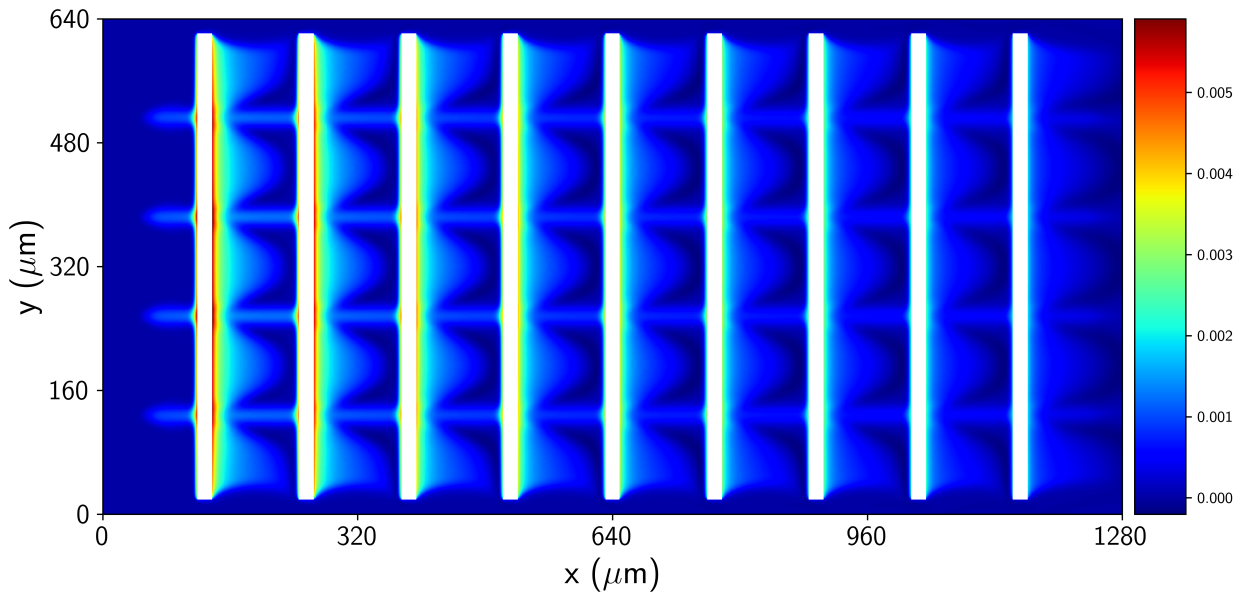


Figure 1.18: SOC difference between BV and SBV models. Lattice geometry at $p = 10 \text{ Pa}$ and $V_{\text{ar}} = 0 \text{ mV}$ plotted at mid-plane $z = 80 \mu\text{m}$. Plotted values are $|s_{\text{SBV}} - s_{\text{BV}}|$.

ble 1.4 shows the root mean square difference in SOC between the simplified Butler-Volmer model (as baseline) against the Nernst and Butler-Volmer simulation results. Both models predict almost the same SOC field at steady state. Figure 1.19 shows the simulated potential ϕ_L in the Butler-Volmer model for

Model	RMSE vs. SBV
Nernst	$2.30 \cdot 10^{-3}$
Butler-Volmer	$8.61 \cdot 10^{-4}$

Table 1.4: Comparison of alternative models to SBV.

the reaction condition discussed in the last section. The potential in the electrolyte is minuscule. It has a mean of 0.16 mV and a max of 0.47 mV. This is negligible in the context of flow batteries that are routinely run with overpotentials on the order of 50-150 mV. We can see a clear trend of increasing potential moving away from the membrane with an approximately linear gradient in z , but the magnitude is very small. We emphasize that the potential in the solid does not have a direct dependence on the potential in the liquid. ϕ_L is the solution to a Poisson equation whose right hand side depends on the movement of charged species. The applied potential only impacts it indirectly by increasing the reaction rate. The biggest potential buildups occur near the first few transverse filaments where the fastest reactions are occurring, requiring a net movement of protons towards the filament to maintain charge balance. The physical intuition here is simple: in the presence of a strong supporting electrolyte, the standing electric field will be so small as to be negligible in flow battery operation. While the precise size of the effect will vary with different electrochemical systems, we hypothesize that in most systems of interest for energy storage, supporting electrolytes will be sufficiently conductive to make this an insignificant effect.

I.7 CONCLUSIONS

In this work we have created a digital twin for a porous electrode in a redox flow battery, consisting of a direct numerical solution to the governing Navier-Stokes and Nernst-Planck equations. This numerical

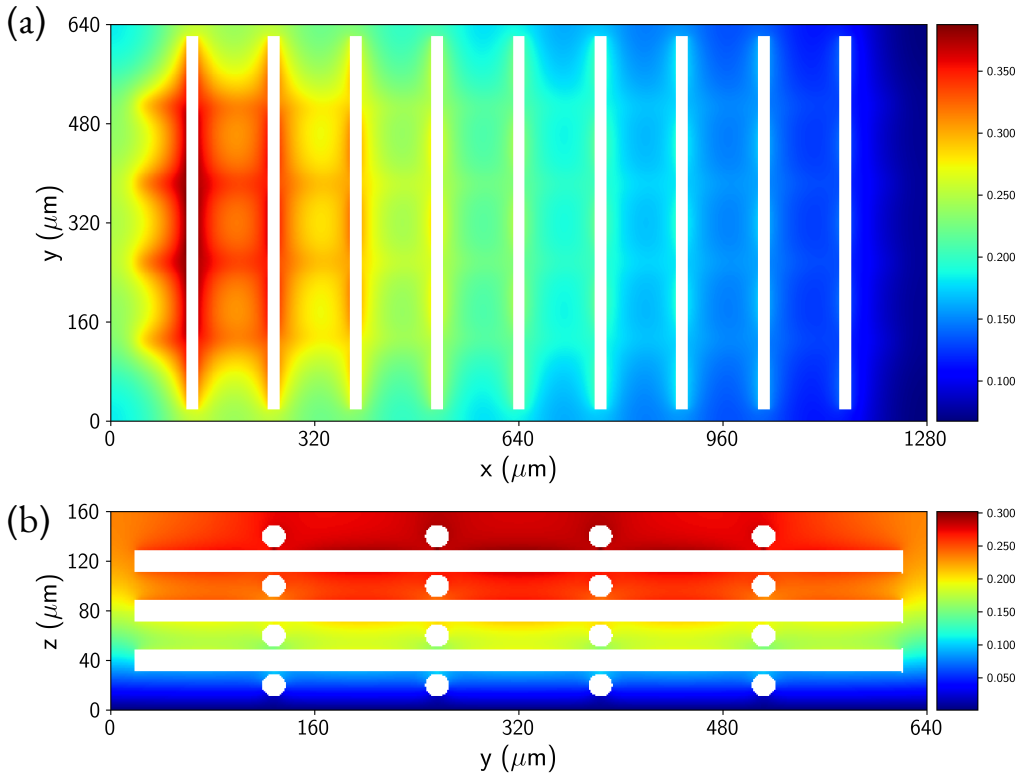


Figure 1.19: Simulated potential ϕ_L in the BV model with $p = 10 \text{ Pa}$ and $V_{\text{ar}} = 0 \text{ mV}$. Panel (a) shows an xy projection at mid-plane $z = 80 \mu\text{m}$ and (b) shows a yz projection at mid-plane $x = 512 \mu\text{m}$. Potentials are in mV (scale bar at right).

solution is performed with minimal compromises at a sub-fiber scale of $1.25 \mu\text{m}$ using only open-source software that is highly performant, parallelizable, and compatible with the largest modern scientific supercomputers. We have demonstrated that our method converges as expected on a fixed grid, and shown the efficacy of fixed mesh refinement to achieve reliable results in less time and with lower memory usage than would be required on a uniform fixed grid. We have shown these points separately for the incompressible fluid flow and electrochemical reaction parts of the simulations. We also briefly discuss an experimental validation of this model carried out by Barber et al [36].

We have elucidated the theory of the porous electrode system and made a novel presentation of several fundamental ideas. We have shown that the total concentration of redox active species is a constant under modest assumptions that are nearly true in practice, allowing the Nernst-Planck equation to be written in terms of only the state of charge s . We have further demonstrated that in many practical systems including our experimental model, the electromigration term is negligible and can be safely disregarded, creating a simplified advection-diffusion-reaction PDE that describes the steady state condition. This will be true whenever the supporting electrolyte is a significantly better conductor than the active species, thereby minimizing standing electric fields in the electrolyte at steady state.

Our simulations are carried out using the minimal required set of materials parameters, including the electrolyte density ρ and viscosity μ , the kinetic constant k_0 , and charge transfer coefficient α . We do not assume a specific area a , but model it directly from the electrode geometry. We similarly do not assume an empirical mass transfer coefficient k_m , but instead directly simulate the reaction on each cut cell, allowing k_m to manifest as an emergent property of the system.

We have derived an equivalent reformulation of the steady state PDE that exchanges the Robin boundary condition on the electrode surface with a Dirichlet boundary condition, leading to a computationally efficient method (the Nernst model) for solving the steady state by iteratively constructing consistent estimates for the state of charge and overpotential. Crucially, we have shown that the Nernst model can be implemented efficiently with an explicit algorithm once a fluid flow has been calculated, so that in practice finding the state of charge field is actually easier than solving the incompressible flow problem. We

have introduced a novel figure of merit, U_{mt} , the mass-transport limiting utilization for a porous electrode geometry, and shown how it can be efficiently computed. And we have shown the novel and broadly applicable result that under dilute-solution thermodynamics and Butler-Volmer reaction kinetics, when a battery is charged at a controlled voltage, the local reaction rate is an affine function of the local state of charge.

We have introduced a number of novel numerical techniques for speeding the computation of the electrode steady state and demonstrated their efficacy. Iterative upsampling works by simulating the system to steady state at a coarse resolution, then using the converged steady state as a starting point for a simulation at a finer resolution. It can thus be seen as a generalization of the idea behind multigrid solvers. Model refinement works by simulating the electrochemical system to steady state at a lower level of fidelity (e.g. disregarding electromigration) and then initializing the higher fidelity model. In this way, it is possible to quickly check the validity of the assumption that electromigration is small. One can then go on to complete a higher fidelity simulation if it is required and still achieve significant time savings.

Our key finding is that in an age of exascale scientific supercomputers, it is not only possible, but computationally feasible to obtain a high fidelity numerical solution of the governing equations for a porous electrode at steady state. This capability can serve many useful ends in porous electrode science. A digital twin can validate other modeling frameworks such as LBM and PNM to a higher degree of precision than is possible with experimental methods on unstructured commercial carbon electrodes. It can also be used for inverse design and to generate synthetic data to train and validate surrogate models

using techniques such as machine learning. And it is a valuable adjunct to experimental characterizations of 3D printed electrodes, allowing experimental images to be compared side by side with their numerically predicted counterparts for a greater understanding of both.

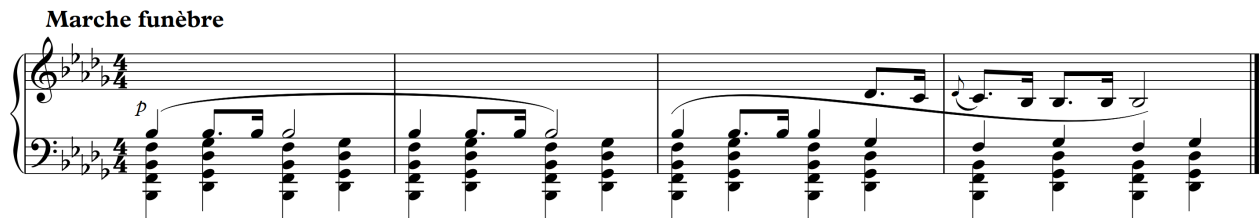
I.8 CODE AVAILABILITY STATEMENT

All source code for this work is available at github.com/memmanuel/rfb-twin.

„Das Wissen ist der Tod der Forschung.“

[Knowledge is the death of research.]

Walther Nernst [89]



Frédéric Chopin, Piano Sonata No. 2 in B \flat minor, op. 35. Marche funèbre (Funeral march).

2

Simulating an Acid-Base Generator

This chapter is adapted from D. Xi, Z. Yang, M. S. Emanuel, P. Zhao, M. J. Aziz, *Electrochemical Acid-Base Generators for Decoupled Carbon Management*, Energy & Environmental Sciences (2025) [2]. I was not the first author of this work, and was primarily responsible for the numerical simulations presented. I will reprise from the published article the abstract (2.1), some background about carbon capture (2.2) and its methods (2.3), the system design (2.4), and the experimental procedures and results (2.5). I did *not* conduct this experimental work, nor did I originally draft the experimental discussion. I produced the published simulation figure and collaborated in revising the manuscript. My original numerical contributions to the paper are described in Sections 2.6 and 2.7 and written in my own words.

2.1 ABSTRACT

Carbon dioxide capture and management are critical technologies for achieving carbon neutrality and mitigating the impacts of global warming. One promising approach for decarbonization involves electrochemical generation of concentrated acid and base. This effectively decouples the carbon capture-release process from the electrochemical cell, avoiding the kinetic limitations associated with reactions involving CO₂. Designing an electrochemical acid-base generator with high current efficiency and low energy cost is challenging. Following investigations of the crossover rates of protons and hydroxide ions through ion-exchange membranes, we designed a multichambered electrochemical cell for generating weak acid and strong base, which significantly suppressed acid-base crossover. By equipping the center chamber with a serpentine flow field, we achieved acid-base production at high concentrations (>1 M) and high Coulombic efficiency (>95%), while maintaining relatively low energy costs. With this device, we demonstrated carbon management examples of simulated flue gas capture, direct air capture, and green production of slaked lime, as one step toward green cement production. The key components of the prototype can be adapted for use in other electrochemical cell designs, ensuring high efficiency in concentrated acid-base generation in other application scenarios

2.2 BACKGROUND

Global warming is accelerating [9, 10] even as the governments of some of the largest emitting nations are backsliding on previous commitments [11] to reduce greenhouse gas emissions. Against this backdrop, there is a clear and urgent need to investigate technologies that can capture and store carbon dioxide

(CO₂), the most important greenhouse gas [90]. Reducing the combustion of fossil fuels and replacing them with clean, sustainable energy sources should be the immediate policy response of responsible governments to this impending catastrophe. But carbon capture and storage (CCS) may nevertheless play an important secondary role in limiting emissions. In a more pessimistic scenario, CCS may also be a key technology for future generations to rectify the harms caused by Earth's present inhabitants. One promising CCS method is to separate a solution into acid and base using electricity. The generated base can in turn be used to capture CO₂ using the pH-swing method. This approach can be fine tuned to capture CO₂ from flue gas, and with future improvements, it might even lead to a viable path for direct air capture (DAC).

This research explores how to improve an electrochemical acid-base generator by designing a specialized electrochemical cell that produces both a strong base and a weak acid, while minimizing energy waste. The cell design uses multiple chambers and specific flow fields to efficiently produce high concentrations of both the acid and base. A key idea is to reduce the so-called "crossover," i.e. undesired mixing between acid and base that dissipates electrical energy into heat. By minimizing crossover, this cell minimizes energy waste and has lower energy requirements than other systems that have been experimentally characterized in previous work (Table A.1). It offers an engineering solution to efficiently generate concentrated acid and base for use in varied applications outside of the electrochemical cell.

2.3 CARBON CAPTURE METHODS

A process to collect high concentration CO₂ from dilute sources such as flue gas, the atmosphere or ocean water is a necessary first step before any downstream carbon utilization [91] or storage [92] can occur. Various methodologies have been explored to address this problem [93]. CO₂ can be captured from flue gas using liquid amine absorbents by applying a thermal swing, but this approach is infeasible for DAC due to ventilation of amines [94]. For the more challenging DAC application, thermal swing [95] or moisture swing [96] on porous solid adsorbents have been used. Metal-organic frameworks [97, 98], amine-decorated silica [99], and alkaline polymers [100] have all been developed for DAC, though these are still hampered by limited thermal and chemical stability. Meanwhile, cycling methods involving the thermal decomposition of calcium carbonate (CaCO₃) into calcium oxide (CaO) present a scalable approach for DAC [101], but they suffer from high energy requirements [102].

Electrochemical methods do not require activating the whole substrate as in thermal swing methods, and have been recognized as promising alternatives that can utilize renewable energy sources and facilitate decentralized operations with improved energy efficiency [103]. Electrochemical amine regeneration for the carbon capture cycle has been realized through mediated regeneration [104, 105] and direct carbon dioxide reduction of the post-capture solvent [106]. One notable technique involves redox-active materials that have reversible binding with CO₂ [107, 108]. Taking quinones as one instance, CO₂ can chemically bind with reduced quinones (i.e. hydroquinones) and then be released upon oxidation of the reduced quinone [109, 110]. Most of the reduced forms of these molecules, however, are sensitive to

oxygen, which is prevalent in carbon capture environments. Moreover, the inherent correlation between the reduced molecules' binding affinity with CO₂ and their reactivity with O₂ makes the development of redox active molecules for DAC challenging [111]. Redox-active molecules undergoing proton-coupled electron transfer (PCET) enable effective pH-swing cycles during charge and discharge, facilitating CO₂ absorption by reaction with hydroxide to form bicarbonate and carbonate, and achieving high current density operation [111, 112]. Unfortunately, most known electrochemically activated molecules for CO₂ capture are susceptible to reversible chemical oxidation by atmospheric oxygen, requiring further development of rebalancing methods [113] and oxygen-stable molecules [114].

Electrochemical acid-base generators have the potential to overcome the challenge of oxygen sensitivity by separating the generated acid and base from the redox mediators. Two examples of electrochemical acid-base generators are the chlor-alkali process and the water splitting driven salt splitting process, but both of these have low energy efficiency [115–120]. Similar acid-base generators using the iodine-alkali process have lower working voltages [45]. Other acid-base generators have been developed including non-PCET redox mediators with bipolar membranes (BPMs) [46] and PCET mediators [121] such as oxygen [47] or hydrogen [48, 122–125] with multichambered cells for acid-base generation. Water dissociation driven salt splitting using BPMs, though suffering from high ohmic resistance due to multiple chambers and membranes, has been used historically and at industrial scale for acid-base generation [46, 126].

However, there are still several desirable properties for carbon capture applications that most electrochemical acid-base generators have not yet fully met. First, for any electrochemically driven carbon

capture process, a low ohmic resistance is crucial to lower both capital and operating costs (Figure A.1). Resistance is the major source of voltage load under high current density operation, in accordance with Ohm's law [125]. Furthermore, for DAC, decoupling CO₂ capture and release from the electrochemical cell can avoid the challenges of slow kinetics for the CO₂ reactions [47] and CO₂ bubble formation in the cell center chambers [124], by creating design flexibility to engineer CO₂ mass transport and kinetics (e.g. by utilizing carbonic anhydrase [127]). Furthermore, the capability to decouple CO₂ reactions from the electrochemical cell can make accessible other carbon management related applications that require acid and base [128]. Finally, a goal of the decoupled generator is to achieve high current efficiency over a wide range of current densities. Important parameters such as current density, energy cost, current efficiency of CO₂ capture, CO₂ source concentration, CO₂ outgas concentration, and dead volume can all become coupled to each other if the cell is tightly tied to the carbon capture process. By decoupling these vital steps, the operating parameters can be jointly optimized for efficient cycling or steady-state operation, thereby improving the resulting process and moving closer to a techno-economically feasible, practical industrial process. A comparison between reported electrochemical acid-base generators is shown in Table A.1.

2.4 ACID-BASE GENERATOR DESIGN

In this work, we present a three-chamber electrochemical cell as shown in Figure 2.1(a). The cell configuration comprises an anode chamber, a central chamber, and a cathode chamber, each separated by cation exchange membranes (CEMs). The center chamber has a serpentine flow field, as well as an ion

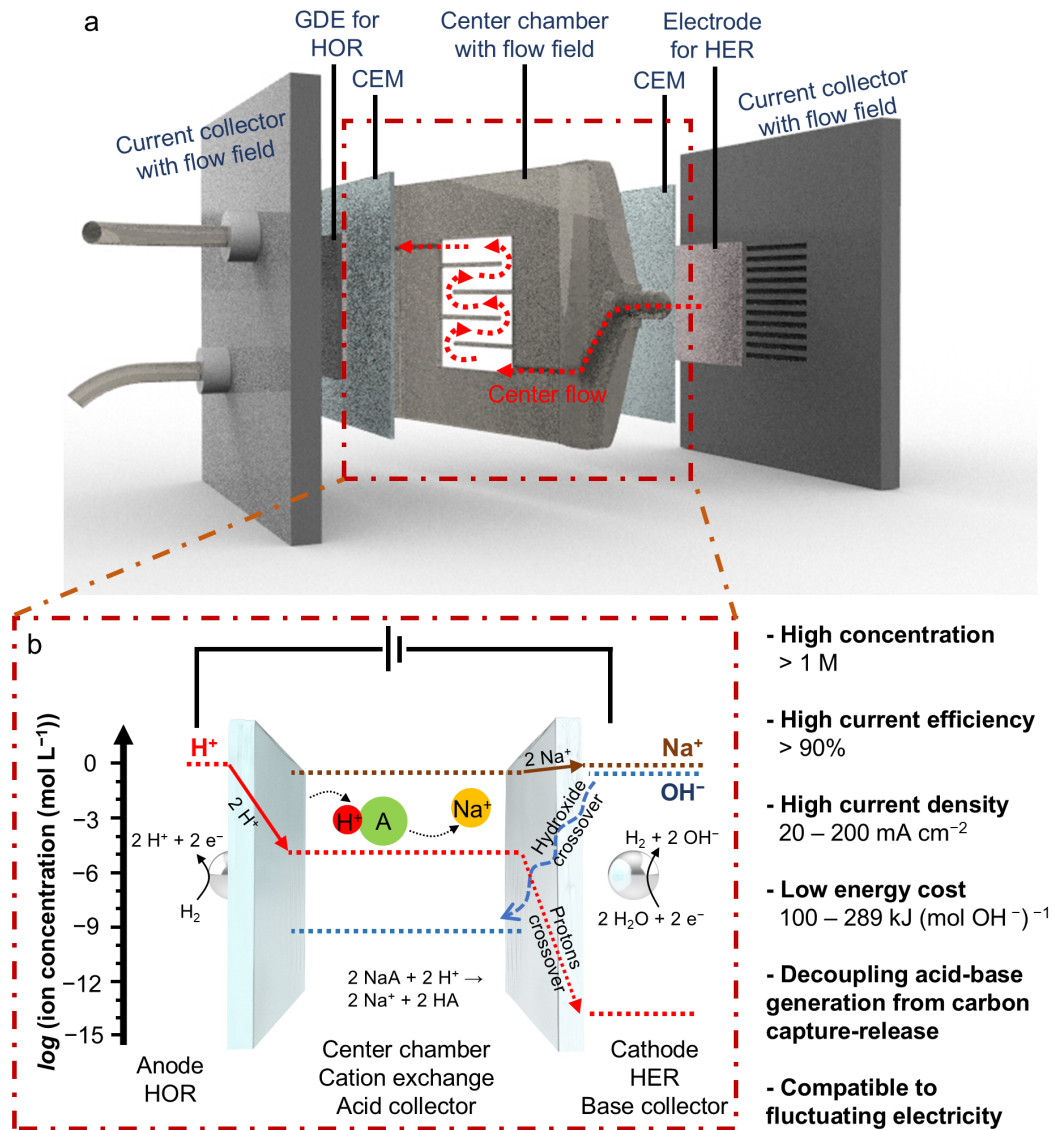
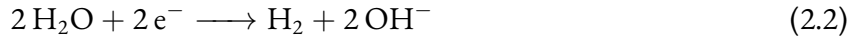


Figure 2.1: Cell structure with technique comparison. a, Structure of the three-chamber, two-membrane acid-base generator with components and flow labeled. b, Schematic of ion transport and concentration in the acid-base generator. Flux of protons (left solid arrow) and sodium ions (right solid arrow) are the major charge carriers. Crossover of protons and hydroxide ions (dashed arrows) are only minor charge carriers penalizing the current efficiency.

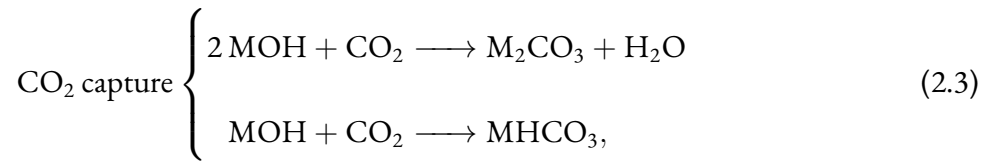
buffer system to manipulate the charge carrier type, in order to achieve a high current efficiency. We utilized cycled hydrogen gas as an example of a low overpotential PCET redox mediator for acid-base generation. The hydrogen oxidation reaction (HOR)



and hydrogen evolution reaction (HER)

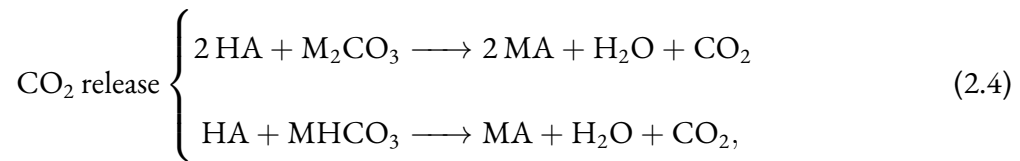


occur at the anode and cathode, respectively. Only a small initial quantity of H_2 is necessary to initiate operation, without further consumption. Specifically, hydrogen is introduced into the anode chamber, where it undergoes oxidation on a gas diffusion electrode (GDE) to yield protons. These protons traverse the anode CEM, binding with weak acid anions (A^-) and thereby accumulating weak acid (HA) that can be collected.¹ Concurrently, to maintain charge neutrality, sodium ions migrate through the cathode CEM into the cathode chamber, where the hydrogen evolution reaction occurs, leading to the production of metal hydroxide (MOH) and enabling the collection of base as shown in Figure 2.1(b). Consequently, the generated acid and base can be used to facilitate carbon capture via the chemical reactions



¹ A denotes a generic anion with a charge of -1 , e.g. chloride (Cl^{-1}) or acetate (CH_3CO_2^-) in the working acid-base generator. Similarly, M denotes a generic metal ion with a charge of $+1$, e.g. sodium (Na^+) or potassium (K^+).

and subsequent carbon release following acid-base recombination via the reactions



where the two reactions in each of Eqs. (2.3) and (2.4) show the capture and release cycle for carbonate and bicarbonate, respectively. These four chemical reactions together comprise the pH-swing cycle for carbon capture and release.

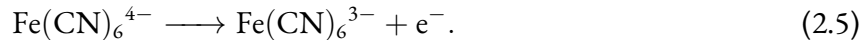
Using weak acid buffering couples, the charge carrier exchange occurring in the center chamber is the key process to maintain high current efficiency under high current density. With improved cell structure and operating conditions, we were able to achieve high current density acid-base generation for decoupled carbon capture with relatively low energy cost. The high concentration acid and base that are generated can be used outside of the electrochemical cell, avoiding problems including solids clogging up the cell, turbulent resistance, and slow reaction kinetics in the cell.

2.5 EXPERIMENTAL MEASUREMENT OF CROSSOVER IN THE ACID-BASE GENERATOR

We systematically studied the crossover of acid and base to gain insights into how to design high efficiency cells. To assess the extent of current efficiency loss attributable to the crossover of hydroxide and protons (Figure 2.1(b)), it is essential to accurately quantify the crossover flux through each membrane.

We first studied hydroxide crossover in the acid-base generator independently. We implemented a two-chamber, one-membrane cell configuration, featuring a hydrogen evolution reaction (HER) cath-

ode alongside a non-PCET neutral anode, in which the ferrocyanide oxidation reaction (FOR) occurs:



The pH was measured during operation by an *in-situ* pH sensor in the anode chamber. Different concentrations of NaOH were cycled at varying current densities. By correlating pH values with concentration, we calculated the time-dependent molarity of hydroxide. The operating conditions are listed in [Table A.2](#) and the results are shown in [Figure A.3](#). Notably, the hydroxide concentration showed a linear trend over time, enabling us to determine the average crossover flux by fitting a linear curve to each experimental run, with the results shown in [Table A.3](#). As shown in [Figure 2.2\(b\)](#), a higher concentration of hydroxide ions in the source side and a higher current density exacerbates the crossover flux. Further details of the experimental approach and data can be found in the published work [\[2\]](#).

Subsequently, to measure proton crossover, we employed a three-chamber, two-membrane cell similar to the structure of the acid-base generator. In this cell, the iodine reduction reaction



was used as a non-PCET, neutral cathode reaction. The HOR [Eq. \(2.1\)](#) was the anode reaction, donating protons into the center chamber, as shown in [Figure 2.2\(c\)](#). The volume of the solution in the center chamber was augmented to maintain stability in the solution composition, while an *in-situ* pH sensor was deployed in the cathode chamber to monitor pH changes resulting from proton crossover.

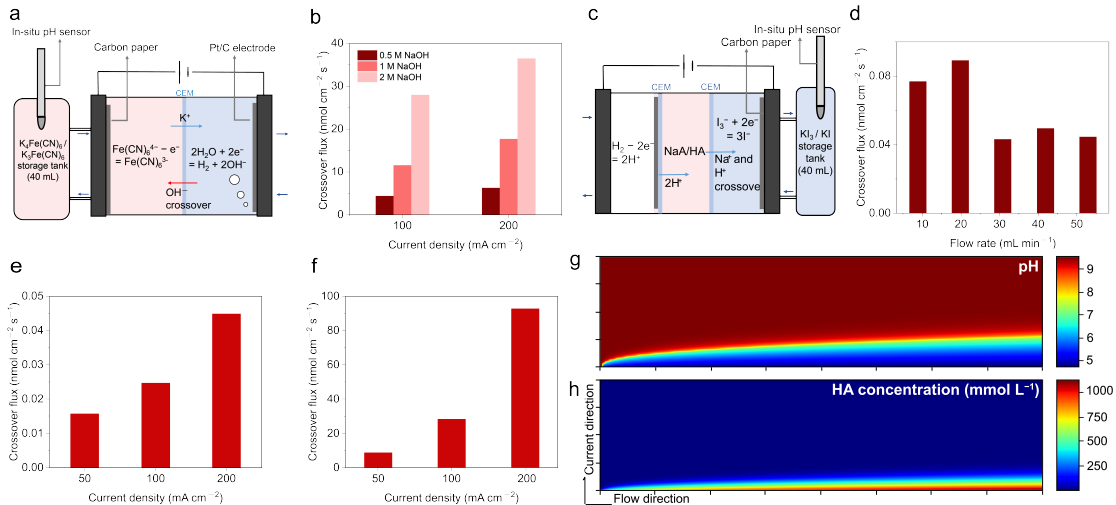


Figure 2.2: Hydroxide and proton crossover test. **a**, Schematic of a two-chamber, one-membrane cell used for hydroxide crossover test. **b**, Crossover flux of hydroxide under varying current densities and concentrations of sodium hydroxide on the cathode side. **c**, Schematic of a three-chamber, two-membrane cell used for proton crossover test. **d**, Proton crossover flux with various flow rates of 2M NaAc in the center chamber. The current density is $200 \text{ mA} \cdot \text{cm}^{-2}$. **e**, Proton crossover flux with various current densities applied, cycling 2M NaAc in the center chamber with a flow rate of $53 \text{ mL} \cdot \text{min}^{-1}$. **f**, Proton crossover flux with various current densities applied, cycling 1M NaAc + 1M HAc in the center chamber with a flow rate of $53 \text{ mL} \cdot \text{min}^{-1}$. Simulation of the distribution of **g**, pH and **h**, HAc in the center chamber (horizontal length: 11.18 cm, vertical length: 1.0 mm), with a pK_a of HAc equaling 4.76. The figures are ideal top views from the orientation of the center chamber in Figure 2.1. The direction of the flow is from left to right. Bottom boundaries indicate the anode membrane where protons enter. The top boundaries indicate the cathode membrane where sodium ions exit, with minor proton crossover.

We ran this cell with a solution of 2M sodium acetate (NaAc)² in the center chamber, corresponding to the initial condition during operation of the acid-base generator. By analyzing the accumulated molarities of protons in the catholyte under different flow rates in the center chamber as shown in Figure A.4, we quantified the proton crossover flux and calculated linear fits as shown in Table A.4. We observed a slight increase under lower flow rate ($< 30 \text{ mL} \cdot \text{min}^{-1}$) of the center chamber electrolyte (Figure 2.2(d)) at

²Ac denotes acetate ion, CH_3CO_2^- .

a current density of $200 \text{ mA} \cdot \text{cm}^{-2}$. We attribute the increase in crossover to weaker washout of accumulated HAc and protons, and decreased NaAc supply. Additionally, for a fixed flow rate of $53 \text{ mL} \cdot \text{min}^{-1}$ in the center chamber, proton crossover increased with higher current density ([Figure 2.2\(e\)](#)).

2.6 CROSSOVER ANALYSIS IN THE ACID-BASE GENERATOR

I became involved late in this project when the first author Dawei Xi mentioned in an Aziz group meeting that he wanted a numerical simulation of the system to better understand what flow rate should be necessary to achieve sufficient “washout” and avoid an excessive buildup of protons at the cathode where they might contribute to crossover. In his inimitable way, Dawei said that COMSOL “didn’t work” and that after multiple days of work, the authors then on the project were unable to configure a problem instance in COMSOL corresponding to their system that converged with sensible answers. I recognized that like the porous electrode in a redox flow battery, the acid-base generator system is also governed by the Nernst-Planck equation, so I rashly volunteered to write a numerical simulation from scratch. It’s been a privilege to work on this interesting and unusual problem, and I thank Dawei and the other authors for the opportunity join their effort.

My first contribution to this paper was to analyze the hydroxide crossover as a function of both the hydroxide concentration $[\text{OH}^-]$ and the current density, hereinafter denoted j . From the univariate data shown in [Figure 2.2\(b\)](#), it is clear that there is an increasing trend in crossover as both hydroxide concentration and current density increase. The precise nature of the functional relationship is not, however,

immediately apparent. I took as my starting point the Nernst-Planck equation

$$\boxed{\frac{\partial C_i}{\partial t} = - \underbrace{\mathbf{u} \cdot \nabla C_i}_{\text{Advection}} + \underbrace{D_i \nabla^2 C_i}_{\text{Diffusion}} + \underbrace{\frac{z_i D_i F}{RT} \nabla \cdot (C_i \nabla \phi_L)}_{\text{Electromigration}}, \quad (2.7)}$$

where C_i is the concentration of species i in $\text{mol} \cdot \text{m}^{-3}$, D_i is the diffusivity of species i in $\text{m}^2 \cdot \text{s}^{-1}$, z_i is the dimensionless charge number as an integer, and ϕ_L is the electric potential in the liquid electrolyte in volts. This variation of the Nernst-Planck equation is different from Eq. (1.21) to describe the redox flow battery because there is no chemical source term S_j . That is because there is no electrochemical reaction in the center chamber of the acid-base generator. Instead, the electrochemical effects are limited to ion fluxes at the membranes on the boundary of the anode and cathode, which appear as boundary conditions in the problem formulation.

From the terms appearing in Eq. (2.7), we can see the form of dependence on the two variables in question, hydroxide concentration and current density. The first two terms, corresponding to advection and diffusion respectively, are both linear in C_{OH^-} when the flow velocity \mathbf{u} is left unchanged. Formally, we can write the effect of the combined advection-diffusion operator ($\mathcal{A} + \mathcal{D}$) as

$$(\mathcal{A} + \mathcal{D}) [C_{\text{OH}^-}] = (-\mathbf{u} \cdot \nabla + D_{\text{OH}^-} \nabla^2) [C_{\text{OH}^-}] = \alpha C_{\text{OH}^-}, \quad (2.8)$$

where α is an empirical constant combining the advection and diffusion terms with units of s^{-1} .

For the electromigration term, observe that at steady state, there is ohmic current flow with ionic charge carriers. Thus the electric field $E = -\nabla \phi_L$ is proportional to the current density j via Ohm's law in

its tensor form, $j = \kappa_L E$, where κ_L is the ionic conductivity of the liquid as explained further in the discussion preceding Eq. (1.23). This relationship can be inverted to write the electric field on the left hand side, $E = \rho j$, where $\rho = \kappa_L^{-1}$ is the resistivity. Thus we can write the electromigration operator \mathcal{E} in the form

$$\mathcal{E}[C_{\text{OH}^-}] = \left(-\frac{z_i D_i F}{RT \kappa_L} \right) \nabla \cdot (C_{\text{OH}^-} \cdot j) = \beta(C_{\text{OH}^-} \cdot j), \quad (2.9)$$

where β is a second empirical constant encapsulating the dependence of the electromigration term on the product of the hydroxide concentration and current density. Eqs. (2.8) and (2.9) thus lead to the two factor regression model for hydroxide crossover flux ϕ_{OH^-} ,

$$\phi_{\text{OH}^-} = \alpha C_{\text{OH}^-} + \beta(C_{\text{OH}^-} \cdot j). \quad (2.10)$$

The replacement of advection and diffusion with a single phenomenological coefficient α is justified here because the fluid flow is in a viscous, Stokes flow regime where the velocity field is nearly linear in the volumetric flow rate. The replacement of electromigration with a coefficient β is likewise justified because the ionic current here is in an ohmic regime with a spatial current density that is nearly linear in the total current density for the cell. This regression model is evaluated by treating the two independent variables as the hydroxide concentration C_{OH^-} and the product term $(C_{\text{OH}^-} \cdot j)$. The results of this regression are shown in Figure 2.3, and we can see an excellent fit with an R^2 of 0.993052. This is a nontrivial result because a model with two free parameters is precisely fitting six observations.

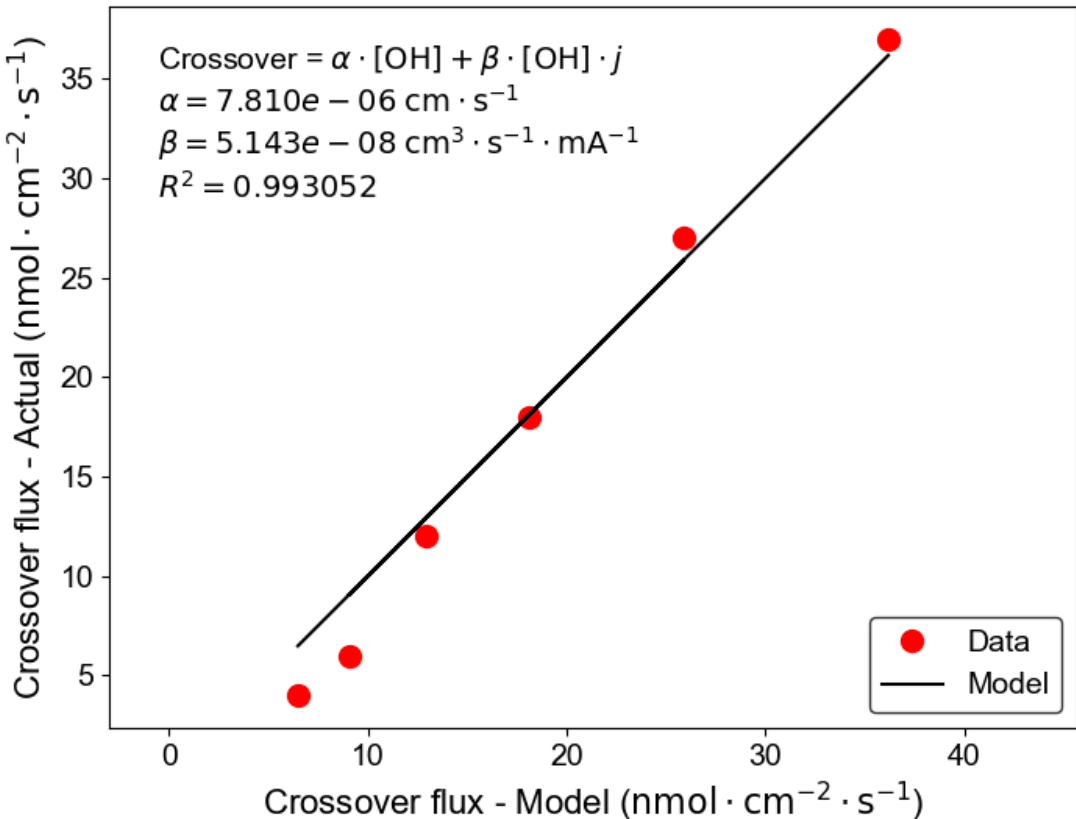


Figure 2.3: Regression fit of hydroxide ion crossover data. The x -axis is the predicted hydroxide crossover flux from the two factor regression model of Eq. (2.10). The y -axis is the experimentally measured crossover flux. The black line denotes the model fit, which by definition is the line $y = x$. The fit is excellent, with an R^2 of 0.993052.

2.7 NUMERICAL SIMULATION OF THE ACID-BASE GENERATOR

The full numerical simulation modeled the acid-base generator system in two dimensions by unfurling the serpentine flow field into one dimensions along the flow direction (x). The x coordinate measures the distance along the path traced by the dashed red arrow in the diagram of the flow field in Figure 2.1(a).

Figure 2.4 depicts this unfurling schematically, with the x axis following the blue arrows. The second

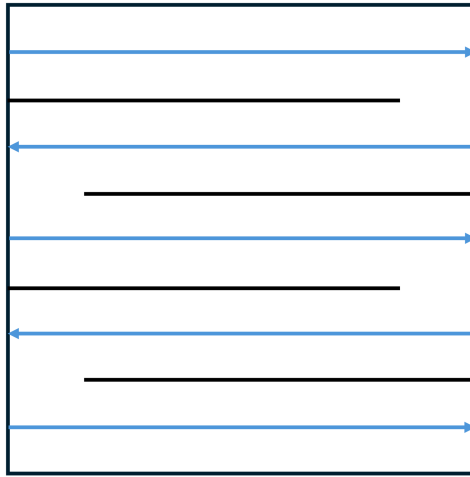


Figure 2.4: Unfurling of serpentine flow field for 2D modeling. The planar flow is unwrapped along the center line of each flow channel, in the direction of the flow.

dimension in the simulation (y) is normal to the plane of the flow field. The third spatial dimension is implicitly treated as being uniform and not included directly in the calculations. This idealization is justified because the thickness of the center chamber (0.1 cm) is significantly less than the width of the channels in the flow field ($11.2 \text{ cm} / 5 = 2.24 \text{ cm}$).

The physical phenomena modeled include advection, diffusion, electromigration and chemical equilibrium. The three mass transport phenomena were described by the Nernst-Planck Equation (2.7). Parameters named with suffix i correspond to the i -th species. The five species under consideration in this

simulation are H^+ , Na^+ , HAc , Ac^- , and OH^- . Units for concentration in the simulation are in millimolar because this corresponds to moles per cubic meter and is therefore consistent with the selected SI units for all the other quantities in the simulation.

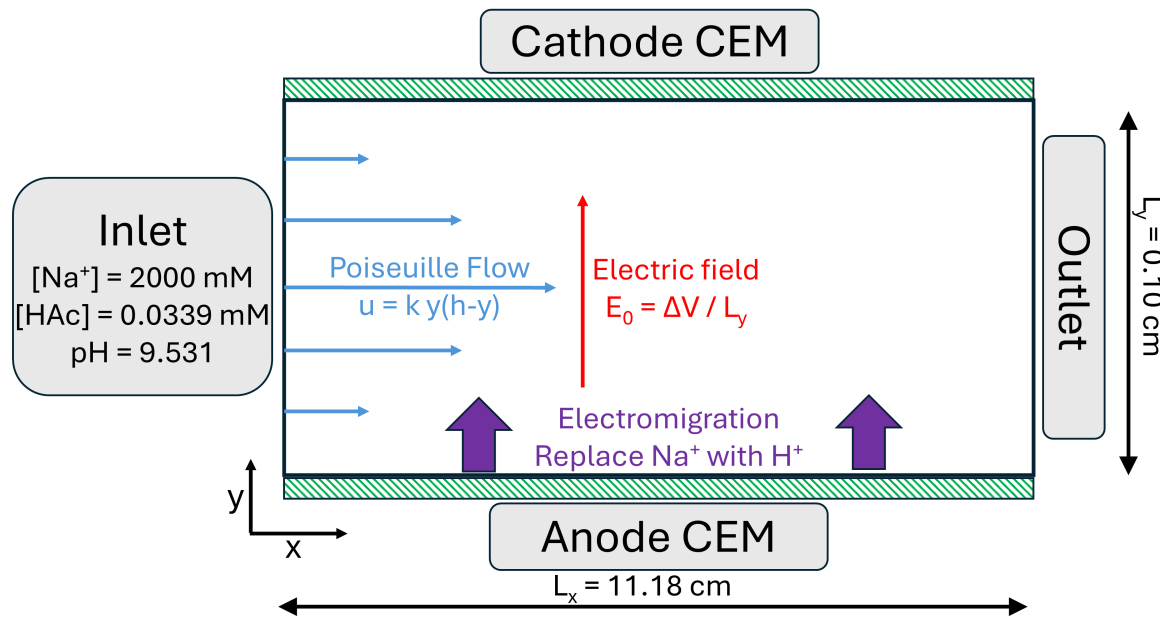


Figure 2.5: Schematic of acid-base generator simulation. The three dimensional problem is modeled in two dimensions. The x -axis is the flow direction along the center line of each flow channel. The y axis is the small space between the anode ($y = 0$) and the cathode ($y = 0.1 \text{ cm}$). Fluid flow is modeled analytically as plane Poiseuille flow. Electromigration is modeled at the anode boundary as a replacement of sodium ions with protons.

Figure 2.5 shows a schematic of the simulation domain and boundary conditions. Fluid enters the inlet at the left side at known concentrations of each species arising from a 2.0M solution of NaAc. The solution of the chemical equilibria³ at these concentrations are: $[\text{Na}^+] = 2000 \text{ mM}$, $[\text{HAc}] = 0.0339 \text{ mM}$

³The calculation of the concentrations at equilibrium is detailed below in Eq. (2.14).

and $\text{pH} = 9.531$. A uniform electric field E_0 points upward from the anode to the cathode. The resulting electromigration pushes cations (H^+ and Na^+) up, and pulls anions (Ac^- and OH^-) down, the y -axis. The bottom of the simulation domain ($y = 0$) is in contact with the anodic CEM. There is a very low sodium concentration in the anolyte solution, so electromigration in the bottom row of cells is modeled by maintaining charge balance with its neighbors and assuming that the net charge flowing out of each cell (mostly due to sodium ions being pushed up) is replaced exclusively by protons entering the cell at the bottom through the anodic CEM. It is not necessary to impose a boundary condition at the top, corresponding to the cathodic CEM, because the electric field is pushing mainly Na^+ with a small amount of H^+ through the cathodic CEM.

The fluid velocity \mathbf{u} was solved analytically by treating the system as a plane Poiseuille flow with a known volumetric flow rate. The simulation assumes a uniform electric field oriented along the y -axis between the anode and cathode. The following diffusion coefficients (D_i) were used for each species in the simulation:

- H^+ and OH^- : $9.30 \times 10^{-5} \text{ cm}^2 \cdot \text{s}^{-1}$
- HAc and AC^- : $1.11 \times 10^{-5} \text{ cm}^2 \cdot \text{s}^{-1}$
- Na^+ : $1.33 \times 10^{-5} \text{ cm}^2 \cdot \text{s}^{-1}$

The operating temperature was taken as 25°C . The applied potential was selected iteratively so the output current density matched the experimentally observed current density of $200 \text{ mA} \cdot \text{cm}^{-2}$. The result of this iteration was an applied potential of 109 mV .

The simulation domain was divided into a grid of 256×64 rectangular cells with dimensions of $0.044 \text{ cm} \times 0.0016 \text{ cm}$ in the x and y dimensions, respectively. The advection operator \mathcal{A} was calculated with a first order finite difference with upwinding, i.e. the concentration gradient was taken by comparing a cell to its left-hand neighbor because the flow is from left to right. The diffusion operator \mathcal{D} was calculated with the standard centered finite difference stencil comparing a cell to its four neighbors. I assumed a constant, uniform electric field E_0 from the anode to the cathode. This assumption is justified because the ensuing simulation shows that the ionic conductivity in the solution is close to uniform. This, in turn, is not surprising, because the concentration of sodium and acetate ions in the supporting electrolyte are much higher than the concentrations of protons being pumped across the channel. Indeed, the whole point of the supporting electrolyte is to ensure that the sodium acetate buffer is the dominant charge carrier inside the channel. With this simplifying assumption about E_0 , the electromigration term also significantly simplifies, and only depends on the gradient of the concentration along the y -axis multiplied by known scalars. This concentration gradient was calculated analogously to the x gradient for advection.

One time step of the simulation begins with the application of the discretized advection, diffusion and electromigration operators, respectively, to all five species under consideration. A small correction is then made to impose electroneutrality, which would not otherwise hold exactly. Electroneutrality is imposed by separately calculating the positive and negative charge density in each cell. The ratio r is then calculated of the larger charge density divided by the smaller charge density. A dimensionless correction

factor $f = \sqrt{r}$ is then applied, multiplying the concentrations of the sign with lower charge density, and dividing the concentrations of the sign with higher charge density. These adjustments were very small, less than 10^{-6} , providing confidence that the electroneutrality assumption was not producing spurious results.

The preliminary concentrations of the five species will typically not be in chemical equilibrium. We consider two chemical equilibria to apply: acid dissociation for acetic acid, with a pK_a of 4.76; and the water dissociation equilibrium, $K_w = [H^+][OH^-] = 10^{-14} M^2$. These two equilibrium conditions are imposed in order, by solving a simple quadratic equation for each equilibrium. The physical rationale is that these are fast chemical equilibria that are achieved at time scales significantly smaller than each time step in this simulation (which are on the order of 0.1 ms).

Here is a brief explanation of how the equilibria are solved. Suppose we begin a time step with predicted concentrations $[H^+] = H$, $[Ac^-] = A$ and $[HAc] = B$.⁴ The acid dissociation constant K_a is defined by the relationship

$$K_a = \frac{[H^+][Ac^-]}{[HAc]}. \quad (2.11)$$

As mentioned above, there is no *a priori* reason to suppose that $B/(H \cdot A) = K_a$ when H , A and B are the intermediate results of the $\mathcal{A} + \mathcal{D} + \mathcal{E}$ operator. Consider the acid ionization reaction (the opposite of the acid dissociation reaction),



⁴The notation B for the concentration of acetic acid stands for “bound acid” and was selected to avoid notational confusion with the product HA .

Suppose this reaction Eq. (2.12) runs forward by t millimolar of concentration. Then following the reaction, the reaction quotient $Q(t)$ for the acid dissociation equilibrium will be given by

$$Q(t) = \frac{(B + t)}{(H - t)(A - t)}. \quad (2.13)$$

Thus, to achieve the acid dissociation equilibrium Eq. (2.11), we solve the equation $Q(t) = K_a$. This simplifies to a monic quadratic polynomial in t , $t^2 + pt + q = 0$, with coefficients and solution given by

$$\begin{aligned} p &= -(H + A + K_a) \\ q &= H \cdot A - K_a B \\ t &= \frac{-p - \sqrt{p^2 - 4q}}{2}. \end{aligned} \quad (2.14)$$

Note that there is only one solution with a small change in concentration, and it is the one shown. p is always negative, so the opposite sign in front of the discriminant produces a spurious, non-physical root that would lead to negative concentrations. The same approach is equally applicable to solve the water equilibrium.

To recap, a time step consists of the following explicit calculations: advection, diffusion, electromigration, electroneutrality, and chemical equilibrium. At the end of each time step, the root mean square (RMS) change in concentration is calculated. Time steps are repeated until the RMS concentration change drops below a small threshold indicating that the simulation has converged to a steady state. This tolerance was set at 10^{-4} in the simulations in this work. Plots of the key simulation outputs are shown in Figure 2.6. The simulated pH is plotted in panel (a). We can see a notable buildup of acid along the

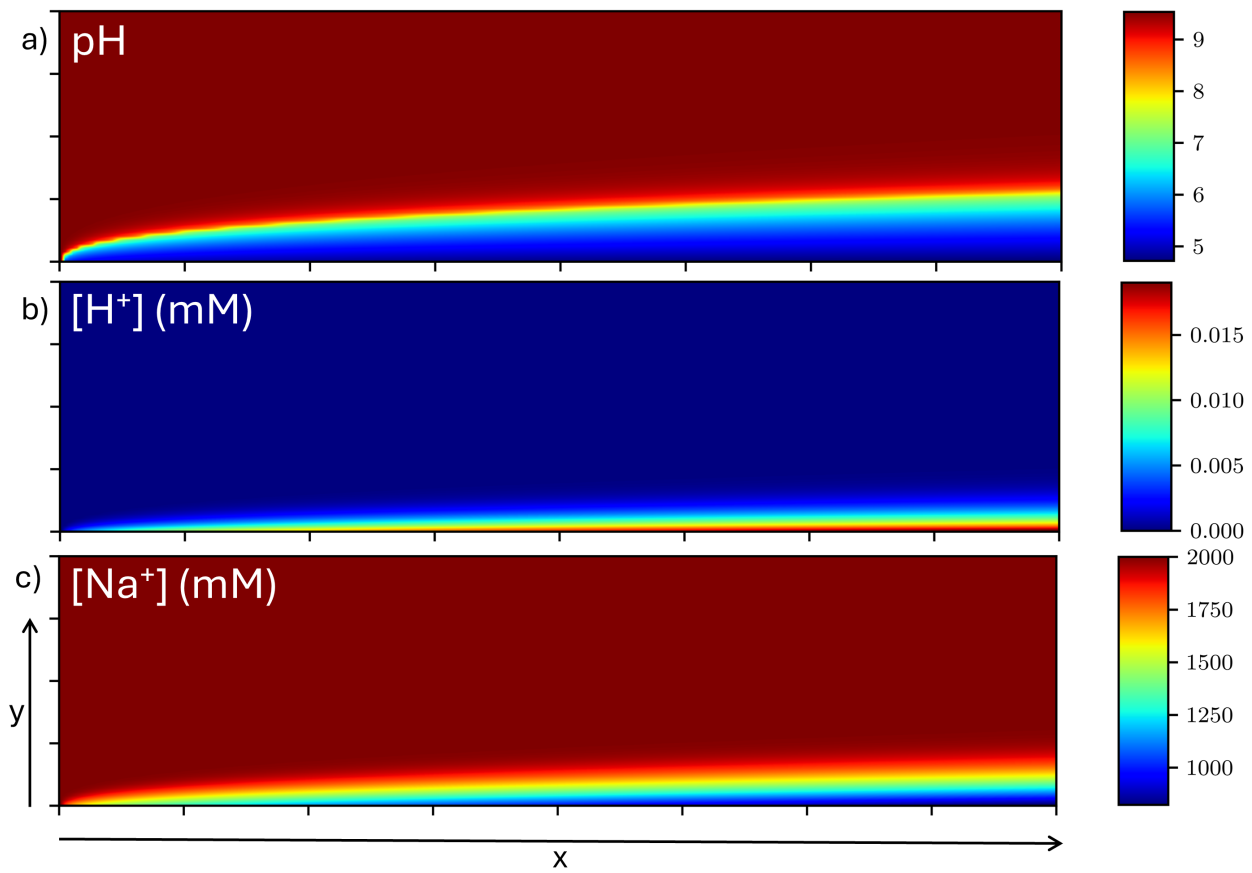


Figure 2.6: Simulated acid-base generator. The length (x axis, same as the direction of the center flow) is 11.18 cm. The height (y axis, representing the thickness of the center chamber) is 0.10 cm. The width, z axis, not shown, is 0.4472 cm. The geometric area of the flow field is 5.00 cm^2 . The length is 25 times longer than the width, reflecting a serpentine flow path with 5 “zig zags” in the flow field. Simulated operating conditions are 2.0M NaAc at inlet, 109 mV applied voltage, and pumping rate $10.4 \text{ mL} \cdot \text{min}^{-1}$. Each panel shows one simulation output. **a**, pH. **b**, acetic acid concentration (mM). **c**, sodium concentration (mM).

bottom of the plot, corresponding to the anode CEM where protons are being pumped in. While the pH drop is readily apparent on a log scale, in absolute terms it is still very small, and the pH never drops below the pK_a of acetic acid, 4.76, showing that the buffer is behaving as expected. Panel (b) shows the simulated acetic acid concentration. We can see that that on a linear scale, it is very close to zero every-

where outside of a narrow envelope surrounding the anode CEM. Panel (c) shows the simulated sodium concentration. Once again, there is a small envelope where it drops by a factor of roughly two, but the sodium concentration is maintained close to its value at the inlet on the substantial majority of the area of the acid-base generator. Sodium depletion is a problem because with a weak acid such as acetic acid, most of the protons are in their bound state as acetic acid rather than dissociated. This causes a significant drop in ionic conductivity of the electrolyte, which in turn increases area specific resistance and thermal losses.

In addition to producing graphical outputs of the concentration fields, this model predicts summary electrical performance statistics including current, current density, resistance, and area specific resistance. For the simulated generator, these results are shown in [Table 2.1](#).

The applied voltage of 109 mV was selected by iterating until the predicted current density matched the

Parameter	Value
Current	998.772 mA
Current Density	$199.767 \text{ mA} \cdot \text{cm}^{-2}$
Resistance	0.197Ω
Area-Specific Resistance	$0.546 \Omega \cdot \text{cm}^2$

Table 2.1: Predicted electrical summary statistics for acid-base generator.

observed current density of $200 \text{ mA} \cdot \text{cm}^{-2}$, terminating the iteration once it converged to the nearest millivolt.

In addition to the electrical attributes, this model predicts proton crossover at the top (cathode) membrane. This prediction *only* accounts for electromigration within electrolyte at the cells touching the

cathode CEM. Because the pH at the top of the channel is nearly equal to the pH at the inlet (9.53), the concentration of protons is orders of magnitude smaller than the sodium concentration, and the predicted proton crossover ratio in this model is 1.03×10^{-9} . The observed proton crossover ratio, while still low in an absolute sense, was not nearly this small. This experimental result does *not* invalidate this model. Rather, the combination of experimental data and this simulation demonstrates that proton crossover attributable to mass transport as described by the Nernst-Planck equation is very small. Cation exchange membranes imbibed with aqueous electrolytes and subject to strong electric fields are extremely complex systems that are well beyond the scope of this simulation. We hypothesize that the observed small proton crossover is primarily driven by membrane effects of this kind.

2.8 CONCLUSIONS

The published work [2] goes on to describe an experimental characterization of the acid-base generator and a discussion of some of its applications. The one sentence summary of these results is that this decoupled acid-base generator is indeed a promising approach to efficiently produce acid and base for a host of applications including carbon capture, and it is worthy of further study. The forthcoming publication in *Energy & Environmental Sciences* has all the details. I will confine my conclusions here to the applicability of numerical methods to this problem.

A review of the literature cited here describing prior work in this field makes it clear that it is highly unusual to conduct a detailed, bottom-up physics simulation for studies of this kind. Indeed, we only ran this analysis here because of a serendipitous collaboration between an applied mathematician and a

larger group of materials scientists, physicists, and chemists in the Aziz group studying topics relevant to energy and the environment. Nevertheless, these results demonstrate the value of this kind of analysis. The headline conclusion of this numerical study is that the cell design parameters selected by Dawei et al. do indeed provide adequate mass and charge transport to achieve their engineering goals. A second conclusion is that the small amounts of observed proton crossover in the experiment are attributable to phenomena other than advection, diffusion and electromigration described by the Nernst-Planck equation. A likely hypothesis is that they are due to membrane effects beyond the scope of this simulation.

Beyond the conclusions about this one particular design, the graphics produced in [Figure 2.6](#) provide a level of physical intuition for understanding and designing an acid-base generator that would be difficult to match with purely experimental methods. We can see at a glance that the proposed flow rate, concentrations, and applied voltage provide adequate flow to wash out accumulated acetic acid and avoid excessive sodium depletion in the generator. These are valuable insights, and once a numerical simulation harness is built, the marginal cost to experiment with different parameter settings is much lower than the cost of running additional experiments. Furthermore, we have published along with the paper all the source code required to run these simulations as detailed in [Section 2.9](#). The code is all open source, and is highly accessible to any scientist with basic computing skills. It is my hope that other workers on carbon capture and related problems will see this publication and appreciate the possible value of numerical simulations to their own future studies.

2.9 DATA AND CODE AVAILABILITY STATEMENT

Data supporting the findings in this study were published alongside the article in *Energy & Environmental Science* [2]. The code to simulate the acid-base generator described in Section 2.7 was written in Python using the numpy library and can be obtained on github.com/memmanuel/acid-base-gen.

“Everything is easy when you know how to do it.”

Steven L. Emanuel[†]



Johann Sebastian Bach, Chromatic Fantasia and Fugue in D minor, BWV 903

3

Thermodynamics of Quinone-Mediated Carbon Capture

This chapter is adapted from K. Amini, T. Cochard, Y. Jing, J. D. Sosa, D. Xi, M. Alberts, M. S. Emanuel, E. Kerr, R. G. Gordon, M. J. Aziz, *In Situ Techniques for Aqueous Quinone-Mediated Carbon Capture and Release*, Nature Chemical Engineering (2024) [6]. I was not the first author of this work, and was primarily responsible for the numerical analysis of the thermodynamics of CO₂ capture presented in the manuscript. I excerpt from the published article the abstract (3.1), some background about carbon capture (3.2), the results of our thermodynamic analysis (3.3), and a discussion of the impact of the capture mechanism on system design and performance (3.4). I did *not* conduct the experimental work, nor did I originally draft these sections, though I was heavily involved in the manuscript revisions. I wrote the code to solve the equilibrium equations, which was used to generate the published Figures 1 and S1, and was the underpinning for the thermodynamics discussion in (3.3). My original numerical contributions to the paper are described in Section 3.5 and written in my own words.

[†]Of course my father didn't invent this quote. It's a popular aphorism with many variants. Barring an authoritative source, I attribute it to him.

3.1 ABSTRACT

Here we elucidate the intricate interplay between the nucleophilicity swing and pH swing mechanisms in aqueous quinone-mediated carbon capture systems, showcasing the critical role of understanding this interplay in the material discovery cycle. This insight prompts the development of two in-situ techniques. The first technique employs in situ reference electrodes and capitalizes on discernible voltage signature differences between quinone and quinone-CO₂ adducts, allowing for the quantification of the isolated contributions of the two mechanisms. The second method is developed based on our finding that the adduct form of the quinone exhibits a fluorescence emission from an incident light at wavelengths distinct from the fluorescence of the reduced form. Thus, we introduce a noninvasive, in situ approach using fluorescence microscopy, providing the capability to distinguish species with subsecond time resolution at single-digit micrometer resolution. This technique holds promise for studying quinone-based systems for carbon capture and beyond.

3.2 INTRODUCTION

Effective carbon management is vital for addressing emissions from some of the toughest-to-abate sectors, including heavy industries such as steel production and cement manufacturing [129]. The conventional approach to capturing CO₂ from dilute sources involves amine scrubbing technology, where CO₂ is captured at 40 °C and released at 120 °C [130, 131]. In pursuit of more efficient alternatives, researchers have directed their focus toward the development of electrochemical technologies for this purpose. Electrochemical systems offer the advantage of isothermal operation, relying on an electrical

gradient to drive a redox reaction that can directly or indirectly create an affinity in the system for CO₂ capture [53, 54, 132–136].

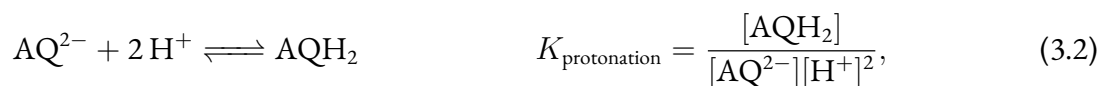
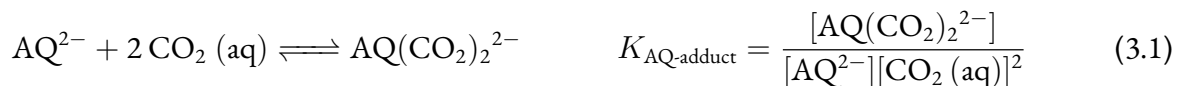
One of the most promising electrochemical carbon capture systems relies on quinone chemistry. Quinones exhibit two potential mechanisms of CO₂ capture. First, the nucleophilicity swing mechanism occurs, where the phenolate groups upon quinone reduction reversibly react with carbon dioxide via nucleophilic addition, which results in the formation of quinone-CO₂ adducts. This mechanism is observed with quinones dissolved in aprotic solvents [137–139] or immobilized on the electrodes [135, 137, 140, 141]. However, in protic solvents, depending on the pK_a of the hydroquinones and the local pH, the electrochemical reduction of quinones can be proton coupled and create hydroxide ions, which capture CO₂ as carbonate or bicarbonate [142–144]. Thus, in an aqueous solvent, both pH swing and nucleophilicity swing mechanisms may contribute to CO₂ capture across a range of operational conditions. However, traditional methods of measuring the total amount of CO₂ captured or released allow for reporting only the combined contribution of these two mechanisms, while the relative contributions are unknown. We expect continued progress in developing aqueous quinone-based technologies for carbon capture, attracted by the safety, economic viability and excellent ionic conductivity offered by water serving as a solvent. However, to pave the way for these innovations, it is essential to deepen our understanding of the underlying mechanisms and their relative contributions to overall process performance.

In this chapter, we address the need to quantify the contributions of the nucleophilicity swing and pH swing mechanisms. The first two sections lay the foundation for this exploration. First, we provide a ther-

modynamic overview elucidating the interplay between these mechanisms, emphasizing how the dominance of one over the other influences critical performance metrics of the final engineered electrochemical cell and necessitates specific molecular engineering considerations in the context of the material discovery cycle. Second, we delve into a case study focusing on bis[3-(trimethylammonio)propyl]-anthraquinones (BTMAPAQs)^[142], extracting both thermodynamic and kinetic insights for its three isomers. Building on these foundational sections, we introduce two *in situ* experimental methods for quantifying the contributions of these mechanisms in the system.¹

3.3 THERMODYNAMIC OVERVIEW

To demonstrate the influence of various properties of the hypothetical anthraquinone molecule employed in the system on the interplay between nucleophilicity swing and pH swing mechanisms, we analyzed a set of reaction equilibrium equations inherent to the system. The fully reduced anthraquinone (AQ^{2-}) molecule in an aqueous solution can either undergo the direct capture of CO_2 through $\text{AQ}(\text{CO}_2)_2^{2-}$ adduct formation or engage in a proton coupled reaction



where $K_{\text{AQ-adduct}}$ and $K_{\text{protonation}}$ are the $\text{AQ}(\text{CO}_2)_2^{2-}$ adduct formation and protonation equilibrium constants, respectively. Both reactions can occur in two steps, involving the sequential acceptance of the

¹The case study on BTMAPAQs and description of the *in situ* experimental methods can be found in the published article but are omitted here.

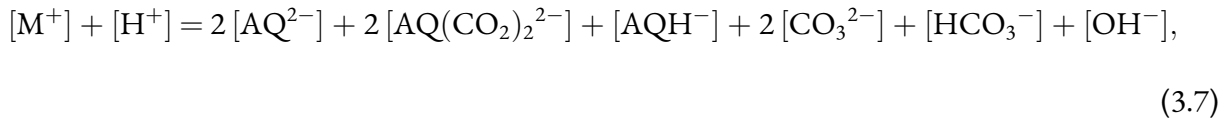
first CO_2 or H^+ molecule followed by the second. The experimental determination of $K_{\text{AQ-adduct}}$ is elucidated in the published paper through cyclic voltammetry, although extracting the equilibrium constant for the initial step in isolation presents challenges. Conversely, the double step protonation / deprotonation can be deduced from the Pourbaix diagram, resulting in the following equilibrium equations:



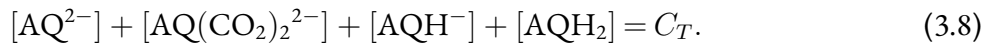
In these reactions, K_{a1} and K_{a2} are the equilibrium constants for the first and second deprotonation steps, respectively. The corresponding pK_a values are calculated by taking the negative base 10 logarithm of K_a . For reactions (3.3) and (3.4), occurring from right to left (protonation reaction), the result is the consumption of protons and an increase in the pH of the solution. The produced hydroxides can then undergo bicarbonate and carbonate formation reactions, resulting in an indirect capture of CO_2



Reactions (3.1 – 3.6) involve the consumption or production of various charged species. In the solution, charge neutrality must always be maintained. Thus



where $[M^+]$ represents the monovalent counterion resulting from dissolving the anthraquinone salt in the solution (for example, K^+ or Na^+). Additionally, the sum of concentrations of all AQ-containing ions is conserved at its total dissolved concentration (C_T). Therefore



An additional constraint arises from the water dissociation equilibrium, resulting in



Finally, the concentration of aqueous carbon dioxide CO_2 (aq) is dictated by the partial pressure of CO_2 , p_{CO_2} and follows Henry's law,

$$[CO_2 \text{ (aq)}] = C_{\text{Henry}} \cdot p_{CO_2}, \quad (3.10)$$

where C_{Henry} is Henry's constant, taken to be $35 \text{ mM} \cdot \text{bar}^{-1}$ at room temperature [53], representing its solubility in water and assumed to be unchanged in the presence of 0.1 M AQ . Given that the present thermodynamic analysis serves as an overview of the interplay between the nucleophilicity swing and pH swing mechanisms, we focus on the above main reactions Eqs. (3.1–3.10), while those leading to interme-

diate compounds such as $\text{AQ}(\text{CO}_2)_2^{2-}$ and AQHCO_2^- and species formed owing to mixed mechanisms are disregarded by assumption, both for lack of estimation and simplicity.

Here, we begin by considering a total concentration of 0.1 M AQ dissolved under a partial pressure p_{CO_2} of 0.1 bar. With $\text{p}K_{\text{a}1}$ and $\text{p}K_{\text{a}2}$ set at 11 and 13, respectively—values typical for several anthrahydroquinones reported so far [142, 145–147]—we further consider equilibrium constants K_4 , K_5 and K_w as $K_4 = 1.1 \times 10^{-6} \text{ M}$ [148], $K_5 = 4.1 \times 10^{-10} \text{ M}$ [148], and $K_w = 10^{-14} \text{ M}^2$. Regarding the equilibrium constants for bicarbonate and carbonate formation, we assume that the presence of 0.1 M AQ has not substantially altered the salinity of the solution, and the numbers are taken at a salinity of zero. Under these specified conditions, Figure 3.1(a) illustrates the dynamic interplay between nucleophilicity swing and pH swing mechanisms in the capture of CO_2 as a function of $\text{AQ}(\text{CO}_2)_2^{2-}$ adduct formation equilibrium constant $K_{\text{AQ-adduct}}$. This analysis predicts that at $K_{\text{AQ-adduct}}$ less than 10^{12} M^{-2} , the thermodynamic driving force for the nucleophilicity swing mechanism is too low, and thus the CO_2 capture proceeds mainly via the pH swing mechanism. The opposite is true for $K_{\text{AQ-adduct}}$ values above 10^{17} M^{-2} . Between these two limits, both mechanisms contribute to the capture of CO_2 . Understanding this interplay in relation to the properties of the employed molecule is crucial in the context of the material discovery cycle for carbon capture applications. For instance, if a newly synthesized molecule, under the desired operational conditions, exhibits primarily the pH swing capture mechanism, optimizing the molecule's capture capacity necessitates a focus on maximizing its $\text{p}K_a$, as well as solubility, to increase the concentration of OH^- molecules produced. Conversely, for molecules with strong adduct

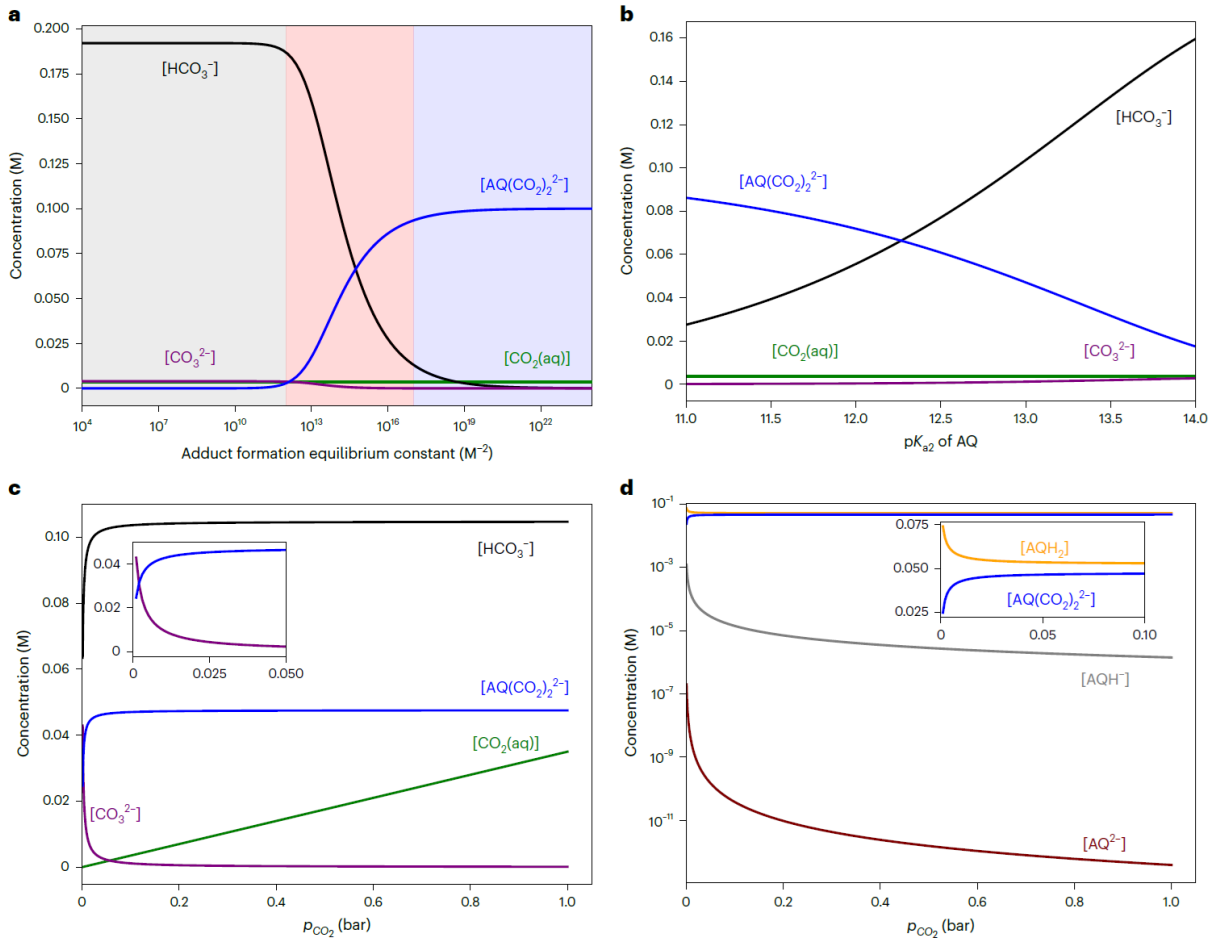


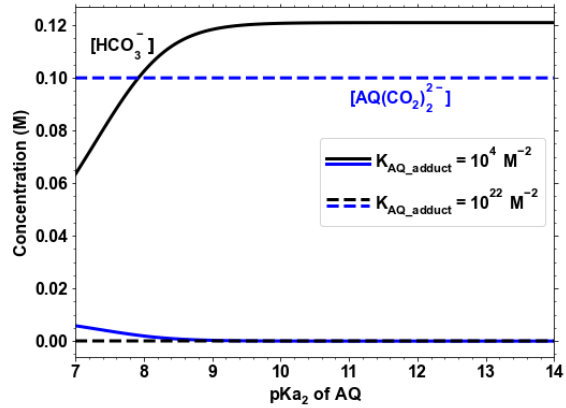
Figure 3.1: Equilibrium concentrations resulting from solving equilibrium equations (3.1–3.10). Unless otherwise specified, a total concentration of 0.1 M AQ dissolved under a partial pressure 0.1 bar of CO_2 is assumed. The AQ pK_a values are set at $pK_{a1} = 11$ and $pK_{a2} = 13$, with equilibrium constants $K_4 = 1.1 \times 10^{-6} M$, $K_5 = 4.1 \times 10^{-10} M$, $K_w = 10^{-14} M^2$, and $K_{AQ\text{-adduct}} = 10^{14} M^{-2}$. **(a)**, The concentration profiles of HCO_3^- , CO_3^{2-} , $CO_2(aq)$ and $AQ(CO_2)_2^{2-}$ at different $K_{AQ\text{-adduct}}$ values. **(b)**, The concentrations of HCO_3^- , CO_3^{2-} , $CO_2(aq)$ and $AQ(CO_2)_2^{2-}$ at varying pK_{a2} values of the AQ molecule. **(c)**, The concentrations of HCO_3^- , CO_3^{2-} , $CO_2(aq)$ and $AQ(CO_2)_2^{2-}$ at different partial pressures of CO_2 . **(d)**, The concentrations of AQ^{2-} , $AQ(CO_2)_2^{2-}$ and AQH^- at different partial pressures of CO_2 .

formation equilibrium constants, maximizing pK_a becomes irrelevant, and attention should be directed exclusively toward enhancing the solubility of the AQ molecule.

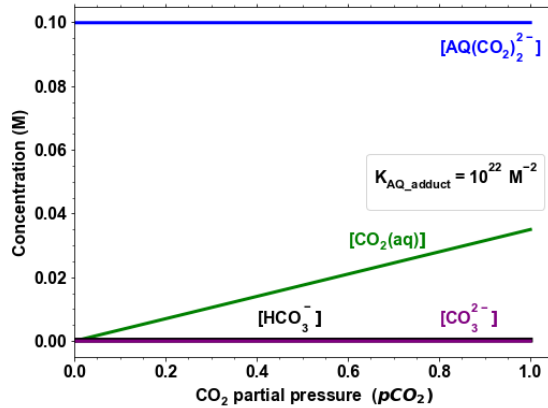
It is important to note that basicity and nucleophilicity are intrinsically linked, as both properties are governed by the electron-donating ability of the molecule. Consequently, these properties cannot be independently modified in isolation. However, the molecular structure can be strategically optimized to favor either of the two mechanisms (examples are provided in Supplementary Information, §3).

The results of such an optimization are illustrated in [Figure 3.1\(b,c\)](#) and [Figure 3.2](#). For intermediate values of $K_{\text{AQ-adduct}}$ (for example, 10^{14} M^{-2}), where both mechanisms are at play, increasing the $\text{p}K_a$ of the AQ molecule shifts the contribution more toward bicarbonate/carbonate formation, as depicted in [Figure 3.1\(b\)](#) and the zoomed-in image in [Figure 3.2\(d\)](#). In contrast, under conditions where $K_{\text{AQ-adduct}}$ is strong (for example, 10^{22} M^{-2}), even with limited $\text{p}K_a$ values (for example, $\text{p}K_{a1} = 7$ and $\text{p}K_{a2} = 7$), the $\text{AQ}(\text{CO}_2)_2^{2-}$ adduct formation mechanism captures up to the expected capacity independent of enhancements in $\text{p}K_{a2}$ ([Figure 3.2\(a\)](#)). However, under such limiting conditions, when $K_{\text{AQ-adduct}}$ is weak (for example, 10^4 M^{-2}), increasing the $\text{p}K_a$ of the anthrahydroquinone molecule becomes a crucial factor for enhancing the capture capacity, as depicted in [Figure 3.2\(a\)](#). Note that capture capacity is defined as the molar ratio of CO_2 molecules captured to AQ molecules present.

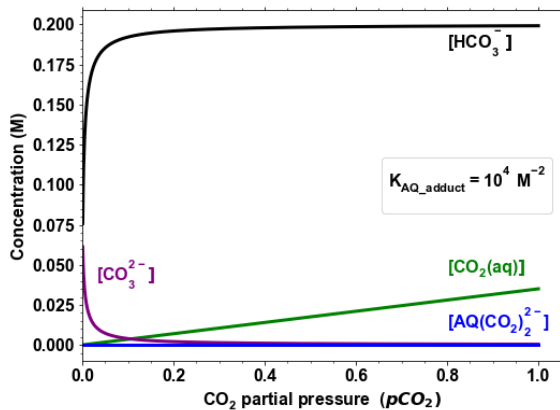
Another important factor is the effect of the CO_2 partial pressure. Under the conditions set in [Figure 3.1\(a\)](#) and for intermediate values of $K_{\text{AQ-adduct}}$ (for example, 10^{14} M^{-2}), where both mechanisms are at play, increasing p_{CO_2} to values higher than 0.1 bar would indeed increase the CO_2 (aq) concentration according to Henry's law, but it results in negligible change in the individual contribution of nucleophilicity swing and pH swing mechanisms toward the total capture, as shown in [Figure 3.1\(c,d\)](#). However, at di-



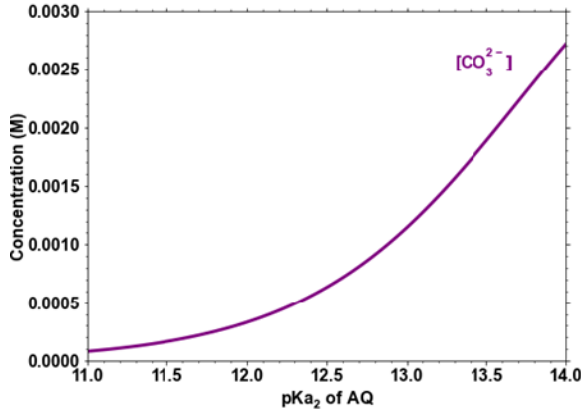
(a) Varying pK_{a2} and two different $K_{\text{AQ-adduct}}$.



(b) Varying pCO_2 and a strong $K_{\text{AQ-adduct}} = 10^{22} \text{ M}^{-2}$.



(c) Varying pCO_2 and a weak $K_{\text{AQ-adduct}} = 10^4 \text{ M}^{-2}$.



(d) Zoomed inset of Figure 3.1(b).

Figure 3.2: Equilibrium concentrations with varying parameter values for pK_{a2} and pCO_2 . (a)–(c): Equilibrium concentrations determined by solving the corresponding equilibrium equations (3.1–3.10). A total concentration of 0.1 M AQ with equilibrium constants $K_4 = 1.1 \times 10^{-6} \text{ M}$, $K_5 = 4.1 \times 10^{-10} \text{ M}$ and $K_w = 10^{-14} \text{ M}$ is assumed. (a) Concentrations of HCO_3^- and $\text{AQ}(\text{CO}_2)_2^{2-}$ at varying pK_{a2} values of the AQ molecule and at two different $K_{\text{AQ-adduct}}$ values. Here the pK_{a1} is assumed to be 7. (b) Concentrations of AQ^{2-} , $\text{AQ}(\text{CO}_2)_2^{2-}$, AQ and AQH^- at different partial pressures of CO_2 and at a strong $K_{\text{AQ-adduct}}$ of 10^{22} M^{-2} . Here $pK_{a1} = 11$ and $pK_{a2} = 13$. (c) Concentrations of HCO_3^- , CO_3^{2-} , $\text{CO}_2(\text{aq})$, and $\text{AQ}(\text{CO}_2)_2^{2-}$ at different partial pressures of CO_2 and at a weak $K_{\text{AQ-adduct}}$ of 10^4 M^{-2} . Here $pK_{a1} = 11$ and $pK_{a2} = 13$. (d) Zoomed-in inset of Figure 3.1(b), demonstrating the increase in carbonate concentration $[\text{CO}_3^{2-}]$ with the increase in pK_{a2} .

lute CO_2 concentrations (less than 0.05 bar), the thermodynamic driving force for $\text{AQ}(\text{CO}_2)_2^{2-}$ adduct formation drops and, in the bicarbonate/carbonate equilibration, carbonate formation contribution increases, which would have an effect on the capacity of the capture. In the adduct formation pathway, each AQ molecule captures two CO_2 molecules by engaging both nucleophilic oxygen sites. Meanwhile, in the pH swing pathway, a two-step protonation process yields two OH^- ions per AQ molecule. When these hydroxides predominantly form bicarbonate groups, each OH^- captures one CO_2 , resulting in a two CO_2 capture capacity per one AQ molecule. Contrastingly, carbonate formation consumes two OH^- ions, resulting in a one CO_2 capture capacity per one AQ molecule. Therefore, $\text{AQ}(\text{CO}_2)_2^{2-}$ adduct formation and bicarbonate formation both exhibit a capture capacity ratio of two to one, while carbonate formation yields a one to one ratio. In the context of the interplay between nucleophilicity swing and pH swing mechanisms, one can see that for the molecules where $K_{\text{AQ-adduct}}$ is strong (for example, 10^{22} M^{-2}), the thermodynamic driving force for $\text{AQ}(\text{CO}_2)_2^{2-}$ adduct formation is very strong, and even at dilute CO_2 concentrations (400 ppm), the capture capacity proceeds at a two to one ratio through nucleophilicity swing mechanisms (Figure 3.2b). Conversely, when $K_{\text{AQ-adduct}}$ is weak (for example, 10^4 M^{-2}), the dominant mechanism becomes pH swing, and reducing the p_{CO_2} to values less than 0.05 bar shifts the equilibrium toward carbonate formation, diminishing the capture capacity to a one to one ratio, which is particularly relevant for cells engineered for direct air capture where CO_2 partial pressure is low. The potential impact of these mechanisms on the performance is further discussed in the next section.

3.4 IMPACT OF CAPTURE MECHANISMS ON SYSTEM PERFORMANCE

In this section, we elucidate examples showing how each mechanism impacts critical performance metrics of the final system, and explain why developing these systems as a “black box,” without understanding the contributions of the underlying mechanisms, is inadequate. A comprehensive understanding of the nucleophilicity-swing and pH-swing mechanisms is essential for optimizing system performance in terms of capture capacity, energy requirements, stability, kinetic and reaction rates, and material choice:

- 1. Capture Capacity:** The carbonate formation in the pH-swing route results in half the capture capacity compared to the bicarbonate and nucleophilicity-swing pathways. Our thermodynamic overview shows that this distinction is particularly relevant for cells engineered for direct air capture (DAC), where CO₂ partial pressure is low. Under these conditions, the carbonate pathway dominates, leading to a significant reduction in capture capacity if the pH-swing mechanism is prevalent. Conversely, if the nucleophilicity-swing mechanism is dominant, the capture capacity can be twice as high. Thus, understanding the contributions of each mechanism is important for estimating capture capacity, especially for DAC applications.
- 2. Energy Requirements:** The energy requirements for driving each mechanism differ, affecting the final energetic cost of the designed system. The nucleophilicity-swing mechanism involves the formation of the AQ – CO₂ adduct,² where CO₂ acts as an electron-withdrawing group. This increases the electron density around the quinone core and stabilizes the reduced AQ – CO₂ adduct. This stabilization effect makes the AQ – CO₂ adduct less likely to lose electrons (i.e., be oxidized), resulting in a more positive oxidation potential (BTMAPAQ case study in the published paper with a strong binding constant shows this new oxidation peak). In contrast, AQH₂ (formed during the pH-swing mechanism) represents the fully reduced form of the anthraquinone, having accepted two protons and two electrons. The reduction of AQ to AQH₂ lacks the stabilizing effect of an electron-withdrawing group like CO₂. Therefore, the oxidation potential for AQH₂ is less positive compared to the AQ – CO₂ adduct. From a thermodynamic energy requirement per-

²In this section, I denote the $\text{AQ}(\text{CO}_2)_2^{2-}$ adduct by AQ – CO₂ to lighten the notation.

spective (ignoring kinetic and real-world losses), in a system where the AQ – CO₂ mechanism is dominant, the energy requirement is expected to be higher due to the larger ΔE (change in potential). Thus, understanding the contributions of each mechanism is important for estimating the energetic cost of the designed system.

3. **Stability and System Lifetime:** The stability of the quinone molecules and the overall system is influenced by the contribution of each mechanism. For instance, in the nucleophilicity-swing mechanism, the degradation rate of the organic molecule AQ – CO₂, as opposed to AQH₂, needs to be studied. AQs have shown degradation pathways such as dimerization and anthrone formation, and thus, the lifetime of the cell would depend on the degradation rate of AQH₂ (for pH-swing) versus AQ – CO₂ (for nucleophilicity swing). Quantifying the amount of AQ – CO₂ formed versus AQH₂, coupled with their respective degradation rates, would allow us to estimate the lifetime of the cell in terms of chemical degradation.

Another important aspect of performance is the oxygen stability of the system, which depends on the contribution of each mechanism. As described in point (2) above, the formation of AQ – CO₂ results in a compound with a more positive oxidation peak. This closer oxidation peak of the AQ – CO₂ adduct to the oxygen redox potential reduces the thermodynamic tendency for oxidation by oxygen. As a result, the AQ – CO₂ adduct would be more oxygen-stable compared to AQH₂ (pH-swing mechanism) from a thermodynamic point of view. Thus, understanding the dominance and contribution of the nucleophilicity-swing mechanism versus the pH-swing mechanism allows us to make better predictions regarding oxygen stability.

4. **Kinetic and Reaction Rates:** Each mechanism exhibits different kinetic and reaction rates, which would affect the overall rate of CO₂ capture in the designed system. In our specific case study, we determined the individual kinetic rate constant for each mechanism (detailed in the SI Section 4 of the published paper). Understanding these kinetic differences allows us to optimize the system accordingly. For instance, if one mechanism is kinetically hindered compared to the other, we can modify the operational conditions or the AQ molecule itself to favor the faster mechanism. This understanding is thus important for maximizing the capture rates and overall performance under various conditions.
5. **Materials Choice for System:** Understanding and quantifying the contribution of each mechanism will also affect the choice of materials for system engineering. For example, with the pH-

swing mechanism, the formation of bicarbonate and carbonate ions introduces additional considerations for membrane selection. Bicarbonate and carbonate ions are smaller and less sterically hindered compared to AQ–CO₂ adducts, which can result in higher membrane crossover rates, especially with anion exchange membranes. This affects the choice of membrane materials, as more selective membranes are required to prevent ion crossover and maintain system efficiency.

Thus, the contributions and interplay between the nucleophilicity-swing and pH-swing mechanisms impact capture capacity, energy requirements, system stability, reaction kinetics, and material choices. When a new AQ molecule is designed, we need tools to gather information about the contributions of these two sub-mechanisms to better understand whether the material fits the specific scenario it has been designed for, or if it needs further modification. As such, we believe that understanding the interplay between the above two mechanisms is critical in the material discovery cycle.

3.5 NUMERICAL METHODS FOR DETERMINING EQUILIBRIUM CONCENTRATIONS

I became involved in this project serendipitously when the first author Kiana mentioned at an Aziz group meeting that she was stuck on what should be a simple calculation and needed help. Kiana had a set of nine of equations in nine unknowns corresponding to Eqs. (3.1–3.10).³ Kiana strongly believed this was a well posed mathematical problem. She had made several substitutions and reduced it a numerical optimization problem with five variables. But when she attempted to solve this problem using the `scipy` optimization routines available in Python, she was getting nonsensical results. In fact, the results were not even deterministic. I volunteered to take a crack at it, and had a working prototype within two days.

³There are only nine independent equations because Eq. (3.2) is implied by Eqs. (3.3) and (3.4). In particular, $K_{\text{protonation}}^{-1} = K_{\text{a1}} \cdot K_{\text{a2}}$.

It was the single most productive project I've ever undertaken in terms of impact per hour of labor in my admittedly short scientific career.

During the course of my studies, I've worked on many problems in both problem sets and research that required using numerical optimizers. I've learned a few broadly applicable principles about how to reformulate optimization problems to maximize the probability of obtaining good results with an off the shelf optimization algorithm:

1. Begin by eliminating as many variables as possible using analytical (pencil and paper) techniques. As long as a variable can be expressed explicitly in terms of elementary functions of other variables, it is almost always advantageous to do so.
2. Variables corresponding to physical quantities with units should be nondimensionalized.
3. Nondimensionalized physical variables should, in turn, be translated and rescaled when necessary so that typical values fall in an interval that is not too different from $[-1, 1]$.
4. It is usually better to work with unconstrained variables. When possible, apply a mathematical transformation to any constrained variables to map them to the real line. A good choice for positive quantities is the log function. A good choice for quantities in the open unit interval $(0, 1)$ is the logit function, $\text{logit}(x) = \log\left(\frac{x}{1-x}\right)$.
5. When minimizing a composite error function, a good starting point is a two norm error of individual components, each of which is scaled to dimensionless terms of comparable magnitude. So if ε_1 and ε_2 are two separate error terms of comparable size, the combined error is $\varepsilon = \sqrt{\varepsilon_1^2 + \varepsilon_2^2}$.
6. When formulating an initial guess, don't be overly clever in the first instance. Start with "neutral" guesses that are close enough to the answer that the optimizer converges.
7. However, if you need greater speed and can come up with a strong guess, don't hesitate to use it. If you use a clever guess, check at least once that your assumptions aren't driving the results by comparing it to the output using a neutral guess. If you get the same answer faster, then the clever guess has been validated.

8. Always verify that the results of the optimizer are physically plausible and that the output satisfies any physical constraints that were encoded as minimization terms to a reasonable tolerance.

The principles above proved to be sufficient to quickly wrangle the equilibrium problem into a form that was dispatched easily by `scipy.optimize` using default settings with minimal tweaks. I will begin by reviewing the parameters and assigning them to different categories: well established physical constants, varying physical constants, operating conditions, and state variables. The state variables, in turn, can be divided into categories of inputs to be set by the optimizer, and those implied by the optimized state variables. The problem we wish to solve, then, is to compute the concentrations of all the chemical species given specified values for both the varying physical constants and the operating conditions. The means of solving this problem will be to run a numerical optimizer on the input state variables until they minimize a composite error metric indicating that they satisfy the expected physical constraints.

The established physical constants have known values we do not need to adjust, and indeed we had better not do so. The water equilibrium constant $K_w = 10^{-14} \text{ M}^2$ is a staple of high school chemistry, and Henry's constant $C_{\text{Henry}} = 0.035 \text{ M} \cdot \text{bar}^{-1}$ dates to 1803 [149]. The two equilibrium constants $K_4 = 1.1 \times 10^{-6} \text{ M}^{-1}$ and $K_5 = 4.1 \times 10^{-10} \text{ M}^{-1}$ for the carbonate / bicarbonate equilibrium are also standard reference values published in 1993 [148]. K_4 governs the equilibrium between aqueous CO_2 and bicarbonate, and is akin to the first dissociation of carbonic acid, while K_5 is the second acid dissociation constant, in which bicarbonate dissociates into carbonate and a second proton. On the other hand, the equilibrium values governing the behavior of the anthraquinone will vary with different samples being characterized, or hypothetical materials to be designed. These varying parameters include $K_{\text{AQ-adduct}}$

governing adduct formation, and the two acid dissociation constants K_{a1} and K_{a2} for the anthraquinone. These three equilibrium constants will be set by the caller as inputs to the routine that computes equilibrium concentrations for all species as an output.

The operating conditions for this problem are the total concentration of anthraquinone, C_T , and the partial pressure, p_{CO_2} . Both of these are controlled in a physical experiment, and they are also inputs to the concentration problem that are not adjusted by the optimizer. The state variables in the problem are the aqueous concentrations of the following ten chemical species: M^+ , H^+ , OH^- , CO_2 (aq), HCO_3^- , CO_3^{2-} , AQH_2 , AQH^- , AQ^{2-} , and $AQ(CO_2)_2^{2-}$. These have been listed with the inorganic compounds preceding the organic compounds, in an order that will later make it easy to calculate them sequentially from the selected input state variables.

The first step was to systematically eliminate as many variables as possible. Reviewing the state variables, it seems logical to first consider the six inorganic compounds M^+ , H^+ , OH^- , CO_2 (aq), HCO_3^- , CO_3^{2-} as their own discrete subproblem. The physical intuition is that once an experimenter were to impose the pH in addition to the CO_2 partial pressure, all five concentrations would be determined, and this is indeed the case. The metal ion concentration $[M^+]$ is known to be equal to twice the total AQ concentration C_T , because the initial solution is prepared by dissolving a solution of the salt M_2AQ , e.g. K_2AQ , thus

$$[M^+] = 2 \cdot C_T. \quad (3.11)$$

We are assuming the proton concentration $[H^+]$ is one of the known inputs to the optimizer.⁴ From the water equilibrium Eq. (3.9) we have

$$[OH^-] = K_w / [H^+]. \quad (3.12)$$

Since p_{CO_2} is an operating condition, from Henry's law Eq. (3.10) we have

$$[CO_2(aq)] = C_{Henry} \cdot p_{CO_2}. \quad (3.13)$$

From the first and second dissociations of carbonic acid, Eqs. (3.5) and (3.6) respectively, we have bicarbonate and carbonate via

$$[HCO_3^-] = K_4 \cdot [CO_2(aq)] / [H^+] \quad (3.14)$$

$$[CO_3^{2-}] = K_5 \cdot [HCO_3^-] / [H^+]. \quad (3.15)$$

Collectively, Eqs. (3.11)–(3.15) give us efficient sequential calculations for all the inorganic concentrations given the operating conditions and the pH.

A similar intuition suggests that once a single one of the organic species has its concentration specified, the rest will be determined. After examining the AQ equilibrium equations Eqs. (3.1), (3.3) and (3.4), it soon becomes apparent that the doubly protonated species AQH_2 is the lynchpin for the system. Supposing we set $[AQH_2]$ as an input to the optimizer, everything else falls into place. The two acid dissociations

⁴At the risk of stating the obvious, the pH is known, so $[H^+] = 10^{-pH}$ by the definition of pH.

of the anthraquinone immediately give us the singly protonated and deprotonated concentrations:

$$[\text{AQH}^-] = K_{\text{a}1} \cdot [\text{AQH}_2] / [\text{H}^+] \quad (3.16)$$

$$[\text{AQ}^{2-}] = K_{\text{a}2} \cdot [\text{AQH}^-] / [\text{H}^+]. \quad (3.17)$$

And likewise, having the concentrations of both AQH_2 and CO_2 (aq) directly implies the adduct concentration

$$[\text{AQ}(\text{CO}_2)_2^{2-}] = K_{\text{AQ-adduct}} \cdot [\text{AQ}^{2-}] \cdot [\text{CO}_2 \text{ (aq)}]^2. \quad (3.18)$$

Combining Eqs. (3.11)–(3.18) we can directly calculate the concentrations of all ten chemical species given the operating conditions plus assumed values for the two input concentrations, $[\text{H}^+]$ and $[\text{AQH}_2]$.

The next step is to formulate transformed values of optimization input parameters corresponding to the physical state variables $[\text{H}^+]$ and $[\text{AQH}_2]$, which I will denote x and y , respectively. $[\text{H}^+]$ is a concentration, so it is known to be positive. Therefore I selected the log transformation

$$[\text{H}^+] = e^x \quad x = \ln [\text{H}^+]. \quad (3.19)$$

This one transformation simultaneously nondimensionalizes $[\text{H}^+]$, maps a constrained range of physically admissible values to the whole real line, and puts x on a numerical scale typically in the range $[-32.2, 0]$, close enough to the desired range of $[-1, 1]$ for numerical stability.⁵ $[\text{AQH}_2]$ is naturally interpreted in relation to the total anthraquinone concentration C_T . The first step of the transforma-

⁵Most solutions have a pH between 0 and 14, leading to a range of -32.2 to 0 for x since $\ln(10^{-7}) \approx -32.2$.

tion is to nondimensionalize $[AQH_2]$ via division by C_T . This leads to the fraction of all AQ that is in the hydroquinone form, which is constrained to the interval $(0, 1)$. Following my precepts, I then applied the logit transformation to this ratio to map it to the real line, obtaining

$$[AQH_2] = \frac{C_T}{1 + e^{-y}} \quad y = \ln\left(\frac{[AQH_2]}{C_T - [AQH_2]}\right). \quad (3.20)$$

This transformation also puts y into a numerical range that, in practice, is not too far from zero.

The last step to defining the objective function for the optimizer is to incorporate the remaining two equations governing conservation constraints into a single scalar output to be minimized. Start with the conservation of charge condition⁶ in Eq. (3.7). To nondimensionalize this, a natural choice is to divide by the absolute value of the charges of either sign, which should be identical. We first compute the positive and negative charge densities (in units of moles of elementary charge per liter, $N_A \cdot e \cdot L^{-1}$) separately,

$$\rho^+ = [M^+] + [H^+] \quad (3.21)$$

$$\rho^- = [OH^-] + [HCO_3^-] + 2[CO_3^{2-}] + [AQH^-] + 2[AQ^{2-}] + 2[AQ(CO_2)_2^{2-}] \quad (3.22)$$

The nondimensionalized, signed charge error is then given by

$$\varepsilon_c = 2 \cdot \frac{(\rho^+ - \rho^-)}{(\rho^+ + \rho^-)}. \quad (3.23)$$

The final constraint is conservation of anthraquinones, Eq. (3.8). By similar reasoning, the canonical way

⁶While Eq. (3.7) was introduced as an electroneutrality condition, it can equally be understood to be a charge conservation equation. A neutral salt M_2AQ is dissolved into a neutral solution of water, which in turn dissolves neutral CO_2 gas. So the whole solution must remain neutral.

to nondimensionalize errors in AQ conservation is to divide through by the total AQ concentration. The total concentration of AQ implied by the state variables is

$$Q_T = [\text{AQH}_2] + [\text{AQH}^-] + [\text{AQ}^{2-}] + [\text{AQ}(\text{CO}_2)_2^{2-}], \quad (3.24)$$

leading to the definition of the signed quinone conservation error

$$\varepsilon_Q = \frac{Q_T - C_T}{C_T}. \quad (3.25)$$

Finally, we define our composite error ε as the two norm of these error components

$$\varepsilon = \sqrt{\varepsilon_c^2 + \varepsilon_Q^2}. \quad (3.26)$$

Algorithm 3.1 Objective Function for Equilibrium Concentrations

```

1: function MAKEOBJECTIVEFUNC( $K_{\text{add}}$ ,  $K_{\text{a1}}$ ,  $K_{\text{a2}}$ ,  $p_{\text{CO}_2}$ ,  $C_T$ )
2:   ▷ Physical constants ▷
3:   const  $K_w = 1.0E-14$ ,  $C_{\text{Henry}} = 0.035$ ,  $K_4 = 1.1E-6$ ,  $K_5 = 4.1E-5$ 
4:   ▷ AQ equilibrium constants and operating conditions - make visible in scope of objective function ▷
5:   extern  $K_{\text{add}}$ ,  $K_{\text{a1}}$ ,  $K_{\text{a2}}$ ,  $p_{\text{CO}_2}$ ,  $C_T$ 
6:   ▷ Construct objective function binding these parameters ▷
7:   function OBJECTIVEFUNC( $x, y$ )
8:     ▷ Transform optimizer arguments to input concentrations ▷
9:      $[\text{H}^+] = e^x$  ▷ Eq. (3.19)
10:     $[\text{AQH}_2] = C_T / (1 + \exp(-y))$  ▷ Eq. (3.20)
11:    ▷ Solve remaining concentrations ▷
12:     $[\text{M}^+] = 2 \times C_T$  ▷ Eq. (3.11)
13:     $[\text{OH}^-] = K_w / [\text{H}^+]$  ▷ Eq. (3.12)
14:     $[\text{CO}_2(\text{aq})] = C_{\text{Henry}} \cdot p_{\text{CO}_2}$  ▷ Eq. (3.13)
15:     $[\text{HCO}_3^-] = K_4 \times [\text{CO}_2(\text{aq})] / [\text{H}^+]$  ▷ Eq. (3.14)
16:     $[\text{CO}_3^{2-}] = K_5 \times [\text{HCO}_3^-] / [\text{H}^+]$  ▷ Eq. (3.15)
17:     $[\text{AQH}^-] = K_{\text{a1}} \times [\text{AQH}_2] / [\text{H}^+]$  ▷ Eq. (3.16)
18:     $[\text{AQ}^{2-}] = K_{\text{a2}} \times [\text{AQH}^-] / [\text{H}^+]$  ▷ Eq. (3.17)
19:     $[\text{AQ}(\text{CO}_2)_2^{2-}] = K_{\text{add}} \times [\text{AQ}^{2-}] \times [\text{CO}_2(\text{aq})]^2$  ▷ Eq. (3.18)
20:    ▷ Calculate charge conservation error ▷
21:     $\rho^+ = [\text{M}^+] + [\text{H}^+]$  ▷ Eq. (3.21)
22:     $\rho^- = 2([\text{CO}_3^{2-}] + [\text{AQ}^{2-}] + [\text{AQ}(\text{CO}_2)_2^{2-}]) + ([\text{OH}^-] + [\text{AQH}^-])$  ▷ Eq. (3.22)
23:     $\varepsilon_c = 2 \times (\rho^+ - \rho^-) / (\rho^+ + \rho^-)$  ▷ Eq. (3.23)
24:    ▷ Calculate AQ conservation error ▷
25:     $Q_T = [\text{QH}_2] + [\text{QH}^-] + [\text{Q}^{2-}] + [\text{Q}(\text{CO}_2)_2^{2-}]$  ▷ Eq. (3.24)
26:     $\varepsilon_Q = (Q_T - C_T) / C_T$  ▷ Eq. (3.25)
27:    ▷ Return the composite error ▷
28:    return  $\sqrt{\varepsilon_c^2 + \varepsilon_Q^2}$  ▷ Eq. (3.26)
29:    ▷ Return the objective function with its bound parameters ▷
30:    return ObjectiveFunc

```

The ideas in this section, Eqs. (3.11)–(3.26), are combined into a single optimization objective function $f(x, y)$ according to [Algorithm 3.1](#). Once this objective function is available, we need only specify a reasonable initial guess for the input state variables $[H^+]$ and $[QH_2]$, and we can then readily solve for the equilibrium concentrations given equilibrium constants and operating conditions. Following the precept to use neutral initial guesses, I set the starting pH at 7.0 and $x_0 = \ln(10^{-7}) \approx -16.1$. For the QH_2 fraction, I observed that in the usual context of flow batteries, the state of charge would be defined by $s = [QH_2]/C_T$. A neutral assumption is that the state of charge is equal to one half, leading to the initial guess $y_0 = 0$ after application of the logit function. These guesses were used in the code to calculate the equilibrium concentrations.

The results of this entire effort were successful. We produced physically sensible answers that were in good qualitative agreement with the experimental data, to the extent it was possible to compare the two due to measurement difficulties on some of the parameters alluded to in the manuscript. In addition to producing plausible outputs for a given scenario, the thermodynamic equilibrium solver produced smoothly varying outputs as plotted in [Figures 3.1](#) and [3.2](#) which held up under intensive scrutiny, and indeed were the foundation for the entire thermodynamics discussion given in [Section 3.3](#). In addition to producing correct answers, this code runs very fast. Each plot requires hundreds or more calls to the optimization routine, as a parameter of interest (e.g. $K_{AQ\text{-adduct}}$ or p_{CO_2}) is varied and the equilibrium concentrations are calculated. The code was fast enough that Kiana was able to experiment with several iterations of the plots on an ordinary laptop without any tedious computational delays. This leads me

to the observation that for an applied mathematician, a sound operating definition of a good code is one that your collaborator can run herself, on her own computer, to quickly get the right answer, without any hassles.

3.6 CONCLUSIONS

The published paper includes a large amount of additional work by my coauthors. I will provide here the briefest of summaries, and refer readers to the publication for additional details. By using cyclic voltammetry, we identified a potential peak corresponding to reduction of the normal quinone to its hydroquinone, i.e. the reaction $AQ + 2 E^- \rightleftharpoons AQ^{2-}$. This same experiment was then repeated in the presence of CO_2 , and a shift in the location of the peak was observed, allowing us to calculate $K_{AQ\text{-adduct}}$ as explained section 4.2 of the SI. Different CO_2 concentrations were flowed through the system, and upstream and downstream p_{CO_2} measurements were taken synchronously with pH and voltage. UV-vis spectroscopy was applied, taking advantage of different fluorescence signatures of the reduced, oxidized and adduct species. Finally, *in situ* fluorescence microscopy was applied to visualize the operating electrode.

The key scientific conclusions of the work are that the pH-swing and nucleophilic-swing carbon capture mechanisms are both important; they can have a complex interplay; and they can be measured independently using the techniques we introduced. In many cases, one will dominate the other, simplifying analysis of the system and design optimization. Thermodynamic analysis, performed using this code to calculate equilibrium concentrations, is a key tool to determine the dominant mode. Numerous experi-

mental techniques developed in this study, including cyclic voltammetry, UV-vis spectroscopy, flow cell operation with gas sensing, and fluorescence microscopy, allow estimation of both thermodynamic and kinetic parameters, and measurement of the separate contributions of the two carbon capture mechanisms in a working flow cell.

I am fortunate to have had the opportunity to collaborate on this work, and grateful to Kiana and the rest of the author group for including me on their team. The others—especially Kiana—worked much longer on this, whereas I played a minor but important role in advancing the project. The experimental work in this paper was cutting edge and could not have been done by many other groups in my estimation. By comparison, the numerical problem I solved was routine, and I’m sure many other practitioners could have accomplished the same goal. My main contribution, then, was to be in the right place at the right time, and to offer my services as an applied mathematician to a team of physical scientists with different training. For them, this task not in fact easy, bringing to mind one of my father’s favorite sayings, “everything is easy when you know how to do it” as foreshadowed at the start of the chapter. In that vein, my last conclusion from this work is that applied mathematicians should spend more time attending group meetings with scientists working in other areas.

3.7 DATA AND CODE AVAILABILITY STATEMENT

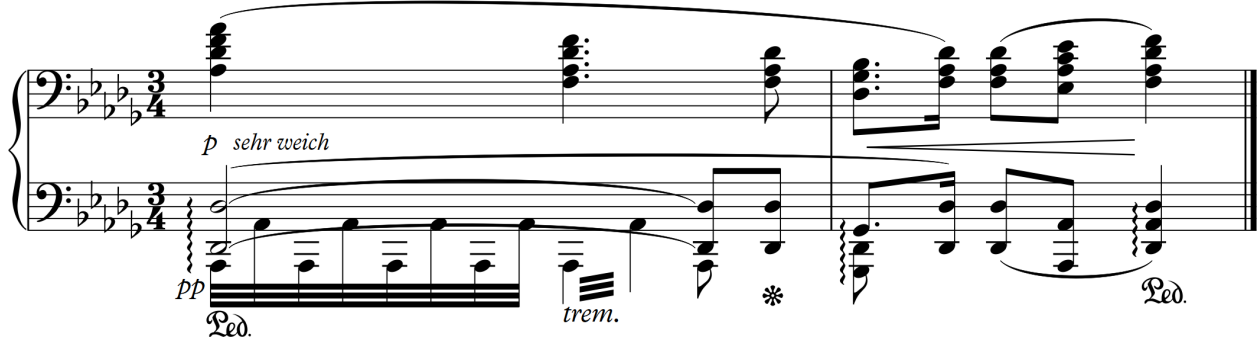
Further data supporting the findings in this study are provided in the Supplementary Information (SI) of the published work. All the source data for the original article (both the main manuscript and the SI) are available on [GitHub](#). Source data were also provided with the published paper.

The code for solving the set of equilibrium equations described in the Thermodynamic Overview ([Section 3.3](#)) was written in Python using the `numpy` library. It can also be found at the above mentioned URL, with a mirror copy on my GitHub page at github.com/memmanuel/2024-06-Quinone-CO2.

“If I have seen further, it is by standing on the shoulders of giants.”

Isaac Newton [150]

Ruhiges Zeitmaß



Richard Wagner, *Das Rheingold* [The Rhinegold], WWV 86A.

Valhalla leitmotif arranged for piano by Franz Liszt (S. 449).

4

Quantitative State of Charge Mapping by Fluorescence Microscopy in Porous Electrodes

This chapter is adapted from A. M. Graf, T. Cochard, K. Amini, M. S. Emanuel, S. M. Rubinstein, M.J. Aziz, *Quantitative Local State of Charge Mapping by Operando Electrochemical Fluorescence Microscopy in Porous Electrodes*, Energy Advances 3, 2468 (2024) [7]. I was not the first author of this work, and was primarily responsible for the method used to calculate the state of charge from the optical data that was presented in the manuscript. I reproduce here the entirety of the main text of published article as well as the sections of the SI describing my contributions. I did *not* conduct the experimental work, nor did I originally draft the sections explaining it, though I was heavily involved in the manuscript revision and submission process. I originally drafted the narrative describing my work in both the main text and the SI. In particular, I was the sole author of [Section 4.5](#) and the primary contributor to the numerical and analytical portions of [Section 4.4.2](#).

4.1 ABSTRACT

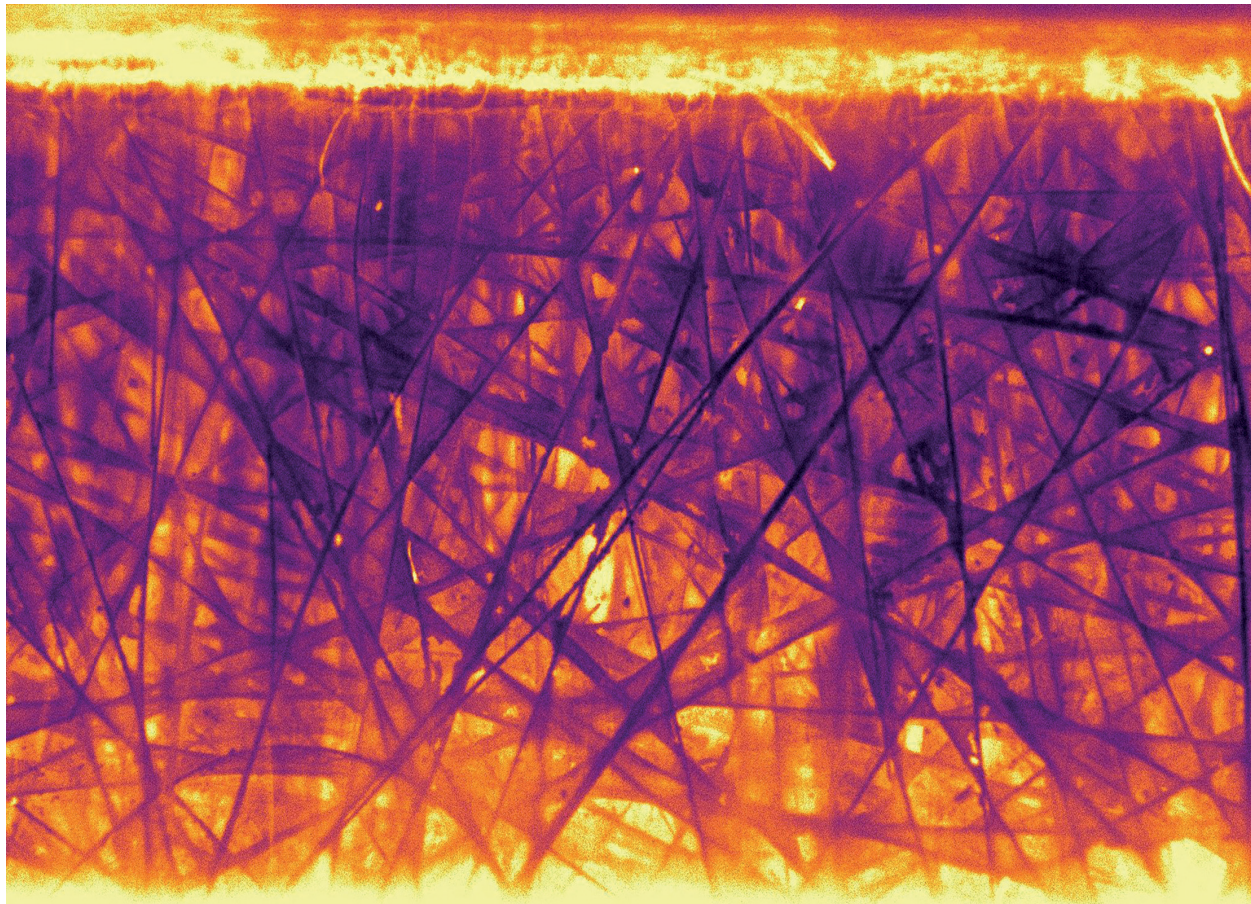


Figure 4.1: State of charge mapping by *operando* electrochemical fluorescence microscopy in a porous electrode. This is an artistically styled rendering of a quantitative state of charge mapping explained more fully in [Figure 4.6](#). This image appeared on the inside back cover of *Energy Advances* along with the paper's original publication. It offers a peek inside an operating porous electrode, where electrolyte flow from top to bottom, and the redox-active organic species light up as they are charged along fibers. By coupling confocal fluorescence microscopy with *in situ* electrochemistry and rigorously calibrating the brightness, the state of charge and multi-species concentration fields are mapped with micron scale resolution at video frame rates. This technique provides insights into the transport and chemical mechanisms in electrochemical flow devices.

We introduce *operando* quantitative electrochemical fluorescence state of charge mapping (QEFSM),

a non-invasive technique to study operating electrochemical systems along with a new design of optically transparent microfluidic flow cells compatible with the most demanding optical requirements. QEFSM allows quantitative mappings of the concentration of a particular oxidation state of a redox-actives species within a porous electrode during its operation. In this study, we used confocal microscopy to map the fluorescence signal of the reduced form of 2,7-anthraquinone disulfonate (AQDS) in a set of multistep chronoamperometry experiments. Calibrating these and incorporating an analytical model of quinhydrone heterodimer formation with no free parameters, and accounting for the emission of each species involved, we determined the local molecular concentration and the state of charge (SOC) fields within a commercial porous electrode during operation. With this method, electrochemical conversion and species advection, reaction, and diffusion can be monitored at heretofore unprecedented resolution ($1\text{ }\mu\text{m}$ and $25\text{ }\mu\text{m}$, respectively) at frame rates of 0.5 Hz , opening new routes to understanding local electrochemical processes in porous electrodes. We observed pore-scale SOC inhomogeneities appearing when the fraction of electroactive species converted in a single pass through the electrolyte becomes large. **Figure 4.1** shows the end results of our analysis: we looked inside a working porous electrode.

4.2 INTRODUCTION

To respond to the growing concerns over environmental consequences of the consumption of fossil fuels, our economy needs to rapidly undergo a transition to sustainable energy sources and technologies. Electrochemical devices and related systems are playing an increasing part in this energy transition. Electrochemical flow cells operate, for example, in redox flow batteries, fuel cells, electrolyzers and de-

salinators. Most such systems employ high surface area porous electrodes as the central neighborhood for electrochemical conversion, specifically to facilitate mass transport and increase reaction rates in 3D architectures.

Whereas considerable amounts of research have been conducted on macroscopic reaction-flow properties [151–153] and the microscopic properties such as surface functionalization and nanopores [154–156], more work is required to understand the mesoscopic length scales in between, e.g. the concentrations, transport, and conversion of chemical species at scales from fibers to microstructures, which could make electrochemical flow devices more viable. Conventional electrochemical techniques, such as voltammetry, typically lack spatial resolution [157]. Voltages probes provide only sparse sample sets and are often invasive. Although, from voltage probes, losses can be attributed to processes occurring within porous electrodes [158], the understanding of how these losses depend on the electrode microstructure, e.g. pore size or fiber diameter and their respective distributions and orientations, is still missing. Other *in situ* analytical methods, e.g. UV/Vis spectrophotometry [159], nuclear magnetic resonance spectroscopy (NMR) [160, 161], electron paramagnetic resonance spectroscopy (EPR) [162], or X-ray imaging [163, 164] are under ongoing development, but have not yet yielded data spatially resolved inside porous electrodes over mesoscopic length-scales.

A promising technique to overcome the current limitations and gain further insight into geometric effects of electrochemical conversion inside porous electrodes is offered by coupling *in situ* fluorescence microscopy with electrochemical monitoring. A variety of studies from the last decades utilized fluores-

cence microscopy coupled to electrochemistry [165] have been performed mainly to study electrochemical processes on planar electrodes in 2D [166–170], defects [171, 172], or for application in biomolecules [173–178].

Recently, the remarkable ability of confocal microscopes to quantify optical information from three spatial dimensions has been harnessed in electrochemical reactions. This advancement has enhanced the interpretation of variations in the adsorption patterns of organic agents informed by surface morphology, and enabled the quantification of pH gradients in proximity to the electrode surface [171, 179, 180].

Recently, 2D widefield fluorescence microscopy revealed substantial heterogeneities in the state of charge and electrolyte velocity field within commercial electrodes operating inside a flow cell [181]. The scale of these heterogeneities exceeded the characteristic pore size ($\sim 50 \mu\text{m}$) by more than an order of magnitude, reaching length scales relevant to commercial flow batteries. This work called into question the validity of assuming a homogeneous Darcy-like flow and the use of Newman's porous electrode model in practical electrochemical devices at these scales [182]. The real-time investigation of electrochemical conversion was performed with 2,7-anthraquinone disulfonate (AQDS) and its corresponding hydroquinone, H₂AQDS, which results from a two-electron, two proton reduction and is accompanied by a significant change in its fluorescence signal.

The study of anthraquinone derivatives in flow batteries is also of great interest due to their synthetically controllable properties [181–183], potential low cost [184–186], earth-abundant building blocks, and chemically mild operation [187]. Their realized lab-scale power densities, however, remain below

those of vanadium flow batteries [188] and, in some cases, their internal resistance has been shown to be due, in large part, to the losses within the porous electrode imbibed with flowing aqueous organic electrolyte [158]. Such power losses are inherent obstacles in most electrochemical flow devices, underscoring the demand for the development of novel techniques to comprehend these losses across diverse length scales through accurate quantification of electrochemical conversion and local transport coefficients. Given that many organic-based, redox-active systems are optically active, they are amenable to analysis using *operando* confocal microscopy. Achieving spatial resolution in the quantification of electrochemical conversion provides a valuable opportunity to gain deeper insight into the nature and extent of these power losses.

Here, we introduce a non-invasive *operando* technique, namely quantitative electrochemical fluorescence state of charge mapping (QEFSM), to precisely quantify electrochemical conversion of redox active molecules at the single-digit micron scale and over time within electrochemical flow systems.

We transcended previous techniques by employing confocal fluorescence microscopy inside an operating porous electrode during the reduction of AQDS to quantify and map the local state of charge (SOC). This entails quantitatively differentiating the signal contributions originating from the various molecular species present. The incorporation of a confocal microscope enhances previous studies by providing depth-focused imaging which, in turn, enables accurate measurement of fluorescence intensity within a specified volume; this is crucial in relating the local species concentrations to spatial features of the electrode. Along with the technique, we present a new microfluidic flow cell compatible with the optical

requirements of the confocal microscope. Except for the electrode, current collector, and membrane, the flow cell is fully transparent, enabling excellent optical access to the pore space. The high porosity of the electrode allows access to the volume inside except for the regions where light is blocked by electrode fibers. Shadows and artifacts due to opaque fibers were removed through calibration and post-processing of the images. The SOC is evaluated locally at these optically accessible positions inside the porous electrode.

We further demonstrate that the dimerization of one AQDS molecule with one H₂AQDS to form quinhydrone (QH) affects the fluorescence intensity. While this can be quantified by our visualization technique, it cannot be discerned with the electrochemical measurements of the cell alone. The SOC is estimated by iteratively calibrating observed image intensities using a model with no free parameters, which includes a reversible 1:1 (AQDS:H₂AQDS) binding dimer, which is further supported by prior experimental work [159]. Whereas the heterodimer can influence the intensity, it should not impact the detected current or the accessible storage capacity in AQDS solutions at the concentrations used in this study, as over 90% of theoretical capacity has been demonstrated in 1 M solutions [189]. By employing a calibration technique that incorporates dimer formation and enables the separation of distinct signal contributions of AQDS, H₂AQDS and dimer, we develop a consistent quantification of fluorescence, the local optical environment, and all three concentrations.

Under the operating conditions considered in this study, the spatially averaged and dimer-corrected image intensity monotonically increases with (and is approximately linear in) the total current. The re-

sulting local SOC maps offer a robust tool for quantifying and evaluating local variations in electrochemical conversion and transport within complex porous electrodes. Our findings contrast with the simple assumption of a constant gradient along the macroscopic flow direction. Such insights are valuable for future research evaluating the domain of suitability of such assumptions. We expect QEFSM to not only improve the understanding of electrochemical conversion and transport of other redox-active species, but also to greatly aid in the understanding of porous electrodes and their microstructures as active materials in electrochemical devices.

4.3 WORKING PRINCIPLES AND EXPERIMENTAL SETUP OF *OPERANDO* QEFSM

4.3.I DESIGN AND FABRICATION OF TRANSPARENT MICROFLUIDIC FLOW CELLS

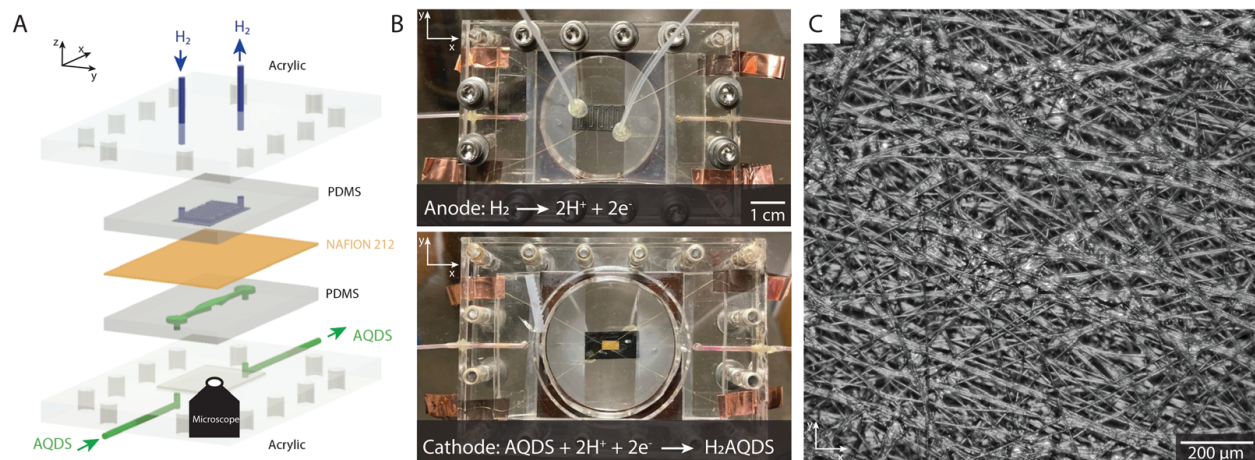


Figure 4.2: Microfluidic flow cell compatible with electrochemistry and confocal microscopy. (A) Exploded view of the individual components with Cartesian coordinate nomenclature identified. (B) Images of the assembled cell from above (top) and below (bottom). The working electrode ($3\text{ mm} \times 6\text{ mm}$) is visible in the center of the bottom image. For the bottom picture, a working electrode made of gold was used to ensure visibility against the counterelectrode in the background. (C) Widefield optical microscopy image of a section of a commercial AvCarb MGL 190 porous carbon paper electrode inside the electrochemical cell.

Our microfluidic electrochemical cell design, shown in [Figure 4.2](#), enables the synchronous study of electrochemical reaction with a conventional potentiostat and the spatially resolved fluorescence intensity. The non-invasive *operando* study of optically active electrolytes via confocal fluorescence microscopy necessitates the design of an electrochemical cell that is compatible with optical imaging. The cell we introduce in this study is optically transparent and permits optical access to the entire electrode, as shown in [Figure 4.2\(A,B\)](#). Two half cells are fabricated from polydimethylsiloxane (PDMS) with acrylic backing. To visualize the inside of the electrode, a relatively long working distance (<11 cm), high-resolution microscopy objective was used.

The flow cell is designed for small working electrodes (3 mm × 6 mm), allowing an effective study of the entire electrode under high magnification (10×). A single flow channel transports the electrolyte into, through, and out of the electrochemical cell ([Figure 4.2](#)). The cell was constructed of two half cells, an anode and a cathode, each embedded in a thin, optically transparent PDMS slab (see ESI, §1 of the original publication for details). The anode side includes 1 mm × 1 mm channels in a serpentine geometry supplying the Pt-coated carbon electrode with humidified hydrogen gas. This electrode is much larger (10 mm × 20 mm) than the one on the cathode side, ensuring that the cathodic reaction on the working electrode remains rate limiting. Hydrogen flow was controlled via a manual pressure adjusted to ensure that a bubble emerged approximately every two seconds from a plastic tube at the cell exit, which was immersed in water. Hydrogen underwent oxidation on a Pt-coated carbon electrode, with resulting protons crossing the membrane for net charge neutrality.

On the cathode or working electrode side, the PDMS contained a $1\text{ mm} \times 0.5\text{ mm}$ flow channel that supplied the porous electrode with electrolyte as shown in [Figure 4.2\(A\)](#). The aqueous electrolyte on the cathode side consisted of 10, 20, 30 and 40 mM of AQDS in 1 M sulfuric acid. The acid served as a supporting electrolyte whose protons were involved in the proton-coupled electron transfer in the AQDS reduction reaction (see [Section 4.3.2](#)). A syringe pump was used to drive the electrolyte flow at a constant flow rate. The superficial flow velocity, defined as the ratio of the volumetric flow rate Q to the nominal cross-sectional area A of the electrode by the formula $u_s = Q/A$ and without correcting for the porosity or the compression of the electrode, was $2.3\text{ mm} \cdot \text{s}^{-1}$. A Reynolds number of ≈ 14 indicates laminar flow, suggesting steady-state conditions with no expected time-dependent variations in the flow. A commercial AvCarb MGL 190 carbon paper of nominal thickness $190\text{ }\mu\text{m}$ was used as the working electrode. This electrode has a disordered fiber microstructure held together by a binder material, as shown in [Figure 4.2\(C\)](#). The electrode was baked for 24 h at $400\text{ }^\circ\text{C}$ to increase its hydrophilicity [[152](#)]. The proton-conducting separator (Nafion 212) was soaked in 1 M sulfuric acid prior to the experiments. The PDMS half cells, electrodes and membrane were compressed by transparent acrylic end plates and screws, providing an excellent seal that obviates the use of gaskets, as shown in [Figure 4.2\(B\)](#).

Experimentally, we showcased the capabilities of QEFSM utilizing the AQDS/ H_2AQDS redox system as the optically active electrolyte. In all experiments, the electrochemical cell was placed on top of an inverted spinning disk confocal microscope with a $10 \times 0.3\text{ NA}$ air objective and $50\text{ }\mu\text{m}$ pinhole size. Transverse ($x - y$) and axial (z) resolution are $1\text{ }\mu\text{m}$ and $25\text{ }\mu\text{m}$, respectively. The short depth of field is

one of the major advantages of QEFSM compared to previous studies that used fluorescence microscopy, as it allows us to determine a precise volume for each frame. In this study, images of fluorescence intensity were captured simultaneously over a 1.2 mm × 1.2 mm field of view close to the center of the working electrode. The transparent PDMS casing allowed the study of an arbitrary position inside the electrode as well as an arbitrary depth from the surface toward the opaque membrane as the focal plane is adjusted. For orientation inside the electrode, we located the interface between PDMS and electrolyte and moved toward the membrane to a depth of 50 μm. The electrochemistry was controlled and measured by a potentiostat (see ESI §1 and 2 of the original publication). We acquired dynamical fluorescence image stacks at 2 seconds exposure time spanning over predefined volumes within the porous electrode while varying the applied potential. While it is possible to significantly reduce the exposure time, a deliberate choice was made to employ a longer exposure time in this study in order to enhance signal resolution and generate high-quality maps.

4.3.2 PROPERTIES OF THE OPTICALLY ACTIVE AQDS ELECTROLYTE

The redox-active species AQDS in its various oxidation states, shown in [Figure 4.3\(A\)](#), is a suitable molecular system to study electrochemical conversion inside porous electrodes [159, 181]. We distinguish between the oxidized and reduced species (AQDS and H₂AQDS, respectively) by imaging at an emission band dominated by H₂AQDS as shown in [Figure 4.3\(B\)](#). Calibration was performed with samples of known concentrations of AQDS, the stable form in equilibrium with air, and then reducing it by controlled amounts to obtain electrolyte emissions spectra at various proportions between the species.

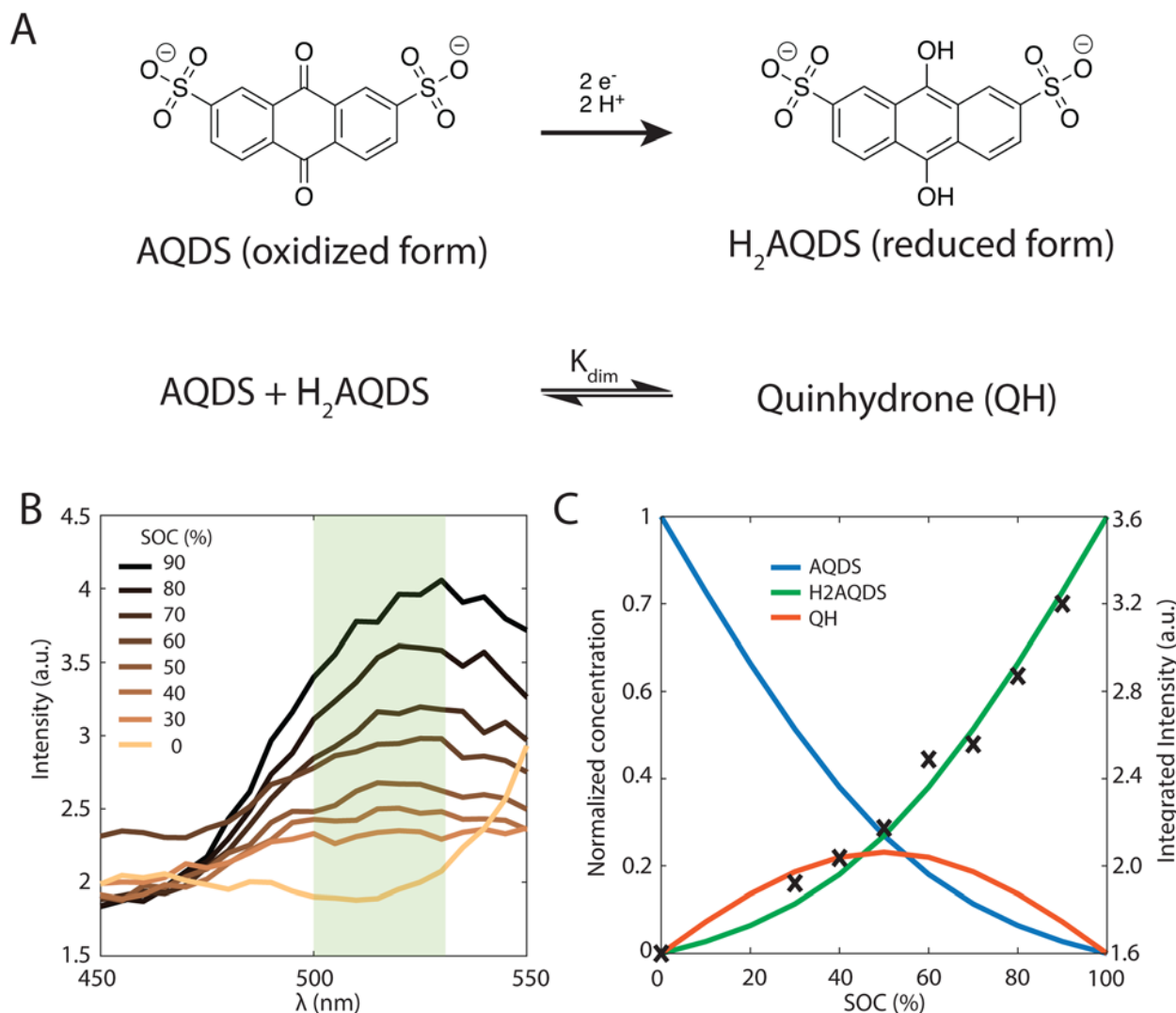


Figure 4.3: Fluorescence properties of AQDS/H₂AQDS redox couple. (A) Reduction scheme of AQDS to H₂AQDS via proton-coupled electron transfer (top). Stoichiometric equation for the heterodimerization of AQDS and H₂AQDS to quinhydrone (QH) (bottom). (B) Emission spectra of 40 mM AQDS solutions as a function of emission wavelength λ at different SOCs obtained at an excitation wavelength $\lambda_{ex} = 405$ nm. The shaded rectangle indicates the range accepted by the green band-pass filter of our confocal microscope. (C) Raw intensities integrated over the shaded region in (B) vs. SOC (right y -axis). The solid lines are the theoretical normalized concentrations of H₂AQDS (green), AQDS (blue) and QH dimer (red) predicted by the 1:1 (AQDS:H₂AQDS) binding dimer model for initial concentrations of 40 mM (left y -axis).

We obtained the emission spectra of the 40 mM AQDS electrolyte at multiple SOCs using a plate reader after different amounts of electrochemical reduction aiding the quantitative correlation between state of charge (SOC) and fluorescence intensity, as shown in [Figure 4.3\(B\)](#) and [\(C\)](#). Electrolytes were prepared from a pure and degassed 40 mM AQDS stock solution. The electrolytes were charged in a conventional bench scale flow battery vs. V^{+3}/V^{+4} across a Nafion 212 membrane to obtain a series of different SOCs (0, 30, 40, 50, 60, 70, 80, and 90%). A 405 nm wavelength laser was used to excite the optically active molecules in the system. H_2AQDS exhibits an absorption peak proportional to its concentration.[\[159\]](#) The emission spectra of the AQDS/ H_2AQDS system at various SOC, shown in [Figure 4.3\(B\)](#), showed a broad peak whose height increases with SOC. This broad emission peak was captured by the microscope's imaging sensor with a green band-pass filter with a range between 500 and 525 nm and integrated in the microscopy studies described below. Contrary to initial expectations [\[181\]](#), the integrated raw fluorescence intensity measured by the microscope as a function of SOC shows a nonlinear increase, as illustrated in [Figure 4.3\(C\)](#).

If the only contribution to the SOC were from H_2AQDS , we would expect the fluorescence intensity to be linearly increasing with SOC. Thus, the observed nonlinear response indicates that competitive photophysical processes due to chemical electrolyte interactions, such as self-absorption, fluorescence quenching, molecular decomposition or electrolyte interactions, should be considered. We eliminated electrolyte decomposition as an explanation because the capacity fade rate of the AQDS/ H_2AQDS system lies around 0.08 % / day [\[190\]](#). Although we were not able to exclude other mechanisms with cer-

tainty, the dynamical formation of quinhydrone dimers (QH), as shown in Figure 4.3(A), provides a logical and quantitative explanation of the nonlinearity measured in fluorescence intensity. In previous studies [159] measuring the absorption spectra for these species, it was found that when both are present, one molecule of AQDS and one molecule of H₂AQDS can reversibly bind to form a quinhydrone heterodimer (QH) as shown in Figure 4.3(A). A value of 80 M⁻¹ was deduced for the equilibrium constant K_{dim} of the association reaction.

We propose that the dimer species does not contribute to the detected fluorescence and therefore reduces the measured intensity by lowering the concentration of H₂AQDS, the only significantly fluorescent species in the mixture. Based on this hypothesis, we are able to construct an effective 1:1 (AQDS:H₂AQDS) binding dimer model that quantitatively corrects the SOC by the amount of reduced electrolyte that became invisible due to dynamic dimer incorporation (see Section 4.5.1). During the electrochemical reduction of AQDS, some of the charge resides in the H₂AQDS and some in the dimer. Thus, the dimer should be regarded as another reduced species. If [QH] represents the concentration of the QH, then the state of charge (SOC) may be defined as

$$\text{SOC} = \frac{[\text{H}_2\text{AQDS}] + [\text{QH}]}{[\text{AQDS}] + [\text{H}_2\text{AQDS}] + 2[\text{QH}]}, \quad (4.1)$$

where, in the absence of decomposition, the denominator is invariant in the chemical and electrochemical processes involved. A SOC of 0% corresponds to a fully oxidized solution of pure AQDS, while a SOC of 100% corresponds to a fully reduced solution of pure H₂AQDS. At those two extremes, no dimer is

present. This provides us with a system of equations that can be solved for different initial concentrations of AQDS, denoted $[AQDS]_0$, to predict the expected concentrations of AQDS, H_2AQDS and QH , as functions of SOC, as shown in [Section 4.5.1](#). Assuming the initial electrolyte is always in its fully oxidized form, having equilibrated with air, the denominator of [Eq. \(4.1\)](#) equals $[AQDS]_0$.

The results shown in [Figure 4.3\(C\)](#) demonstrate that overlaying the experimental intensity data with the theoretical normalized H_2AQDS concentrations predicted from the dimer model reproduces this nonlinear increase closely. Hence, we concluded that the fluorescence intensity is proportional to $[H_2AQDS]$, and $[QH]$ does not significantly contribute to the total intensity of the redox system. Whereas the dimer formation lowers the measured fluorescence intensity, it participates in the current extracted. For the given dimerization mechanism, the ratio of dimer formed to $[AQDS]_0$ increases as $[AQDS]_0$ grows, as shown for all experimentally relevant cases in [4.5.1](#). Because of the thermodynamic equilibrium of the equation shown in [Figure 4.3\(A\)](#), the dimer fraction as a function of the SOC has the functional form of an inverted parabola. The dimer concentration initially grows and is largest at 50% SOC when the concentrations of AQDS and H_2AQDS are equal, beyond which it decreases to 0 M at 100% SOC, as shown in [Figure 4.3\(C\)](#). In experimental data with sufficiently high $[AQDS]_0$, such as the presented case of 40 mM, the concentration of QH can surpass that of H_2AQDS , indicating a prevalence of charged species in the form of the dimer, which affects the fluorescence intensity significantly. As a consequence, the intensity calibration vs. SOC, which must account for the amount of dimer that contributes to the SOC but only weakly to the emitted intensity, varies with $[AQDS]_0$. This calibration qualifies the AQDS/ H_2AQDS

system as a suitable system to exactly quantify SOC maps through QEFSM.

4.4 RESULTS AND DISCUSSION

4.4.1 MULTI-STEP CHRONOAMPEROMETRY STUDIES WITH *OPERANDO* CONFOCAL FLUORESCENCE MICROSCOPY

With electrolyte flowing steadily, we imposed stepped cell voltages and measured the resulting current according to a multi-step chronoamperometry (MSC) protocol (*vide infra*). Simultaneously, we measured the varying fluorescence intensity field with the optical apparatus of a confocal fluorescence microscope, from which we obtained the concentration fields. In a flow cell, the temporal change of the concentration field C_j of species j has contributions from advection \mathcal{A}_j , diffusion \mathcal{D}_j , and electromigration \mathcal{E}_j in addition to the electrochemical source S_j , which is proportional to the faradaic component of the electrical current. That is, the Nernst-Planck equation applies:

$$\frac{\partial C_j}{\partial t} = \mathcal{A}_j + \mathcal{D}_j + \mathcal{E}_j + S_j. \quad (4.2)$$

In steady-state, the concentration of a species converted in a specified volume element is determined by the balance between the source term, which depends on the overvoltage through the current, and the removal from that volume element via the net combined effects of advection, diffusion, and electromigration, which scale with concentration, as further described in [Section 4.5.2](#).

In the MSC experiment, each potential step was held constant for 60 seconds to obtain a stable steady-state-current as shown in [Figure 4.4\(A\)](#). We measured the current i as we increased the overpotential

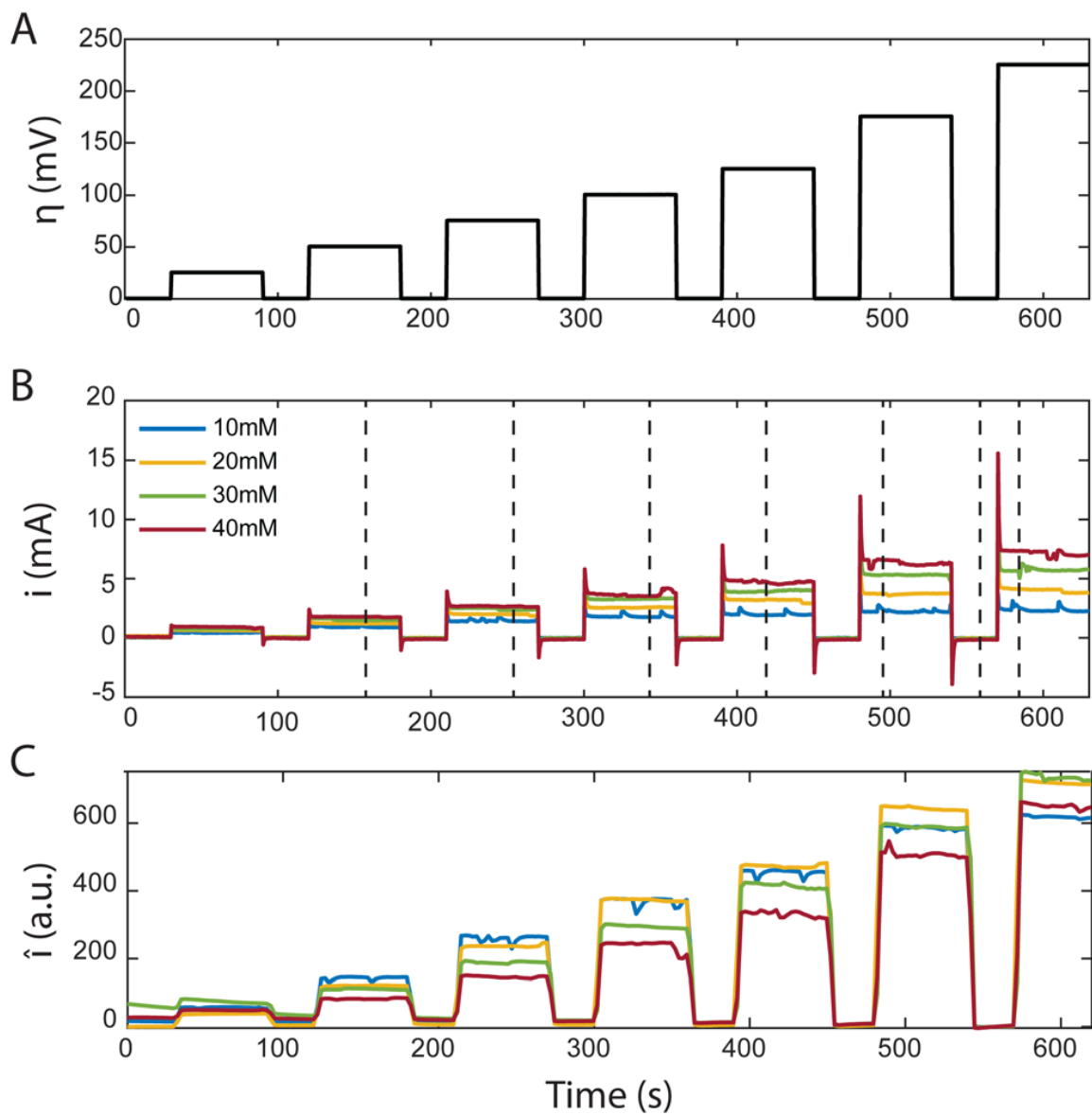


Figure 4.4: Characteristic plots from multi-step chronoamperometry of AQDS at different concentrations flowing through an AvCarb MGL 190 porous carbon electrode paper. (A) Time dependence of the applied stepped cell overpotentials (25, 50, 7, 100, 127, 175 and 225 mV. (B) Measured reduction current corresponding to the overpotentials above for different reactant concentrations. (C) Mean fluorescence intensity detected in a 1.2 mm × 1.2 mm frame inside the confocal microscope over the same period. All average intensity values were background corrected.

η successively from 25 to 225 mV in increments of 25 or 50 mV, which increased the electrochemical driving force that governs the reaction rate, as shown in [Figure 4.4\(B\)](#). To prevent hydrogen evolution, we refrained from using higher overpotentials. Before each change in the step-potential, we set the cell potential to open-circuit voltage (OCV), the potential at which no current is passing, for 30 seconds maintaining the flow of degassed electrolyte.

The current spike following each change in cell potential was caused by capacitative current. This event was followed by a steady-state faradaic current that was monitored for the remainder of each potential step. The faradaic current is governed by the reaction rate at the electrode. Despite maintaining a steady voltage, we observed small fluctuations in the current over time, which are captured in [Figure 4.4\(B\)](#). These fluctuations can be caused by the competing reaction of hydrogen evolution from the electrolyte. For increasing values of $[AQDS]_0$, higher steady-state currents were observed because greater reactant concentrations were available to become reduced in each time interval.

The confocal microscope simultaneously produced raw intensity maps I_{raw} for each image. To investigate the relationship between the current and the fluorescence intensity, we first quantified the average fluorescence of each image (sampling time interval $\Delta t = 2.5$ s). Our initial analysis entailed averaging I_{raw} across the entire image, yielding \bar{I}_{raw} . For better visualization in [Figure 4.4\(C\)](#), we subtracted the background fluorescence image captured at OCV prior to the spatial averaging of the intensity in each individual frame. The resulting mean background-corrected fluorescence intensity \hat{I} follows the current response closely for all potentials applied. Interestingly, the small variations in current were relatively

well captured by the average fluorescence intensity \bar{I}_{raw} . Any negative intensity fluctuation was correlated to a positive current fluctuation. This supports the hypothesis that hydrogen evolution computes with AQDS reduction. Small hydrogen bubbles, nucleating in pockets of presumably inhibited flow, transiently cross the image, momentarily decreasing average intensity, despite contributing to the overall detected current through water reduction to hydrogen. This behavior, depicted in [Figure 4.4](#) comparing (B) and (C), exhibits minor variations relative to their average values at each chronoamperometry step.

The current, sampled in steady state after each potential step, indicated by the dashed lines in [Figure 4.4](#)(B) and reported in the polarization curve in [Figure 4.5](#)(A), increased linearly with overpotential for the first ~ 100 mV. Superlinear behavior, apparent at higher potentials, is indicative of mass transport limitations. The overall utilization of electrolyte, u , defined as the faradaic charge passed to the electrolyte on a single pass through the device divided by its theoretical maximum value set by the charge capacity of the molecules, decreased for increasing $[\text{AQDS}]_0$, as shown in [Figure 4.5](#)(B). When the electrolyte at the inlet is fully oxidized, as it always is in work reported here, the utilization can be expressed analytically in terms of the total current J , the volumetric flow rate Q , the concentration of species available for reduction in the entering electrolyte given by $[\text{AQDS}]_0$, Faraday's constant F , and the number of transferred charges per molecule n :

$$u = \frac{J}{Q \cdot [\text{AQDS}]_0 \cdot F \cdot n}. \quad (4.3)$$

Despite the higher currents at increasing concentrations of electrolyte under the same applied potentials, [Figure 4.5](#)(B) shows the utilization of electrolyte decreasing with increasing $[\text{AQDS}]_0$. Furthermore, we

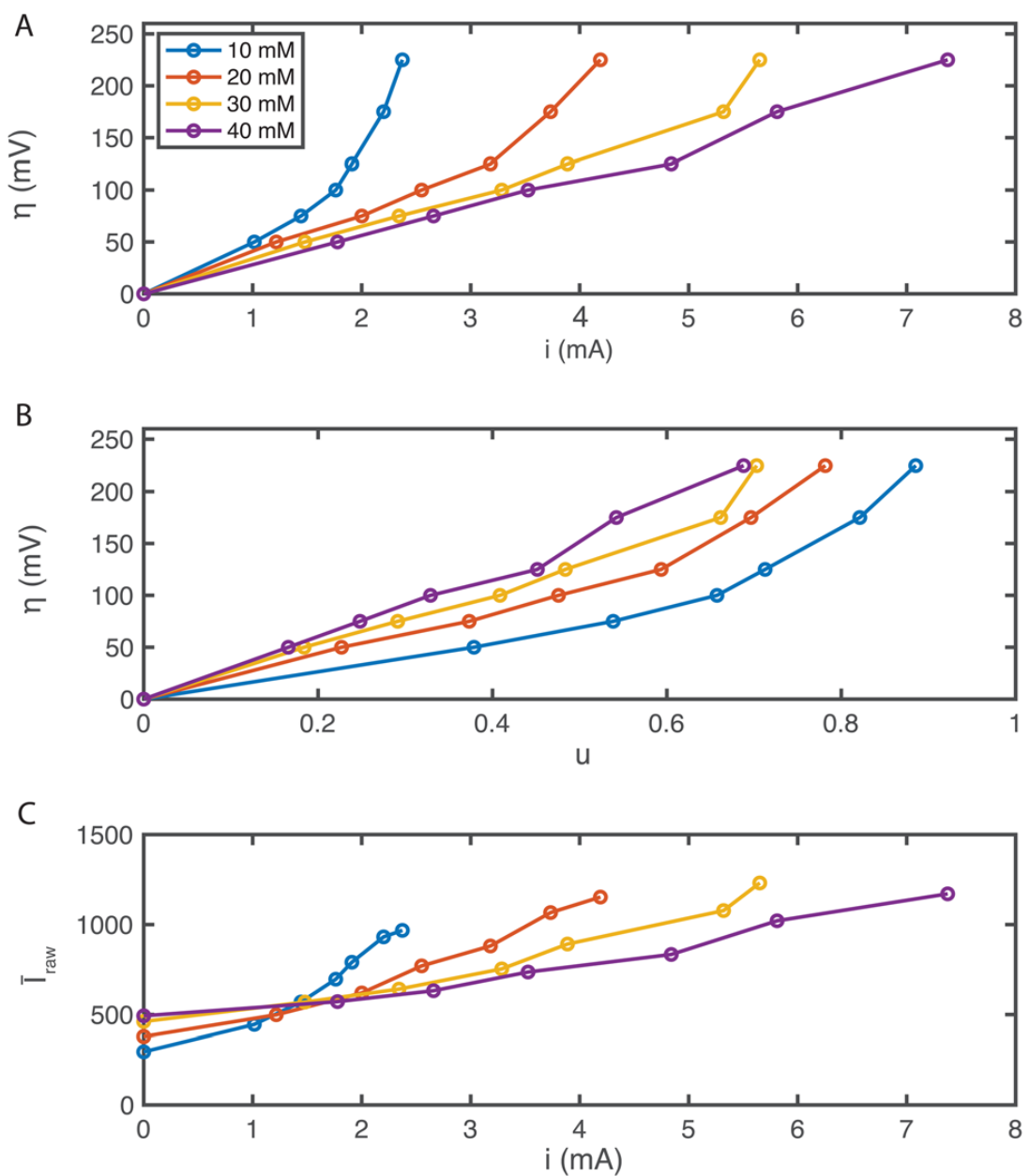


Figure 4.5: Polarization curves and related measurements from MSC experiments. (A) Polarization plot as a result of the MSC experiment for $[AQDS]_0$ values indicated. (B) Applied overpotentials as a function of the electrolyte utilization u . (C) Mean raw fluorescence intensity \bar{I}_{raw} averaged over the entire confocal microscope image as a function of the current i .

observed that for $[AQDS]_0$ of 10 mM, high utilizations of up to 88% were achieved while the utilizations of electrolytes with higher concentrations are lower and closer to each other for the same applied potentials.

We posited that the fluorescence intensity of every molecular species under consideration is linearly proportional to its concentration with the examined regime. Consequently, the aggregate raw intensity I_{raw} is the cumulative sum of these individual contributions depending on the concentrations at each specified SOC, with each species possessing a distinct emission coefficient. A schematic representation of the various fluorescence contributions is provided in [Section 4.5.3](#). As depicted in [Figure 4.5\(C\)](#), the uncorrected mean intensities \bar{I}_{raw} (extracted at the same sampling times indicated by the dashed lines in [Figure 4.4\(B\)](#)) associated with their varying initial concentrations, $[AQDS]_0$, do not conform to a singular linear calibration curve. Because of dynamic formation of dimer, which has notably reduced fluorescence, the total intensities do not directly correlate with the amount of charge transferred. It is observed that discrepancies, or nonlinear effects, amplify with increasing $[AQDS]_0$, which is again supported by the dimer model with fixed equilibrium constant K_{dim} . At OCV, in the absence of H₂AQDS and QH, the observed increase of I_{raw} corresponding to elevated $[AQDS]_0$ reveals the intrinsic fluorescence of AQDS, alongside an assumed constant background. With a correct calibration, accounting for both the intrinsic fluorescence of AQDS, the dynamic dimer formation, and the background, the curves should overlay one another, irrespective of the initial concentration $[AQDS]_0$. As a possible solution, we introduce a calibration tailored for each location (pixel). This calibration is predicated on a numerical fit, taking into

account the emission profile of each molecular species relative to its concentration, all as functions of SOC. The detailed calibration procedure is presented in the subsequent section.

4.4.2 LOCAL SOC AND CONCENTRATION MAPPING

CALIBRATION

Assuming a linear model of light emission P by each chemical species present, the theoretical light intensity mapped to a single pixel of the imaging sensor is given by

$$P_{ri} = \alpha[\text{AQDS}]_{\text{ri}} + \beta[\text{H}_2\text{AQDS}]_{\text{ri}} + \gamma[\text{QH}]_{\text{ri}} + \delta, \quad (4.4)$$

where α , β , and γ are the brightness coefficients of the three electroactive species, and δ is the brightness of the supporting electrolyte. The subscripts denote reaction condition r , specified by overpotential η and initial AQDS concentration $[\text{AQDS}]_0$, and pixel i . In practice we need to consider optical aberrations, e.g. due to sample irregularities, out-of-focus light, reflections, and background noise. Thus, we further propose a linear model of observed image intensity I which is proportional to light production,

$$I_{ri} = F_i P_{ri}, \quad (4.5)$$

where F_i is the optical factor at pixel i and is higher in regions that are less obstructed by fibers. To account for the finite axial resolution, we interpret the results from each pixel as representing the average SOC within an electrolyte column. The depth of each column is equal to the portion of the slab's thickness contributing to the image, excluding the volume blocked by a fiber at the far end of the column. Pixels

for which this column is deeper have higher optical factors. Given the chemical equilibrium of dimer formation, we can uniquely solve for the concentration of all three species with the only free parameter for each pixel being the fraction of reduced species Y , defined by

$$Y_{ri} = \frac{[\text{H}_2\text{AQDS}]_{ri}}{[\text{AQDS}]_{ri} + [\text{H}_2\text{AQDS}]_{ri} + 2[\text{QH}]_{ri}} = \frac{[\text{H}_2\text{AQDS}]_{ri}}{[\text{AQDS}]_{0r}}. \quad (4.6)$$

Our general approach, elaborated in detail in [Section 4.5.3](#), is to map the state of charge by jointly estimating the brightness coefficients $\alpha, \beta, \gamma, \delta$; the optical factors F_i ; and the reduced species fraction Y_{ri} , from which we can directly calculate the SOC.

OPERANDO SOC MAPPING

As a result, the intensity of each pixel is mapped into an SOC value, as shown in [Figure 4.6](#). The potential-SOC chart in panel (A) shows the 2D operando SOC maps for 10, 20, 30 and 40 mM electrolytes from the top to the bottom. From the left to the right, increasing overpotentials of 50, 100, and 175 mV are displayed, with the insets indicating utilization derived from the steady-state current. The fiber structure of the electrode now appears as the white areas. With the increase in overpotential leading to enhanced utilizations, a corresponding rise in local SOC values is observed. Across the selected imaging region, higher utilizations consistently elevate local SOC values, even near the center of the electrode, though not uniformly. Thus, a shift in the mean SOC, \bar{S} , across the image cannot be solely attributed to a straightforward multiplicative effect on each pixel. Instead, specific regions where the SOC appears less sensitive to variations in overpotential can be identified. These areas have a lower contribution to the overall elec-

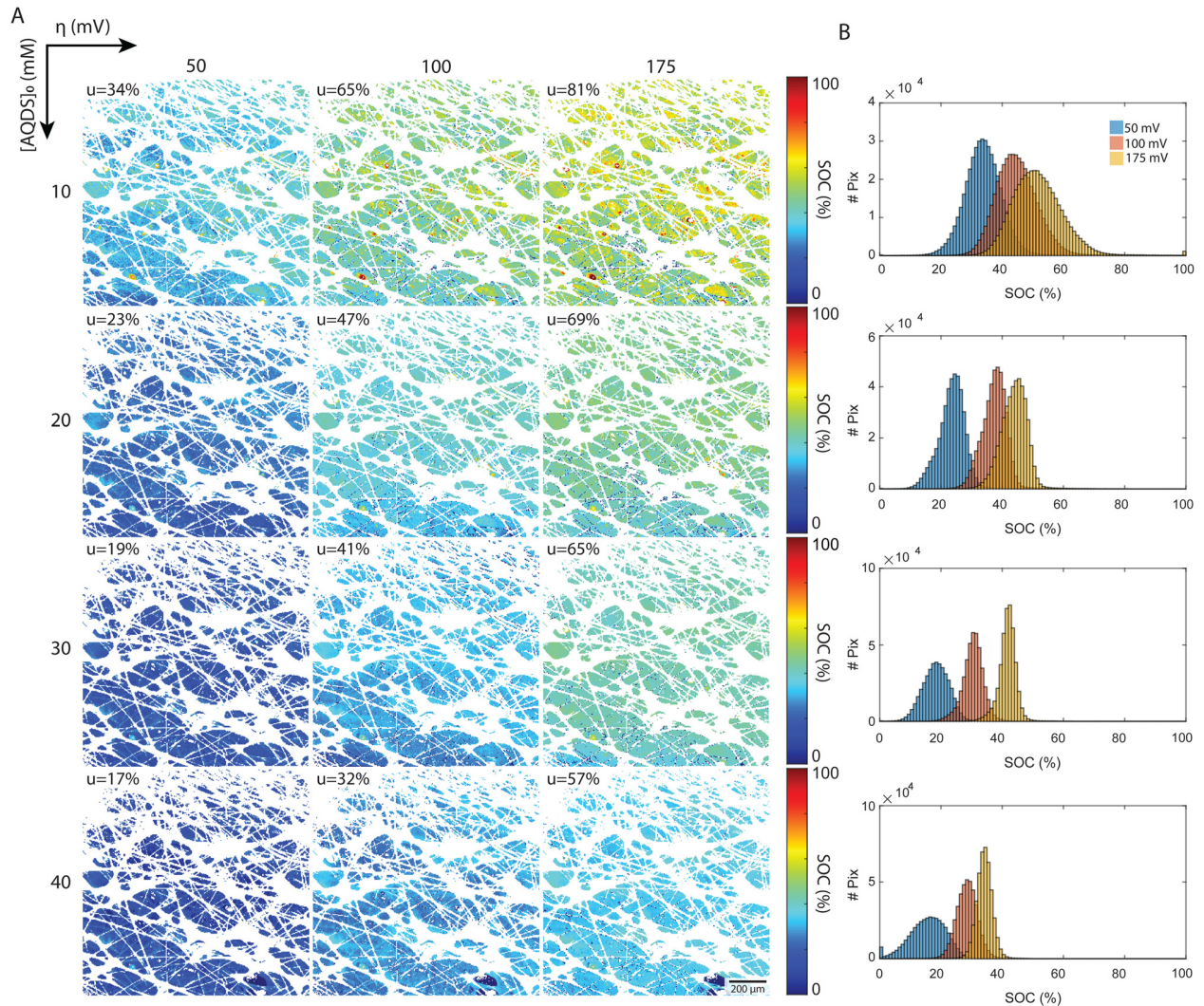


Figure 4.6: Local SOC deduced from fluorescence intensity maps. (A) Chart of steady-state fluorescence maps under varying conditions. The applied overpotentials are increasing from left to right (50, 100, 175 mV). The initial concentrations of redox-active AQDS (10, 20, 30, 40 mM) are increasing from top to bottom. The color map indicates the state of charge SOC as defined in Eq. (4.1). The white pixels correspond to fibers and hetero-phase impurities that are removed during image processing. (B) Histograms of the SOC distribution over all pixels for each image; pixels removed during image processing are not included. Each plot corresponds to the SOC in the row to its left.

trochemical conversion process, highlighting the opportunity for a better understanding of their mass transport characteristics in future studies.

The local SOC maps of the $1.2\text{ mm} \times 1.2\text{ mm}$ field reveal a trend of increasing SOC, transitioning from the lower left to the upper right of each image. Given that the optical factor F_i corrects for spatial variations in emitted and detected light, we believe that this trend represents real physical processes and suggests that Darcy flow is an inadequate description of flow at these length scales. The 2D SOC maps at the highest utilization show pronounced local variation at length-scales from the fiber diameter to the characteristic pore size. These are the length scales where reactant depletion should be most severe. That this pattern is not apparent at lower utilizations might be related to the fact that we are working with integrated intensity through a slab of roughly $25\text{ }\mu\text{m}$ in the direction of the optical path. Large regions exhibiting uniform SOC may indicate low electrochemical conversion, suggesting the possibility of low electrode and flow path efficacy in the region.

A more detailed quantitative look is reported in the histograms, which depict the distribution of pixels by their SOC values. All experimental distributions resemble normal or skewed distributions, as shown in [Figure 4.6\(B\)](#). In the low concentration experiments ($[\text{AQDS}]_0 = 10$ and 20 mM), the histograms exhibit broader distributions than in the other cases. For $[\text{AQDS}]_0 = 30$ and 40 mM , histograms show that the SOC distributions become narrower as overpotential and utilization increase. At these higher concentrations, the SOC histograms have a distinct peak, indicating a mostly uniform SOC across the entire image.

For comparison, in the simple picture with a constant gradient in SOC along x , the macroscopic flow direction, the expected SOC histograms result in rectangular distributions centered at \bar{S} with a width given by $u\Delta x/L$, where Δx is the width of the image and L is the length of the entire electrode in x . For our setup with $\Delta x = 1.2$ mm and $L = 6$ mm, those rectangular distributions would have a width of $0.2u$ SOC values for each histogram (see [Section 4.5.3](#) for comparison.) The histograms derived from the experiments are typically narrower than this. Intriguingly, for the specimen with the highest utilization, $[AQDS]_0 = 10$ mM, under conditions where mass-transport limitations become apparent ([Figure 4.5\(A\)](#)), the width of the SOC distributions from experiments exceeds the width of the hypothetical rectangular distributions.

Remarkably, combined analysis of the experimental histograms and SOC maps reveals that under varying conditions, we can observe either heightened local heterogeneity or enhanced uniformity. While these deviations might average out across larger areas, they are significant at the scale of the displayed 1.2 mm \times 1.2 mm image frame. Such nuances might impact mesoscopic transport in electrochemical flow devices operating under practical conditions. Because this particular experiment collected the fluorescence from only a limited depth range of the electrode—the focal plane is set at $z = 50$ μm within the 190 μm thick electrode, with the $z = 190$ μm coordinate denoting the interface of the electrode with the membrane—we cannot determine the average state of charge throughout the entire thickness. We expect more comprehensive investigations to provide further insight, guide model development and, ultimately, permit the design of higher performance electrodes. These investigations might encompass

imaging across the entire $x - y$ plane of the electrode, and at varied z -depths, and to examine transient, in addition to steady-state behavior. For an example of visualization of transient concentration field evolution, dynamical videos are shown in the published ESI, §7.

Utilizing the SOC maps, we can infer the concentration fields of other species involved in the electrochemical process, specifically AQDS, H₂AQDS and QH. [Figure 4.7](#) illustrates the average concentrations of these species within the imaging frame as functions of the average SOC, \bar{S} . These plots reflect the close alignment with the average concentrations predicted by the dimer model discussed in [Sections 4.3.2](#) and [4.5.1](#). This reaffirms the pronounced influence of dimer formation at elevated concentrations. Such influence introduces nonlinearities in the concentration profiles which, in turn, have implications for the measured intensities, emphasizing the necessity for precise calibration.

The formation of dimers has previously been discussed as having a limiting impact on accessible capacity, even at low electrolyte concentrations [[191](#), [192](#)]. This is in contradiction with other findings, where over 90% of theoretical capacity has been accessed in a flow battery utilizing 1 M AQDS concentration [[158](#)]. In the present study, we reached electrolyte utilizations of 70% or more at all concentrations, and 88% utilization at 10 mM, despite dimer formation at concentrations shown in [Figure 4.7\(C\)](#). As dimerization is concentration dependent, QEFSM at higher concentrations of active material might reveal larger dimer effects on electrochemical behavior.

In this first demonstration of QEFSM, we show the potential this technique holds for mapping the concentrations of electrochemically active species within complex architectures, such as in electrochemi-

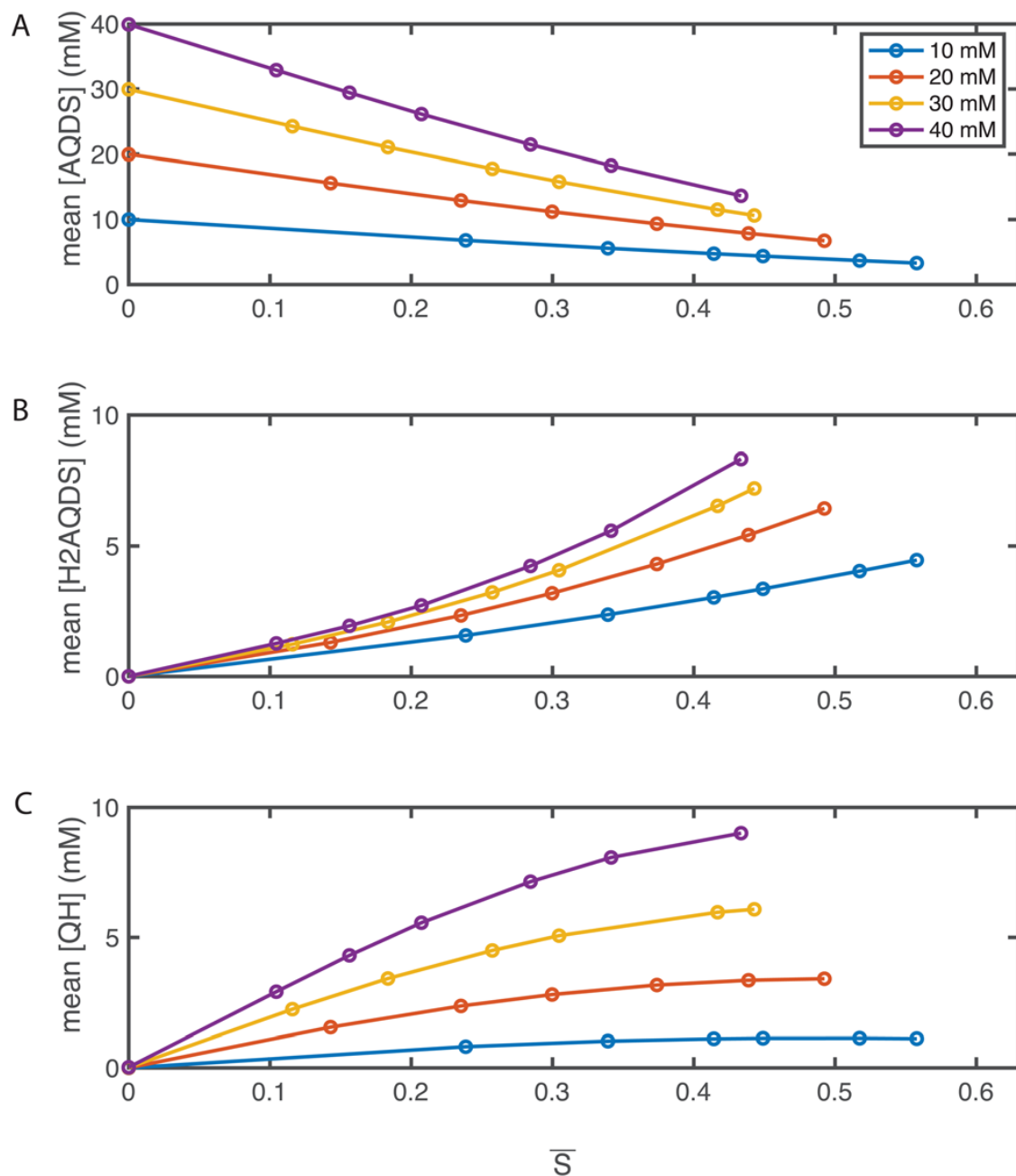


Figure 4.7: Operando concentration profiles. Mean concentrations of (A) AQDS; (B) H_2AQDS ; (C) QH, as functions of the mean soc \bar{S} within the field of view.

cal flow cell porous electrodes. This approach allows for in-depth examination of these systems across a range of operating conditions, offering valuable insights into intricate transport phenomena. Although not demonstrated here, by obtaining two dimensional (2D) SOC maps at different depths within the porous electrode, we have the potential to reconstruct three dimensional (3D) volumes encompassing local SOC and concentration fields.

As research in this domain becomes more rigorous, it will require more precise quantification, such as that provided by QEFSM, of local transport behavior and a deeper understanding of structure-function relationships from the pore-scale to the macro-scale. Such advancements are poised to enhance the design and performance of the next generation of electrochemical devices.

4.5 NUMERICAL METHODS FOR CONCENTRATION MAPPING

4.5.I AQDS:H₂AQDS DIMERIZATION MODEL

The quinhydrone concentration at each SOC value can be calculated from a system of equations. Using the equilibrium constant of dimer formation $K_{\text{dim}} = 80 \text{ M}^{-1}$ from Tong et al. [193] and the total concentration of the reactants participating in the electrochemical reaction, which is equal to the initial concentration of AQDS in each experiment, a parametric curve for each species concentration of SOC can be computed. The system of equations is

$$K_{\text{dim}} = \frac{[\text{QH}]}{[\text{AQDS}][\text{H}_2\text{AQDS}]}, \quad (4.7a)$$

$$[\text{AQDS}]_0 = [\text{AQDS}] + [\text{H}_2\text{AQDS}] + 2[\text{QH}], \quad (4.7b)$$

$$SOC = \frac{[H_2AQDS] + [QH]}{[AQDS] + [H_2AQDS] + 2[QH]}. \quad (4.7c)$$

This system can be solved algebraically in terms of the concentration fractions of the oxidized, reduced and dimerized species,

$$x = \frac{[AQDS]}{[AQDS]_0}, \quad y = \frac{[H_2AQDS]}{[AQDS]_0}, \quad z = \frac{[QH]}{[AQDS]_0}. \quad (4.8)$$

Define the dimensionless rate constant

$$R = K_{\text{dim}} \cdot [AQDS]_0. \quad (4.9)$$

Denote the state of charge by s to lighten the notation. It is readily seen that the original system of equations Eqs. (4.7a)–(4.7c) is equivalent to the nondimensionalized system

$$z = Rxy, \quad (4.10a)$$

$$x + y + 2z = 1, \quad (4.10b)$$

$$y + z = s. \quad (4.10c)$$

Given the fraction of reduced species y , the other two fractions x and z are given by

$$x = \frac{(1-y)}{(1+2Ry)}, \quad z = \frac{Ry(1-y)}{(1+2Ry)}. \quad (4.11)$$

We can verify that Eq. (4.11) is consistent with Eq. (4.10a) by simplifying Rxy in terms of y to obtain the definition of z in Eq. (4.11). We can likewise verify consistency with Eq. (4.10b) by simplifying $x +$

$y + 2z$ in terms of y , obtaining a fraction that simplifies to one. Given an input value of y , we can calculate x and z using Eq. (4.11), and then we can calculate the SOC using $s = y + z$. While we cannot

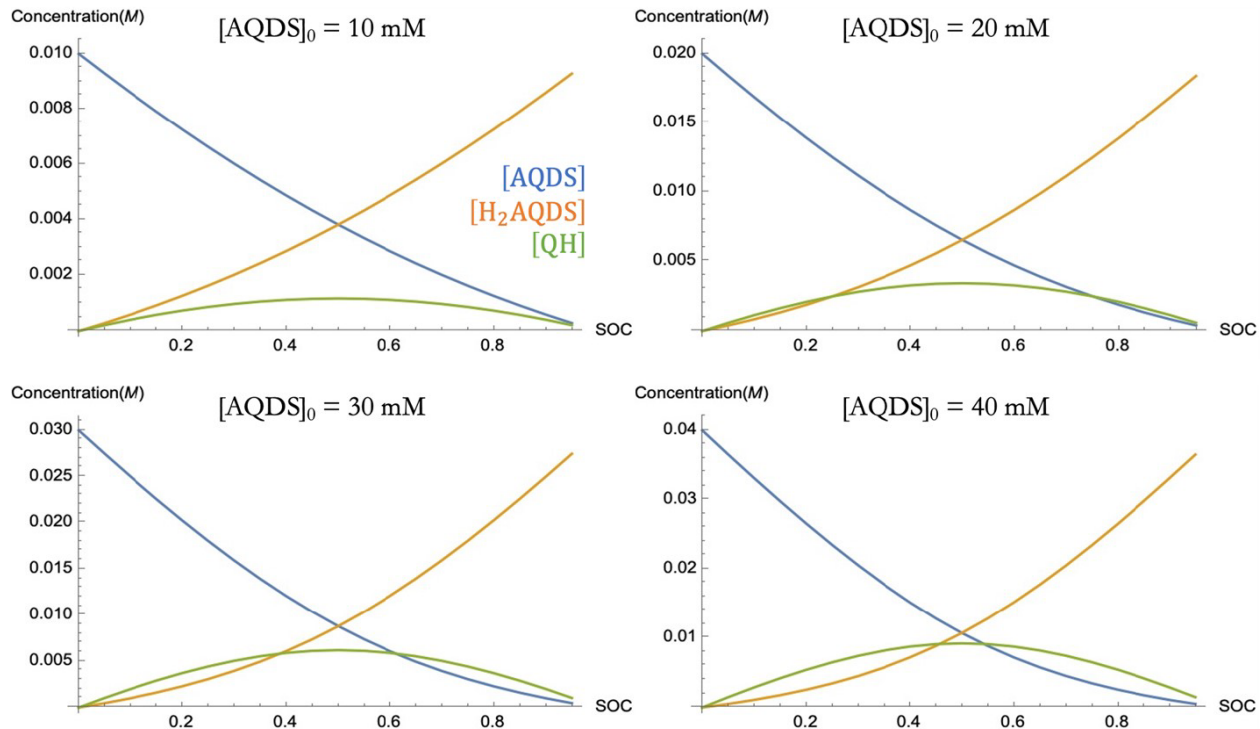


Figure 4.8: 1:1 (AQDS: H_2AQDS) binding dimer model. Predictions of the theoretical concentration profiles for AQDS, H_2AQDS and QH as a function of SOC, calculated using the dimer model. The calculations are performed at fixed $[AQDS]_0$ values for which we ran experiments. (A) $[AQDS]_0 = 10 \text{ mM}$, (B) $[AQDS]_0 = 20 \text{ mM}$, (C) $[AQDS]_0 = 30 \text{ mM}$, (D) $[AQDS]_0 = 40 \text{ mM}$.

calculate the three concentrations algebraically in terms of s , the algebraic function $s(y)$ is monotonically increasing, allowing us to plot concentrations as a function of s for a given value of $[AQDS]_0$ as shown in Figure 4.8. We can also readily invert $s(y)$ numerically to obtain $y(s)$. With increasing $[AQDS]_0$, it is evident that the proportion of dimer to the total concentration grows, and the concentrations of the three species exhibit increasingly nonlinear variations with respect to the state of charge. Consequently,

it is essential to account for the influence of dimer formation on fluorescence intensity, particularly at high concentrations, in order to accurately quantify the SOC. The plate reader data in [Figure 4.3\(C\)](#) demonstrate that the intensity of the 40 mM solution follows the same nonlinear trend as the H₂AQDS concentration profile in [Figure 4.8\(D\)](#).

4.5.2 THEORETICAL BACKGROUND FOR CONCENTRATION FIELDS IN FLOW DEVICES

In electrochemical flow devices, the change of concentration fields over time can be modeled by the sum of mass transport and electrochemical source terms, namely advection \mathcal{A}_j , diffusion \mathcal{D}_j , electromigration \mathcal{E}_j and the (Butler-Volmer) source term S_j by the Nernst-Planck equation

$$\frac{\partial C_j}{\partial t} = \mathcal{A}_j + \mathcal{D}_j + \mathcal{E}_j + S_j. \quad (4.12)$$

The advective term \mathcal{A}_j describes the net flow through the electrode and is given in terms of the steady state fluid velocity \mathbf{u} and concentration gradient ∇C_j by

$$\mathcal{A}_j = -\mathbf{u} \cdot \nabla C_j. \quad (4.13)$$

The diffusion term \mathcal{D}_j is derived by Fick's law and can be calculated from the diffusion coefficient D_j of the molecular species and the Laplacian of the concentration of interest by

$$\mathcal{D}_j = D_j \nabla^2 C_j. \quad (4.14)$$

The electromigration term \mathcal{E}_j describes the bias of charged entities moving under an electric field and is given by

$$\mathcal{E}_j = \left(\frac{z_j D_j F}{RT} \right) \nabla \cdot (C_j \nabla \phi_L) \quad (4.15)$$

where z_j is the charge number; F is Faraday's constant; R is the ideal gas constant; T the temperature in Kelvin; and ϕ_L is the electric potential in the liquid. Adding all the terms, we obtain the Nernst-Planck equation

$$\frac{\partial C_i}{\partial t} = -\mathbf{u} \cdot \nabla C_i + D_i \nabla^2 C_i + \frac{z_i D_i F}{RT} \nabla \cdot (C_i \nabla \phi_L). \quad (4.16)$$

The connection between the applied potential and the current is given through the electrochemical source term (Butler-Volmer equation) measuring the overall rate of the redox reaction of AQDS. The source term can be computed given the overpotential (η), the specific area of the electrode interface (a), the reaction rate constant k_0 , the charge transfer coefficients of the respective redox states α_i and the concentration of each redox active species:

$$S = a k_0 C_A^{\alpha_A} C_B^{\alpha_B} \left[\exp \left(\frac{n_e F \alpha_A}{RT} \cdot \eta \right) - \exp \left(\frac{n_e F \alpha_B}{RT} \cdot \eta \right) \right]. \quad (4.17)$$

The applied overpotentials cause the current response which is monitored over the duration of the experiment. Consequently, current and overpotential as well as fluorescence intensity can be directly related. Both pairs of physical parameters must be connected to finally interpret the fluorescence data and derive conclusions about current, potential and flow.

4.5.3 DATA CALIBRATION AND SOC MAPPING

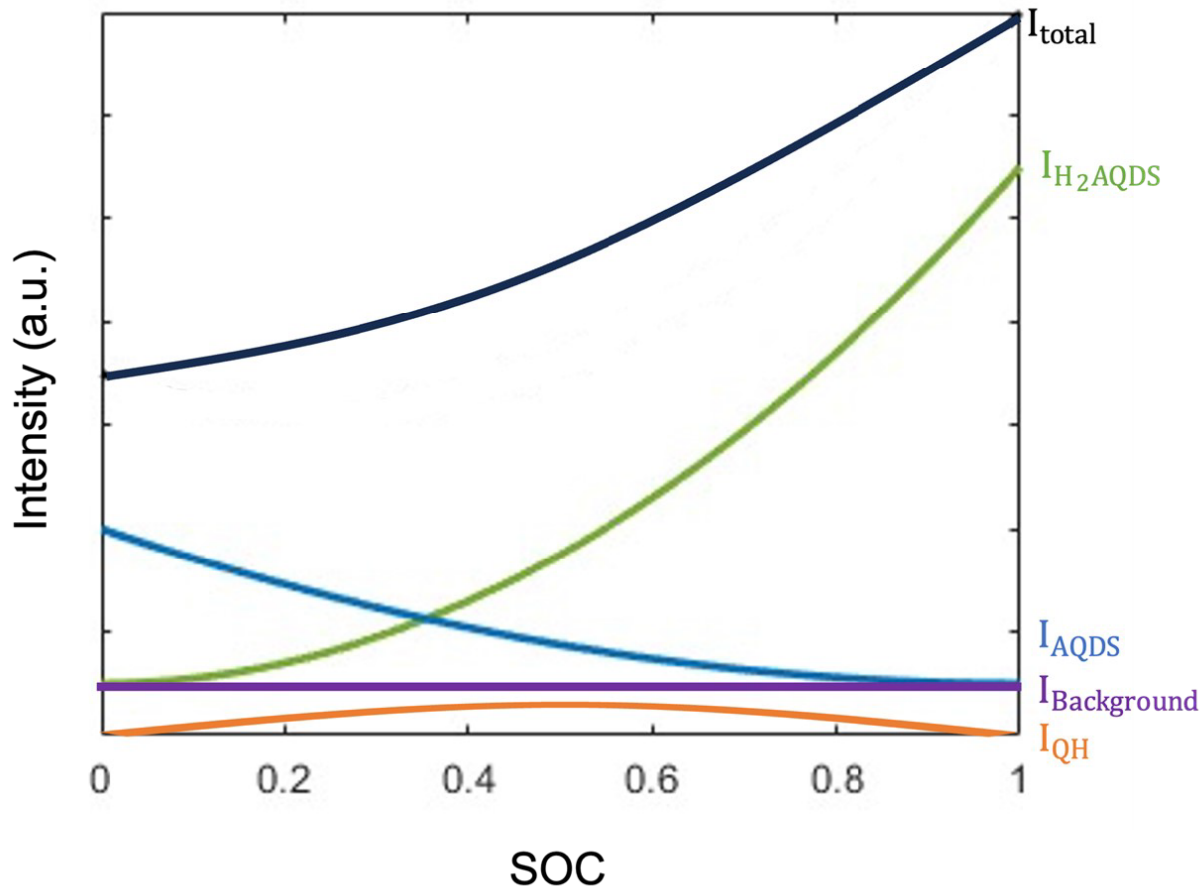


Figure 4.9: Schematic depiction (not to scale) of different contributions to spatially averaged raw intensity I_{total} . For the calibration of the intensity maps to obtain SOC maps, we need to distinguish between the different species contributing to I_{total} . The black solid line schematically shows I_{total} that is obtained in an experiment. $I_{\text{Background}}$ is the background signal which remains constant in every image. I_{QH} corresponds to the dimer intensity, which is expected to have small contributions to I_{total} but is estimated independently. I_{AQDS} is the native fluorescence of AQDS and $I_{\text{H}_2\text{AQDS}}$ is the fluorescence of H₂AQDS, which has the largest contribution to I_{total} .

As part of our calibration procedure, we considered the fluorescence contributions of each molecular

species involved, i.e. AQDS, H₂AQDS and QH, which are required for proper quantification of the local SOC. The various contributions are displayed in [Figure 4.9](#). Our experimental data for the SOC estimation comprised 29 images. A single *ex situ* image taken at a high and homogeneous (but unknown) H₂AQDS concentration; and 28 images taken for varying applied overpotentials with 4 total AQDS concentrations crossed with 7 applied voltages. As the analysis is done at the individual pixel level, it is critical for the images to be aligned on that scale based on the *ex situ* image. This was done using the CV2 computer vision library [194] and resulted in a mean shift of 1.8 pixels. Once all the images were aligned, we assigned pixels into three categories: excessively dim; excessively bright; and reliable pixels to be included in the analysis. We hypothesize that excessively dim pixels were due to obstructing fibers, and excessively bright pixels were caused by highly reflective heterophase impurities.

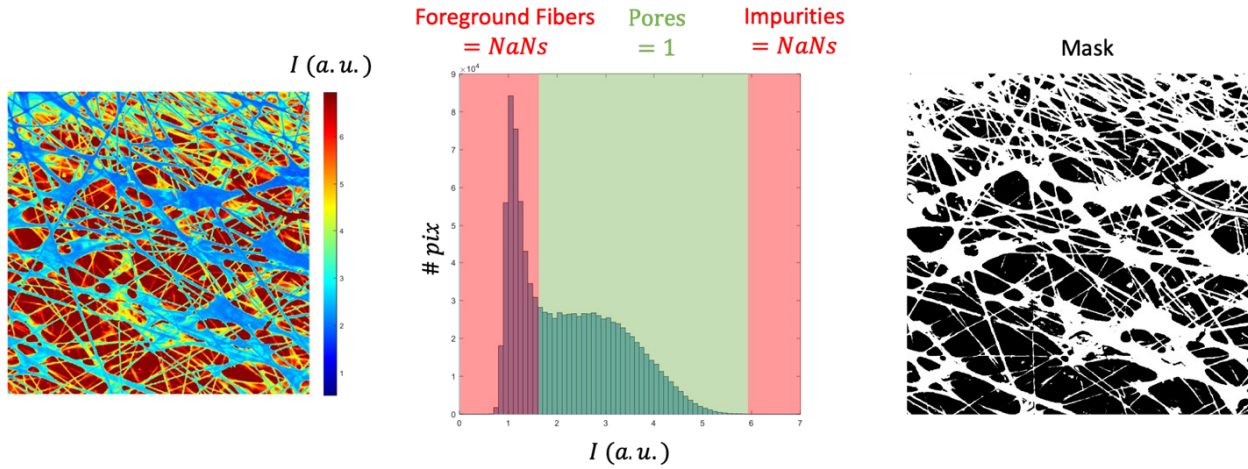


Figure 4.10: Selection of valid pixels for SOC maps. **(Left)** - the raw intensity image in arbitrary units. **(Middle)** - the histogram of the image is shown with schematics of the manually selected low and high intensity cutoffs. The green area corresponds to the “good” pixels in the pores filled with electrolyte that are considered for further image processing. **(Right)** - a visualization of the mask image that contains all valid pixels (in black) and unreliable pixels in white.

We set thresholds for dim and bright pixels at quantiles 0.55 and 0.995, respectively. These thresholds were set by a combination of a qualitative visual review of the data, and a Gaussian mixture model to set the lower threshold. As the location of the fibers remains fixed in every image, a pixel I_{ri} on one of the reaction images was considered valid when the corresponding pixel B_i was valid on the *ex situ* image, *and* the pixel fell within the specified quantiles of intensity for that reaction. The remaining pixels, corresponding to fibers and other heterophase impurities, were masked out and were not further considered in our analysis, as demonstrated for the example shown in [Figure 4.10](#).

This data filtering reduced the size of our calibration set from 29.4 million to 11.7 million pixels. The result of the image data processing was an array of *ex situ* intensities B_i and arrays I_r for each reaction condition.

We also had 28 utilizations u_r corresponding to each reaction and calculated by [Eq. \(4.3\)](#). We posit a linear relationship between the electrochemical utilization u_r and the mean state of charge \bar{S}_r . When the system is not mass transport limited, the mean field theory should be a highly accurate approximation *on average* over a mesoscale patch of space, even if it does not hold uniformly over very small areas. Most of our reactions had utilizations below 50%, justifying the claim that mass transport limitations were not binding and the use of this approximation. In the simple mean field theory without mass transport limitations, the solution is a smooth constant gradient in the state of charge between 0 at the inlet and u at the outlet. The mean state of charge \bar{S} and utilization u are thus related by $\bar{S} = u x_m / L$ where x_m is the position of the midpoint of the image and L is the length of the electrode. In our study, the ratio

$x_m/L = 0.63$.

There are three electroactive species in this study, namely the oxidized state AQDS; the reduced state H₂AQDS; and the dimer QH. The concentrations of these species are subject to two constraints,

$$[\text{AQDS}] + [\text{H}_2\text{AQDS}] + 2[\text{QH}] = [\text{AQDS}]_0, \quad (4.18\text{a})$$

$$[\text{QH}] = K[\text{AQDS}][\text{H}_2\text{AQDS}]. \quad (4.18\text{b})$$

[Eq. \(4.18a\)](#) is conservation of the anthraquinone species in their various forms, and [Eq. \(4.18b\)](#) is the chemical equilibrium governing dimer formation. As shown in [Section 4.5.1](#), it is straightforward to solve these equations given the relative concentration Y of the reduced species as defined in [Eq. \(4.6\)](#).

The solutions are

$$[\text{AQDS}] = \left(\frac{1 - Y}{1 + 2RY} \right) \cdot [\text{AQDS}]_0, \quad (4.19\text{a})$$

$$[\text{H}_2\text{AQDS}] = \left(\frac{Y}{1 + 2RY} \right) \cdot [\text{AQDS}]_0, \quad (4.19\text{b})$$

$$[\text{QH}] = \left(\frac{RY}{1 + 2RY} \right) \cdot [\text{AQDS}]_0, \quad (4.19\text{c})$$

where $R = K[\text{AQDS}]_0$ is the dimensionless rate constant for dimer formation defined in [Eq. \(4.9\)](#).

We next made an initial estimate of the brightness coefficients $\alpha, \beta, \gamma, \delta$. To formulate this estimate, we made the preliminary assumption (later relaxed in the final estimation) that the concentrations of the electroactive species were uniform for each reaction. Using [Eq. \(4.19\)](#), we constructed a numerical table mapping an input reduced fraction Y to an output state of charge. There is one table for each initial concentration $[\text{AQDS}]_0$. These tables were all monotonically increasing as we expected, and we

used the data points to construct four numerical functions mapping between SOC and Y at the various $[AQDS]_0$ under consideration. We converted the utilizations u_r to a mean SOC \bar{S}_r for each reaction; interpolated \bar{S}_r to obtain \bar{Y}_r ; and then solved for the equation of each species using Eq. (4.19). We completed this step by solving a linear least squares problem of the form $\mathbf{I} = \mathbf{X}\mathbf{C}$. The left-hand side was the mean image intensity for the 28 reactions. The design matrix \mathbf{X} has 28 rows and four columns, $[AQDS]$, $[H_2AQDS]$, $[QH]$, 1. The estimated coefficients are $\mathbf{C} = [\alpha, \beta, \gamma, \delta]$. This regression achieved an excellent fit with an R squared value of 0.9632. The estimated coefficients included a large, positive value for β (the brightness of H_2AQDS) and much smaller values for AQDS and QH, as expected.

Once the brightness coefficients were available, we built a second table with the predicted light production P as a function of Y by Eq. (4.4). This led to a monotonic function that was interpolated to produce a mapping function $Y(P)$. We finally estimated the state of charge by applying Eq. (4.5) once we have the optical factor F_i at each pixel. We obtained the optical factor by applying the assumption that the bright *ex situ* image is homogeneous, yielding the direct calculation $F_i = B_i/\bar{B}$, where \bar{B} is the mean intensity on the *ex situ* image. The resulting estimates of the state of charge are visually plausible and have an excellent fit to the experimental brightness.

At this stage, we made a further refinement to the model. We relinquished the assumption used to estimate the brightness coefficients that the concentration was uniform on each reaction image. We also insisted that the model recover the assumed mean state of charge on each reaction; the initial estimate was close, but had an RMS error of 0.031. This model was estimated by an iterative application of three

computational steps until convergence was achieved. These steps are

- refine the estimate of the optical factors F_i ,
- refine the estimate of the brightness coefficients $\alpha, \beta, \gamma, \delta$,
- shift the estimated concentrations to match the mean state of charge \bar{S}_r .

The concentration shifts are performed after applying a logit transform of the estimated Y for each reaction. At each step, $\text{logit}(Y)$ is shifted by one step of Newton's method using a numerical derivative. Four steps of Newton's method are sufficient to match \bar{S}_r to six decimal places. The update to the brightness coefficients is analogous to the initial estimate. This time, however, instead of a least squares problem with 28 rows (one per reaction), there are 11.7 million rows (!), one row per pixel. The left hand side of the least squares equation is the observed intensity, and the design matrix is as before, but each row is now scaled by the optical factor. We can succinctly write the design matrix entries as

$$\mathbf{X}_{ri} = [\text{AQDS}, \text{H}_2\text{AQDS}, \text{QH}, 1] \cdot F_i. \quad (4.20)$$

This regression $\mathbf{I} = \mathbf{XC}$ provides both an updated estimate of the brightness coefficients and a standard error σ_I on the recovered brightness.

The update to the optical factors \mathbf{F} is new to this stage of the estimation. If we consider pixel i in isolation, Eq. (4.5) implies that we can construct a linear regression $\mathbf{I}_r = \mathbf{P}_r F$, where \mathbf{I}_r and \mathbf{P}_r are both column vectors with 28 rows, and F is the optical factor to be estimated. This regression can be augmented to include an additional 29th row from the *ex situ* image with left and right side B_i and \bar{B} , respectively. This regression also provides a standard error σ_Y on the optical factor.

This model was initialized with preliminary estimates for the brightness coefficients and optical factors described above. It was then iterated for nine steps until convergence criteria for small changes in parameter values were met. The converged model includes estimates for the concentrations of all three species, from which we can easily compute the estimated SOC. The model also estimates standard errors in I and F . It is important to acknowledge that even after the calibration procedure, certain residual background fibers and pore depth effects persisted, which have the potential to introduce minor systematic errors.

4.5.4 COMPARISON WITH A CONSTANT SOC GRADIENT ASSUMPTION

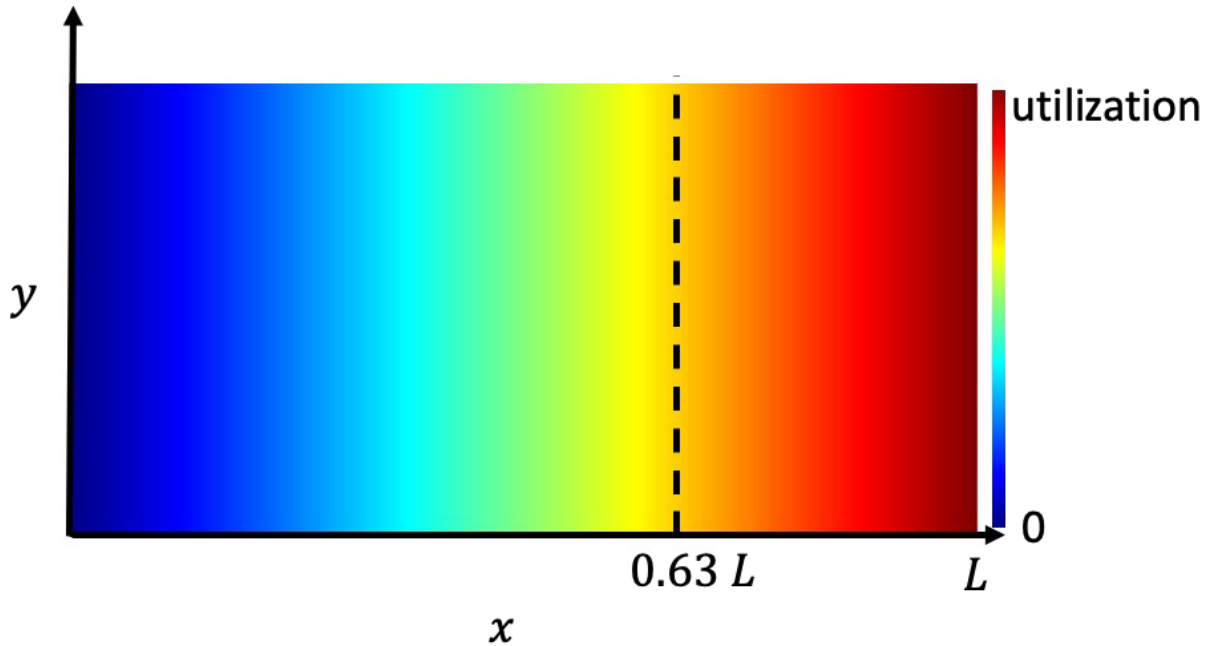


Figure 4.11: Schematic of simple constant gradient assumption. The rectangle corresponds to the working electrode where the fully oxidized electrolyte enters on the left side and gets reduced in the form of a constant gradient along x towards the outlet. The color map indicates the utilization of 0% in blue and the maximum utilization, at the end of the electrode, in red. In our study, the image is centered at $x_m/L = 0.63$.

We posited that over large scales, such as the $1.2 \text{ mm} \times 1.2 \text{ mm}$ imaging frame, a simplified assumption of a constant SOC gradient along x and uniform along y can be used to estimate \bar{S} . The results are then given by $\bar{S} = ux_m/L$ as demonstrated in Figure 4.11.

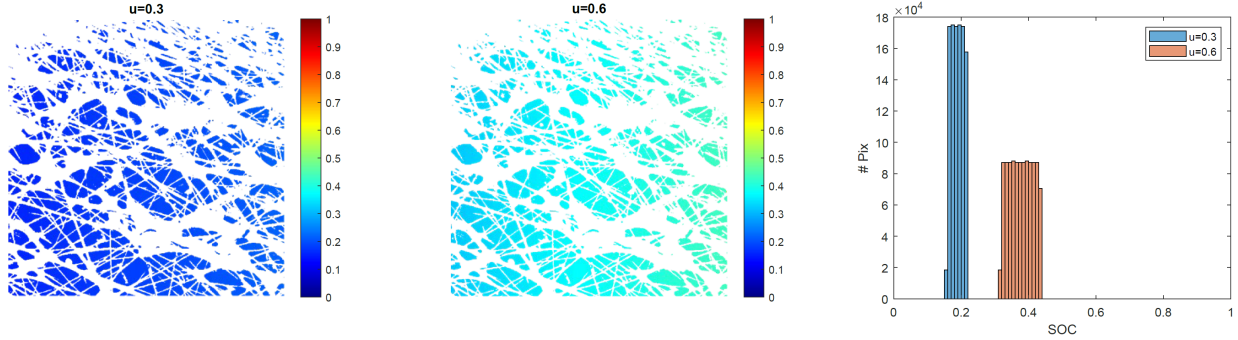


Figure 4.12: Spatial mapping of the simplified model featuring a constant gradient, tailored to the specific imaging frame and incorporating the position and mask derived from the actual experiments. Left - a simulated 2D SOC corresponds to an electrolyte utilization of 0.3. Center - a utilization of 0.6. Right - associated histograms of image intensity, which largely maintain rectangular distributions even after masking out invalid pixels.

For a comparison of our results with the simple assumption of a smooth, constant gradient, we generated simulated SOC maps at two distinct utilizations (0.3 and 0.6), maintaining x_m consistent with the experimental location of the imaging center at $0.63L$, as depicted in Figure 4.12. A mask was superimposed on the images, removing pixels in regions obscured by fibers and coloring them white. Notably, the histograms indicate that the distributions largely resemble rectangular shapes, even after the exclusions of the masked pixels.

4.6 CONCLUSIONS

In this study, we have demonstrated a non-invasive *operando* technique for the precise mapping of concentration fields within a functioning porous electrode. By coupling electrochemistry and confocal

microscopy inside the device, we are able to derive spatially and temporally resolved SOC maps in well defined volumes inside the electrode architecture. Transverse and axial resolutions of 1 and 25 μm , respectively were achieved.

We developed an optically transparent flow cell that facilitates the investigation of the entire electrode and is compatible with confocal microscope hardware. The versatility of this configuration makes it suitable for a wide range of porous architectures and optically active electrolytes. We demonstrated an effective image processing technique to address challenges associated with the presence of opaque components, including fibers various z -heights and heterophase artifacts. Because the detected signal comprises distinct contributions from reactants, products, other interacting species, and background, we developed a calibration technique that enables quantification of concentration fields for all relevant molecular species within the system: the oxidized species [AQDS], the reduced species [H_2AQDS], and the dynamically formed heterodimer [QH]. Consideration of individual species concentration fields yields quantitative local SOC maps.

We have demonstrated that 2D mapping techniques offer a powerful method for characterizing local heterogeneity in concentration and SOC fields over mesoscopic areas inside of porous electrodes. This technique should permit experimental testing of multiphysics transport models from sub-pore scale to the scale of the field of view, which may be tiled to study larger areas. Within the limited 1.2 mm \times 1.2 mm field of view of these experiments, we observed the average gradient in the SOC field not parallel to the nominal flow direction, suggesting that Darcy flow is too simple a model for this length scale. We iden-

tified more uniform SOC fields at high concentrations and low utilizations, and broad SOC distributions for the lowest concentration with—particularly at the highest utilization—significant local heterogeneities at length scales from the fiber diameter to the characteristic pore size.

QEFSM is a valuable method to quantitatively study porous electrodes as active materials during electrochemical transformations. It should facilitate the understanding of local voltage losses and the development of structure-function relationships for various electrode architectures. It may lead to electrochemical systems with improved performance and a new generation of electrode designs.

4.7 DATA AND CODE AVAILABILITY STATEMENT

Data for this chapter, including micrograph images and Python source code for data analysis, are available at <https://github.com/memmanuel/qefsm> and <https://doi.org/10.5281/zenodo.11505668>.

"You must be ready to give up even the most attractive ideas when experiment shows them to be wrong."

Alessandro Volta [195]

Allegretto



Ludwig van Beethoven, Seventh Symphony in A major, op. 92. Second movement.

Conclusion

4.8 SCIENTIFIC CONCLUSIONS

A theme I noted in both of the system simulations I ran is that it may be easier to model a system at steady state than to solve the general problem of integrating the system's dynamics. While there is a certain satisfaction in solving a problem in full generality, in the cases of both flow batteries and the acid-base generator, we are ultimately motivated by our desire to solve an engineering problem. And both of these engineered systems spend almost all their time at steady state. This is not a universal result—a model for a car that only considers a steady state of cruising at 55 mph on the highway may see little difference in performance between a Prius and a Ferrari. But for both RFBs and CCS, it is enough to understand the steady state.

Of course, it is always possible to attempt to solve for steady state by writing a dynamical solver and advancing it until convergence criteria are met. But as I demonstrated in [Section 1.4.3](#), we can often ob-

Some of the text about future research directions for porous electrodes was adapted from a renewal proposal our team recently submitted to the U.S. Department of Energy, Basic Energy Sciences program. I was the primary author of these parts of the proposal.

tain the same result much faster by considering the special properties of a steady state. While the idea of converting a Neumann condition governing boundary fluxes to a Dirichlet condition governing overpotential values may be specific to porous electrodes, the broader theme may generalize to a number of other modeling problems. In particular, any engineered system depending on mass transport and described by the Nernst-Planck equation should be amenable to this treatment. A key takeaway here is that when one is solving for steady state, *all is fair in love and war*, by which I mean, you can use *any* method whatsoever to formulate an initial guess. The only criterion that matters is how much computational effort is required to iterate it to a steady state. Assuming that you have also coded a dynamical solver, you can always verify that your putative steady state computed by other means is in fact steady as claimed.

A related theme I observed in modeling porous at steady state is the utility of having a series of related models built on the same computing infrastructure, describing different levels of the system's physical phenomena. This arose most clearly in the consideration of electromigration. The most elaborate version of the RFB twin model solved at every step a Poisson equation for the electric field in the electrolyte and a coupled equation for electrochemical reactions following Butler-Volmer reaction kinetics. This is an exquisitely detailed description of multiple physical phenomena. Yet as I demonstrated in [Section 1.6.3](#), for both the particular systems we wanted to model, and a much broader category of porous electrodes we might wish to consider for any practical application, the presence of a strong supporting electrolyte renders electromigration negligible, and the electric potential in the electrolyte can be safely disregarded. This is a large computational savings. The validity of this assumption can and should be verified by com-

paring the simpler and richer models. This can be done most efficiently by first determining a steady state in the simpler model, and then using the resulting steady state as a starting point for the richer model.

My last simulation finding applies to porous electrodes with some generality. The fluid flows relevant to flow battery operation are decidedly in the Stokes regime, meaning that a single flow simulation is sufficient to obtain a useful approximation to *all* the flows of interest when designing a flow battery. Under some mild assumptions that are usually nearly true in practice—dilute solution thermodynamics, equal diffusivity between oxidized and reduced species, no degradation side reactions—we can simplify the Nernst-Planck equation governing the electrochemistry in a flow battery to a single PDE in terms of the state of charge, rather than one PDE for each species. As mentioned above, in the presence of a strong supporting electrolyte, we can also safely disregard the electromigration term. And as shown in [Algorithm 1.8](#), the state of charge at steady state can be efficiently calculated from a given fluid velocity field using only explicit calculations. Combined, these finding show that we can produce a rich description of the behavior of a proposed electrode geometry at a range of flow rates relevant to practical operation by performing a single incompressible flow simulation and a handful of explicit steady state charge distributions at varying multiples of the reference velocity field.

4.9 COMMENTS ON SCIENTIFIC COMPUTING

In an age of exascale computing capabilities, numerical analysts should revisit our previous beliefs about the optimal tradeoff between the fidelity of a model and how expensive it is to run in time and dollars. It is now feasible to perform ambitious direct numerical solutions of the governing PDEs for

porous electrodes at laboratory scale using a single high end server. By a simple scaling analysis, we can conclude that commercial scale electrodes may be simulated in three dimensions at micron scale resolutions on some of the modern supercomputing facilities available today such as Frontier, Aurora and El Capitan [196]. Previously, we in the scientific computing community were forced to accept some compromises and make some clever approximations to get any kind of an answer to problems of this scale on our available computing hardware. Now we should redeploy some of that cleverness to build algorithms that scale efficiently on the massively parallel hardware that has recently come online. I believe that this result generalizes to many other problem areas where we have a good understanding of the governing PDEs. We should increase the scope of our ambitions and reimagine our capabilities; to (mis)quote Yoda, we “must unlearn what [we] have learned.”¹

A major advantage of a constructive, direct numerical solution of a PDE is that we may consider it to be a so-called digital twin to a physical system [197, 198]. These models can and should be verified against experimental results to the extent possible. Once a digital twin has been validated, we can treat it as a gold standard of simulation results. We can use it to interrogate systems at a level that would be impossible in physical experiments, e.g. drawing a 3D map of the state of charge at a micron resolution in the entirety of an electrode. By the time a simulation code has been developed and tested, the marginal cost of running one more scenario is typically dramatically lower than the cost of running an additional

¹In *Star Wars: Episode V*, Luke Skywalker fails to use the Force to lift his crashed X-wing starfighter from the swamp on Dagobah because he thinks it is too heavy. Yoda tells Luke Skywalker, “No! No different! Only different in your mind. You must unlearn what you have learned.”

experiment [199].

I have spent four years attending group meetings for a multidisciplinary team investigating porous electrodes in flow batteries. Much of our meeting time was spent discussing experimental questions, interpreting results, and on other topics usually understood not to have much to do with numerical simulations and applied math. Yet in those meetings, I repeatedly found that having access to a reliable, interpretable physics model for our electrodes was valuable in ways I would not have predicted. I often had a different perspective on qualitative phenomena than the experimentalists, and a lively back and forth frequently advanced our efforts. I think that more experimental scientists should consider adding at least one applied mathematician to their teams if budgets make it feasible.

I believe that two reasons we do not see more participation by mathematicians in experimental groups are institutional structures and incentives. There is essentially no organizational structure to systematically support PhD students admitted into applied math to do this kind of work; it is all ad hoc. Junior faculty members in applied math may not get the professional advancement and reputation they need to gain tenure by playing a supporting role in team efforts where the first author comes from another discipline. As a result of these structures and incentives, a recent survey of the job talks given by aspiring applied math faculty members is dominated by “solo” topics, often related to machine learning. While I believe that many of these research questions are fascinating and worth investigating, I claim that the larger scientific enterprise could make a better use of the talents of these mathematicians by offering us more collaborative opportunities with experimental scientists, and rewarding the successful ones with

real recognition for those contributions.

I will now say a few words in support of explicit methods for solving PDEs. We who do scientific computing often emphasize implicit and semi-implicit methods for sound reasons including longer time steps and superior numerical stability. But explicit methods have some excellent qualities that I think are too often underappreciated. Explicit methods are very simple to understand. They can be coded quickly and directly, and they allow one to avoid the solution of linear equations. In practice, I often found many of the thorniest problems I faced during my PhD came when a Krylov solver for what I expected to be a well conditioned linear system failed to converge. I spent literally months buried in painful rabbit holes of this type. By comparison, when I took on the acid-base generator, I was able to code it explicitly within a matter of days. While an implicit solver might have been “better” in some abstract sense, and might have run faster, this is a program that was run only a handful of times, and the explicit solver was fast enough to converge within minutes. Would it have been a superior strategy to invest weeks of extra development time to save 30 minutes of run time at the end? A second advantage of explicit methods is that they typically require far less communication between different CPU cores when they are implemented as parallel algorithms. This makes them particularly well suited to run on the largest supercomputer systems, increasingly so as they adopt heterogeneous architectures with a mix of CPU and GPU hardware.

I will conclude with some thematic findings about analyzing data from electrochemical systems. Typically this kind of work is performed by PhD students in the discipline of the experimental science, rather than by a specialist in data analysis. Before joining the PhD program, I completed a Data Science masters

program and received extensive training in data analysis and statistics. I also wrote many numerical programs that included data analysis and plotting of the results. This was invaluable when faced with the data analysis questions covered in this thesis, and provided me with many tools to do this work. Traditional approaches to experimental science often led to small, manageable data sets that could be analyzed credibly using the skills taught in a first semester course in statistics. In the modern era with huge data sets coming from multiple instruments, which might have small alignment mismatches and other artifacts, we have entered a new regime of much more challenging data analysis. My role in both of the data analysis projects was largely serendipitous, as I was in the right place at the right time to use the skills I had learned. I advocate that in the future, experimental science groups devote more systematic effort to analyzing their complex data sets, either through collaboration with other groups that have specialist training, or by revising plans of study so at least a few group members take some additional coursework in these areas.

4.10 FUTURE RESEARCH DIRECTIONS

Having access to a digital twin opens up powerful lines of inquiry. Taking porous electrodes as one motivating example, a multidisciplinary team can design, simulate, print and characterize a range of electrode designs. [Figure 4.13](#) provides an overview of how a digital twin can play a vital role in advancing a broad based research program on porous electrodes. Generative artificial intelligence (AI) may be used alongside traditional machine learning (ML) to produce proposed electrode geometries. Some of these geometries might be infeasible to fabricate and accessible to study only via modeling. We can run a sim-

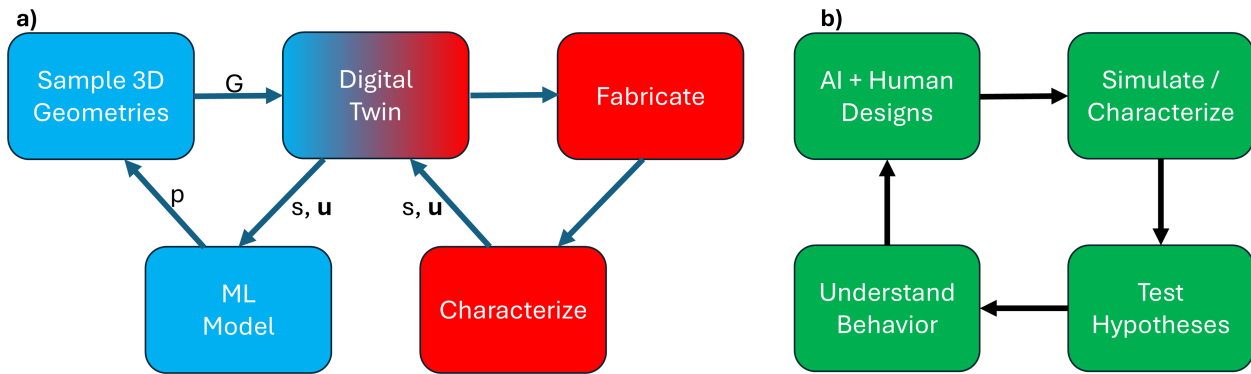


Figure 4.13: Learning loops to understand electrode processes and behavior. **a**, Active learning to train surrogate models. Geometries G are sampled and evaluated by the digital twin to predict SOC s and velocity u . These predictions are used as synthetic data to train surrogate ML models. Predicted performance from ML models is used to set sample probability weights p , closing the first loop. The most promising designs, e.g., with high predicted utilization, are fabricated and characterized. Experimental measurements are used to validate the digital twin, closing the second loop. **b**, Designs from both AI and humans are simulated and characterized. The results are used to test hypotheses and answer research questions. This leads to better understanding of electrode behavior, which is used for novel human-generated designs and AI sampling algorithms, closing the third loop.

ulation with a proposed electrode geometry as input and predict the state of charge spatial map as well as summary electrical performance statistics. Nothing in this discussion is inherently limited to porous electrodes. The same approach generalizes to any problem where it is now feasible to perform a direct numerical simulation of the governing equations to a scientific or engineering problem of interest.

A promising approach to efficiently simulating larger porous electrodes is to model it hierarchically in an approach we call a *Darcy mosaic model*. The *mesoscale model* describes the entire system as a 3D grid of box-shaped “tiles” that are coupled hydraulically by Darcy flow and electrochemically by shared SOC values on tile faces. The *microscale model* to describe each tile is the digital twin of Chapter 1. The key idea behind this approach is that while a rich pore-scale description is necessary to accurately simulate the internal dynamics of a tile, its dependence on its neighbors can be summarized by a handful of scalars,

namely the mean pressure and SOC on each shared face. We can test, refine, and validate this model computationally against the underlying pore scale model run on a supercomputer.

A surrogate model is a simplified model that approximates a richer, more computationally expensive model and can be used for design exploration [197, 200]. With the use of a digital twin, we can develop surrogate models to predict the velocity field, state of charge field, and utilization from a 3D electrode design. We call this approach *machine learning enabled surrogate models*. We can use microstructural features previously identified in the literature to be relevant to performance as features for these models. As an example, the distribution of pore sizes has been found to be significant [201–203]. We can encode a granular description of this information as a 3D spatial grid containing the signed distance at each cell center to the nearest electrode surface as seen in [Figure 4.14](#). By using 3D features aligned to the electrode geometry, we can take advantage of a rich literature of convolutional neural network (CNN) architectures and software libraries to predict scalar fields (e.g. state of charge) or vector fields (e.g. fluid velocity). We can leverage existing machine learning frameworks [204–206], supported by large-scale datasets generated from physical simulations, to develop benchmark datasets for simulated operating electrodes. We can train and validate these models on synthetic data sets containing the output of our digital twin run on a diverse collection of geometries. One example of how we might generate random but relevant geometries is work done by Rycroft group alumna Xiaoxiao (Catherine) Ding [207].

A further line of inquiry is to generalize and extend the idea of the mass transfer coefficient. At the porous electrode-electrolyte interface, the flux of an electroactive species j_{in} is commonly modeled

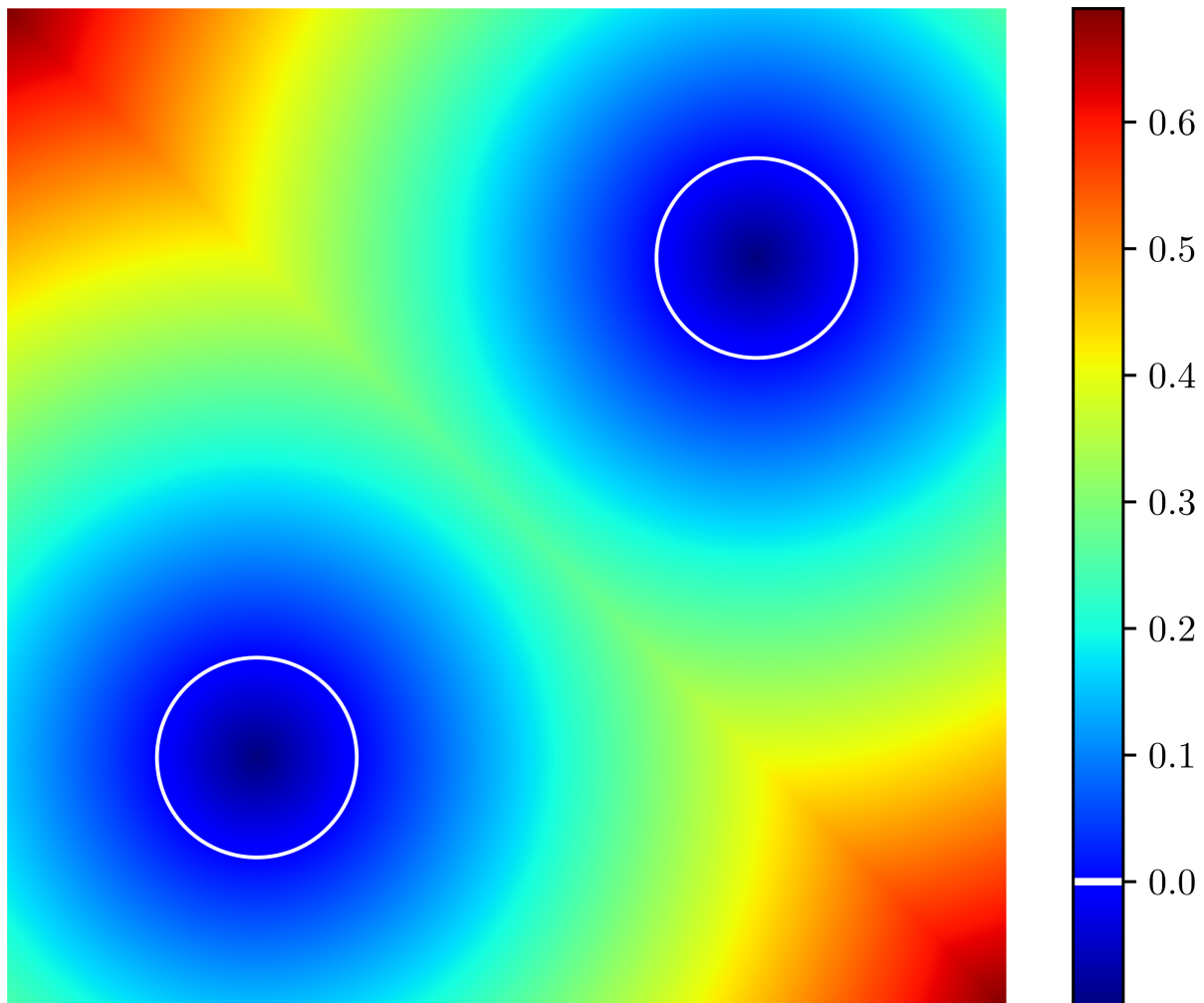


Figure 4.14: Signed distance to the nearest electrode surface in a 2D geometry. The surfaces of two circular conducting filaments are shown in white. The scale bar at right indicates signed distance in the electrolyte to the nearest electrode surface, with negative values indicating the electrode interior. Distance is in dimensionless units; the radius of the circles was set to 0.1 units.

through a mass transfer coefficient k_m , which is defined as the ratio of average diffusive flux at the electrode surface to the average concentration difference between the surface and the bulk electrolyte accord-

ing to [208, Eq. 22.45],

$$j_{\text{in}} = k_m(c_s - c_b), \quad (4.21)$$

where c_s and c_b are the concentrations on the surface and in the bulk, respectively. k_m has units of $\text{m} \cdot \text{s}^{-1}$ and can be thought of as an effective diffusivity divided by an effective diffusive boundary layer thickness. Wilson and Geankopolis [209] measured the mass transfer coefficient of a packed bed of benzoic acid spheres under a range of Schmidt and Reynolds numbers to find an empirical correlation; their correlation was amended by Darling and Perry [210] for cylindrical fibers to

$$k_m = \frac{0.832 D^{2/3} |v|^{1/3}}{\varepsilon d_p^{2/3}}, \quad (4.22)$$

where D is the diffusivity of the reacting species, ε is the porosity, $|v|$ is the magnitude of the volume-averaged velocity, and d_p is the fiber diameter. The correlation assumes a constant and species-independent diffusivity, so k_m is not a function of the concentration of oxidized or reduced species.

The most developed models to date incorporate a mass transfer coefficient that is a function of an average characteristic feature size and porosity, typically in a formalism qualitatively similar to Eq. (4.22). These models, however, do not incorporate the potentially significant impact of real porous electrode architecture, including distributions of local fluid velocities, diffusion lengths, and pore sizes; this limits their efficacy to an unknown extent. In contrast to this approach, our pore scale model uses a rate constant k_0 that is a material property with a strong justification in Butler-Volmer theory, and the empirical k_m of an arbitrary electrode is an emergent, potentially position-dependent property that we can evaluate.

A proposed research direction is to perform detailed tests of existing models based on mass transport coefficients against our digital twin. If this comparison finds the current crop of models wanting, we can develop improvements. For example, we can predict a 3D map of the mass transport coefficient by examining nearby microstructural features. We may also develop ML models to predict the local k_m by analyzing the local geometry. This could lead to a “drop-in replacement” for existing Newman-style models in which an empirical k_m predicted by Eq. (4.22) is replaced by the k_m predicted by an ML model.

For my final proposed research direction, I will introduce a completely new idea: spectral methods for solving the steady state velocity field and state of charge for a porous electrode. The idea of the spectral method is to take a physical quantity of interest and expand it in terms of a basis of functions. If these functions are chosen strategically, a complex problem can simplify dramatically, and in extreme cases may become completely separable. The canonical example of this idea is Fourier analysis, in which choosing a basis of eigenfunctions for a relevant linear operator can transform the solution of a complex PDE into a trivial operation in the eigenbasis. The porous electrode problem is not as analytically tractable as the heat equation on a 1D rod, but the idea still applies. The second selection that must be made is a set of sample points at which the fields are evaluated and where the PDE should be nearly satisfied.

Suppose we choose a collection of basis functions $\{f_1, \dots, f_n\}$ and a collection of sample points $\{\mathbf{p}_1, \dots, \mathbf{p}_m\}$. We should choose C^2 basis functions (i.e. functions with continuous second derivatives) that we can evaluate efficiently at an arbitrary point. In this way, the result of a linear operator on the selected sample points can be written as a matrix vector product of the form \mathbf{Ax} where \mathbf{A} is an $m \times n$ matrix of weights

and A_{ij} is defined by the linear operator's action on the basis function f_j on sample point \mathbf{p}_i . We can define a scalar objective function that calculates the sum of squares error in how well the resultant fields satisfy the PDE. This objective will also include terms to measure how well the boundary conditions are satisfied. Using this structure, we can then reformulate the question of solving the steady fields as a least squares problem. In the expected case that $m \gg n$ (more sample points than basis functions), this will be an underdetermined least square problem that should be well conditioned and have a unique solution. The motivating idea is that with the correct choices of basis functions and sample points, we can capture the symmetries and structures inherent in the problem geometry, thereby allowing us to use a much smaller number of basis functions and sample points than the number of cells in a 3D geometry when using a finite volume method. A concrete suggestion for basis functions is Bessel functions with a matching symmetry type to relevant geometric features, e.g. spherical or cylindrical. For the sample points, I suggest a mixture of uniformly sampled points on the interior and points sampled uniformly on the boundary of each reactive surface to enforce flux equality constraints. Additional sample points should be introduced on surfaces with boundary conditions such as membranes and no-slip boundaries as required.

4.II PARTING THOUGHTS

My broad goals at the outset of this PhD program were to learn the most sophisticated methods in applied mathematics and scientific computing, and to use these tools to advance research in fields where they might help to solve pressing challenges. In this thesis I have reported on four scientific projects where

I made varying contributions in simulation and data analysis. Two projects were related to porous electrodes in flow batteries, a promising technology for energy storage that can help the world move to clean, intermittent, renewable energy sources such as solar and wind power. The other two were related to carbon capture and storage, a technology that is currently techno-economically infeasible at scale, but may hold the key for future generations to stabilize Earth's climate. In each of these topic areas, I presented one numerical simulation and one data analysis. All of this work was conducted either jointly with a team led by experimentalists, or as first author of a numerical work heavily influenced by the needs and finding of experimental science. I've closed with some high level suggestions for the scientific computing community and a roadmap for future research in porous electrodes. Taken in sum, this research program has included some strong and novel results, and demonstrates the value of applied mathematics when applied to topics in electrochemical systems and engineering.

“Only the penitent man will pass.”

Indiana Jones, *Indiana Jones and the Last Crusade* (first riddle)[†]

Andante

The musical score consists of two staves. The top staff is for the 'Commendatore' in bass clef, 2/4 time, and B-flat major. The lyrics are: 'Don Gio-van - ni! a ce-nar te - co m'in-vi - tas - ti, e son ve - nu - to;'. The bottom staff is for the 'Piano' in treble clef, 2/4 time, and B-flat major. The piano accompaniment features a steady eighth-note pattern. The score is set against a background of a white page with a light gray grid.

Wolfgang Amadeus Mozart, *Don Giovanni*, K. 527. Libretto by Lorenzo DaPonte.
Entrance of the Commendatore in the penultimate scene.

Afterword

I began my PhD in July 2020 and am defending my thesis in April 2025. My brief career as a scientist has been bookended by crises, beginning with Covid-19 lockdowns and ending in the midst of an unprecedented attack on science by the United States government [211, 212]. I have followed an unusual career path, returning to graduate school in my forties after a career in finance. A big part of my previous job as a fixed income portfolio manager was reading political news, and predicting both the policy actions of governments and choices of voters.² I believe this experience gives me a non-consensus perspective on the current existential threat faced by scientists, and indeed by science as an enterprise, that might be useful. So it is with some trepidation that I share a few opinions about this sorry state of affairs in American science, how we got here, and how we might get out of it.

Science has been a spectacularly successful endeavor for humanity. The scientific method has proved its value over centuries of inquiry [213]. Scientists, following a codified set of conventions and collab-

[†] While Indiana Jones (played by Harrison Ford) says this line of dialog in the film, he is reading aloud from the Grail Diary of his father, Dr. Henry Jones, Sr., played by Sean Connery.

² Both government policy choices and election outcomes can have powerful long term effects on macroeconomic conditions including interest rates and currency exchange rates.

inating internationally, have discovered the basic operation of nature to the profound benefit of every person living today. It is because of scientists that we understand the nature of matter [214], the behavior of electricity and magnetism [215], and how germs can make people sick [216]. To get a sense of what it would be like to live in a world without science, we need only read historical accounts of life in Europe before the scientific revolution. This was a time of plagues [217], famines [218], and primitive technologies requiring intensive labor to maintain subsistence food production [219]. These conditions, in turn, set the stage for unspeakable levels of violent conflict, often over land, livestock, and crops [220].

Today we live in a world of plenty where modern agricultural methods ensure that the world can easily produce enough food for everyone [221, 222].³ We enjoy houses that are warm in the winter [223] and cool in the summer [224], with indoor plumbing [225] and electric appliances [226]. We are vaccinated against illnesses that devastated earlier generations [227]. We travel in automobiles [228] and aircraft [229] over distances at great speeds that would have been inconceivable to our ancestors. We use computers [230] and mobile phones [231] powered by semiconductors [232] whose designs depend on understanding quantum mechanics [233]. Violent conflict between and within nation states has never been at a lower level [234], notwithstanding a few wars that are tragically grinding on at present. None of this would be possible without science [235].

Yet for all these advances, trust in science has declined markedly, and now reflects a bitter partisan polarization in which many people with conservative politics doubt science [236, 237]. The United

³The social challenge of distributing this food so that no person goes hungry has proven less tractable than the material challenge of abundant food production.

States federal government, long the leading supporter of science in the world, seems perversely inclined to dismantle one of its signature achievements, America's preeminent position in scientific research [238]. Abruptly cancelling research funding on a pretextual basis [239], terminating clinical trials before their completion [240], summarily rejecting (or retroactively cancelling) research programs because they use a forbidden word like "climate" [241], wholesale employment terminations of career scientists employed by the government [242], bans on publications by remaining government scientists [243] ...the list of recent government actions against science goes on, and it seems incomprehensible. How did we get here, and how do we get things back on track?

One contributor to the decline of trust in science in the US is a larger problem, the collapse of confidence in universities and higher education in this country [244, 245]. So much science is carried out at a small handful of the largest, wealthiest, and most prestigious research universities [246], that it is easy for many Americans to conflate science and elite universities altogether. For reasons that are widely commented upon more than they are understood, universities have fallen sharply in the esteem of American voters, with a political polarization parallel to that seen in views on science, with conservatives in particular turning against universities [247]⁴. Two causes of this deteriorating respect in universities, I think, include a political composition in the faculty that is considerably more liberal than the average American voter [248]⁵, and a pervasive sense that highly educated university graduates look down on others who

⁴In a nine year span from 2015 to 2024, the percentage of Americans with "a great deal" of confidence has declined from 57% to 36%, while the percentage with "very little or none" has increased from 10% to 32%.

⁵This observation about the political composition of the faculty is intended as an empirical explanation for politically polarized disaffection with universities, not a criticism or an allegation of political bias in faculty hiring decisions.

don't hold the same fancy degrees [249]. But I believe the most important driver has been the social construct of a "meritocracy" in which the lion's share of the high paying, high status jobs go increasingly to a small sliver of the population who graduate from a handful of elite institutions, and who often are the children of people who went to the same schools [250]. This dynamic has led to a wave of resentment against a privileged elite who are now perceived to have created a system that benefits them and their children, while leaving the rest of America behind [251].

I don't know how to solve this problem, but I argue it is important that scientists recognize that this is now one driving force for the crisis we are facing. Simply put, American taxpayers are not going to continue funding our research until our universities take steps to address their concerns. One important step in restoring the standing of American universities is for scientists to realize that this is our problem too, and that scientists who are tenured professors need to show up at faculty meetings and wrestle with these issues. A related claim: it is vital that universities take corrective actions on our own terms, rather than being coerced by the government. We will preserve more of our dignity and academic freedom this way; otherwise we will see repeats of the sad spectacle of Columbia University acceding to a public humiliation by the Trump administration to avoid the loss of \$400 million in science funding [252]⁶.

Scientists have a second problem separate from our attachment to universities. We have unwittingly traded our original role as the heralds of nature's truth, for a new role as policy advocates on topics touch-

⁶The Trump administration dictated a new set of university policies on protests and campus security, and demanded that the Middle Eastern studies department be reorganized. Columbia acceded to all of these demands after its federal science funds were terminated, getting in exchange from this concession not a restoration of the funds, but only the start of a dialog with the administration.

ing on science. It is natural and understandable that a scientist who studies an issue carefully might develop strong policy preferences about it. In recent decades, scientists have become much more publicly involved in political advocacy, and they are increasingly perceived (fairly or not) as a bloc that is always aligned with the American left [253]. It would not have taken a political theorist at the Institute of Politics to predict what happened next: conservatives have grown distrustful of scientists and now question our motives, methodology, conclusions, and our very integrity [254]. Decades of bipartisan consensus dating back to the 1940s that scientists were vital experts to inform government policies have given way to overt mutual animus between scientists and conservatives [255]. This topic has been long debated; Lackey [2007] provided a highly cited warning about scientific advocacy broadly aligned with my comments here [256]. A combination of personal experience speaking to scientists and reading news coverage of their public participation, as well as a broader literature search on political advocacy by scientists, suggests that many contemporary scientists disagree with Lackey and embrace political advocacy [257, 258].

I will illustrate these ideas about the tension between trust and advocacy by examining the issue of climate change.⁷ Scientists who study climate change have been increasingly vocal in their advocacy of policies such as carbon taxes, cap-and-trade programs, and support for renewable energy [259]. I am broadly sympathetic to this agenda. But in my opinion, it has been counterproductive for scientists themselves to also be advocates. The problem is that when scientists talk about climate policies, some voters might feel

⁷I think the most vivid demonstration of this tension is actually public advocacy by scientists supporting Covid-19 policies such as lockdowns and remote school in the name of science, but that topic remains highly contentious to this day, and would take this discussion too far afield, so I will keep to calmer waters.

they're being criticized and judged, and then close themselves off from the substance of the argument. I think it would be far better if Americans could decouple facts from policy recommendations. We ought to have a serious policy debate as a country about how much it's going to cost for us to face climate change, and who's going to pay for it. This argument should be founded on uncontroversial, shared facts—dare I call it the truth—that both sides accept, even if they disagree about the policy response. I think this ideal is a fair stylized description of the debate about climate policies during the second Bush administration. George W. Bush might have been a Texas oilman who kept the US out of the Kyoto Protocol to limit carbon emissions [260], but he also had a serious climate change policy centered on technological advancements [261] and never claimed that climate change was a hoax [262].

I urge scientists, and especially climate scientists, to take the difficult step to recuse themselves from the public policy debate about global warming. Many other educated people—including people with scientific training they got from scientists who are biting their tongues—can take up the mantle of advocacy. But only climate scientists can speak authoritatively about the latest findings and the implications if we carry on business as usual. In this way, the role of climate scientists may resemble the frustrating part played by the sovereign in a constitutional monarchy. To maintain the trust and confidence of British citizens of all political leanings, Queen Elizabeth II, like her predecessors, was well known to be aloof from the rough and tumble of British politics [263].

Heisenberg's uncertainty principle famously states that $\sigma_x \sigma_p \geq \hbar/2$, with σ_x and σ_p the standard deviations in the position and momentum, respectively, and \hbar the reduced Planck constant. I propose

an analogy: the scientific policy uncertainty principle. The formula is the same as for the real uncertainty principle, but this time σ_x is the the uncertainty of our fellow citizens in “the truth” (where we are), σ_p is their uncertainty in “what we should do” (where we’re going), and \hbar now reflects the amount of social distrust in society. The more we telegraph a preferred policy direction, the less confidence our listeners will have that we are telling the truth. And the tradeoff becomes exacerbated in periods of low social trust, when people who disagree are more likely to impute ill intentions to their opponents.

The last thing we must do is to repent of using an arrogant or condescending tone that some educated people including scientists have used when speaking to or about people who disagree with us [249]. Few rhetorical choices could be more inimical to the goal of regaining the trust of American voters than this kind of language. When speaking publicly as a scientist, we should take special care to convey respect for the values and intellect of people who disagree with us, without compromising on the substance of the scientific content we wish to convey. Instead of indulging in snarky online comments liked by people who already agree with us, let us instead devote ourselves to a harder labor. Let us listen to the concerns of Americans who have lost trust in science, and make them feel heard. And let us remember Planck’s principle:⁸ it may be impossible to win over many of our opponents. If we can’t persuade them to our side, we can at least speak respectfully to them and find a *modus vivendi*—perhaps scientists don’t pressure adults to get Covid or flu vaccines they distrust, and vaccine skeptics accept crucial childhood inocula-

⁸This was the epigraph that opened Chapter 1. “*A new scientific truth does not triumph by convincing its opponents and making them see the light, but rather because its opponents eventually die and a new generation grows up that is familiar with it.*” [58]

tions and back off cutting science funding. Keeping in mind the second part of Planck's principle about a new generation, we should work to improve science curricula in elementary and secondary schools so the next generation of voters is better educated about science and capable of making well informed policy choices. If scientists can join together in a spirit of humility and follow the program I have outlined in this Afterword, I am optimistic that we can regain the trust of American voters and restore America as a superb place do scientific research.

A

Supplementary Material for Chapter 1

Table A.1: Symbols Used

Symbol	Meaning	SI Units
ρ	Fluid density	$\text{kg} \cdot \text{m}^{-3}$
\mathbf{u}	Fluid velocity vector	$\text{m} \cdot \text{s}^{-1}$
(u, v, w)	x, y and z components of \mathbf{u}	$\text{m} \cdot \text{s}^{-1}$
p	Dynamic pressure (adjusted for gravity)	$\text{Pa} = \text{kg} \cdot \text{m}^{-1} \cdot \text{s}^{-2}$
g	Gravitational field	$\text{m} \cdot \text{s}^{-2}$
μ	Dynamic viscosity	$\text{Pa} \cdot \text{s} = \text{kg} \cdot \text{m}^{-1} \cdot \text{s}^{-1}$
κ	Hydraulic permeability of porous medium	m^2
Q	Volumetric flow rate through electrode	$\text{m}^3 \cdot \text{s}^{-1}$
L	Length of channel in flow direction	m
R_H	Hydraulic resistance of a porous medium	$\text{kg} \cdot \text{m}^{-4} \cdot \text{s}^{-1}$
Δt	Time step	s
C_{CFL}	CFL parameter	1

Continued on next page

Table A.1: Symbols Used (Continued)

Symbol	Meaning	SI Units
C_A	Inverse time step - advection	s^{-1}
C_V	Inverse time step - diffusion	s^{-1}
C_D	Inverse time step - external forces	s^{-1}
$\varepsilon_{\text{flow}}$	Convergence threshold - flow steady state	1
O	Generic oxidized species	1
R	Generic reduced species	1
n_e	Number of electrons transferred in PCET reaction	1
n_p	Number of protons transferred in PCET reaction	1
E°	Equilibrium interfacial potential - standard conditions	V
E_{eq}	Equilibrium interfacial potential - nonstandard conditions	V
R	Ideal gas constant	$\text{J} \cdot \text{mol}^{-1} \cdot \text{K}^{-1}$
T	Temperature in Kelvin	K
C_O	Concentration of oxidized species	$\text{mol} \cdot \text{m}^{-3}$
C_R	Concentration of reduced species	$\text{mol} \cdot \text{m}^{-3}$
C_T	Total concentration of electroactive species	$\text{mol} \cdot \text{m}^{-3}$
c_0	Initial total concentration of electroactive species, a constant	$\text{mol} \cdot \text{m}^{-3}$
ϕ_s	Potential in the solid electrode	V
ϕ_L	Potential in the electrolyte	V
η_{act}	Activation overpotential	V
s	State of charge	1
F	Faraday's constant	$\text{C} \cdot \text{mol}^{-1}$
j_0	Exchange current density in Butler-Volmer model	$\text{A} \cdot \text{m}^{-2}$

Continued on next page

Table A.1: Symbols Used (Continued)

Symbol	Meaning	SI Units
j	Current density in Butler-Volmer model	$\text{A} \cdot \text{m}^{-2}$
k_0	Kinetic rate constant in Butler-Volmer model	$\text{m} \cdot \text{s}^{-1}$
A	Area of solid / liquid boundary in one cut cell	m^2
V	Volume of electrolyte in one cell (regular or cut)	m^3
a	Specific area of a cut cell	m^{-1}
α	Charge transfer coefficient in Butler-Volmer model	1
V_T	Thermal voltage	V
S	Chemical source term - entire reaction	$\text{mol} \cdot \text{m}^{-3} \cdot \text{s}^{-1}$
n_k	Stoichiometric number for k -th species	1
S_k	Chemical source term for k -th species	$\text{mol} \cdot \text{m}^{-3} \cdot \text{s}^{-1}$
$\tilde{\eta}$	Nondimensionalized reducing overpotential	1
\tilde{S}	Nondimensionalized source term for SOC	1
D_j	Diffusivity of j -th species	$\text{m}^2 \cdot \text{s}^{-1}$
z_j	Signed charge number of j -th species	1
κ_L	Ionic conductivity of the electrolyte	$\text{kg}^{-1} \cdot \text{m}^{-3} \cdot \text{s}^3 \cdot \text{C}^2$
S_ϕ	Electron source term	$\text{m}^{-3} \cdot \text{s}^{-1} \cdot \text{C}$
V_{ar}	Applied reducing potential	V
\hat{n}	Normal vector at electrode boundary	1
s_{eq}	Equilibrium state of charge at an applied potential	1
\tilde{V}_{ar}	Nondimensionalized applied reducing potential	1
$\tilde{\phi}_L$	Nondimensionalized potential in the electrolyte	1
$\sigma(x)$	Sigmoid function $\sigma(x) = (1 + e^{-x})^{-1} = \text{logit}^{-1}(x)$	1

Continued on next page

Table A.1: Symbols Used (Continued)

Symbol	Meaning	SI Units
τ	Mean time for fluid to traverse the electrode	s
ε_s	Convergence threshold - reaction SOC change	1
ε_ϕ	Convergence threshold - reaction potential change	1
ε_I	Convergence threshold - total current vs. charge flow	1
$\ \Delta\ $	Root mean square $\ \Delta\ _2/\sqrt{N}$	1
θ_{mrc}	Maximum reactant consumption parameter	1
\mathcal{F}	Flow of charge in electrolyte - inlet, outlet or net	A
I_{tot}	Total current on the electrode surface	A

Table A.2: Simulation Parameters

Symbol	Value	SI Units	Source
ρ	997.0479	$\text{kg} \cdot \text{m}^{-3}$	[41, 264]
μ	8.8891×10^{-4}	$\text{kg} \cdot \text{m}^{-1} \cdot \text{s}^{-2}$	[41, 265]
D_{AQDS}	4×10^{-10}	$\text{m}^2 \cdot \text{s}^{-1}$	[41, 61]
$D_{\text{H}_2\text{AQDS}}$	4×10^{-10}	$\text{m}^2 \cdot \text{s}^{-1}$	[41, 61]
D_{H^+}	9.3×10^{-9}	$\text{m}^2 \cdot \text{s}^{-1}$	[41]
$D_{\text{H}_2^+}$	1.38×10^{-9}	$\text{m}^2 \cdot \text{s}^{-1}$	[41]
k_0	7.2×10^{-5}	$\text{m} \cdot \text{s}^{-1}$	[41, 61]
α	0.5	1	[41, 61]
s_{in}	1.73×10^{-7}	1	†
c_0	2.0×10^{-2}	$\text{mol} \cdot \text{m}^{-3}$	NA - operating condition
p_{in}	various	$\text{kg} \cdot \text{m}^{-1} \cdot \text{s}^{-2}$	NA - operating condition

† Based on unpublished experiments of open circuit voltage in a full cell and inverting the Nernst equation with 200 mV of potential vs. standard conditions. Results are not sensitive to this as long it's near zero; a value of exactly zero is unphysical and causes the Nernst equation to blow up.

B

Supplementary Material for Chapter 2

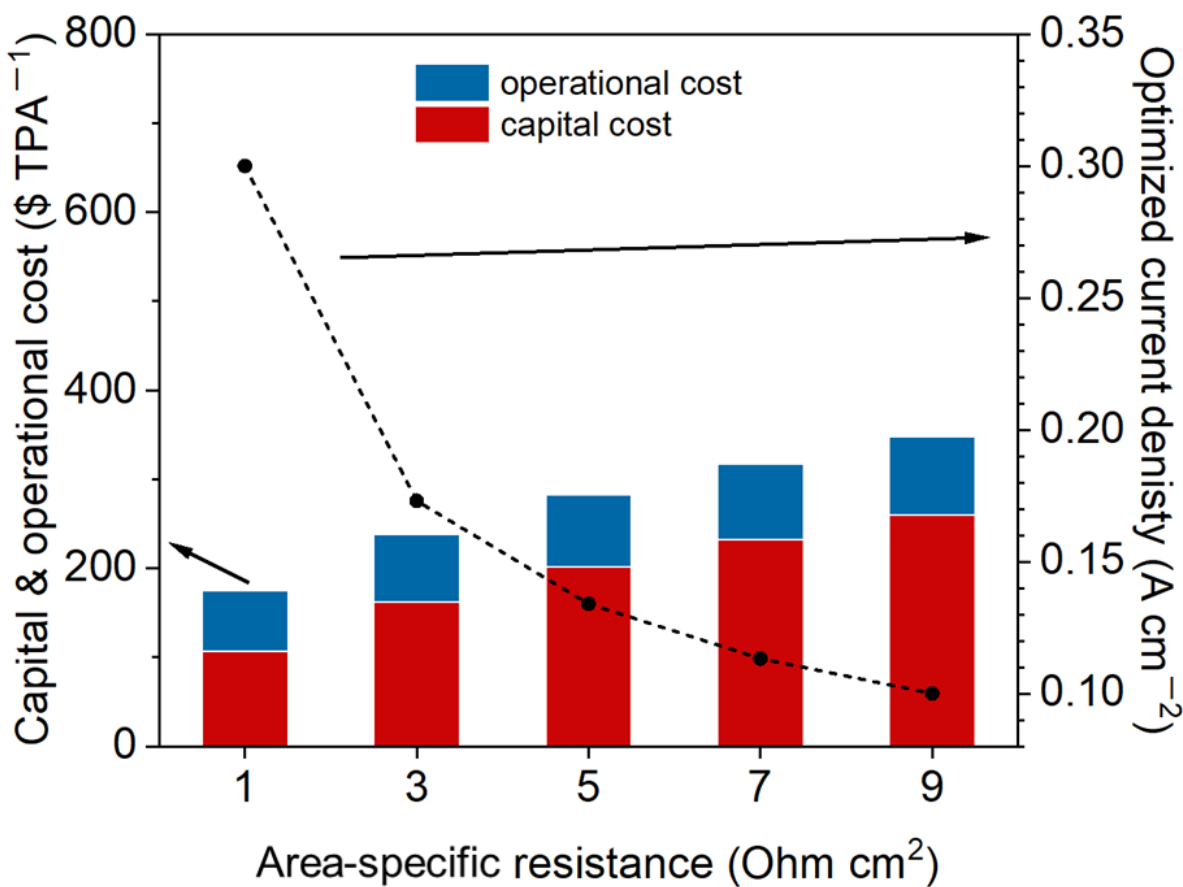


Figure B.1: Increased capital and operating costs with higher area-specific resistance. The capital and operating costs of an electrochemical cell increase with area-specific resistance. With the current density optimized to maximize the net present value (NPV), a higher area-specific resistance will decrease the optimal current density. With a fixed requirement for production capacity, this will in turn require a higher cell area and a larger physical plant, leading to higher capital costs. The operating costs also increase due to larger voltage losses at a given current density according to Ohm's law.

Because pH equals $-\log([H^+])$, we calculate the concentration of protons as 10^{-pH} . The concentration of OH⁻ can be calculated as 10^{14-pH} . The amount of OH⁻ in the solution is $V \cdot 10^{14-pH}$, where V is the volume of the anolyte. Then the amount of OH⁻ is normalized by the cell area to compute a time

Method	Energy Consumption (kJ/mol charge)	Current Efficiency (%)	Note
Solid-electrolyte reactor, CEM-AEM (O_2 looping) [47]	140 (200 $\text{mA} \cdot \text{cm}^{-2}$) 220 (200 $\text{mA} \cdot \text{cm}^{-2}$)	$\sim 80\%$ (6000 ppm CO_2 , 20 $\text{mA} \cdot \text{cm}^{-2}$) $\sim 40\%$ (400 ppm CO_2 , 3 $\text{mA} \cdot \text{cm}^{-2}$)	Coupled oxygen reduction (base generation) and CO_2 capture. CO_2 absorption reaction kinetic limits the current density and efficiency.
Solid-electrolyte reactor, CEM-CEM (H_2 looping) [124]	95 (20 $\text{mA} \cdot \text{cm}^{-2}$) 207 (200 $\text{mA} \cdot \text{cm}^{-2}$)	90% – 98%	CO_2 outgas in the center chamber. Bubble formation in the center can interfere with performance if scaled up.
Salt splitting, CEM-AEM (water splitting) [117, 266]	> 240 (20 $\text{mA} \cdot \text{cm}^{-2}$) > 235 (200 $\text{mA} \cdot \text{cm}^{-2}$)	$\sim 65\%$	Energy consuming. Low efficiency.
Alternating electrolysis (H_2 looping, I_2 mediating) [45]	140 (100 $\text{mA} \cdot \text{cm}^{-2}$)	Not available.	Requires Li, iodide, and alternative electrolysis management.
BPM salt splitting, CEM-BPM-CEM (ferro-ferricyanide looping) [46]	> 150 (50 $\text{mA} \cdot \text{cm}^{-2}$) > 200 (10 $\text{mA} \cdot \text{cm}^{-2}$)	$\sim 70\%$	High resistance, low current density, high energy cost, bubble formation in the center chamber.
Salt splitting, AEM-CEM (H_2 looping) [122]	~ 100 (10 $\text{mA} \cdot \text{cm}^{-2}$)	Not available	Strong acid formation, limited current efficiency
CEM-CEM (H_2 looping) [48, 123]	> 100 (10 $\text{mA} \cdot \text{cm}^{-2}$)	$> 90\%$	High resistance, low current density, high energy cost, bubble formation in center chamber.
Salt splitting, AEM-CEM (water splitting)[128]	~ 250 (6 $\text{mA} \cdot \text{cm}^{-2}$)	Not available	Green $\text{Ca}(\text{OH})_2$, high resistance, low current density, high energy cost, solid formation in the cell.
GDE-AEM-GDE (H_2 looping) [267]	~ 140 (10 $\text{mA} \cdot \text{cm}^{-2}$) ~ 180 (20 $\text{mA} \cdot \text{cm}^{-2}$)	$\sim 50\%$	High resistance, bubble formation in the center.
This work	100 (20 $\text{mA} \cdot \text{cm}^{-2}$) 240 (200 $\text{mA} \cdot \text{cm}^{-2}$)	$> 94\%$	Decoupled acid-base generation with relatively low energy cost. Adjustable accumulated concentration of generated acid-base. Suitable for carbon capture, green $\text{Ca}(\text{OH})_2$ production. Compatible with intermittent sources.

Table B.1: Comparison between electrochemical acid-base generators.

integrated flux. [Figure A.3](#) is derived accordingly using data in [Figure A.2](#). Through linear fitting, we calculated the slope of the normalized amount of OH^- for each experiment. The crossover flux is the slope of this line, because the y -axis is a time-integrated flux and the x axis is time. The linear fitting

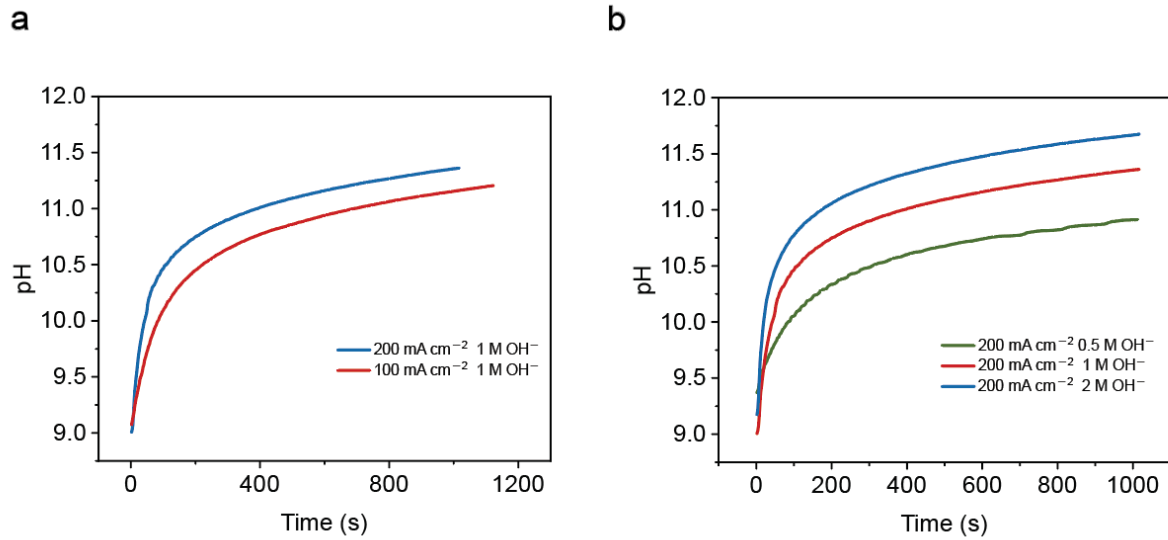


Figure B.2: *In-situ* pH change of the anolyte during hydroxide ion crossover test. **a**, pH changes in the anode side under various current densities with 1M NaOH in the cathode. **b**, pH changes in the anode side under various concentrations of NaOH in the cathode side when applying a current density of $200 \text{ mA} \cdot \text{cm}^{-2}$.

	Exp. 1	Exp. 2	Exp. 3	Exp. 4	Exp. 5	Exp. 6
Current Density (mA · cm ⁻²)	200	200	200	100	100	100
NaOH Concentration in catholyte (mol · L ⁻¹)	0.5	1.0	2.0	0.5	1.0	2.0

Table B.2: Experimental conditions used for hydroxide ion crossover tests.

functions are listed in [Table A.3](#).

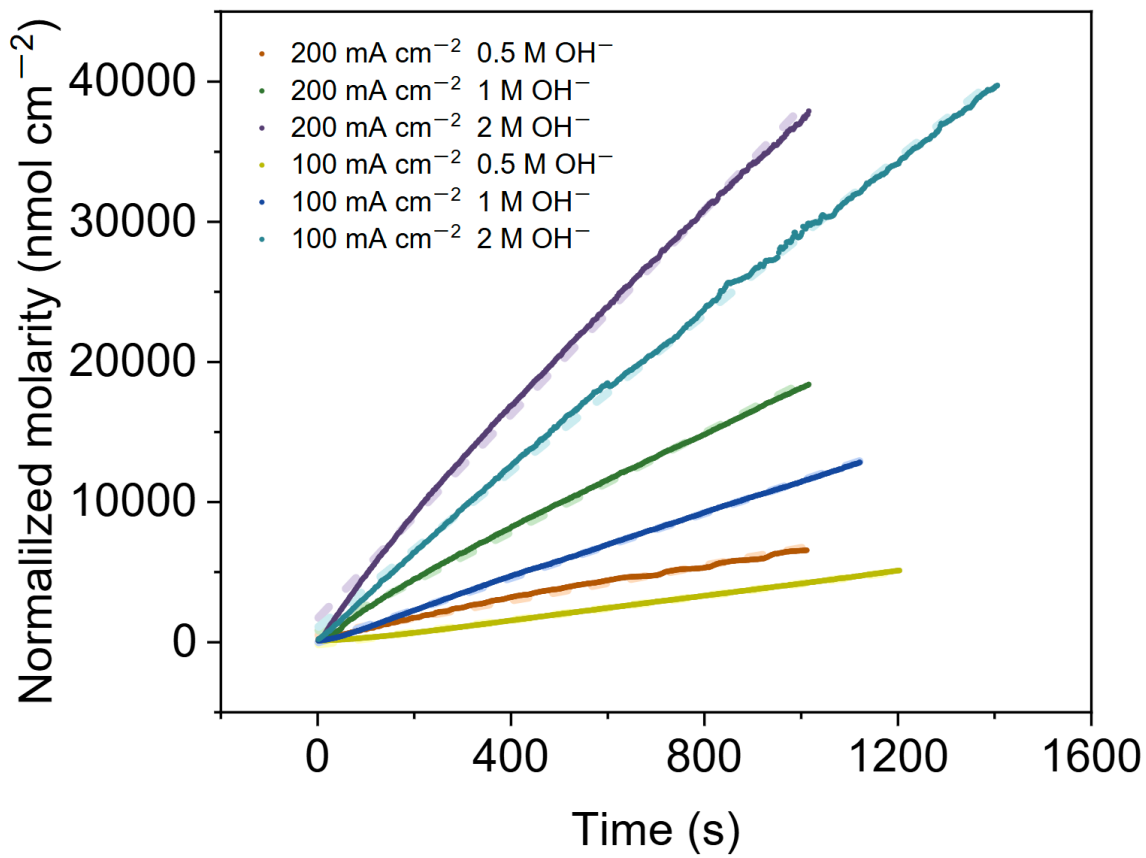


Figure B.3: Area normalized molarity of hydroxide ions in the anolyte (acceptor side) over time during hydroxide crossover test. Dashed lines are the linear fitting curves of the corresponding data.

Parameters (current density / NaOH concentration)	Function	R^2
$200 \text{ mA} \cdot \text{cm}^{-2} / 0.5 \text{ mol} \cdot \text{L}^{-1}$	$y = 6.219x + 495.9$	0.99167
$200 \text{ mA} \cdot \text{cm}^{-2} / 1.0 \text{ mol} \cdot \text{L}^{-1}$	$y = 17.64x + 814.0$	0.99703
$200 \text{ mA} \cdot \text{cm}^{-2} / 2.0 \text{ mol} \cdot \text{L}^{-1}$	$y = 36.44x + 1675$	0.99715
$100 \text{ mA} \cdot \text{cm}^{-2} / 0.5 \text{ mol} \cdot \text{L}^{-1}$	$y = 4.332x - 160.2$	0.99902
$100 \text{ mA} \cdot \text{cm}^{-2} / 1.0 \text{ mol} \cdot \text{L}^{-1}$	$y = 11.52x - 14.27$	0.99961
$100 \text{ mA} \cdot \text{cm}^{-2} / 2.0 \text{ mol} \cdot \text{L}^{-1}$	$y = 27.94x + 1037$	0.99865

Table B.3: Linear fitting results for hydroxide ion crossover tests.

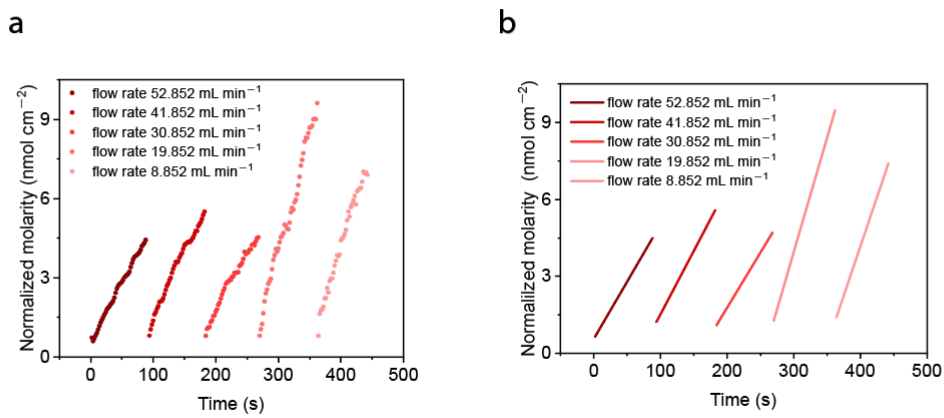


Figure B.4: Area normalized molarity of protons in the catholyte (acceptor side) over time during proton crossover test with various center flow rates. The current density used for the tests was $200 \text{ mA} \cdot \text{cm}^{-2}$ with 2M NaOAc cycled in the center chamber. **a**, Experimental data of area normalized molarity of protons in the catholyte (acceptor side) over time. **b**, Linear fitting curves of the corresponding experimental data.

Flow rate (ml · min⁻¹)	Function	R^2
52.852	$y = 0.04458x + 0.57093$	0.99542
41.852	$y = 0.04943x - 3.41741$	0.99247
30.852	$y = 0.04301x - 6.82107$	0.99268
19.852	$y = 0.08912x - 22.77862$	0.99476
8.852	$y = 0.07687x - 26.57269$	0.99757

Table B.4: Linear fitting results for proton crossover tests with various center flow rates.

C

Musical Epigraphs

Here is a brief explanation of the musical excerpts included in this thesis. These excerpts were chosen both because they had a connection to the content of each epigraph, and also because they are among my very favorite pieces of music.

- The musical dedication comes from the end of the Beatles song “In My Life” and lines up with the lyrics at the end of the song, “In my life / I’ve loved you more,” followed by the coda. The music and lyrics are by John Lennon and Paul McCartney. John Lennon called this song his “first real major piece of work.” It’s always been a sentimental favorite of mine.
- The musical quote in the Foreword is taken from Leporello’s aria “Madamina, il catalogo è questo” [My dear lady, this is the list] from Mozart’s opera *Don Giovanni* with libretto by Lorenzo Da Ponte, K. 527. While this aria is often called “the” catalog aria, it is a stock type of aria that appears commonly in Italian comic operas of the time period [268]. I selected this quote because this PhD thesis, like so many, is essentially a compilation or catalog of the author’s “scientific conquests,” such as they are.
- The musical quote in the Introduction is from the last movement of Beethoven’s majestic ninth symphony (*The Choral Symphony*) in D minor, op. 125, in which the chorus sings the “Ode to Joy” by Friedrich Schiller. It pairs with the inspiring quote from Michael Faraday that “Nothing is too wonderful to be true, if it be consistent with the laws of nature...”

- The musical quote opening Chapter 1 comes from Siegfried’s funeral in *Götterdämmerung* [Twilight of the Gods], the last opera in Richard Wagner’s *Der Ring des Nibelungen* [The Ring of the Nibelung] (WWV 86D). It pairs with the quote from Max Planck, which is often shortened to “science advances one funeral at a time.”
- The musical quote opening Chapter 2 is the Marche funèbre (Funeral march) from Frederic Chopin’s Piano Sonata No. 2 in B \flat minor, Opus 35. It pairs with Walther Nernst’s quote that “knowledge is the death of research.”
- The musical quote opening Chapter 3 is Bach’s *Chromatic Fantasia and Fugue* in D minor, BWV 903. It pairs with my father’s quote that “everything is easy when you know how to do it” via the film *Five Easy Pieces*. It’s the second of the five “easy” pieces in the film, and is played by Bobby’s sister Partita in a recording studio for an album she is making.
- The musical quote opening Chapter 4 is the leitmotif of Valhalla, the heavenly home of the gods in The Ring of the Nibelung (WWV 86A). It’s taken from the wonderful piano arrangement by Franz Liszt (S. 449). Valhalla was built for Wotan by the giants Fafner and Fasolt. It pairs with Newton’s quote that he “has stood on the shoulders of giants” if you think about it metaphorically.
- The musical quote opening the Conclusion is the opening to the slow second movement of Beethoven’s seventh symphony, Opus 92, in A major. It has a somber, haunting melody that pairs with Volta’s quote, “You must be ready to give up even the most attractive ideas when experiment shows them to be wrong.”
- The musical quote opening the Afterword also comes from Don Giovanni. This time, I excerpt from the end of the opera, when the ghost of the Commendatore comes to dinner in the form of a marble statue. The Commendatore has come to bring Don Giovanni to justice for his many crimes. He gives the Don a final chance to repent, but the Don refuses and is dragged off to hell (or at least the basement of the Metropolitan opera). Thus, this quote pairs with the epigraph “Only the penitent man will pass.”

I would like to take this opportunity to thank my brother Samuel Emanuel and my old friend Kivie Cahn-Lipman for their assistance in selecting and engraving these musical epigraphs.

D

Youthful Epigraphs

I have been blessed with tremendous support from my family on my journey through graduate school. In recognition of this support, I have dedicated this thesis to my wife Christie. My three children assisted me in selecting the epigraphs. They lobbied for oft-repeated quotes in our household to appear, a proposal I ultimately rejected. As a consolation prize, I promised each of them one quote in this appendix.

“More ice cubes!”

—Victor M. Emanuel

“I am *not* starting a kerfuffle!”

—Renée E. Emanuel

“Daddy, you ate my pizza!”

—Ruth F. Emanuel

As a special bonus, I am including an all time favorite quote over multiple generations of my family:

“Let’s roll it back!”

—Steven L. Emanuel

Statement on the Use of Artificial Intelligence

I made no use of generative artificial intelligence (AI) in the preparation of this thesis. I typed all the words that I claim to have written, without *any* use of any AI service such as Chat-GPT or its ilk. Much of the text in this thesis was excerpted from published works that were initially drafted by other authors. I provided detailed footnotes at the start of each chapter to clearly delineate my contributions to these published works, and explicitly enumerated the chapters I drafted myself from scratch as compared to the chapters I took from the published works. When I used text from other authors, I was actively involved in the revision process; carefully read all text in multiple drafts before publication; and hand typed all quoted text myself while typesetting it in L^AT_EX for this thesis.

I was the first author on the manuscript incorporated in Chapter 1, and generative AI was used at no point in its preparation. I believe some use of AI enabled translation was made in the original drafting of the manuscript incorporated in Chapter 2; this was subsequently extensively rewritten into idiomatic English by coauthors including me. My understanding from my coauthors is that AI was not used at all in the production of the articles incorporated in Chapters 3 and 4. I also wrote the entirety of the Abstract, Dedication, Acknowledgments, Introduction, and Conclusion in my own words without any use of AI tools.

Bibliography

- [1] M. S. Emanuel and C. H. Rycroft, *Digital Twin for Porous Electrodes in Redox Flow Batteries*, arXiv, preprint (2025).
- [2] D. Xi, Z. Yang, M. S. Emanuel, P. Zhao, and M. J. Aziz, *Electrochemical Acid-Base Generators for Decoupled Carbon Management*, Energy & Environmental Science **n/a**, n/a (2025).
- [3] R. Mander, *The Wagner Companion* (Hawthorn Books, 1978).
- [4] R. Osborne, “Cenerentola, la,” *New Grove Dictionary of Music and Musicians* (Oxford University Press, 2002).
- [5] K. Caldeira and M. E. Wickett, *Anthropogenic carbon and ocean ph*, Nature **425**, 365–365 (2003).
- [6] K. Amini, T. Cochard, Y. Jing, J. D. Sosa, D. Xi, M. Alberts, M. S. Emanuel, E. F. Kerr, R. G. Gordon, and M. J. Aziz, *In situ techniques for aqueous quinone-mediated electrochemical carbon capture and release*, Nature Chemical Engineering **1**, 774–786 (2024).
- [7] A. M. Graf, T. Cochard, K. Amini, M. S. Emanuel, S. M. Rubinstein, and M. J. Aziz, *Quantitative Local State of Charge Mapping by Operando Electrochemical Fluorescence Microscopy in Porous Electrodes*, Energy Advances **3**, 2468–2478 (2024).
- [8] J. Rising, M. Tedesco, F. Piontek, and D. A. Stainforth, *The Missing Risks of Climate Change*, Nature (London) **610**, 643–651 (2022).
- [9] S. Jenkins, A. Povey, A. Gettelman, R. Grainger, P. Stier, and M. Allen, *Is Anthropogenic Global Warming Accelerating?* Journal of Climate **35**, 7873 –7890 (2022).
- [10] J. E. Hansen, P. Kharecha, M. Sato, G. Tselioudis, J. Kelly, S. E. Bauer, R. Ruedy, E. Jeong, Q. Jin, E. Rignot, I. Velicogna, M. R. Schoeberl, K. von Schuckmann, J. Amponsem, J. Cao, A. Keskinen, J. Li, and A. P. and, *Global Warming Has Accelerated: Are the United Nations and the Public Well-Informed?* Environment: Science and Policy for Sustainable Development **67**, 6–44 (2025).
- [11] D. J. Trump, *Putting America First in International Environmental Agreements*, 2025.

- [12] N. Scafetta, *Impacts and Risks of “Realistic” Global Warming Projections for the 21st Century*, Geoscience Frontiers **15**, 101774 (2024).
- [13] T. M. Lenton, C. Xu, J. F. Abrams, A. Ghadiali, S. Loriani, B. Sakschewski, C. Zimm, K. L. Ebi, R. R. Dunn, J.-C. Svenning, et al., *Quantifying the Human Cost of Global Warming*, Nature Sustainability **6**, 1237–1247 (2023).
- [14] Arndt, Channing and Miller, Mackay and Tarp, Finn and Zinaman, Owen and Arent, Douglas, *The Political Economy of Clean Energy Transitions* (Oxford University Press, 2017).
- [15] N. Kittner, F. Lill, and D. M. Kammen, *Energy Storage Deployment and Innovation for the Clean Energy Transition*, Nature Energy **2**, 17125 (2017).
- [16] A. Gallo, J. Simões-Moreira, H. Costa, M. Santos, and E. Moutinho dos Santos, *Energy storage in the energy transition context: A technology review*, Renewable & Sustainable Energy Reviews **65**, 800–822 (2016).
- [17] T. M. Gür, *Review of Electrical Energy Storage Technologies, Materials and Systems: Challenges and Prospects for Large-Scale Grid Storage*, Energy & Environmental Science **11**, 2696–2767 (2018).
- [18] L. F. Arenas, C. Ponce de León, and F. C. Walsh, *Redox Flow Batteries for Energy Storage: Their Promise, Achievements and Challenges*, Current Opinion in Electrochemistry **16**, 117–126 (2019).
- [19] D. L. Coleman, *Transport Infrastructure Rationale for Carbon Dioxide Capture & Storage in the European Union to 2050*, Energy Procedia **1**, 1673–1681 (2009).
- [20] K. Mintz-Woo and J. Lane, *Why and Where to Fund Carbon Capture and Storage*, Science and Engineering Ethics **27**, 70 (2021).
- [21] H. B. Jones, *The life and letters of faraday: by henry bence jones. in 2 volumes.[michael faraday]. i* (Longmans, Green, and Company, 1870).
- [22] J. S. Newman and C. W. Tobias, *Theoretical Analysis of Current Distribution in Porous Electrodes*, Journal of The Electrochemical Society **109**, 1183 (1962).
- [23] J. Newman and W. Tiedemann, *Porous-Electrode Theory with Battery Applications*, AIChE journal **21**, 25–41 (1975).
- [24] R. B. Smith and M. Z. Bazant, *Multiphase Porous Electrode Theory*, Journal of The Electrochemical Society **164**, E3291 (2017).

- [25] A. A. Wong, S. M. Rubinstein, and M. J. Aziz, *Direct Visualization of Electrochemical Reactions and Heterogeneous Transport Within Porous Electrodes in Operando by Fluorescence Microscopy*, *Cell Reports Physical Science* **2**, 100388 (2021).
- [26] I Chatzis and F. A. Dullien, *The Modeling of Mercury Porosimetry and the Relative Permeability of Mercury in Sandstones Using Percolation Theory*, *Int. Chem. Eng.*; (United States) **25:1** (1985).
- [27] R. Larson, L. Scriven, and H. Davis, *Percolation Theory of Two Phase Flow in Porous Media*, *Chemical engineering science* **36**, 57–73 (1981).
- [28] M. M. Dias and A. C. Payatakes, *Network Models for Two-Phase Flow in Porous Media Part 1. Immiscible Microdisplacement of Non-Wetting Fluids*, *Journal of Fluid Mechanics* **164**, 305–336 (1986).
- [29] J. Gostick, A. Burns, W. Lehnert, A. Putz, M. Aghighi, J. Hinebaugh, T. Tranter, M. A. Hoeh, H. Day, B. Spellacy, M. H. Sharqawy, and A. Bazylak, *OpenPNM: a pore network modeling package*, *Computing in science & engineering* **18**, 60–74 (2016).
- [30] M. van der Heijden, R. van Gorp, M. A. Sadeghi, J. Gostick, and A. Forner-Cuenca, *Assessing the Versatility and Robustness of Pore Network Modeling to Simulate Redox Flow Battery Electrode Performance*, *Journal of the Electrochemical Society* **169**, 40505 (2022).
- [31] M. van der Heijden, G. Szendrei, V. de Haas, and A. Forner-Cuenca, *A Versatile Optimization Framework for Porous Electrode Design*, *Digital discovery* **3**, 1292–137 (2024).
- [32] D. Zhang, A. Forner-Cuenca, O. O. Taiwo, V. Yufit, F. R. Brushett, N. P. Brandon, S. Gu, and Q. Cai, *Understanding the Role of the Porous Electrode Microstructure in Redox Flow Battery Performance Using an Experimentally Validated 3D Pore-Scale Lattice Boltzmann Model*, *Journal of power sources* **447**, 227249 (2020).
- [33] A. Xu, W. Shyy, and T. Zhao, *Lattice Boltzmann Modeling of Transport Phenomena in Fuel Cells and Flow Batteries*, *Acta Mechanica Sinica* **33**, 555–574 (2017).
- [34] J. Yu, M. Duquesnoy, C. Liu, and A. A. Franco, *Optimization of the microstructure of carbon felt electrodes by applying the lattice Boltzmann method and Bayesian optimizer*, *Journal of Power Sources* **575**, 233182 (2023).
- [35] Y. Sun and C. H. Rycroft, *A Fully-Integrated Lattice Boltzmann Method for Fluid–Structure Interaction*, *Journal of Computational Physics* **526**, 113774 (2025).

- [36] D. M. Barber, S. Edgar, M. S. Emanuel, M. D. Nelwood, B. Y. Ahn, B. Román-Manso, T. Cochard, J. Platero, K. Amini, C. H. Rycroft, S. Rubinstein, and J. Lewis, *Print-and-plate architected electrodes for electrochemical transformations under flow*, *Advanced Functional Materials* **n/a**, 2419748 (2024).
- [37] COMSOL Inc., *COMSOL*, 2020.
- [38] K. M. Lee, M. Alizadeh, T. Suzuki, S. Tsushima, E. P. L. Roberts, and J. T. Gostick, *Multiphysics Simulation of Multi-layered Fibrous Electrodes for the Vanadium Redox Flow Battery*, *Journal of the Electrochemical Society* **171**, 90534 (2024).
- [39] T. Y. Lin, S. E. Baker, E. B. Duoss, and V. A. Beck, *Topology Optimization of 3D Flow Fields for Flow Batteries*, *Journal of the Electrochemical Society* **169**, 50540 (2022).
- [40] V. A. Beck, J. J. Wong, C. F. Jekel, D. A. Tortorelli, S. E. Baker, E. B. Duoss, and M. A. Worsley, *Computational Design of Microarchitected Porous Electrodes for Redox Flow Batteries*, *Journal of power sources* **512**, 230453 (2021).
- [41] S. Dussi and C. H. Rycroft, *Less Can Be More: Insights on the Role of Electrode Microstructure in Redox Flow Batteries From Two-Dimensional Direct Numerical Simulations*, *Physics of Fluids* **34**, 043111 (2022).
- [42] Z. Yan, R. J. Wycisk, A. S. Metlay, L. Xiao, Y. Yoon, P. N. Pintauro, and T. E. Mallouk, *High-Voltage Aqueous Redox Flow Batteries Enabled by Catalyzed Water Dissociation and Acid–Base Neutralization in Bipolar Membranes*, *ACS Central Science* **7**, 1028–1035 (2021).
- [43] G. Liu, A. Yang, and R. C. Darton, *Numerical Modeling and Comparative Analysis of Electrolysis and Electrodialysis Systems for Direct Air Capture*, *ACS Sustainable Chemistry & Engineering* **12**, 3951–3965 (2024).
- [44] M. Dumortier, T. Bosserez, J. Rongé, J. A. Martens, and S. Haussener, *Combined Experimental-Numerical Analysis of Transient Phenomena in a Photoelectrochemical Water Splitting Cell*, *The Journal of Physical Chemistry C* **120**, 3705–3714 (2016).
- [45] Y. Xu, S. Liu, J. P. Edwards, Y. C. Xiao, Y. Zhao, R. K. Miao, M. Fan, Y. Chen, J. E. Huang, E. H. Sargent, and D. Sinton, *Regeneration of Direct Air CO₂ Capture Liquid via Alternating Electrocatalysis*, *Joule* **7**, 2107–2117 (2023).

- [46] I. A. Digdaya, I. Sullivan, M. Lin, L. Han, W.-H. Cheng, H. A. Atwater, and C. Xiang, *A Direct Coupled Electrochemical System for Capture and Conversion of CO₂ from Oceanwater*, Nature Communications **11**, 4412–4412 (2020).
- [47] P. Zhu, Z.-Y. Wu, A. Elgazzar, C. Dong, T.-U. Wi, F.-Y. Chen, Y. Xia, Y. Feng, M. Shakouri, J. Y. T. Kim, Z. Fang, T. A. Hatton, and H. Wang, *Continuous Carbon Capture in an Electrochemical Solid-Electrolyte Reactor*, Nature **618**, 959–966 (2023).
- [48] Z. J. Schiffer, E. Lucas, N. B. Watkins, S. Ardo, C. Xiang, and H. A. Atwater, *Acid and Base Generation via an Electrochemical Hydrogen-Looping Cell Tailored for Carbon Removal Applications*, Device **2**, 100506 (2024).
- [49] P. Mores, N. Scenna, and S. Mussati, *Post-Combustion CO₂ Capture Process: Equilibrium Stage Mathematical Model of the Chemical Absorption of CO₂ into Monoethanolamine (MEA) Aqueous Solution*, Chemical Engineering Research and Design **89**, 1587–1599 (2011).
- [50] J. Stolaroff, *Carbonate Solutions for Carbon Capture: A Summary*, tech. rep. (Lawrence Livermore National Lab.(LLNL), Livermore, CA (United States), 2013).
- [51] E. R. Monazam, L. J. Shadle, D. C. Miller, H. W. Pennline, D. J. Fauth, J. S. Hoffman, and M. L. Gray, *Equilibrium and Kinetics Analysis of Carbon Dioxide Capture Using Immobilized Amine on a Mesoporous Silica*, AIChE Journal **59**, 923–935 (2013).
- [52] G. Oreggioni, D. Friedrich, M. Luberti, H. Ahn, and S. Brandani, *Development of an Equilibrium Theory Solver Applied to Pressure Swing Adsorption Cycles Used in Carbon Capture Processes*, Computers & Chemical Engineering **94**, 18–27 (2016).
- [53] S. Jin, M. Wu, R. Gordon, M. Aziz, and D. Kwabi, *pH Swing Cycle for CO₂ Capture Electrochemically Driven Through Proton-Coupled Electron Transfer*, Energy & Environmental Science (2020).
- [54] S. Jin, M. Wu, Y. Jing, R. G. Gordon, and M. J. Aziz, *Low Energy Carbon Capture via Electrochemically Induced pH Swing with Electrochemical Rebalancing*, Nature Communications **13**, 2140–2140 (2022).
- [55] K. Amini, Y. Jing, J. Gao, J. D. Sosa, R. G. Gordon, and M. J. Aziz, *Electrochemical Performance of Mixed Redox-Active Organic Molecules in Redox Flow Batteries*, Journal of the Electrochemical Society **170**, 120535 (2023).

- [56] J. Nanda, J. Remillard, A. O'Neill, D. Bernardi, T. Ro, K. E. Nietering, J.-Y. Go, and T. J. Miller, *Local State-of-Charge Mapping of Lithium-Ion Battery Electrodes*, Advanced Functional Materials **21**, 3282–3290 (2011).
- [57] W. C. Chueh, F. El Gabaly, J. D. Sugar, N. C. Bartelt, A. H. McDaniel, K. R. Fenton, K. R. Zavadil, T. Tyliszczak, W. Lai, and K. F. McCarty, *Intercalation Pathway in Many-Particle LiFePO₄ Electrode Revealed by Nanoscale State-of-Charge Mapping*, Nano letters **13**, 866–872 (2013).
- [58] M. Planck, *Scientific autobiography, and other papers* (Philosophical Library, New York, 1949).
- [59] A. Forner-Cuenca and F. R. Brushett, *Engineering porous electrodes for next-generation redox flow batteries: recent progress and opportunities*, Current Opinion in Electrochemistry **18**, 113–122 (2019).
- [60] S. P. Dawson, S. Chen, and G. D. Doolen, *Lattice Boltzmann Computations for Reaction-Diffusion Equations*, The Journal of Chemical Physics **98**, 1514–1523 (1993).
- [61] B. Huskinson, M. P. Marshak, S. Er, M. R. Gerhardt, C. J. Galvin, X. Chen, A. Aspuru-Guzik, R. G. Gordon, and M. J. Aziz, *A metal-free organic-inorganic aqueous flow battery*, Nature **505**, edited by C. Suh, 195–198 (2014).
- [62] M. Ruderman, *Fluid dynamics and linear elasticity: a first course in continuum mechanics*, Springer Undergraduate Mathematics Series (Springer International Publishing, 2019).
- [63] A. J. Chorin, *Numerical solution of the navier-stokes equations*, Mathematics of Computation **22**, 745–762 (1968).
- [64] K. Avila, D. Moxey, A. de Lozar, M. Avila, D. Barkley, and B. Hof, *The onset of turbulence in pipe flow*, Science **333**, 192–196 (2011).
- [65] W. Deen, *Analysis of transport phenomena*, Topics in chemical engineering (Oxford University Press, 2012).
- [66] H. Darcy, *Les fontaines publiques de la ville de dijon: exposition et application des principes à suivre et des formules à employer dans les questions de distribution d'eau*, Les fontaines publiques de la ville de Dijon: exposition et application des principes à suivre et des formules à employer dans les questions de distribution d'eau ... un appendice relatif aux fournitures d'eau de plusieurs villes au filtrage des eaux v. 1 (Victor Dalmont, 1856).

- [67] M. K. Hubbert, *Darcy's law and the field equations of the flow of underground fluids*, *Transactions of the AIME* **207**, 222–239 (1956).
- [68] S. Whitaker, *Flow in porous media i: a theoretical derivation of darcy's law*, *Transport in porous media* **1**, 3–25 (1986).
- [69] A. Bard, L. Faulkner, and H. White, *Electrochemical methods: fundamentals and applications* (Wiley, 2022).
- [70] E.J. Dickinson and A.J. Wain, *The Butler-Volmer equation in electrochemical theory: origins, value, and practical application*, *Journal of Electroanalytical Chemistry* **872**, 114145 (2020).
- [71] W. Dreyer, C. Guhlke, and R. Müller, *A new perspective on the electron transfer: recovering the Butler-Volmer equation in non-equilibrium thermodynamics*, *Physical chemistry chemical physics : PCCP* **18**, 24966–24983 (2016).
- [72] M. van Soestbergen, *Frumkin-butler-volmer theory and mass transfer in electrochemical cells*, *Russian journal of electrochemistry* **48**, 570–579 (2012).
- [73] J. Zhang, H. Guo, L. Lei, S. Shen, K. Zheng, and M. Han, *A critical review of the butler-volmer equation for the activation polarization of solid oxide fuel cells*, *Journal of power sources* **613**, 234871 (2024).
- [74] J. Newman and N. Balsara, *Electrochemical systems*, The ECS Series of Texts and Monographs (Wiley, 2021).
- [75] A. A. Wong and M. J. Aziz, *Method for comparing porous carbon electrode performance in redox flow batteries*, *Journal of the Electrochemical Society* **167**, 110542 (2020).
- [76] K. Sverdrup, A. Almgren, and N. Nikiforakis, *An embedded boundary approach for efficient simulations of viscoplastic fluids in three dimensions*, *Physics of Fluids* **31**, 093102 (2019).
- [77] W. Zhang, A. Almgren, V. Beckner, J. Bell, J. Blaschke, C. Chan, M. Day, B. Friesen, K. Gott, D. Graves, M. P. Katz, A. Myers, T. Nguyen, A. Nonaka, M. Rosso, S. Williams, and M. Zingale, *AMReX: a framework for block-structured adaptive mesh refinement*, *Journal of Open Source Software* **4**, 1370 (2019).
- [78] *Hypre: high performance preconditioners*, <https://llnl.gov/casc/hypre>, <https://github.com/hypre-space/hypre>.

- [79] L. N. Trefethen and D. Bau, *Numerical linear algebra*, Twenty-fifth Anniversary (Society for Industrial and Applied Mathematics, Philadelphia, PA, 2022).
- [80] J. W. Demmel, *Applied numerical linear algebra* (Society for Industrial and Applied Mathematics, 1997).
- [81] R. Courant, K. Friedrichs, and H. Lewy, *On the partial difference equations of mathematical physics*, *IBM journal of research and development*. **11**, 215–234 (1967).
- [82] M. T. Heath, *Scientific computing: an introductory survey*, Second edition, SIAM edition., Classics in applied mathematics ; 80 (Society for Industrial and Applied Mathematics (SIAM), 2002).
- [83] W. Hackbusch, *Multi-grid methods and applications*, Springer series in computational mathematics ; 4 (Springer-Verlag, Berlin ; New York, 1985).
- [84] P. Wesseling, *Introduction to multigrid methods* (Institute for Computer Applications in Science and Engineering, 1995).
- [85] F. A. Bornemann and P. Deuflhard, *The cascadic multigrid method for elliptic problems*, *Numerische Mathematik* **75**, 135–152 (1996).
- [86] K. Pan, D. He, H. Hu, and Z. Ren, *A new extrapolation cascadic multigrid method for three dimensional elliptic boundary value problems*, *Journal of computational physics* **344**, 499–515 (2017).
- [87] C.-S. Chow and J. Tsitsiklis, *An optimal one-way multigrid algorithm for discrete-time stochastic control*, *IEEE transactions on automatic control* **36**, 898–914 (1991).
- [88] C. H. Rycroft, C.-H. Wu, Y. Yu, and K. Kamrin, *Reference map technique for incompressible fluid-structure interaction*, *Journal of Fluid Mechanics* **898**, A9 (2020).
- [89] Quotation attributed to walther nernst, Circa 1930.
- [90] C. Breyer, M. Fasihi, C. Bajamundi, and F. Creutzig, *Direct Air Capture of CO₂: A Key Technology for Ambitious Climate Change Mitigation*, Joule 3, 2053–2057 (2019).
- [91] A. Prajapati, R. Sartape, M. T. Galante, J. Xie, S. L. Leung, I. Bessa, M. H. S. Andrade, R. T. Somich, M. V. Rebouças, G. T. Hutras, N. Diniz, and M. R. Singh, *Fully-integrated electrochemical system that captures CO₂ from flue gas to produce value-added chemicals at ambient conditions*, *Energy & Environmental Science* **15**, 5105–5117 (2022).
- [92] K. S. Lackner, *A Guide to CO₂ Sequestration*, *Science* **300**, 1677–1678 (2003).

- [93] S. P. Singh, P. Hao, X. Liu, C. Wei, W. Q. Xu, N. Wei, X. Li, H. Lu, and A. Y. Ku, *Large-Scale Affordable CO₂ Capture Is Possible by 2030*, Joule **3**, 2154–2164 (2019).
- [94] Z. H. Liang, W. Rongwong, H. Liu, K. Fu, H. Gao, F. Cao, R. Zhang, T. Sema, A. Henni, K. Sumon, D. Nath, D. Gelowitz, W. Srisang, C. Saiwan, A. Benamor, M. Al-Marri, H. Shi, T. Supap, C. Chan, Q. Zhou, M. Abu-Zahra, M. Wilson, W. Olson, R. Idem, and P. P. Tontiwachwuthikul, *Recent progress and new developments in post-combustion carbon-capture technology with amine based solvents*, International Journal of Greenhouse Gas Control **40**, 26–54 (2015).
- [95] W. H. Lee, X. Zhang, S. Banerjee, C. W. Jones, M. J. Realff, and R. P. Lively, *Sorbent-coated carbon fibers for direct air capture using electrically driven temperature swing adsorption*, Joule **7**, 1241–1259 (2023).
- [96] T. Wang, K. S. Lackner, and A. Wright, *Moisture Swing Sorbent for Carbon Dioxide Capture from Ambient Air*, Environmental Science & Technology **45**, 6670–6675 (2011).
- [97] E. J. Kim, R. L. Siegelman, H. Z. H. Jiang, A. C. Forse, J.-H. Lee, J. D. Martell, P. J. Milner, J. M. Falkowski, J. B. Neaton, J. A. Reimer, S. C. Weston, and J. R. Long, *Cooperative carbon capture and steam regeneration with tetraamine-appended metal-organic frameworks*, Science **369**, 392–396 (2020).
- [98] R. L. Siegelman, E. J. Kim, and J. R. Long, *Porous materials for carbon dioxide separations*, Nature Materials **20**, 1060–1072 (2021).
- [99] W. Zhang, E. Gao, Y. Li, M. T. Bernards, Y. He, and Y. Shi, *CO₂ capture with polyamine-based protic ionic liquid functionalized mesoporous silica*, Journal of CO₂ Utilization **34**, 606–615 (2019).
- [100] X. Shi, H. Xiao, H. Azarabadi, J. Song, X. Wu, X. Chen, and K. S. Lackner, *Sorbents for the Direct Capture of CO₂ from Ambient Air*, Angewandte Chemie International Edition **59**, 6984–7006 (2020).
- [101] D. W. Keith, G. Holmes, D. St. Angelo, and K. Heidel, *A Process for Capturing CO₂ from the Atmosphere*, Joule **2**, 1573–1594 (2018).
- [102] N. Mac Dowell, D. M. Reiner, and R. S. Haszeldine, *Comparing approaches for carbon dioxide removal*, Joule **6**, 2233–2239 (2022).

- [103] K. M. Diederichsen, R. Sharifian, J. S. Kang, Y. Liu, S. Kim, B. M. Gallant, D. Vermaas, and T. A. Hatton, *Electrochemical methods for carbon dioxide separations*, Nature Reviews Methods Primers **2** (2022).
- [104] M. C. Stern, F. Simeon, H. Herzog, and T. A. Hatton, *Post-combustion carbon dioxide capture using electrochemically mediated amine regeneration*, Energy & Environmental Science **6**, 255–2517 (2013).
- [105] M. Wang, H. J. Herzog, and T. A. Hatton, *CO₂ Capture Using Electrochemically Mediated Amine Regeneration*, Industrial & Engineering Chemistry Research **59**, 7087–7096 (2020).
- [106] G. Lee, Y. C. Li, J.-Y. Kim, T. Peng, D.-H. Nam, A. Sedighian Rasouli, F. Li, M. Luo, A. H. Ip, Y.-C. Joo, and E. H. Sargent, *Electrochemical upgrade of CO₂ from amine capture solution*, Nature Energy **6**, 46–53 (2021).
- [107] H. Seo, M. Rahimi, and T. A. Hatton, *Electrochemical Carbon Dioxide Capture and Release with a Redox-Active Amine*, Journal of the American Chemical Society **144**, 2164–2170 (2022).
- [108] X. Li, X. Zhao, Y. Liu, T. A. Hatton, and Y. Liu, *Redox-tunable Lewis bases for electrochemical carbon dioxide capture*, Nature Energy **7**, 1065–1075 (2022).
- [109] Y. Liu, H.-Z. Ye, K. M. Diederichsen, T. Van Voorhis, and T. A. Hatton, *Electrochemically mediated carbon dioxide separation with quinone chemistry in salt-concentrated aqueous media*, Nature Communications **11**, 2278–2278 (2020).
- [110] K. M. Diederichsen, Y. Liu, N. Ozbek, H. Seo, and T. A. Hatton, *Toward solvent-free continuous-flow electrochemically mediated carbon capture with high-concentration liquid quinone chemistry*, Joule **6**, 221–239 (2022).
- [111] S. Jin, M. Wu, R. G. Gordon, M. J. Aziz, and D. G. Kwabi, *pH swing cycle for co₂ capture electrochemically driven through proton-coupled electron transfer*, Energy & Environmental Science **13**, 376–3722 (2020).
- [112] S. Pang, S. Jin, F. Yang, M. Alberts, L. Li, D. Xi, R. G. Gordon, P. Wang, M. J. Aziz, and Y. Ji, *A phenazine-based high-capacity and high-stability electrochemical CO₂ capture cell with coupled electricity storage*, Nature Energy **8**, 1126–1136 (2023).

- [113] S. Jin, M. Wu, Y. Jing, R. G. Gordon, and M. J. Aziz, *Low energy carbon capture via electrochemically induced pH swing with electrochemical rebalancing*, Nature Communications **13**, 2140 (2022).
- [114] H. Seo and T. A. Hatton, *Electrochemical direct air capture of CO₂ using neutral red as reversible redox-active material*, Nature Communications **14**, 313 (2023).
- [115] M. Hou, L. Chen, Z. Guo, X. Dong, Y. Wang, and Y. Xia, *A clean and membrane-free chlor-alkali process with decoupled Cl₂ and H₂/NaOH production*, Nature Communications **9**, 1–8 (2018).
- [116] J. Yang, W.-H. Li, H.-T. Tang, Y.-M. Pan, D. Wang, and Y. Li, *CO₂-mediated organocatalytic chlorine evolution under industrial conditions*, Nature **617**, 519–523 (2023).
- [117] S. M. Davis, G. E. Gray, and P. A. Kohl, *Candidate membranes for the electrochemical salt-splitting of Sodium Sulfate*, Journal of Applied Electrochemistry **38**, 777–783 (2008).
- [118] G. H. Rau, *Electrochemical Splitting of Calcium Carbonate to Increase Solution Alkalinity: Implications for Mitigation of Carbon Dioxide and Ocean Acidity*, Environmental Science & Technology **42**, 8935–8940 (2008).
- [119] C. Zhou, J. Ni, H. Chen, and X. Guan, *Harnessing electrochemical pH gradient for direct air capture with hydrogen and oxygen by-products in a calcium-based loop*, Sustainable Energy & Fuels **5**, 4355–4367 (2021).
- [120] J. Zhou and X. Guan, *Closed-Loop and Precipitation-Free CO₂ Capture Process Enabled by Electrochemical pH Gradient*, ChemSusChem **18**, e202401533 (2025).
- [121] M. Rahimi, G. Catalini, S. Hariharan, M. Wang, M. Puccini, and T. A. Hatton, *Carbon Dioxide Capture Using an Electrochemically Driven Proton Concentration Process*, Cell Reports Physical Science **1**, 100033 (2020).
- [122] R. J. Gilliam, B. K. Boggs, V. Decker, M. A. Kostowskyj, S. Gorer, T. A. Albrecht, J. D. Way, D. W. Kirk, and A. J. Bard, *Low Voltage Electrochemical Process for Direct Carbon Dioxide Sequestration*, Journal of the Electrochemical Society **159**, B627–B628 (2012).
- [123] L. Yan, J. Bao, Y. Shao, and W. Wang, *An Electrochemical Hydrogen-Looping System for Low-Cost CO₂ Capture from Seawater*, ACS Energy Letters **7**, 1947–1952 (2022).

- [124] X. Zhang, Z. Fang, P. Zhu, Y. Xia, and H. Wang, *Electrochemical regeneration of high-purity CO₂ from (bi)carbonates in a porous solid electrolyte reactor for efficient carbon capture*, *Nature Energy* **10**, 55–65 (2025).
- [125] B. Charnay, Y. Chen, R. Agarwal, J. Misleh, G. Wright, E. Sauve, W. L. Toh, Y. Surendranath, and M. Kanan, *Membrane-Free Electrochemical Production of Acid and Base Solutions Capable of Processing Ultramafic Rocks*, *ChemRxiv*, 10.26434/chemrxiv-2023-5tndz (2023).
- [126] K. Nagasubramanian, F. Chlanda, and K.-J. Liu, *Use of bipolar membranes for generation of acid and base – an engineering and economic analysis*, *Journal of Membrane Science* **2**, 109–124 (1977).
- [127] C. T. Supuran, *Carbonic Anhydrases — An Overview*, *Current Pharmaceutical Design* **14**, 603–614 (2008).
- [128] L. D. Ellis, A. F. Badel, M. L. Chiang, R. J.-Y. Park, and Y.-M. Chiang, *Toward electrochemical synthesis of cement—An electrolyzer-based process for decarbonating CaCO₃ while producing useful gas streams*, *PNAS* **117**, 12584–12591 (2020).
- [129] M. Bui, C. S. Adjiman, A. Bardow, E. J. Anthony, A. Boston, S. Brown, P. S. Fennell, S. Fuss, A. Galindo, L. A. Hackett, J. P. Hallett, H. J. Herzog, G. Jackson, J. Kemper, S. Krevor, G. C. Maitland, M. Matuszewski, I. S. Metcalfe, C. Petit, G. Puxty, J. Reimer, D. M. Reiner, E. S. Rubin, S. A. Scott, N. Shah, B. Smit, J. P. M. Trusler, P. Webley, J. Wilcox, and N. Mac Dowell, *Carbon capture and storage (CCS): the way forward*, *Energy & Environmental Science* **11**, 1062–1176 (2018).
- [130] G. T. Rochelle, *Amine Scrubbing for CO₂ Capture*, *Science* **325**, 1652–1654 (2009).
- [131] G. T. Rochelle, *Thermal degradation of amines for CO₂ capture*, *Current Opinion in Chemical Engineering* **1**, 183–190 (2012).
- [132] K. M. Diederichsen, R. Sharifian, J. S. Kang, Y. Liu, S. Kim, B. M. Gallant, D. Vermaas, and T. A. Hatton, *Electrochemical methods for carbon dioxide separations*, *Nature Reviews Methods Primers* **2** (2022).
- [133] P. Singh, J. H. Rheinhardt, J. Z. Olson, P. Tarakeshwar, V. Mujica, and D. A. Buttry, *Electrochemical Capture and Release of Carbon Dioxide Using a Disulfide–Thiocarbonate Redox Cycle*, *Journal of the American Chemical Society* **139**, 1033–1036 (2017).

- [134] M. Rahimi, A. Khurram, T. A. Hatton, and B. Gallant, *Electrochemical carbon capture processes for mitigation of CO₂ emissions*, Chemical Society Reviews **51**, 8676–8695 (2022).
- [135] Y. Liu, H.-Z. Ye, K. M. Diederichsen, T. Van Voorhis, and T. A. Hatton, *Electrochemically mediated carbon dioxide separation with quinone chemistry in salt-concentrated aqueous media*, Nature Communications **11**, 2278–2278 (2020).
- [136] X. Li, X. Zhao, Y. Liu, T. A. Hatton, and Y. Liu, *Redox-tunable Lewis bases for electrochemical carbon dioxide capture*. Nature Energy **7**, 1065–1075 (2022).
- [137] B. Gurkan, F. Simeon, and T. A. Hatton, *Quinone Reduction in Ionic Liquids for Electrochemical CO₂ Separation*, ACS Sustain. Chem. Eng. **3**, 1394–1405 (2015).
- [138] K. M. Diederichsen, Y. Liu, N. Ozbek, H. Seo, and T. A. Hatton, *Toward solvent-free continuous-flow electrochemically mediated carbon capture with high-concentration liquid quinone chemistry*, Joule **6**, 221–239 (2022).
- [139] J. M. Barlow and J. Y. Yang, *Oxygen-Stable Electrochemical CO₂ Capture and Concentration with Quinones Using Alcohol Additives*, Journal of the American Chemical Society **144**, 14161–14169 (2022).
- [140] S. Voskian and T. A. Hatton, *Faradaic electro-swing reactive adsorption for CO₂ capture*, Energy & Environmental Science **12**, 3530–3547 (2019).
- [141] *Anthraquinone thin-film electrodes for reversible CO₂ capture and release*, Journal of Materials Chemistry A **6**, 15095–15101 (2018).
- [142] Y. Jing, K. Amini, D. Xi, S. Jin, A. M. Alfaraidi, E. F. Kerr, R. G. Gordon, and M. J. Aziz, *Electrochemically Induced CO₂ Capture Enabled by Aqueous Quinone Flow Chemistry*, ACS Energy Letters **9**, 3526–3535 (2024).
- [143] C. Huang, C. Liu, K. Wu, H. Yue, S. Tang, H. Lu, and B. Liang, *CO₂ Capture from Flue Gas Using an Electrochemically Reversible Hydroquinone/Quinone Solution*, Energy & Fuels **33**, 3380–3389 (2019).
- [144] L. Luo, L. Hou, Y. Liu, K. Wu, Y. Zhu, H. Lu, and B. Liang, *Regeneration of Na₂Q in an Electrochemical CO₂ Capture System*, Energy & Fuels **35**, 12260–12269 (2021).

- [145] E. F. Kerr, Z. Tang, T. Y. George, S. Jin, E. M. Fell, K. Amini, Y. Jing, M. Wu, R. G. Gordon, and M. J. Aziz, *High Energy Density Aqueous Flow Battery Utilizing Extremely Stable, Branching-Induced High-Solubility Anthraquinone near Neutral pH*, ACS Energy Letters **8**, 600–607 (2023).
- [146] D. G. Kwabi, Y. Ji, and M. J. Aziz, *Electrolyte Lifetime in Aqueous Organic Redox Flow Batteries: A Critical Review*, Chemical Reviews **120**, 6467–6489 (2020).
- [147] M. Wu, M. Bahari, Y. Jing, K. Amini, E. M. Fell, T. Y. George, R. G. Gordon, and M. J. Aziz, *Highly Stable, Low Redox Potential Quinone for Aqueous Flow Batteries*, Batteries & Supercaps **5**, n/a (2022).
- [148] R. N. Roy, L. N. Roy, K. M. Vogel, C. Porter-Moore, T. Pearson, C. E. Good, F. J. Millero, and D. M. Campbell, *The dissociation constants of carbonic acid in seawater at salinities 5 to 45 and temperatures 0 to 45°C*, Marine Chemistry **44**, 249–267 (1993).
- [149] W. Henry, *Experiments on the quantity of gases absorbed by water, at different temperatures, and under different pressures*, Philosophical Transactions of the Royal Society of London **93**, 29–274 (1803).
- [150] I. Newton and R. Hooke, *Isaac newton letter to robert hooke*, 1675.
- [151] M.-A. Goulet, M. Eikerling, and E. Kjeang, *Direct measurement of electrochemical reaction kinetics in flow-through porous electrodes*, Electrochemistry Communications **57**, 14–17 (2015).
- [152] K. V. Greco, A. Forner-Cuenca, A. Mularczyk, J. Eller, and F. R. Brushett, *Elucidating the nuanced effects of thermal pretreatment on carbon paper electrodes for vanadium redox flow batteries*, ACS Applied Materials & Interfaces **10**, 44430–44442 (2018).
- [153] H. Park, G. Kwon, H. Lee, K. Lee, S. Y. Park, J. E. Kwon, K. Kang, and S. J. Kim, *In operando visualization of redox flow battery in membrane-free microfluidic platform*, PNAS **119**, e2114947119 (2022).
- [154] X. Huang, Q. Wang, X. Y. Chen, and Z. J. Zhang, *The effects of amine/nitro/hydroxyl groups on the benzene rings of redox additives on the electrochemical performance of carbon-based supercapacitors*, Physical Chemistry Chemical Physics **18**, 10438–10452 (2016).
- [155] A. J. Slate, D. A. Brownson, A. S. A. Dena, G. C. Smith, K. A. Whitehead, and C. E. Banks, *Exploring the electrochemical performance of graphite and graphene paste electrodes composed of varying lateral flake sizes*, Physical Chemistry Chemical Physics **20**, 20010–20022 (2018).

- [156] X. Zhou, T. Zhao, Y. Zeng, L. An, and L. Wei, *A highly permeable and enhanced surface area carbon-cloth electrode for vanadium redox flow batteries*, Journal of Power Sources **329**, 247–254 (2016).
- [157] Y. A. Gandomi, D. Aaron, T. Zawodzinski, and M. Mench, *In situ potential distribution measurement and validated model for all-vanadium redox flow battery*, Journal of The Electrochemical Society **163**, A5188 (2015).
- [158] Q. Chen, M. R. Gerhardt, and M. J. Aziz, *Dissection of the voltage losses of an acidic quinone redox flow battery*, Journal of The Electrochemical Society **164**, A1126 (2017).
- [159] L. Tong, Q. Chen, A. A. Wong, R. Gómez-Bombarelli, A. Aspuru-Guzik, R. G. Gordon, and M. J. Aziz, *UV-Vis spectrophotometry of quinone flow battery electrolyte for in situ monitoring and improved electrochemical modeling of potential and quinhydrone formation*, Physical Chemistry Chemical Physics **19**, 31684–31691 (2017).
- [160] E. W. Zhao, T. Liu, E. Jónsson, J. Lee, I. Temprano, R. B. Jethwa, A. Wang, H. Smith, J. Carretero-González, Q. Song, et al., *In situ NMR metrology reveals reaction mechanisms in redox flow batteries*, Nature **579**, 224–228 (2020).
- [161] Y. Jing, E. W. Zhao, M.-A. Goulet, M. Bahari, E. M. Fell, S. Jin, A. Davoodi, E. Jónsson, M. Wu, C. P. Grey, et al., *In situ electrochemical recombination of decomposed redox-active species in aqueous organic flow batteries*, Nature Chemistry **14**, 1103–1109 (2022).
- [162] E. W. Zhao, E. Jónsson, R. B. Jethwa, D. Hey, D. Lyu, A. Brookfield, P. A. Klusener, D. Collison, and C. P. Grey, *Coupled in situ NMR and EPR studies reveal the electron transfer rate and electrolyte decomposition in redox flow batteries*, Journal of the American Chemical Society **143**, 1885–1895 (2021).
- [163] C. Jia, Q. Liu, C.-J. Sun, F. Yang, Y. Ren, S. M. Heald, Y. Liu, Z.-F. Li, W. Lu, and J. Xie, *In situ x-ray near-edge absorption spectroscopy investigation of the state of charge of all-vanadium redox flow batteries*, ACS Applied Materials & Interfaces **6**, 17920–17925 (2014).
- [164] R. Jervis, L. D. Brown, T. P. Neville, J. Millichamp, D. P. Finegan, T. M. Heenan, D. J. Brett, and P. R. Shearing, *Design of a miniature flow cell for in situ x-ray imaging of redox flow batteries*, Journal of Physics D: Applied Physics **49**, 434002 (2016).
- [165] L. Bouffier and T. Doneux, *Coupling electrochemistry with in situ fluorescence (confocal) microscopy*, Current Opinion in Electrochemistry **6**, 31–37 (2017).

- [166] R. C. Engstrom, S. Ghaffari, and H. Qu, *Fluorescence imaging of electrode-solution interfacial processes*, Analytical Chemistry **64**, 2525–2529 (1992).
- [167] W. J. Bowyer, J. Xie, and R. C. Engstrom, *Fluorescence imaging of the heterogeneous reduction of oxygen*, Analytical Chemistry **68**, 2005–2009 (1996).
- [168] J. E. Vitt and R. C. Engstrom, *Imaging of oxygen evolution and oxide formation using quinine fluorescence*, Analytical Chemistry **69**, 1070–1076 (1997).
- [169] J. C. O'Brien, J. Shumaker-Parry, and R. C. Engstrom, *Microelectrode control of surface-bound enzymatic activity*, Analytical Chemistry **70**, 1307–1311 (1998).
- [170] J. P. Guerrette, S. J. Percival, and B. Zhang, *Fluorescence coupling for direct imaging of electrocatalytic heterogeneity*, Journal of the American Chemical Society **135**, 855–861 (2013).
- [171] N. C. Rudd, S. Cannan, E. Bitziou, I. Ciani, A. L. Whitworth, and P. R. Unwin, *Fluorescence confocal laser scanning microscopy as a probe of pH gradients in electrode reactions and surface activity*, Analytical Chemistry **77**, 6205–6217 (2005).
- [172] C. Renault, K. Marchuk, H. S. Ahn, E. J. Titus, J. Kim, K. A. Willets, and A. J. Bard, *Observation of nanometer-sized electro-active defects in insulating layers by fluorescence microscopy and electrochemistry*, Analytical Chemistry **87**, 5730–5737 (2015).
- [173] J. L. Shepherd, A. Kell, E. Chung, C. W. Sinclair, M. S. Workentin, and D. Bizzotto, *Selective reductive desorption of a SAM-coated gold electrode revealed using fluorescence microscopy*, Journal of the American Chemical Society **126**, 8329–8335 (2004).
- [174] A. Musgrove, A. Kell, and D. Bizzotto, *Fluorescence imaging of the oxidative desorption of a BODIPY-alkyl-thiol monolayer coated Au bead*, Langmuir **24**, 7881–7888 (2008).
- [175] J. R. Casanova-Moreno and D. Bizzotto, *What happens to the thiolates created by reductively desorbing SAMs? An in situ study using fluorescence microscopy and electrochemistry*, Langmuir **29**, 2065–2074 (2013).
- [176] A. Meunier, E. Triffaux, D. Bizzotto, C. Buess-Herman, and T. Doneux, *In Situ Fluorescence Microscopy Study of the Interfacial Inhomogeneity of DNA Mixed Self-Assembled Monolayers at Gold Electrodes*, ChemElectroChem **2**, 434–442 (2015).

- [177] Z. L. Yu, J. Casanova-Moreno, I. Guryanov, F. Maran, and D. Bizzotto, *Influence of surface structure on single or mixed component self-assembled monolayers via in situ spectroelectrochemical fluorescence imaging of the complete stereographic triangle on a single crystal Au bead electrode*, Journal of the American Chemical Society **137**, 276–288 (2015).
- [178] C. Amatore, S. Arbault, Y. Chen, C. Crozatier, F. Lemaître, and Y. Verchier, *Coupling of electrochemistry and fluorescence microscopy at indium tin oxide microelectrodes for the analysis of single exocytotic events*, Angewandte Chemie International Edition **45**, 4000–4003 (2006).
- [179] D. S. Chung and R. C. Alkire, *Confocal microscopy for simultaneous imaging of Cu electrodeposit morphology and adsorbate fluorescence*, Journal of the Electrochemical Society **144**, 1529 (1997).
- [180] S. Cannan, I. D. Macklam, and P. R. Unwin, *Three-dimensional imaging of proton gradients at microelectrode surfaces using confocal laser scanning microscopy*, Electrochemistry communications **4**, 886–892 (2002).
- [181] A. A. Wong, S. M. Rubinstein, and M. J. Aziz, *Direct visualization of electrochemical reactions and heterogeneous transport within porous electrodes in operando by fluorescence microscopy*, Cell Reports Physical Science **2** (2021).
- [182] J. Newman and W. Tiedemann, *Flow-through Porous Electrodes*, Advances in Electrochemistry and Electrochemical Engineering **11**, 352–438 (1978).
- [183] Y. Jing, E. M. Fell, M. Wu, S. Jin, Y. Ji, D. A. Pollack, Z. Tang, D. Ding, M. Bahari, M.-A. Goulet, et al., *Anthraquinone flow battery reactants with nonhydrolyzable water-solubilizing chains introduced via a generic cross-coupling method*, ACS Energy Letters **7**, 226–235 (2021).
- [184] B. Huskinson, M. P. Marshak, C. Suh, S. Er, M. R. Gerhardt, C. J. Galvin, X. Chen, A. Aspuru-Guzik, R. G. Gordon, and M. J. Aziz, *A metal-free organic–inorganic aqueous flow battery*, Nature **505**, 195–198 (2014).
- [185] M. Wu, M. Bahari, E. M. Fell, R. G. Gordon, and M. J. Aziz, *High-performance anthraquinone with potentially low cost for aqueous redox flow batteries*, Journal of Materials Chemistry A **9**, 26709–26716 (2021).
- [186] Z. Yang, L. Tong, D. P. Tabor, E. S. Beh, M.-A. Goulet, D. De Porcellinis, A. Aspuru-Guzik, R. G. Gordon, and M. J. Aziz, *Alkaline benzoquinone aqueous flow battery for large-scale storage of electrical energy*, Advanced Energy Materials **8**, 1702056 (2018).

- [187] D. G. Kwabi, K. Lin, Y. Ji, E. F. Kerr, M.-A. Goulet, D. De Porcellinis, D. P. Tabor, D. A. Pollock, A. Aspuru-Guzik, R. G. Gordon, and M. J. Aziz, *Alkaline Quinone Flow Battery with Long Lifetime at pH 12*, Joule 2, 1907–1908 (2018).
- [188] M. L. Perry, R. M. Darling, and R. Zaffou, *High Power Density Redox Flow Battery Cells*, ECS transactions 53, 7–16 (2013).
- [189] Q. Chen, L. Eisenach, and M. J. Aziz, *Cycling Analysis of a Quinone-Bromide Redox Flow Battery*, Journal of the Electrochemical Society 163, A5057–A5063 (2016).
- [190] M.-A. Goulet and M. J. Aziz, *Flow Battery Molecular Reactant Stability Determined by Symmetric Cell Cycling Methods*, Journal of the Electrochemical Society 165, A1466–A1477 (2018).
- [191] C. Wiberg, T.J. Carney, F. Brushett, E. Ahlberg, and E. Wang, *Dimerization of 9,10-anthraquinone-2,7-Disulfonic acid (AQDS)*, Electrochimica Acta 317, 478–485 (2019).
- [192] T.J. Carney, S. J. Collins, J. S. Moore, and F. R. Brushett, *Concentration-Dependent Dimerization of Anthraquinone Disulfonic Acid and Its Impact on Charge Storage*, Chemistry of Materials 29, 4801–4810 (2017).
- [193] L. Tong, Q. Chen, A. A. Wong, R. Gómez-Bombarelli, A. Aspuru-Guzik, R. G. Gordon, and M. J. Aziz, *UV-Vis spectrophotometry of quinone flow battery electrolyte for in situ monitoring and improved electrochemical modeling of potential and quinhydrone formation*, Physical Chemistry Chemical Physics 19, 31684–31691 (2017).
- [194] G. Bradski, *The opencv library*. Dr. Dobb's Journal: Software Tools for the Professional Programmer 25, 120–123 (2000).
- [195] A. Volta, *De vi attractiva ignis electrici, ac phaenomenis inde pendentibus alexandri voluae... dissertatione epistolaris* (typis Octavii Staurenghi, 1769).
- [196] D. Trebotich, *Exascale Computational Fluid Dynamics in Heterogeneous Systems*, Journal of Fluids Engineering 146, 041104 (2024).
- [197] L. Wright and S. Davidson, *How to Tell the Difference Between a Model and a Digital Twin*, Advanced Modeling and Simulation in Engineering Sciences 7, 1–13 (2020).
- [198] F. Tao, B. Xiao, Q. Qi, J. Cheng, and P. Ji, *Digital Twin Modeling*, Journal of Manufacturing Systems 64, 372–389 (2022).

- [199] A. McClenaghan, J. Gopsill, R. Ballantyne, and B. Hicks, *Cost Benefit Analysis for Digital Twin Model Selection at the Time of Investment*, *Procedia CIRP* **120**, 56th CIRP International Conference on Manufacturing Systems 2023, 1197–1202 (2023).
- [200] A. Berkowitz, A. A. Caiado, S. R. Aravamuthan, A. Roy, E. Agar, and M. Inalpolat, *Optimization framework for redox flow battery electrodes with improved microstructural characteristics*, *Energy Advances* **3**, 222–2237 (2024).
- [201] M. D. R. Kok, R. Jervis, T. G. Tranter, M. A. Sadeghi, D. J. L. Brett, P. R. Shearing, and J. T. Gostick, *Mass Transfer in Fibrous Media with Varying Anisotropy for Flow Battery Electrodes: Direct Numerical Simulations with 3d X-Ray Computed Tomography*, *Chemical Engineering Science* **196**, 104–115 (2019).
- [202] D. Zhang, A. Forner-Cuenca, O. O. Taiwo, V. Yufit, F. R. Brushett, N. P. Brandon, S. Gu, and Q. Cai, *Understanding the Role of the Porous Electrode Microstructure in Redox Flow Battery Performance Using an Experimentally Validated 3d Pore-Scale Lattice Boltzmann Model*, *Journal of Power Sources* **447**, 227249 (2020).
- [203] M. van der Heijden, M. Kroese, Z. Borneman, and A. Forner-Cuenca, *Investigating mass transfer relationships in stereolithography 3d printed electrodes for redox flow batteries*, *Advanced Materials Technologies* **8**, 2300611 (2023).
- [204] R. Ohana, M. McCabe, L. T. Meyer, R. Morel, F. J. Agocs, M. Beneitez, M. Berger, B. Burkhart, S. B. Dalziel, D. B. Fielding, D. Fortunato, J. A. Goldberg, K. Hirashima, Y.-F. Jiang, R. Kerswell, S. Maddu, J. M. Miller, P. Mukhopadhyay, S. S. Nixon, J. Shen, R. Watteaux, B. R.-S. Blancard, F. Rozet, L. H. Parker, M. Cranmer, and S. Ho, “The well: a large-scale collection of diverse physics simulations for machine learning,” *The thirty-eight conference on neural information processing systems datasets and benchmarks track* (2024).
- [205] S. Wan, X. Liang, H. Jiang, J. Sun, N. Djilali, and T. Zhao, *A coupled machine learning and genetic algorithm approach to the design of porous electrodes for redox flow batteries*, *Applied Energy* **298**, 117177 (2021).
- [206] S. Wan, H. Jiang, Z. Guo, C. He, X. Liang, N. Djilali, and T. Zhao, *Machine learning-assisted design of flow fields for redox flow batteries*, *Energy & Environmental Science* **15**, 2874–2888 (2022).

- [207] X. Ding, V. Sanchez, K. Bertoldi, and C. H. Rycroft, *Unravelling the mechanics of knitted fabrics through hierarchical geometric representation*, *Proceedings of the Royal Society A: Mathematical, Physical and Engineering Sciences* **480**, 20230753 (2024).
- [208] J. Newman and N. Balsara, *Electrochemical systems*, The ECS Series of Texts and Monographs (Wiley, 2021).
- [209] E. J. Wilson and C. J. Geankolis, *Liquid Mass Transfer at Very Low Reynolds Numbers in Packed Beds*, *Industrial & Engineering Chemistry Fundamentals* **5**, 9–14 (1966).
- [210] R. M. Darling and M. L. Perry, *The Influence of Electrode and Channel Configurations on Flow Battery Performance*, *Journal of The Electrochemical Society* **161**, A1381 (2014).
- [211] R. N. Aslin, P. Braverman, A. V. D. Roux, M. Gold, K. M. Harris, B. Landau, C. F. Manski, D. S. Massey, L. Nadel, B. D. Santer, K. Struhl, R. Weymann, and S. H. Woolf, *Public Statement on Supporting Science for the Benefit of All Citizens*, Open Letter, addressed by leading researchers to Trump Administration, 2025.
- [212] *Trump Administration Has Begun a War on Science, Researchers Say*, The New York Times (2025).
- [213] H. Gauch, *Scientific Method in Practice* (Cambridge University Press, 2003).
- [214] J. Dalton, *A New System of Chemical Philosophy*, Vol. 2 (S. Russell, 1810).
- [215] J. C. Maxwell, *A Treatise on Electricity and Magnetism*, Vol. 1 (Clarendon press, 1873).
- [216] L. Pasteur, *On alcoholic fermentation*, The London, Edinburgh, and Dublin Philosophical Magazine and Journal of Science **18**, 239–240 (1859).
- [217] D. Raoult, N. Mouffok, I. Bitam, R. Piarroux, and M. Drancourt, *Plague: History and Contemporary Analysis*, *Journal of Infection* **66**, 18–26 (2013).
- [218] G. Alfani and C. Ó. Gráda, *Famine in European History* (Cambridge University Press, 2017).
- [219] L. White Jr, *Technology and Invention in the Middle Ages*, *Speculum* **15**, 141–159 (1940).
- [220] W. C. Brown, *Violence in Medieval Europe* (Routledge, 2014).
- [221] D. L. Plucknett, *Science and Agricultural Transformation*, (1993).

- [222] N. Koning, M. Van Ittersum, G. Becx, M. Van Boekel, W. Brandenburg, J. Van Den Broek, J. Goudriaan, G. Van Hofwegen, R. Jongeneel, J. Schiere, et al., *Long-term Global Availability of Food: Continued Abundance or New Scarcity?* NJAS: Wageningen Journal of Life Sciences **55**, 229–292 (2008).
- [223] L. Kuijer and M. Watson, ‘*That’s when we started using the living room’: Lessons from a Local History of Domestic Heating in the United Kingdom*, Energy Research & Social Science **28**, 77–85 (2017).
- [224] S. Basile, *Cool: How Air Conditioning Changed Everything* (Fordham University Press, 2014).
- [225] W. H. Carter, *Flushed: How the Plumber Saved Civilization* (Simon and Schuster, 2006).
- [226] S. Bowden and A. Offer, *Household Appliances and the Use of Time: the United States and Britain Since the 1920s*, Economic History Review, 725–748 (1994).
- [227] A. Saleh, S. Qamar, A. Tekin, R. Singh, and R. Kashyap, *Vaccine Development Throughout History*, Cureus **13** (2021).
- [228] T. Barker, *The Economic and Social Effects of the Spread of Motor Vehicles: an International Centenary Tribute* (Springer, 2016).
- [229] J. Whitelegg, *Aviation: the Social, Economic and Environmental Impact of Flying*, Ashden Trust, London (2000).
- [230] R. S. Rosenberg, *The Social Impact of Computers* (Elsevier, 2013).
- [231] J. Agar, *Constant Touch: A Global History of the Mobile Phone* (Icon Books Ltd, 2013).
- [232] B. Lojek, *History of Semiconductor Engineering* (Springer, 2007).
- [233] H. Haug and S. W. Koch, *Quantum Theory of the Optical and Electronic Properties of Semiconductors* (World Scientific, 2009).
- [234] S. Pinker, *The Better Angels of our Nature: Why Violence has Declined* (Penguin books, 2012).
- [235] A. N. Whitehead, *Science and the Modern World: Lowell Lectures, 1925* (New American Library, 1925).
- [236] B. Kennedy, A. Tyson, and C. Funk, *Americans’ Trust in Scientists, Other Groups Declines*, Vol. 1 (JSTOR, 2022).
- [237] *Why So Many Americans are Losing Trust in Science*, [The New York Times \(2023\)](#).

- [238] J. Cole, *The Great American University: Its Rise to Preeminence, Its Indispensable National Role, Why It Must Be Protected* (PublicAffairs, 2010).
- [239] *Trump Administration Makes Deep Cuts to Science Funding*, NPR (2023).
- [240] *Abandoned in the Middle of Clinical Trials, Because of a Trump Order*, The New York Times (2025).
- [241] *These Words Are Disappearing in the New Trump Administration*, The New York Times (2025).
- [242] *The US Agency that Monitors Weather Will Cut Another 1,000 jobs, AP Sources Say*, Associated Press (2025).
- [243] *Trump Bars Federal Scientists from Working on Pivotal Global Climate Report*, CNN (2025).
- [244] H. E. Brady and T. B. Kent, *Fifty Years of Declining Confidence & Increasing Polarization in Trust in American Institutions*, Daedalus **151**, 43–66 (2022).
- [245] D. Bok, *Reclaiming the public trust*, Change: The magazine of higher learning **24**, 13–19 (1992).
- [246] R. L. Geiger, *To Advance Knowledge: The Growth of American Research Universities, 1900-1940* (Routledge, 2017).
- [247] *U.S. Confidence in Higher Education Now Closely Divided*, Gallup (2024).
- [248] N. Gross and S. Simmons, *Professors and Their Politics* (JHU Press, 2014).
- [249] *Disdain for the Less Educated: Letter*, The New York Times (2020).
- [250] J. J. Mijs and M. Savage, *Meritocracy, Elitism and Inequality*, The Political Quarterly **91**, 397–404 (2020).
- [251] M. J. Sandel, *How Meritocracy Fuels Inequality—Part I The Tyranny of Merit: An Overview*, American Journal of Law and Equality **1**, 4–14 (2021).
- [252] *Columbia Agrees to Trump's Demands After Federal Funds Are Stripped*, The New York Times (2025).
- [253] *Trends in American scientists' political donations and implications for trust in science*, author=Kaurov, Alexander A and Cologna, Viktoria and Tyson, Charlie and Oreskes, Naomi, Humanities and Social Sciences Communications **9**, 1–8 (2022).
- [254] A. C. Kozlowski, *How Conservatives Lost Confidence in Science: The Role of Ideological Alignment in Political Polarization*, Social Forces **100**, 1415–1443 (2021).

- [255] B. Smith, *American Science Policy Since World War II* (Brookings Institution Press, 2011).
- [256] R. T. Lackey, *Science, Scientists, and Policy Advocacy*, Conservation Biology **21**, 12–17 (2007).
- [257] T. D. Pollard, *The Obligation for Biologists to Commit to Political Advocacy*, Cell **151**, 239–243 (2012).
- [258] M. Cockrell, K. Dubickas, M. Hepner, A. Ilich, and M. McCarthy, *Embracing Advocacy in Science, Fisheries* **43**, 179–182 (2018).
- [259] M. Boykoff and D. Oonk, *Evaluating the Perils and Promises of Academic Climate Advocacy*, Climatic Change **163**, 27–41 (2020).
- [260] C. Böhringer, *The Kyoto Protocol: a Review and Perspectives*, Oxford Review of Economic Policy **19**, 451–466 (2003).
- [261] S. Abraham, *The Bush Administration’s Approach to Climate Change*, Science **305**, 616–617 (2004).
- [262] G. W. Bush, *US Council on Environmental Quality - Clean Energy Policy*, 2001.
- [263] W. Shawcross, *Queen and Country: the Fifty-Year Reign of Elizabeth II* (Simon and Schuster, 2002).
- [264] F. S. University, *Water density calculator*, 2025.
- [265] E. Toolbox, *Water - dynamic (absolute) and kinematic viscosity vs. temperature and pressure*, 2025.
- [266] N. Tzanetakis, J. Varcoe, R. Slade, and K. Scott, *Salt splitting with radiation grafted PVDF anion-exchange membrane*, Electrochemistry Communications **5**, 115–119 (2003).
- [267] X. Guan, G. Zhang, J. Li, S. C. Kim, G. Feng, Y. Li, T. Cui, A. Brest, and Y. Cui, *Seawater alkalization via an energy-efficient electrochemical process for CO₂ capture*, PNAS **121**, 1 (2024).
- [268] J. Platoff, “Catalogue Arias and the ‘Catalogue Aria’,” *Wolfgang Amadè Mozart: Essays on His Life and His Music*, edited by Sadie, Stanley (Clarendon Press; Oxford University Press, 1996), pp. 296–311.

THIS THESIS WAS TYPESET using L^AT_EX, originally developed by Leslie Lamport and based on Donald Knuth's T_EX. The body text is set in 11 point Egenolff-Berner Garamond, a revival of Claude Garamont's humanist typeface. Musical engravings were done in Sibelius by Kivie Cahn-Lipman and typeset as images, except for the dedication, which I set myself using Dorico.